Université du Québec

INRS -Énergie, matériaux et télécommunications

Electrocatalytic Activity of Small Organic Molecules at PtAu Alloy Nanoparticles for Fuel Cells and Electrochemical Biosensing Applications

Par

Daniel Nii OKO

Thèse présentée pour l'obtention du grade de
Philosophiae doctor (Ph.D.) en Science de l'Énergie et des Matériaux

Jury d'évaluation

President of the Jury et Examinateur interne:	Professeur Shuhui Sun INRS - Énergie, matériaux et télécommunications
Examinatrice externe:	Professeur E. Bradley Easton Université du Ontario Institute of Technology
Examinateur externe:	Professeur Sasha Omanovic Université Mcgill
Directrice de recherche:	Professeure Ana Tavares INRS - Énergie, matériaux et télécommunications
Co-Directeur de recherche:	Professeur Daniel Guay INRS - Énergie, matériaux et télécommunications

Declaration

I hereby certify that this thesis, which I now submit for assessment on the programme of study leading to the award of Ph.D, is entirely my own work and has not been taken from the work of others save and to the extent that such work has been cited and acknowledged within the text of my work.

Signed……………………………………………………

Name> Daniel Nii OKO

Date……………………………………………

Abstract

Nano science and technology have received much attention recently due to their exciting applications in the fields of clean energy technology and biomedical sensing devices. Also what makes nano science and technology more relevant in this 21st century is the increasing environmental concern and accelerated depletion of fossil fuels. This realization has spark the renewed research interests in the development of new technology using alternative energy sources, most noticeably those fuels that can be utilized by proton exchange membrane fuel cells (PEMFCs). A broad spectrum of nano materials of distinct sizes, morphologies and compositions are now available for application in clean energy and biosensing technologies.

Platinum (Pt), gold (Au) and PtAu alloy nanoparticles (NPs), were applied in this work for designing cost effective novel electrocatalysts for PEMFCs and biosensing systems. These nanoparticles did not only improve the electrocatalysis of small organic molecules for fuel cell application (Methanol Fuel cells and Direct Formic acid fuel cells) but also showed enhanced performance towards the oxidation of bio-analytical molecules (ascorbic acid and dopamine) with promising values of sensitivity and selectivity. The goal of the research is to provide deeper insight into the mechanisms and structure-sensitivity of these oxidation reactions on these metal nanoparticles electrodes.

.

The specific objective of the thesis work was to study the oxidation of formic acid, methanol, dopamine and ascorbic acid on platinum-gold nanoparticles by employing conventional electrochemical methods. The platinum-gold alloy nanoparticles of varying composition. (Pt_xAu_{100-x} alloy NPs) were supplied by our collaborators and were synthesized by pulsed laser ablation in aqueous medium via a single metal target prepared from mixtures of pure platinum and pure gold nanoparticles. Cyclic voltammetry and chronoamperometry studies of formic acid and methanol oxidation on platinum-gold alloy nanoparticles in sulphuric acid electrolyte solution were performed to determine the influence of the nanoparticles composition on the mechanism and kinetics of the oxidation reactions. As a result of the low catalytic activity of the nanoparticles towards methanol oxidation in acidic medium, we also investigated the methanol oxidation in alkaline medium. In the case of ascorbic acid and dopamine oxidation, in addition

to the voltammetric studies, differential pulse voltammetry was also employed to probe the current response as an evolution of the analytes concentration changes in phosphate buffer solution (PBS) in a neutral medium.

During the electrocatalytic performances of the PtAu alloy NPs towards the formic acid oxidation, the formic acid oxidation followed a dehydrogenation pathway on these as-prepared PtAu alloy NPs. However, the dehydration was the privileged mechanism on as-prepared mixtures of pure Pt and pure Au NPs. After electrochemical aging in 0.5 M sulphuric acid, the dehydrogenation pathway was the privileged reaction pathway on both PtAu alloy and Pt+Au mixture NPs. This was attributed to the structure modification of Pt and Au nanoparticles through electrochemical aging which makes the Pt+Au mixture to behavior as an alloy. It was suggested that metal dissolution and metal redeposition occur during the electrochemical aging process resulting in possible atomistic re-organization on the catalyst surface. Also, after 600 s of potentiostatic polarization, the mass activities of PtAu alloy NPs displayed a factor of 2 times larger than that of the Pt+Au mixtures with the same surface composition. Nevertheless, both types of catalysts display similar activity with respect to the total electrochemically active surface area.

During methanol oxidation in alkaline environment, the bifunctional character of PtAu alloys emerged quite clearly with 50-50 bimetallic composition: the ability of Au surface atoms to provide active sites for oxygen-containing species such as OH_{ads} at low electrode potentials facilitated the oxidation of CO migrating to these sites from either Pt or Au sites. In addition, it was found that the intrinsic activity and mass activity of Pt in the PtAu NPs towards oxidation reaction of methanol reaction was 8 times and 5 times larger for $Pt_{30}Au_{70}$ NPs (Au-rich alloy) with respect to Pt NPs and $Pt_{70}Au_{30}$ NPs (Pt-rich alloy). We suggested that this enhancement was due to an additional electronic effect on the adsorption strength of CO and CO-like species on Pt-Au pair sites as against the Au sites, therefore shifting the equilibrium position of the methanol oxidation reaction (MOR) to more negative omset potential. The strong synergistic effect PtAu alloy electrode toward the electrooxidation of MOR in alkaline medium was not observed for the same composition of PtAu alloy electrodes in acidic environment. Instead, a continuous decrease in activity with increasing Au content in PtAu NPs was found in acid medium. The

electrocatalytic behavior of the PtAu alloy NPs electrodes towards MOR in acidic medium were merely due to ensemble effect of neighboring atoms.

This thesis also describes results of an investigation of the electrocatalytic oxidation of dopamine (DA) and ascorbic acid (AA) on Au_xPt_{100-x} alloy nanoparticles catalysts prepared by pulsed laser ablation in water. The electrochemical sensing and properties of AuPt NPs was found to be dependent on the bimetallic compositions of the NPs. Electrochemical studies have shown that the catalytic oxidation of DA and AA on AuPt NPs electrodes can afford a peak potential separation of 156 mV and 190 mV on Au and $Au_{50}Pt_{50}$ alloy NPs respectively which was large enough for the determination of DA in AA/DA mixed solution. The Au-rich alloy electrode exhibited superior electrocatalytic activity towards AA oxidation due to synergic effect between alloy Au and Pt in AuPt alloy shifting the potential to the more negative direction as compared to Au NPs. Further, while the Au and $Au_{50}P_{t50}$ NPs favored sensing of dopamine, the $Au_{70}Pt_{30}$ NPs favored AA oxidation. The DA and AA oxidation current increases linearly with DA and AA concentration respectively for all selected electrodes.

Prior to the electro-oxidation of these small organic molecules (formic acid, methanol oxidation, ascorbic acid and dopamine) on the AuPt-based alloy nanoparticles, electrochemical cycling was performed in acid, neutral and alkaline medium based on the type of molecules studied. The effect of alloying on the peak positions of the metal oxide reduction of the nanoparticles in these media was correlated. While the Pt-oxide reduction peak shifted negatively in all media with increasing Au content in the bimetallic AuPt NPs, the Au-oxide reduction peak remain fairly constant in all media with Au content in the AuPt bimetallic NPs. In general, the application of these nanoparticles could bring many advantages for the fuel cell and sensing systems investigated in this work.

Daniel Nii OKO

Prof. Ana C. Tavares

Acknowledgments

I would like to express my heartfelt gratitude and appreciation to my advisor and co-advisor, messers Prof. Ana Tavares and Prof. Daniel Guay for offering me the opportunity to work on this project. During these years, I particularly appreciated their unfailing zeal, patience, diligence, dedication determination and constant presence, motivation and involvement in the research activity, even in the busiest moments of their private life.

A special thanks to Dr. Sebastein Garbarino, a Research Associate at Prof Guay's laboratory (INRS-EMT) for sharing with me his knowledge about electrochemical systems and electrocatalysis of small molecules and to Prof Dongling Ma and her student Jiianming Zhang (INRS-EMT) for preparing the platinum-gold nanoparticles for this project.

I want also to thank Tountian Dihourahouni and Spyridon Ntais, for their contribution to this work on the data analysis. Of course, I cannot forget Maria Joao Paulo, for being always collaborative and supportive.

And yet, a special thanks to Christophe Chabanier for his professionalism and willingness to help at all times, and all the technicians at INRS-EMT machine shop with whom I interacted almost daily during these years of my Ph.D.

Last but not the least, I would like to thank INRS for granting me the opportunity to work in its prestigious facility and environment and also, to thank NSERC and FRQNT for providing financial support for this work.

Table of Contents

Contents

List of Figures

Chapter One

Chapter Two

Chapter Three

Chapter Four

Chapter Five

Chapter Six

Chapter Seven

List of Tables

Chapter One

Chapter Six

List of Abbreviations

AA	Ascorbic Acid
Ag/AgCl	Siiver/Silver Chloride Reference Electrode
Au NPs	Gold Nanoparticles
b	Slope
BE	Binding Energy
CA	Chronoamperometry
CE	Counter Electrode
CL	Catalyst Layer
C_o	Concentration of Redox Active Species in Bulk Solution
CV	Cyclic Voltammetry
D_o	Diffusion Coefficient
DA	Dopamine
DFAFCs	Direct Formic Acid Fuel Cells
DFT	Density Functional Theory
DMFCs	Direct Methanol Fuel Cells
DHA	Dehydro Ascorbic Acid
DPV	Differential Pulse Voltammetry
E	Applied Potential
$E_{l/2}$	Half-Wave Potential
EASA	Electrochemical Active Surface Area
ECSA	Electrochemical Surface Area
EDAX	Energy-Dispersive X-ray Analysis or Energy-Dispersive Analysis of X-ray
EDL	Electric double Layer
EG	Ethylene Glycol
E°	Standard Electrode Potential
E_{pa}	Anodic Peak Potential
E_{pc}	Cathodic Peak Potential
F	Faraday’s Constant

FA	Formic Acid
FAO	Formic Acid Oxidation
FAOR	Formic Acid Oxidation Reaction
FCs	Fuel Cells
FT-IR	Fourier Transform Infrared
FWHM	Full Width at Half Maximum
GC	Glassy Carbon
GCE	Glassy Carbon Electrode
GDL	Gas Diffusion Layer
Hg/HgO	Mercury/Mercury Oxide
i	Current
l_{max}	Maximum Current
i_{pa}	Anodic Peak Current
i_{pc}	Cathodic Peak Current
i_k	Kinetic Current
i_l	limiting Current
IUPAC	International Union of Pure and Applied Science
LOD	Limit of Detection
LSV	Linear Scan Voltammetry
MOR	Methanol Oxidation Reaction
MSA	Mass Specific Activity
MEA	Membrane Electrode Assembly
n	Number of Electrons Transferred
NAA	Neutron Activation Analysis
NHE	Normal Hydrogen Electrode
OCV	Open Circuit Voltage
OER	Oxygen Evolution Reaction
ORR	Oxygen Reduction Reaction
PANI	Polyaniline
PBS	Phosphate Buffer Solution
PEM	Proton Exchange Membrane

PEMFC	Proton Exchange Membrane Fuel Cell
PLAL	Pulsed Laser Ablation in Liquid
Pt NPs	Platinum Nanoparticles
Q	Charge
R	Universal Gas Constant
RE	Reference Electrode
LOQ	Limit of Quantification
RDE	Rotating Disk Electrode
rds	Rate Determining Step
RHE	Reversible Hydrogen Electrode
s	Seconds
SCE	Saturated Calomel Electrode
SEM	Scanning Electron Microscopy
SPFC	Solid Polymer Fuel Cell
T	Temperature
t	Time
TEM	Transmission Electron Microscopy
WE	Working Electrode
XPS	X-ray Photoelectron Spectroscopy
XRD	X-ray Diffraction

CHAPTER ONE

Introduction

1.1.General Introduction

Metal nanoparticles (MNPs) have proven to exhibit distinct electrical, optical, magnetic, and chemical properties as compared to their bulk materials. The properties of MNPs are usually size and shape dependent, which has resulted in an intensive scientific research, not only for their rudimentary concepts, but also for their many scientific and technical applications [1 - 12]. MNPs have been employed extensively in energy storage and conversion devices, as well as in biosensing devices due to their attractive properties.

With growing concerns about global warming and depletion of petroleum resources, developing renewable energy production and storage technologies represents one of the major scientific challenges of the twenty-first century. Among these energy storage devices, fuel cells stand tall due to its environmentally friendly nature, high-energy density, ease of handling liquid fuels, and their possible use in stationary, portable and electronic applications [13]. At present, tremendous research efforts have been dedicated to the fabrication of efficient fuel cells. In all, MNPs such as Pt and Pt-based nanomaterials are indispensable, the most effective and widely used catalysts for fuel cells. This might be due to the fact that Pt has high exchange current density for oxygen reduction reaction (ORR), high work function (4.6 eV) and good resistance towards corrosion and therefore helps the fuel cell to last longer time [14]. However, one of the critical challenges for Proton Exchange Membrane Fuel Cells (PEMFCs) commercialization is the cost and reliability issues of Pt and Pt-based nanocatalysts used [13-18]. This is because Pt is a rare and expensive metal. Therefore, the effort to design and develop novel cost effective catalysts to meet the requirements of reducing Pt loading while increasing the activity and stability of the Pt-based catalyst is highly desired [13-16].

On the other hand, nano biosensing systems are a growing interdisciplinary domain. It combines the inherent features of analytical techniques such as high sensitivity and rapid detection with the unique electronic, biocompatibility and catalytic properties of nanomaterials [19, 20] to design electrochemical biosensors. MNPs-based electroanalytical techniques show enormous potential for constructing enhanced platforms for sensing of biological molecules like glucose, dopamine, ascorbic acid, uric acid and so on. This is because the use of MNPs with their different sizes, shapes and compositions bring important advantages such as: a) their easy immobilization on electrodes' surface generating a roughened conductive high-surface area interface that enhances the sensitive electrochemical detection of analytes; b) their high conductivity, large surface area and high electron transfer rate can decrease the overpotential of many analytically important electrochemical reactions, and even improve the reversibility of some redox reactions, which are irreversible at common unmodified electrodes. Overall, MNPs based electrodes offer better analytical performance (lower detection limit and shorter detection time) in comparison to conventional electrodes [21, 22**].**

Au was considered to be inert and stable for a long time. Thus, the report of supported Au NPs as highly effective catalysts by Haruta et al. in 1989 was considered a breakthrough in catalysis [23, 24]. The electron-rich core and high surface-area-to-volume ratio make Au NPs very effective in catalysis. Au NPs are among the most popular MNPs for biosensing applications due to their stability, oxidation resistance, electronic conductivity, and good biocompatibility [25-37]. For instance, Au NPs can be conjugated with drug or biomolecules and used as a delivery vehicle in various *in vivo* and *in vitro* systems [38-40].

1.2.Electro-oxidation of Small Organic Molecules and their Applicat

Small organic molecules such as formic acid, methanol, dopamine (DA) and ascorbic acid (AA), have been applied as important molecules in clean energy and biosensing as far as electrocatalysis is concerned. These compounds have received intense scientific attention due to their wide technological applications. For instance, while formic acid and methanol can be used as liquid fuels in low temperature fuel cells, dopamine and ascorbic acid are of interest in biomedical field.

1.2.1 Formic acid and Methanol as Fuels for Proton Exchange Membrane Fuel Cells

1.2.1.1 Principle of Proton Exchange Membrane Fuel Cells

The proton exchange membrane fuel cell (PEMFC), also called the solid polymer fuel cell (SPFC), was first developed by General Electric company in the United States in 1960s for the first manned space vehicles used by NASA [41]. PEMFCs are considered as promising alternatives to internal combustion engines for transportation because of their high-efficiency in energy conversion such as high power density, low emissions, low operating temperature, and low noise [42]. PEMFCs have further advantages such as elimination of electrolyte leakage, lower corrosion of cell components, simplification of stack design and increased robustness. These promising attributes have stimulated applications in areas such as telecommunications and portable electronics.

A single PEM fuel cell consists of a proton conducting membrane sandwiched between two thin porous electrodes. Fuels such as H_2, HCOOH, and CH_3OH etc. are fed to the anode in which oxidation reaction occurs, where Pt catalyst speeds up the separation of negatively charged electrons from positively charged ions (protons). At the cathode, oxygen/air combines with electrons to produce water. The protons are transported from the anode to cathode with the help of a proton conducting membrane (which allows only H^+ ions, not electrons), and electrons through the external. Fig. 1.1 illustrates the operational principle of a PEM fuel cell.

In a H_2 / O_2 PEM fuel cell, anode and cathode half-cell and overall electrochemical reactions are given in equations 1.1, 1.2 and 1. 3 as follows:

$$\text{Anode:} \quad 2H_2\,(g) \rightarrow 4H^+ + 4e^- \qquad E=0.00\ V \tag{1.1}$$

$$\text{Cathode:} \quad O_2\,(g) + 4H^+ + 4e^- \rightarrow 2H_2O \qquad E=1.23\ V \tag{1.2}$$

$$\text{Overall:} \quad 2H_2\,(g) + O_2\,(g) \rightarrow 2H_2O \qquad E=-.23\ V \tag{1.3}$$

The theoretical potential of hydrogen-oxygen fuel cell is 1.23 V. However mainly due to overpotential losses at the anode and cathode during the fuel cell operation, the potential drops as illustrated in the Fig 1.1 (b).

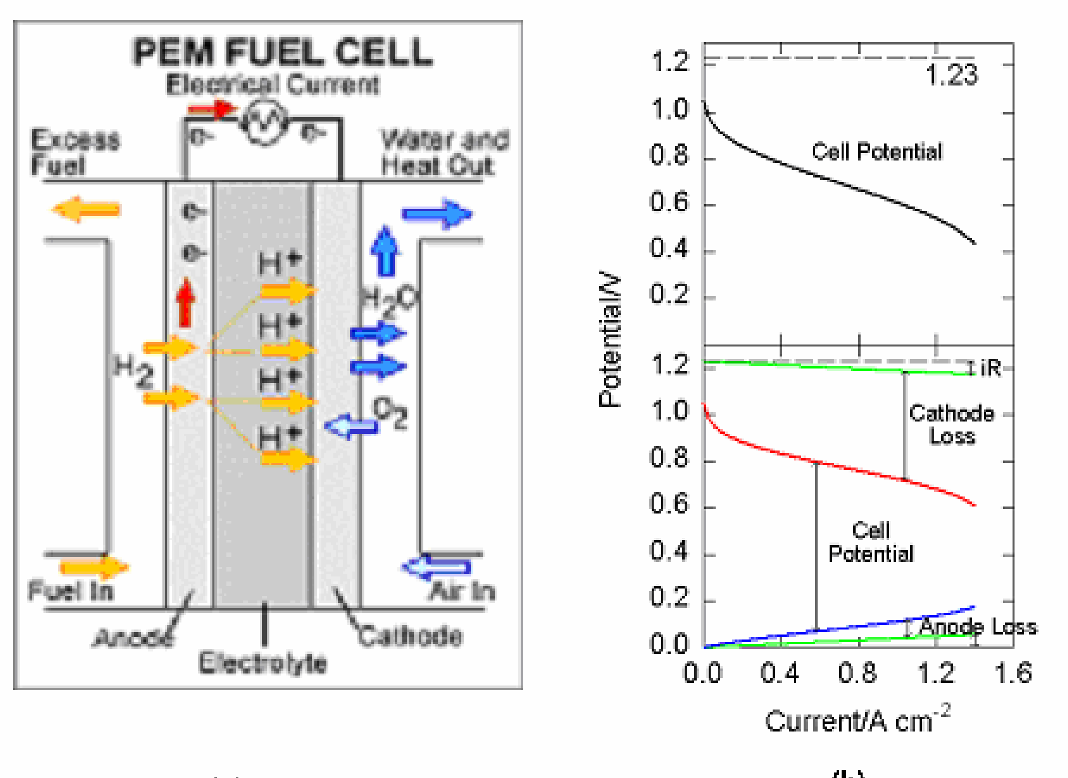

(a) (b)

Fig. 1.1 (a) illustrates working of a $H_2 - O_2$ (PEM) fuel cell including the **(**b**)** anodic and (c) cathodic polarization curves during the fuel cell operation **[**43].

Pt is the most suitable catalyst for the oxidation of hydrogen at the anode and oxygen reduction at the cathode. The kinetic of oxidation of pure H_2 is quite facile on Pt electrocatalysts. In this, H_2 undergoes dissociative adsorption on Pt sites followed by dissociation of the adsorbed H atoms [44, 45].

$$H_2\,(g) + Pt \rightarrow Pt\text{-}H_{ads} + Pt\text{-}H_{ads} \qquad (1.4)$$

$$2Pt\text{-}H_{ads} \rightarrow 2Pt + 2H^+ + 2e^- \qquad (1.5)$$

However, the kinetics of the oxygen reduction reaction (ORR) is very poor because of difficulties in the breaking of O – O bond and the complexity of the reaction.

The reaction pathways and nature of the intermediates for ORR on noble metals like Pt and Pd are open to debate. The most recognized routes in acidic medium are presented in Fig. 1.2. The first step involves the adsorption of molecular oxygen on the surface of the electrocatalyst. This reaction scheme shows that oxygen can be electrochemically reduced to water directly ($4e^-$ process). Alternatively it can be reduced to $(H_2O_2)_{ads}$ ($2e^-$ series process) before it undergoes further reduction ($2e^-$ series process) to form water [44, 45].

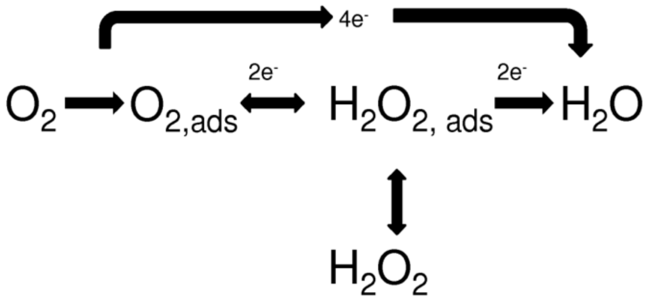

Fig 1.2**:** Oxygen reduction pathways [44, 45].

These primary reactions for the ORR in acid electrolytes can be written as [44]

Direct reaction pathway:

$$O_2 + 4H^+ + 4e^- \rightarrow 2H_2O \qquad E^O = 1.23V \tag{1.6}$$

Indirect reaction pathway:

$$O_2 + 2H^+ + 2e^- \rightarrow H_2O_2 \qquad E^O = 0.682V \tag{1.7}$$

Followed by:

$$H_2O_2 + 2H^+ + 2e^- \rightarrow 2H_2O \qquad E^O = 1.77V \tag{1.8}$$

or chemically decomposed as:

$$2H_2O_2 \rightarrow 2H_2O + O_2$$

(1.9)

On noble metals like Pt and oxides like perovskites and pyrochlores [47], the ORR usually proceeds via the 4 e^- pathway. In the case of non-Pt metals like Au or non-metals like carbon, the ORR in acidic media proceeds via the two electron reduction pathway, leading to the formation of hydrogen peroxide (H_2O_2). For fuel cells operation the four electrons pathway is the preferred reaction since it leads to high performance of the fuel cell without any intermediate species such as peroxides. On Pt NPs, the reduction kinetic is known to be greatly influenced by

i. The extent of Pt loading as well as the particle size (a particle size of ~ 5 nm is believed to be optimum) [45].

ii. Geometry, crystal structure and d – band vacancy of the metal crystal.

   The catalytic activity of Pt towards ORR strongly depends on its O_2 adsorption energy, the dissociation energy of the O-O bond, and the binding energy of OH on the Pt surface.

   The electronic structure of the Pt catalyst (Pt *d*-band vacancy) and the Pt-Pt interatomic distance (geometric effect) can strongly affect these energies [45]. Theoretical calculations on O_2 and OH binding energy on several metals have predicted that Pt should have the highest catalytic activity among other metals with the ORR activity of Pt > Pd > Ir > Rh, which is in agreement with the experimental results. Regarding the Pt alloy catalysts, calculations have also predicted that PtM (M=Fe, Co, Ni, etc.) alloys should have higher catalytic activity than pure Pt, which has again been proven by experiments [44].

   The activity enhancement that occurs when Pt is alloyed with other metals is explainable by the change in electronic structure (the increased Pt *d*-band vacancy) and in geometric effect (Pt-Pt interatomic distance). Alloying causes a lattice contraction, leading to a more favorable Pt-Pt distance for the dissociative adsorption of O_2. The *d*-band vacancy can be increased after alloying, producing a strong metal-O_2 interaction thereby weakening the O-O bonds. It was reported that the Tafel plots of Pt and PtFe alloys for the O_2 reduction reaction are the same. However, the exchange current density of oxygen reduction on PtFe is higher than on Pt. In the Tafel region of 120 mV/dec, the exchange current density for Pt catalyst was 1.63 $\times 10^{-8}$ A/cm^{-2}, while that for PtFe catalyst was 2.15×10^{-7} A/cm^{-2}, indicating a nine-fold increase [45].

iii. Thermal or electrochemical activation of the electrodes.

One of the challenges in the commercialization of the H_2/O_2 PEMFCs is the cathode where Pt is used as a catalyst to enhance the ORR. At present, the typical loading of Pt is the cathode catalyst layer is 0.4 mg cm^{-2} (vs. 0.2-0.4 mg cm^{-2} at the anode) [48] and according to the United States Department of Energy (DoE), this loading should be reduced down to 0.15 mg cm^{-2} to make PEM fuel cells cost competitive [49]. Also, Pt catalysts are not sufficiently stable in the acidic fuel cell reaction conditions, tending to dissolve and coalesce. This reduces their active surface area, deteriorates their performance and limits their lifetime [50]. There are in addition specific challenges related to the use of liquid fuels such as formic acid and methanol which will be addressed in the following sections.

1.2.1.2 Formic acid and Methanol for PEMFCs

Formic acid is the simplest naturally, occurring carboxylic acid notably found in the bodies of ants. It is also known as methanoic acid by the IUPAC. The molecular formula for formic acid is HCOOH. Formic acid has numerous domestic and industrial uses. For example, it is used as an intermediate in chemical synthesis. It is also used in many areas, from leather processing to feed preservation. At room temperature, formic acid exists as a colorless liquid with a highly pungent, penetrating odor. Even though formic acid is an organic compound, it is miscible with water and most polar organic solvents. However, it is also somewhat soluble in hydrocarbons. Formic acid is an environmentally acceptable and highly efficient organic acid. It can be used as a liquid fuel in fuel cells due to it non-toxic nature and high energy density (1.72 kWh/kg) [51]. Moreover, it is easily transported, stored and has low permeability through Nafion membrane (an anionic perflourinated membrane), allowing the use of concentrated formic acid in a direct formic acid fuel cell [51].

Methanol is also an important organic liquid which is the simplest alcohol in the alkanol group. At room temperature, the physical properties are quite similar to ethanol that is colorless, flammable, light, volatile liquid with a distinctive odor. Like Formic acid, methanol is also a polar in nature and therefore used as antifreeze, solvent, and as a denaturant for ethanol. It is also used for producing biodiesel via trans-esterification reaction. Among these domestic applications of methanol is also employed for heat engines and fuel cells due almost the same reasons as formic acid. In this thesis the use of formic acid and methanol as a liquid fuel in fuel cell applications is of concern and the reactions involved during the electro-oxidation of the fuel will be discussed in detail in the subsequent sections.

(a) (b)

Fig. 1.3: Chemical structure of (a) Formic acid and (b) Methanol.

It is important to state that both formic acid and methanol have certain features in common. For example both exist as liquids at room temperature and can, therefore, easily be introduced in the already existing fuel distribution system. Also, both can be produced in large quantities and they have an acceptable toxicity. Moreover, using a liquid fuel eliminates the need for complex fuel vaporizes or reformers and the associated heat sources and controls [51-56].

Direct oxidation formic acid at the anode of direct formic acid fuel cells (DFAFCs) has numerous advantages over other direct liquid fuel cells (DLFCs) as far as clean energy applications are concerned. DFAFCs are a more promising option than direct methanol fuel cell (DMFC**) due to lower fuel cross over**[52]. The DFAFCs are characterized by the oxidation of formic acid at the anode and reduction of oxygen at the cathode according to the following equations:

Anode: $HCOOH \rightarrow CO_2 + 2H^+ + 2e^-$ $E^O = -0.25$ vs. NHE (1.10)

Cathode: $1/2O_2 + 2H^+ + 2e^- \rightarrow H_2O$ $E^O = +1.23V$ vs. NHE (1.11)

Overall: $HCOOH + 1/2O_2 + CO_2 + H_2O$ $E^O = +1.48$ V vs. NHE (1.12)

The theoretical open circuit potential of a DFAFC (1.48 V) is higher than hydrogen oxygen (1.23 V) and methanol-oxygen (1.21 V) fuel cells [51, 53]. Hence, it is desired to achieve high power density under ideal conditions. Despite these numerous advantages, the fuel cell performance and efficiency are hindered due to several limiting issues under the operating conditions [54]. One of the issues is the lack of cost effective and efficient catalysts for formic acid electro-oxidation [51].

On the other hand, direct oxidation of methanol at the anode of a direct methanol fuel cell (DMFC) also has unique advantages over other alcohols and liquid fuels but quite similar to formic acid [55-62]. However, from the fuel cell technology point of view, a more important consideration for choosing methanol is the fact that it can be catalytically oxidized on Pt electrodes in aqueous environment yielding CO_2 and six electrons per methanol molecule at the anode:

Anode: $CH_3OH \rightarrow CO_2 + 6H^+ + 6e^-$ E^o= -0.046 V vs. NHE (1.13)

This reaction is complimented by the reduction of oxygen from the air at the cathode.

Cathode: $O_2 + 4H^+ + 4e^- \rightarrow 2H_2O$ $E^O = +1.23V$ vs. NHE (1.14)

Overall: $CH_3OH + 3/2O_2 + CO_2 + 2H_2O$ E^O = +1.21 V vs. NHE (1.15)

Reaction equation 1.13 has a very promising thermodynamic potential of -0.046 V vs. NHE and may, theoretically, allow for a power nearly as high as that close to a hydrogen-based fuel cell. Unfortunately, the disadvantages of using methanol as fuel are considerable:

1. The decomposition reaction of methanol on Pt produces surface poisoning species, which leads to a low catalytic activity and presents a severe inhibition for the development of a low temperature fuel cell [56 - 58].
2. The current state of the art DMFCs are being operated using acidic proton exchange membranes. As carbonate formation is a serious problem in alkaline media, acid electrolytes must be used, which results in corrosion problems. More importantly, acid electrolytes are responsible for the slow electrode kinetics of the reduction of oxygen at the air cathode.[56 - 60]
3. High noble metal catalyst loadings are necessary in order to obtain a sufficiently high power output, which makes the fuel cell costly.
4. Another challenging issue for the low activity is the methanol cross-over from the anode to the cathode [56, 59, and 60].

Despite these difficulties global benefits of a working at low temperature methanol-based fuel cell over the internal combustion engine and other energy conversion devices has ensured continued interest over the past decades. In order to solve the problems mentioned above, knowledge of the mechanism and kinetics of the reactions is required. Improvements in the following areas would be highly advantageous:

1. The anode activity must be further improved

2. Current loadings of noble metals on the anode need to be reduced
3. Membrane properties for PEMFCs need to be improved

From the above discussion on formic acid and methanol, it is clear that the global effects of these liquid molecules are of relevant as far as clean energy technology is concerned and each molecule has its own strength and weakness. For these reasons, we study both molecules and in the following sections of this thesis, we will summarize concepts, and results on the adsorption and electrooxidation of methanol and formic acid, on Pt and PtAu bimetallic surfaces.

1.2.1.3 Catalysts for electro-oxidation of Hydrogen, Formic acid and Methanol

Compared to H_2, the kinetic of formic acid or methanol oxidation is poor even on Pt. Over the years, the use of Pd [63] and Pt as electrocatalyst for formic acid oxidation reaction (FAOR) has been extensively studied since they are the state of the art catalysts in DFAFCs [51]. However, while Pd catalyst deactivates rapidly over time [63], Pt is not a suitable electrocatalyst for this reaction because it is prone to poisoning by CO. This makes most of the Pt surface sites unavailable for further fuel oxidation, resulting in low overall current.

On Pt, the mechanisms responsible for the oxidation of formic acid include two reaction paths occurring in parallel [51, 64]. The direct pathway (Eq. (1.16)) involves the dehydrogenation of formic acid molecule generating CO_2. In contrast, the indirect pathway (Eq. (1.17) involves the dehydration of formic acid forming CO_{ads} that adsorbs strongly on the Pt surface.

$$HCOOH \rightarrow HCOO^{-}_{ad} + H^{+} + e^{-} \rightarrow CO_2 + 2H^{+} + 2e^{-} \tag{1.16}$$

$$HCOOH \rightarrow CO_{ad} + H_2O \rightarrow CO_2 + 2H^{+} + 2e^{-} \tag{1.17}$$

While the direct pathway of FAOR (eq 1.16) proceeds at low potential, the indirect pathway of formic acid oxidation proceeds at higher potential (Eq. 1.17). Since high activity at low potential is critical for high performance, the presence of CO_{ads} on the electrode surface is to be avoided and its effect diminished. This can be achieved on bimetallic surfaces with the second metal by the bi-functional effects of the electrocatalyst [65]. According to the bi-functional mechanism, the second metal supplies the oxygen species which is formed at lower potential than on Pt through water dissociation and provides these oxygen species into adjacent Pt sites where the adsorbed poisoning intermediates can be oxidized. Also, the presence of a second metal can cause a modification of the electronic structure of Pt and change the energy of adsorption of CO_{ads}, leading possibly to a higher tendency of Pt to dehydrogenate formic acid molecule. Another approach consists in facilitating the direct pathway by favoring the interruption of large Pt surfaces through the inclusion of foreign atoms. It is effective because the indirect pathway needs at least three contiguous Pt atoms, whereas only two Pt atoms are needed for the direct pathway [66].

Using Density Functional Theory (DFT) calculations [67 - 69], it was recently pointed out there is a significant shift of the d-band center from 2.25 eV for Pt to 1.80 eV for PtAu alloys (and Pt over layers onto Au). It is worth mentioning that the latter value is close to the d-band center of pure Pd (ca.1.83 eV), which is a well-known catalyst for the formic acid oxidation (FAO) through the dehydrogenation pathway [63, 70].

The above data showed that PtAu bimetallic catalysts seem to be effective and promising catalysts for formic electro-oxidation favoring the direct pathway. [71 - 86]. While other metals like Pb [87] and Bi [88] showed similar promotion of the dehydrogenation path on Pt, the PtAu system is interesting because of the greater chemical stability of Au compared to these other elements. The reaction mechanism on PtAu bimetallic systems is described as follows:

When Pt is combined with a second metal such Au to form PtAu bimetallic systems, the electronic structure of Pt is modified and reactions readily occurred at low potential leading to reduction of CO_{ads} formation on the surface. Therefore, the catalyst surface is not poisoned.

$$Au + H_2O \rightarrow Au\text{-}OH_{ads} + H^+ + e^- \qquad (1.\ 18)$$

$$Pt\text{-}CO_{ads} + Au\text{-}OH_{ads} \rightarrow Pt + Au + CO_2 + H^+ + e^- \qquad (1.19)$$

Methanol can be electro-oxidized in both acid and alkaline media. The proposed reaction pathway for methanol oxidation in acid solution is presented in Fig. 1.4. It basically consists of two pathways: the direct pathway leading to carbon dioxide formation and the indirect pathway also leading to CO_2 generation via an intermediate CO_{ads} species. However, the mechanistic aspect of methanol oxidation reaction (MOR) consists of stepwise dehydrogenation of protons resulting most often in formation of a Pt – CO type adsorbed intermediate. Apart from the complete oxidation product CO_2, other intermediate products such as carbon monoxide are generated during methanol oxidation reacting on Pt surfaces, which acts as a surface poison [90-97]. The CO generated during MOR is strongly adsorbed on the Pt surface resulting in self-poisoning of the catalyst. This is one of the principal challenges hindering the development of direct methanol fuel cells. Moreover, the detection of CO raised a very critical question regarding whether the CO formation during MOR occurs in a parallel reaction mechanism, or is it a necessary intermediate in a serial reaction? The solution to this interrogation holds the key to the direction of DMFC related research. If a serial pathway proves true, future research will be focused intensively towards developing more CO-tolerant catalysts, while in the case of a parallel pathway mechanism, research can also be geared towards designing catalysts, which selectively oxidize methanol in a pathway not involving the formation of adsorbed CO.

It is noteworthy that, Pt itself is not sufficiently active to be useful in commercial fuel cells and considerable efforts have been undertaken to find more active materials such as bimetallic systems. The phenomena such as bi-functional, electronic and third body effects described for formic acid oxidation on bimetallic systems are also applicable to methanol oxidation mechanism on bimetallic surfaces. Among the bimetallic catalysts for methanol oxidation, Pt-Ru is the state of the art catalyst employed in DMFCs applications [98 - 100]. The second metal such as Ru being more oxophyllic than Pt, results in more efficient decomposition of water to form Ru-OH_{ads} type species (such a species may also be formed by adsorption of hydroxide ions from solution). The latter species then facilitates decomposition of CO_{ads} into CO_2 (g).

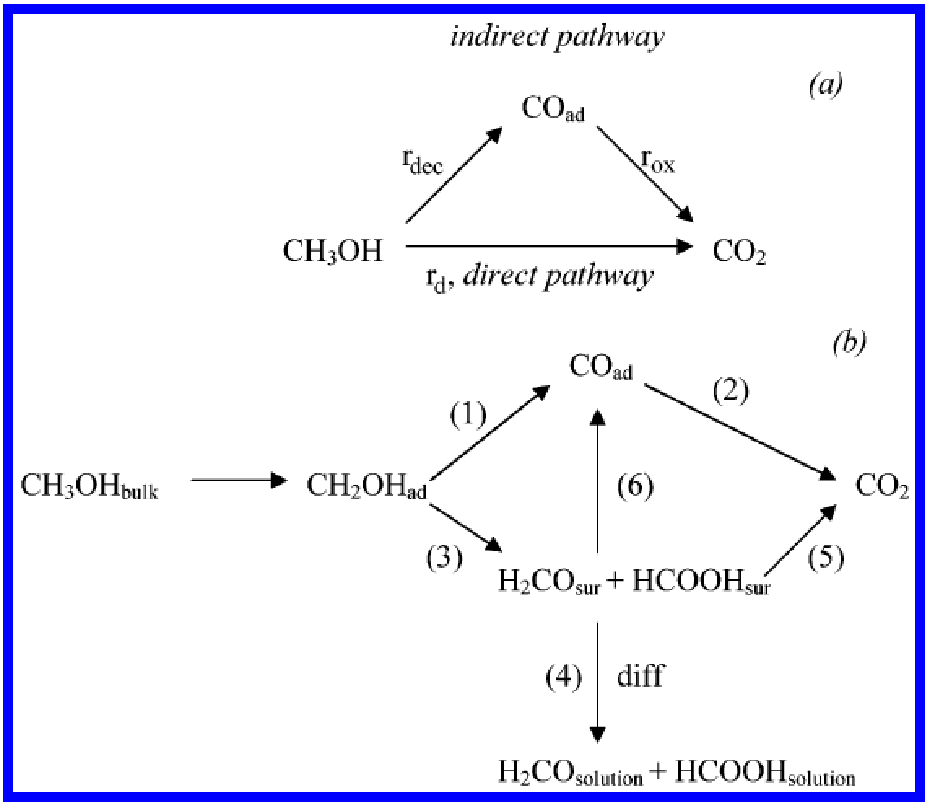

Fig. 1.4: (a) Simplified schematic representation of the parallel pathway for methanol oxidation on platinum electrodes. (b) A more advanced schematic representation of the parallel pathway mechanism for methanol oxidation on platinum electrodes [89].

The current state of the art DMFCs have been operated using acidic proton exchange membranes. However, the polarization performance of the current state of the art DMFCs in the acid medium is relatively low. One of the principal contributions to the relatively low DMFC performance is from kinetic constraints in the MOR due to difficulty in removing CO adsorbed on the catalyst surface [90 -93] resulting in a low catalyst utilization. In fact, the loading of Pt-Ru catalysts on the anode is typically around 2.0 mg cm^{-2} [90] therefore there is a need for developing less expensive and more active catalysts. Basic media had been proven to facilitate the MOR, resulting in better polarization characteristics offering the possibility of employing lower amounts of noble metal catalysts or even non-noble, less expensive metal catalysts (Ni, Ag, etc) for the process [91, 92]. Also in alkaline medium, ionic current is due to conduction of hydroxide ions and is in the opposite direction to that in proton conducting systems. As such, the pathway of the electro-osmotic drag is reversed, reducing the methanol permeation rate [91].

A brief overview of some possible MOR pathways in alkaline medium is given below. Both carbonate and formate have been detected as products of the MOR in alkaline medium. The half-cell reactions leading to formation of these products are represented by eqns (1.20) and (1.21).

$$CH_3OH + 8OH^- \rightarrow CO_3^{2-} + 6\ H_2O + 6e^- \qquad (1.20)$$

$$CH_3OH + 5OH^- \rightarrow HCOO^- + 4\ H_2O + 4e^- \qquad (1.21)$$

Both of these reactions would eventually proceed via various adsorbed intermediates. Eqn (1.20) is known to proceed at least in part via an adsorbed CO intermediate, which is formed according to eqn (1.22).

$$CH_3OH + 4OH^- \rightarrow CO_{ads} + 4\ H_2O + 4e^- \qquad (1.22)$$

Adsorbed CO is subsequently removed according to eqn (1.23).

$$CO_{ads} + 2OH_{\ ads} \rightarrow CO_2 + H_2O \qquad (1.23)$$

Adsorbed OH in eqn (1.23) is formed by discharge of hydroxide ions, as described in eqn (1.24).

$$OH^- \rightarrow OH_{\ ads} + e^- \qquad (1.24)$$

In a carbonate electrolyte dissolved product CO_2 will be rejected from solution as CO_2 gas. In a strongly alkaline environment such as a NaOH solution, CO_2 will be rapidly converted to CO_3^{2-} via eqn (1.25).

$$CO_2 + 2OH^- \rightarrow CO_3^{2-} + \ H_2O + 2e^- \qquad (1.25)$$

Under both potentiodynamic and potentiostatic conditions, MOR rates have been reported to be higher on both unsupported and carbon-supported Pt and Pt/Ru nanoparticle catalysts in alkaline electrolytes than in acid medium [98 - 100]. The enhanced activity in alkaline media results from at least two factors: the lack of specifically-adsorbing spectator ions in alkaline solutions, and the higher coverage of adsorbed OH at low potential, which is required for methanol oxidation.

Apart from the specific properties inherent to the nature of formic acid and methanol, there are some common features in the electro-oxidation of these molecules which have no satisfactory explanation so far. Pt metal has been proven to be the most suitable catalyst for dehydrogenation reactions. The CO generated during methanol and formic acid oxidation reaction is strongly adsorbed on the Pt surface resulting in self-poisoning of the catalyst [52, 90 –97, 100]. Hence to make fuel cells more efficient and economically viable, it is imperative to minimize the overpotential losses by appropriate electrocatalysis. Pt-containing catalysts are anchored on both anode and cathode to catalyze the fuel oxidation and oxygen reduction reactions. Therefore, efficient electrocatalysis would involve improving the activity of Pt catalysts, or its cheaper substitutes provided the latter are almost as stable and have reasonably high activity, in addition to designing of suitable electrodes for efficient utilization of the catalysts.

1.2.2 Electrochemical Detection of Dopamine and Ascorbic acid

An electrochemical biosensor is an analytical device that operates by reacting with the analyte of interest and producing an electrical signal proportional to the analyte concentration via the transfer of electrons.

Today, new biological, chemical, electrochemical and genetic methods show the potential of producing an analytical response against any chemical substance; so theoretically a biosensing device can be built to specifically determine any analyte. Electrochemical techniques, which are highly sensitive and applicable by means of very simple instruments, have also proved to be very suitable for developing disposable, low cost biosensors. The high selectivity of the NPs and/or biological component combined with the simplicity of the electrochemical transduction, determines the increasing use of electrochemical biosensors in clinical, food and environmental analysis.

Dopamine (DA), also known by IUPAC nomenclature as 2-(3,4-dihydroxyphenyl) ethylamine is shown in Fig. 1.5(a). It is one of the principal neurotransmitters located mainly in the central nervous system (CNS) of humans and animals. It plays a significant role in the central nervous, renal, cardiovascular and hormonal systems [101-110]. A loss of DA-containing neurons leads to serious diseases such as Schizophrenia and Parkinson diseases [101, 102]. The concentration of dopamine in the physiological fluid of mammals is very low (0.01-1 µM) for a healthy individuals and is far lower for patients suffering from Parkinsonism [111, 112]. Therefore developing a sensitive, selective and rapid method to determine DA levels in body fluids is very important.

(a) (b)

Fig. 1.5: Chemical structure of (a) dopamine and (b) ascorbic acid.

Electro-oxidation of DA in an aqueous solution involves a 2 electron transfer and two protons process to generate o-dopamino quinone at pH less or equal to 7 as illustrated in Fig. 1.6. However, as the pH increases, different oxidized products such as hydroxyindoline (HI) and aminochrome are produced suggesting that the oxidation reaction of DA oxidation is pH dependent [113]. The oxidation potential of DA on bare electrodes at pH less or equal to 7 is shown below in Fig. 1.6.

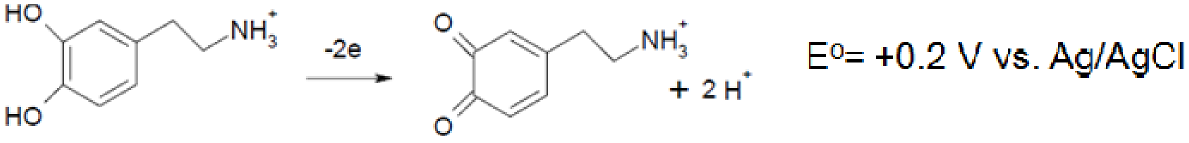

Fig. 1.6: Electrochemical reaction of DA and its standard oxidation potential on in solution of pH 7 on bare electrode

DA has two acid dissociation constants, 8.92 (pKa1) and 10.6 (pKa2) and it usually exists in cationic form at the physiological pH at 25 ^{O}C. [112, 113]. The redox reaction of DA is affected by changes in pH because of the involvement of protons in the overall reaction, being extremely fast when DA is in the protonated form. The anodic peak potential is also affected (shifts negatively) with the increase in the solution pH [112, 113], indicating that the electrocatalytic oxidation of DA is a charge transfer process involving protonation-deprotonation reaction..

Ascorbic acid (AA), commonly called Vitamin C, is water-soluble vitamin present in a wide number of foods such as, fruits and vegetables. The IUPAC nomenclature of AA is known as L-hexuronic acid and it chemical structure is presented in Fig. 1.5(b). AA has numerous applications in domestic and industrial uses. In the food industry, it is used as an antioxidant for stabilizing color and aroma, as well as prolonging the life of commercial products [114 - 117]. The presence of ascorbate, a deprotonated of AA in the mammalian brain plays vital role in bioelectrochemistry, neurochemistry and clinical diagnostics applications [114]. AA also plays an important role in the prevention of infectious diseases. The range of concentration of AA in the extracellular fluid of a healthy person is in the micro molar range (100 - 1000 µM) [110, 111]. This is far lower in an unhealthy person and this may result in several diseases such high blood pressure, scurvy, cancer, etc [110, 111, 115, 117]. Therefore, the development of sensitive, selective and reproducible sensing systems for the analysis of AA can be considered of great importance for both the increasingly strict government guidelines of foodstuff which require precise quantifications of vitamins within this consumable food product [115].

The oxidation of AA to dehydro ascorbic acid involves the transfer of two electrons and two protons as illustrated in Fig. 1.7. AA and dehydroascorbic acid are an irreversible redox couple with a formal potential of E^{o1} = +0.15 V vs. Ag/AgCl in a -neutral pH solution.

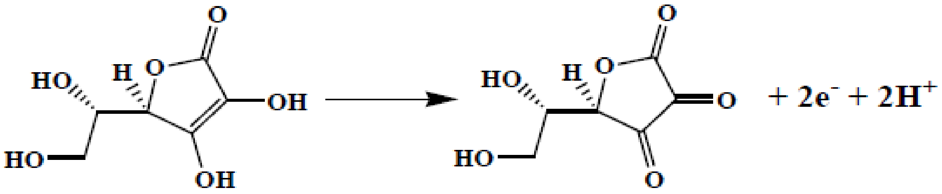

Fig. 1.7: Electrochemical reaction of AA at neutral pH on bare electrode in solution.

In an aqueous solution, AA shows two deprotonation steps with *pKa* values of 4.30 and 11.5 [116, 117]. Thus, in a neutral solution AA exists as a monodeprotonated ascorbate anion.

At unmodified electrodes it is commonly proposed that ascorbate oxidation occurs *via* a radical anion intermediate in a series of first order steps [117] whereas at modified electrode surfaces it is possible that the reaction occurs through a hydride transfer [118]. Whatever the mechanism of oxidation, it is followed, at neutral pH, by rapid hydrolysis of the dehydro-L-ascorbic acid to 2,3-diketogluconic acid [116].

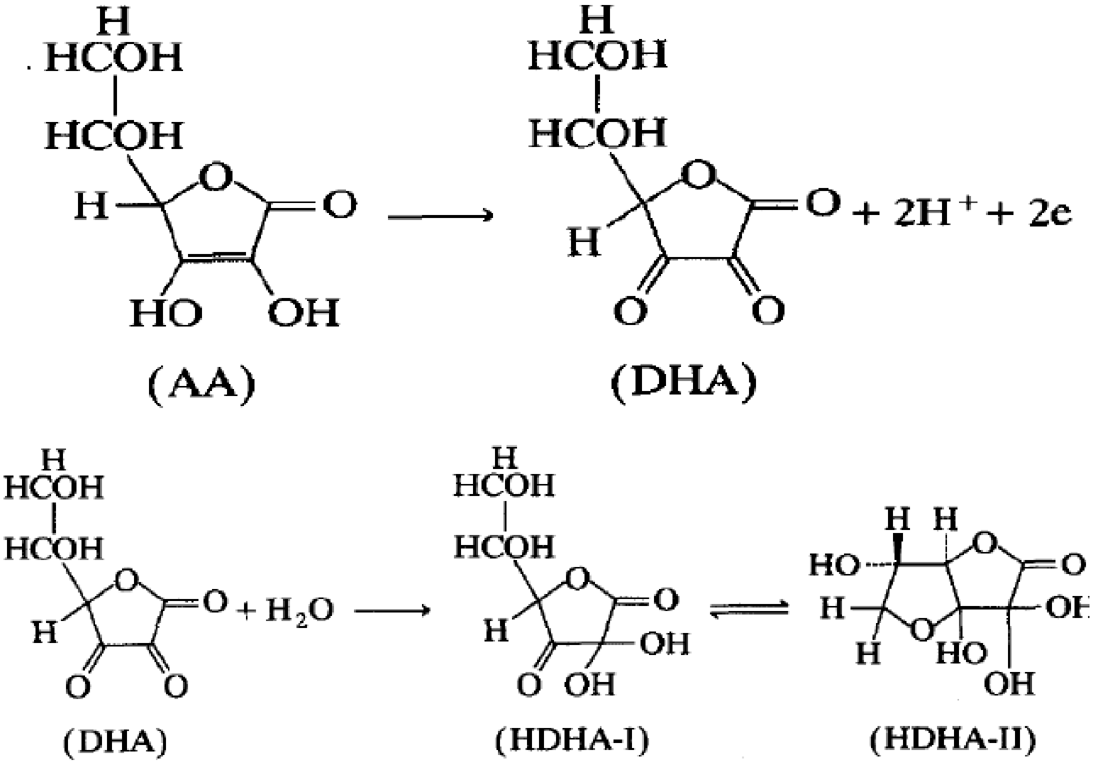

Fig 1.8: Steps of electrochemical oxidation of Ascorbic Acid on Pt electrode [123].

where AA, DHA, HDHA-I and HDHA-II represent ascorbic acid, dehydro-ascorbic acid, and open side-chain and bicyclic forms of hydrated dehydro-ascorbic acid respectively

There is not much reported for electrochemical oxidation of AA on platinum and gold electrodes [118-122]. The adsorption of AA at Pt surface was first reported by Breina and co-workers [122]. These researchers concluded that the adsorption of AA on Pt surfaces was reversible, non-destructive with a maximum coverage of ca. 68% of hydrogen adsorption sites. This adsorption is responsible for the high overvoltage of the AA oxidation reaction on Pt that proceeds in aqueous medium. A divergent conclusion was arrived recently by Xing et al. [123] based on their study on Pt electrodes. It was proposed that at these electrodes, AA undergoes a spontaneous dissociative adsorption at the Pt electrode in acid solution prior to its direct oxidation. This dissociative adsorption probably takes place via an interaction between the side-chain of the AA molecule and the Pt surface, with (CO), as the adsorbate. Recently, the structure-sensitive character of AA electrochemical oxidation has been demonstrated by using Pt single-crystal electrodes. Electrochemical evidence has also been given for the existence of spontaneous dissociative adsorption of AA on a Pt(100) surface.

Therefore the oxidation of AA on Pt electrodes would consist of two pathways: direct oxidation to DHA without adsorption, and another mechanism leading to CO, as a final product through dissociative adsorption of AA and formation of CO as an adsorbed intermediate. The oxidation of AA on Pt electrode in aqueous media towards an irreversible process giving DHA; the adsorbed species would be oxidized in the potential range of surface oxide formation. The radical intermediate formed during the electrochemical oxidation of ascorbate on Pt plays an important role in the reaction mechanism. Formation of the same species on a polycrystalline Pt electrode has been confirmed spectroscopically in an in situ Fourier-transform infrared reflection-absorption spectroscopy (FTIRRAS) study by Xing and co-workers [123]. The reaction scheme of AA oxidation in an aqueous media is presented in Fig. 1.8.

The catalytic effects of several metal ions on the oxidation of AA on Pt electrodes was reported elsewhere in literature [121].. It has been shown that single-crystal Pt surfaces modified by irreversibly adsorbed Bi catalyze the oxidation of AA, changing the mechanism to a structure-insensitive process [121]. This effect was attributed to the suppression of the dissociative adsorption pathway. The oxidation of AA on gold electrodes is also a structure-insensitive process and does not produce adsorbed CO [39, 118, 121].

1.2.2.1 Challenges in selective determination of dopamine in the presence of Ascorbic acid

The ease with which dopamine is electrochemically oxidized on conventional electrodes such as glassy carbon, Au and Pt bulk electrodes, has been used to detect the neurotransmitter both *in vitro* and *in vivo* [125]. However, several challenges are associated with the quantitative analysis of DA such as its tendency to autoxidize in solution to form DAQ causing fouling effects on electrodes [110 -118]. This is due to the nature of the oxidative electrode reaction of DA on the overly large potential on the conventional electrodes [103, 105, 110, 126].

Moreover, DA detection in body fluids by electrochemical methods on conventional electrodes suffers from poor selectivity and reproducibility due to the presence of interfering species such as AA. Both molecules undergo oxidation within the same potential window and AA concentration in body fluids is 100–1000 times higher than that of DA [110, 111, 126].

Similar to DA detection, AA is very difficult to determine electrochemically by direct oxidation on a conventional electrode, such as glassy carbon, Au and Pt electrode. This is due to the high over-potential on these bare electrodes. Also the electrode surface is poisoned by oxidation products of AA [127].

To alleviate or eliminate these challenges, many strategies have been adopted to enhance performance in DA and AA determination based on chemically modified electrodes such as conductive polymers [101, 102, 104], carbon materials [105, 107, 110, 126] and self-assembly monolayer (SAM) films [103, 106]. The chemically modified electrodes have shown various degrees of success by impeding the interference reactions or promoting DA oxidation at different potentials. It also decreases the over-potential, accelerate mass transport rate or greatly enrich the substrates on the electrode surface.

The desirable performance of MNPs have attracted attention in recent years as sensing elements due to their excellent surface effects, optical, electronic and electrochemical properties [24 – 26, 103], which are different from those of bulk metal materials. Particularly, due the unique characteristics of Au NPs, such as good electronic conductivity, relevant electrocatalytic and biocompatibility related to their size, several researcher scientists utilized Au NPs to fabricate electrochemical sensors and biosensors [24, 25, 26–36]. For example, Au NPs are widely used to catalyze the oxidization of AA by decreasing the over-potential and enhancing the oxidization current [25, 127 - 129]. However, leaching of the biological component from these electrodes surface and reduction of the reaction selectivity is the principal drawback. Also, it was demonstrated elsewhere that Au NPs with certain morphological structures such as rod like nanoparticles, spikes, dendrites, nanopores, and hierarchical flower like structures, have shown interesting catalytic, electrocatalytic and sensing properties and can be utilized to fabricate electrochemical biosensors [24, 25, 26–36] to catalyze the oxidization of DA and AA by decreasing the over-potential and enhancing the oxidization current with high selectivity and sensitivity. However, the self-poisoning of the electrodes surface due to the nature of the reaction products lead to poor selectivity of oxidation peaks is the principal drawback.

On the other hand, it is well known that Pt has outstanding catalytic properties for the oxidation of many organic molecules [52 – 70]. However, the Pt surfaces are easily poison by the oxidation products during the electrooxidation reactions [52 -70]. Recently, AuPt alloy NPs has invoked much interest due to its potential to provide a synergistic catalytic effect via the interaction between the two components in bimetallic alloys [130, 131]. One important property of the AuPt alloy is its much higher surface area and better electron transport that differ massively from the individual Au and Pt NPs [130, 131]. In addition, the electrocatalytic oxidation of AA at gold electrode electrodeposited with platinum [132] has been reported. Recently, the findings reported on PtAu hybrid nanocomposite by electrochemical deposition of gold and platinum complexes showed excellent properties toward DA in the presence of AA and uric acid via synergistic effects of the component materials [133]. This was very similar to that reported on a graphite electrode in which the over-potential for AA oxidization was reduced on rough surface of carbon electrode and fractured glassy carbon electrodes which also offered the exposure of active fresh edge planes [134]. As a result, AuPt alloy NPs with enhanced surface area and morphology could work as an ideal material for biosensors. In our previous work, well-dispersed AuPt alloy nanoparticles with improved morphological features were prepared by pulse laser ablation via an aqueous medium, and the resulting alloy nanoparticles electrodes exhibited excellent catalysis to the electrochemical oxidation of formic acid [135] and methanol [69].

1.3. Pt-Au bimetallic Catalysts for liquid fed PEMFCs and DA/AA detection

Pt itself is not sufficiently active to be useful in commercial direct liquid fuel cells and considerable efforts have been undertaken to find more active materials such as binary and ternary systems. It is well known that a catalyst must not be only capable of chemisorbing small organic molecules but also oxidizing the resultant chemisorbed fragments. This may be achieved using the so called “bifunctional mechanism” on binary metallic systems [65]. The bi-functional mechanism is hooked on the idea that the more oxophilic metal sites act as adsorption platforms for oxygen-containing species (e.g. OH_{ads}), which can react with CO adsorbed on platinum to form CO_2. The reactivity of the surface may also be influenced by altering the electronic structure of the catalyst surface (specifically Pt). The presence of a second metal in the form of Au, Ru, Bi, Pb, Pd (or any other metal modifier) can induce a change in the CO (and OH) binding strength on Pt, thus facilitating surface poison oxidation. This effect is known as the “electronic” or “ligand” effect. A third way for improving catalyst performance is based on an “ensemble effect”. Here, adding a catalytically inert material to the active compound in the form of Au is assumed to change the distribution of active sites, thereby opening different reaction pathways [66].

Au is one of only two transition metals more electronegative than Pt, so the incorporation of Au into Pt NPs [130] may have exceptional effects on the electrocatalytic properties. Therefore, PtAu bimetallic NPs are of fundamental interest and importance as fuel cell electrocatalysts, especially FAO [71-86] and MOR [136 - 141]. Also, due to the high stability of Au and its co-catalytic or promoting effect has put PtAu catalysts in the spotlight of intensive scientific research [142]. The chemical and physical properties of metal alloy NPs can be well tuned by varying the size, composition and atomic ordering. PtAu bimetallic alloy catalysts are effective in promoting the adsorption/dissociation of formic acid and methanol with lower tendencies to CO poisoning on these surfaces as compared to pure Pt [71 - 86].

On the other hand, Au NPs are of interest for the detection of DA in the presence of large amounts of interfering species such as AA. Due to the need of improving the detection limit of the electrode, considerable efforts are been undertaken to increase the activity and selectivity of Au NPs and the overall electrochemical performance of the biosensor. Pt NPs do not possess biocompatibility and sensing properties towards molecules like DA and AA. However, due to their capability of electro-oxidize organic molecules such as formic acid and methanol, PtAu hybrid nanocomposite prepared by electrochemical deposition of Au and Pt complexes was recently proposed for the detection of DA in the presence of AA and uric acid [143**]**. The excellent properties of the hybrid system (with sensitivity of 0.05 µA µA µM^{-1} and linear dynamic range of 24 – 384µM) were explained in terms of synergistic effect between the component materials. In addition, the electrocatalytic oxidation of AA at gold electrode electrodeposited with platinum [33] has been reported. Therefore, in this work, we also investigate Au and $Au_{100-x}Pt_x$ alloyed nanoparticles for the sensitive and selective electrochemical determination of dopamine.

It is well known that, alloy NPs exhibit unique and extraordinary binding properties with reacting species compared to those for monometallic or bimetal systems. As a result, stronger metal–metal bond interactions exist and the reaction between the catalyst surfaces and the reacting species is better. Also, there is an extra stabilization of the transition or activate complex state on the alloy catalysts in comparison to the corresponding interaction on the monometallic or bimetallic catalyst surfaces, which is an additional benefit. Normally, preparation of alloy NPs can be done by simultaneous chemical reduction of two or more metal ions [144-152] with a relatively strong reducing agent. This method is usually used in the synthesis of monometallic NPs or bimetallic NPs using two metal precursors. In some cases, the deposition of Pt and Au was achieved by first depositing a monolayer of Cu (Under Potential Deposition (UPD) of Cu) and then proceeding to a Pt- or Au-redox replacement reaction [153,154]. Other preparation methods of PtAu bimetallic catalyst include de-alloying of Pt-Cu-Au [155] or Al-Pt-Au [156,157], electrostatic self-assembly of positively charged Pt and negatively charged Au nanoparticles [158], electro-deposition of PtAu 3D foam films through hydrogen bubble dynamic templating [151], photo-assisted reduction of Pt and Au salts [152], and galvanic replacement using sacrificial Ag templates of various forms [159]. In most cases, high surface area carbon supports were used [145,147,148], although both graphene [1500, 160] and TiO_2 [152] were also used.

But, the preparation of single homogenous Pt–Au alloy NPs is very complex due to the different reduction kinetics of Pt and Au ions [130] and the wide immiscibility gap between Pt and Au NPs [144 - 152]. Therefore the preparation, of PtAu alloy NPs is a complex challenge due to the composition control vis-a-vis particle size and size distribution control.

Besides this challenge of preparing the bimetallic alloy, is the possible segregation of these different metals either immediately upon contact with the support or under the conditions necessary to form an active catalyst. For this reason, the controllable synthesis of PtAu alloy NPs a prerequisite for the advancement of electrochemical oxidation of molecules because the properties and functions are better when alloyed at the nanoscale.

Recently, at Institut National de la Recherche Scientifique (Energie, Materiaux et Telecommunications) (INRS-EMT), PtAu alloy NPs with controllable composition were synthesized for the first time using Pulsed Laser Ablation of Pt-Au mixture targets in water [130]. The scheme of the synthesis route is shown in Fig 1.9. For the preparation of PtAu alloy NPs, Pt and Au powders mixtures with different ratios (Pt_xAu_{100-x}, $x = 0, 30, 50, 70, 100$) were mechanically mixed for 30 minutes before being compression molded into a disk. In a typical process, 500 mg of Pt+Au powder mixture with the right composition was placed into a steel die with a diameter of 8 mm and pressed (CARVER Press, maximum pressure = 12 tons, durration 10 minutes) to form a compact disk with a thickness of *ca* 1.5 mm. Then, this disk was used as a target to perform pulsed laser deposition in liquid [130]. All the operations were performed at room temperature. It is worth mentioning that the synthesis was performed by another PhD student at INRS-EMT.

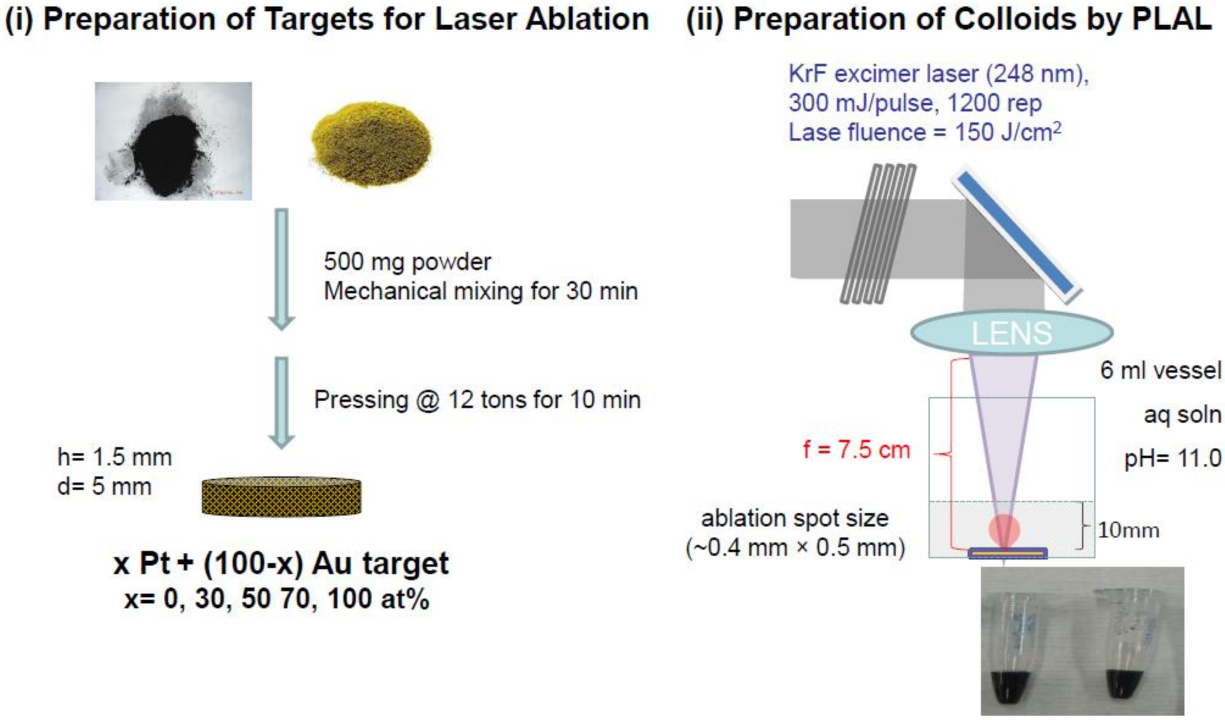

Fig 1.9: Schematic Synthesis of PtAu alloy NPs by PLAL [130]

The Pt_xAu_{100-x} alloys were characterized by X-ray diffraction to (XRD) determine their crystalline structure, by transmission electron microscopy (TEM) for the particle size and X-ray Photoelectron spectroscopy for their surface composition. As displayed in Fig 1.10, the X-ray diffractograms showed a single set of diffraction peaks corresponding to a fcc structure. The linear variation of the lattice constant with Pt atomic feeding coupled with the two different sets of peaks displayed by the mixture of pure Au NPs and pure Pt NPs in Fig. 1.10B is a strong evidence of PtAu (fcc structure) alloy formation over the entire range of composition.

The TEM images are shown in Fig. 1.11. The particle size values calculated from the TEM were close to those determined from XRD analysis, indicating that these NPs are basically single crystals. Table 1.1 summarizes the main features of the PtAu NPs prepared by PLAL by our colleagues. In this dissertation, we studied the electrochemical oxidation of formic acid, methanol, dopamine and ascorbic acid on these NPs.

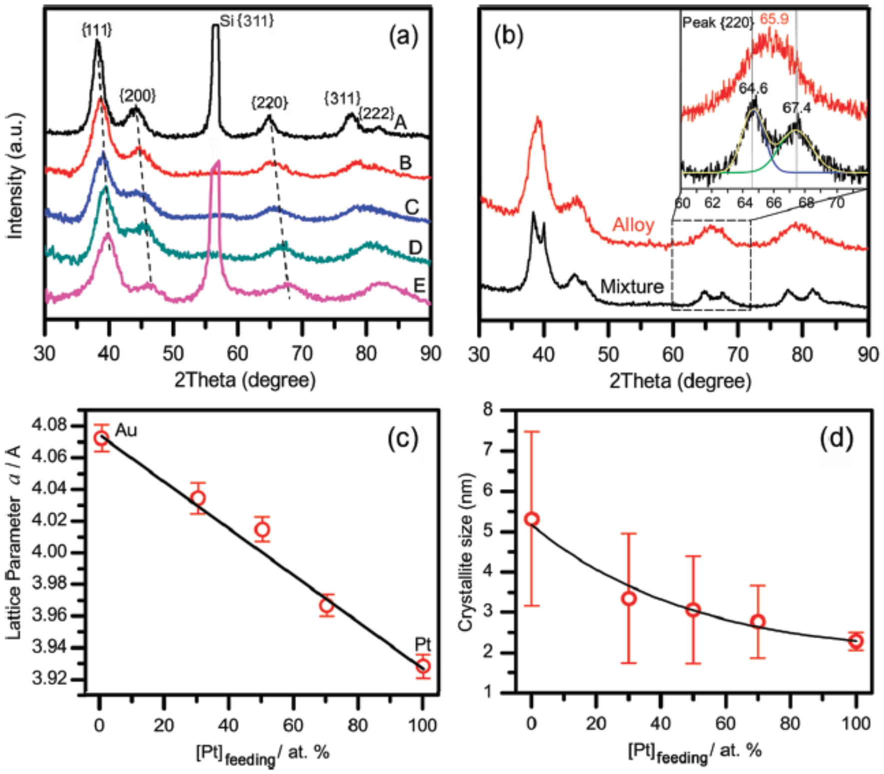

Fig. 1.10: X-ray diffraction patterns of (a) Pt_xAu_{100-x} NPs and (b) a nominal (50:50) mixture of pure Au NPs and pure Pt NPs (c) Lattice parameter and (d) crystallite size of NPs, estimated from XRD patterns, as a function of [Pt] feeding.

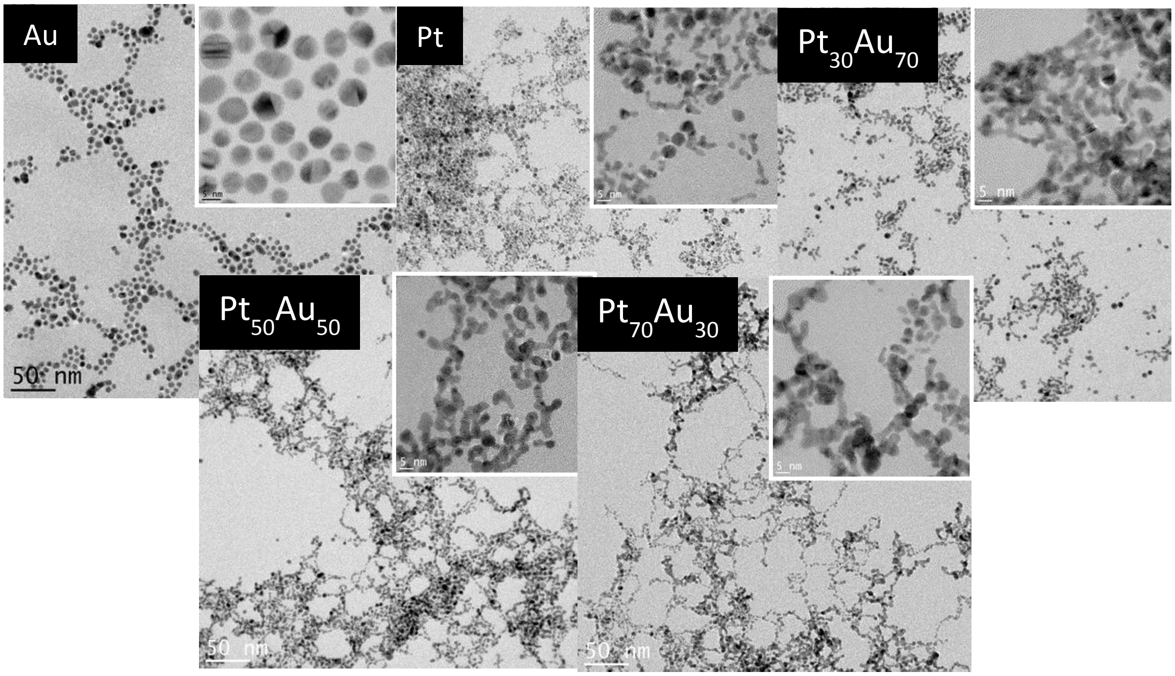

Fig. 1.11: Transmission electron microscopy micrographs of Pt, Au, nominal $Pt_{30}Au_{7,}$ $Pt_{50}Au_{5}$ and $Pt_{70}Au_{30}$ alloy NPs.

Table 1.1: Description of the different properties catalysts

Nanoparticles	**Lattice constant (a_0)**	**Crystal size (nm)**	**Particlesize (TEM) (nm)**	**Structure**
Pt	3.92	2.7	2.5 ±1.1	FCC
$Pt_{70}Au_{30}$ alloy	3.96	2.9	2.8±0.8	FCC
$Pt_{50}Au_{50}$ alloy	4.015	3.86	3.9±1.7	FCC
$Pt_{30}Au_{70}$ alloy	4.03	3.7	3.4±1.6	FCC
Au	4.07	5.2	5.2 ±1.6	FCC

1.4 Objectives of the Thesis ,

The global objective of this dissertation is to study the electrochemical oxidation of formic acid, methanol, dopamine and ascorbic acid on PtAu NPs prepared by PLAL in water.

Accordingly, Pt, Au, PtAu alloy nanoparticles (NPs) and mixture of Pt and Au NPs with controlled size and composition will be investigated. PtAu alloy NPs were prepared by pulsed laser deposition from mixed Pt + Au single metal target with the appropriate composition [124], whilst mixtures of Pt and Au NPs were obtained by physical mixture of Pt NPs and Au NPs.

To achieve this objective, PtAu NPs were systematically characterized by cyclic voltammetry in H_2SO_4, NaOH and phosphate buffer solution (PBS) electrolytes. Their electrocatalytic activity towards formic acid and methanol were evaluated by cyclic voltammetry and chronoamperometry, whereas cyclic voltammetry and differential pulse voltammetry were used for DA and AA oxidation studies. The electrocatalytic activity of the NPs towards the chosen molecules was correlated with the NPs composition and discussed in light of the proposed mechanism in the literature. In the specific case of formic acid a comparative study with Pt+Au mixtures was done to support that the PtAu NPs prepared by PLAL are indeed alloyed NPs and not intimate mixtures of the two metals.

1.5 Outline of the Thesis

The research presented in this thesis principally focuses on electro-oxidation of formic acid, methanol, ascorbic acid and dopamine on PtAu NPs, to develop an understanding of the effect of the alloying of transition metals on the catalytic activity. However, these PtAu NPs catalysts were also tested for oxygen reduction reactions (ORR) and these results are briefly reported in chapter three of thesis. While the electro-oxidation of formic acid and methanol envisage proton exchange membrane fuel cells, the electro-oxidation of dopamine and ascorbic acid target electrochemical biosensors. A qualitative correlation between the electrocatalytic activity, surface coverage of adsorbed species and the composition of the catalytically active metal surfaces was sought.

In *Chapter 1, we* described the general information about electrochemistry including the electro-oxidation mechanisms of these small organic molecules, the physical properties and preparation method of these PtAu NPs. The mechanism of ORR at the cathodic part of fuel cell reaction is also included in this chapter.

In *Chapter 2,* we report on the materials and chemicals, physical characterization and electrochemical characterization techniques employed in this dissertation along with a brief overview of the techniques.

In *Chapter 3*, we report on how the catalyst electrodes (i. e. catalyst and Nafion loading of the Pt nanoparticles) were optimized. The voltammetric studies on the surface activity of Pt_xAu_{100-x} alloy NPs (x= 0, 30, 50, 70, 100) synthesized by pulsed laser ablation in liquid (PLAL) in nitrogen-saturated 0.5 mol dm^{-3} H_2SO_4 was investigated. The surface activity has greater importance of the overall performance of the electrodes. The PtAu NPs catalysts were also tested for oxygen reduction reactions (ORR) and these results are briefly reported in chapter three of thesis

The systematic study of the influence of the composition and structure of PtAu bimetallic catalysts on the electrocatalytic activity for the FAO is discussed in *Chapter 4*. Through a detailed study of the NPs' electrochemical properties involving both cyclic voltammetry and chronoamperometry, a correlation is established between the surface composition of the PtAu alloy NPs and their electrocatalytic activity towards formic acid oxidation. Also, it is shown that the surface structure and surface composition of physically mixed Pt and Au NPs can be modified through electrochemical aging, and that the activity and poisoning tolerance of the resulting materials approach that of PtAu alloy NPs, although the latter still exhibits larger mass specific electrocatalytic activity for the FAO.

The results of methanol oxidation reaction on PtAu alloy NPs electrodes in both acidic and alkaline medium were reported in *Chapter 5*. The effect of OH anion adsorption in alkaline medium on the PtAu alloy system is discussed. It is suggested that increasing Au content in the PtAu bimetallic systems increases the OH anion adsorption strength with increase in the surface coverage of OHads and, thus, results in a considerable change in the kinetics and dynamics of the reaction. Results of chronoamperometric transients obtained on PtAu alloy NPs surfaces indicate that the electrocatalytic reaction of methanol preferably increases with PtAu alloy surface with high Au content in alkaline medium.

In *Chapter 6* the electro-oxidation properties of dopamine and ascorbic acid on the PtAu alloy electrodes are investigated using cyclic voltammetry and differential pulse voltammetry.

The electrocatalytic properties of the PtAu alloy surfaces are correlated to the surface structure and extensively discussed with respect to reported results in literature.

Finally, perspectives and future work of the thesis presented in *Chapter 7*.

References

1. M.C. Daniel, D. Astruc, Chem. Rev. 104 (2004) 293.
2. C. Cobley, J. Chen, E. Cho, L. Wang, Y. Xia, Chem. Soc. Rev. 40 (2010) 44.
3. T. Sau, A. Rogach, Adv. Mater. 22 (2010) 1781.
4. X.M. Lu, M. Rycenga, S.E. Skrabalak, B. Wiley, Y. Xia, Annu. Rev. Phys Chem. 60 (2009) 167.
5. Y. Xia, Y. Xiong, B. Lim, S. Skrabalak, Angew. Chem. Int. Ed. 48 (2009) 60.
6. A. Tao, J. Huang, P. Yang, Acc. Chem. Res. 41 (2008) 1662.
7. R. Murray, Chem. Rev. 108 (2008) 2688.
8. Z. Peng, H. Yang, Nano Today 4 (2009) 143.
9. A. Tao, S. Habas, P. Yang, Small 4 (2008) 310.
10. J. Chen, B. Lim, E. Lee, Y. Xia, Nano Today 4 (2009) 81.
11. S. Skrabalak, J. Chen, Y. Sun, X. Lu, L. Au, C. Cobley, Y. Xia, Acc. Chem. Res. 41 (2008) 1587.
12. B. Wiley, Y. Sun, Y. Xia, Acc. Chem. Res. 40 (2007) 1067.
13. . Mazumder, Y. Lee, S. Sun, Adv. Funct. Mater. 20 (2010) 1224-1231
14. J. J. Lingane, *J. Electroanal. Chem.,* 2 (1961) 296
15. Gasteiger, H. A. & Markovic, N. M. Just a dream-or future reality? Science 324, 48–49 (2009).
16. Whitesides, G. M. & Crabtree, G. W. Don’t forget long-term fundamental research in energy. Science 315, 796–798 (2007)
17. Gray, H. B. Powering the planet: chemical challenges in solar energy ultilization 1, 7 (2009)
18. Lewis, N. S. & Nocera, D. G. Powering the planet: chemical challenges in solar energy utilization. Proc. Natl Acad. Sci. USA 103, 15729–15735 (2006).

19. S. Guo, S. Dong, TrAC Trends Anal. Chem. 28 (2009) 96.
20. S. Guo, E. Wang, Anal. Chim. Acta 598 (2007) 181.
21. S. Guo, J. Li, W. Ren, D. Wen, S. Dong, E. Wang, Chem. Mater. 21 (2009) 2247.
22. S. Guo, S. Dong, E. Wang, Small 5 (2009) 1869.
23. M. Haruta, N. Yamada, T. Kobayashi and S. Iijima, *J. Catal.*, 1989, **115**, 301-309.
24. M. Haruta, *Catal. Today,* 1997, **36**, 153-166.
25. P.Y. Ge, Y. Du, J. J. Xu, H.Y. Chen, J. Electroanal. Chem. 633 (2009) 182–186
26. C.R. Raj, T. Okajima, T. Ohsaka, J. Electroanal. Chem. 543 (2003) 127_ 133
27. M. Ahn, J. Kim, J. Electroanal. Chem. 683 (2012) 75–79
28. B.J. Plowman, M. Mahajan, A. P. O'Mullane, S. K. Bhargava, Electrochimica Acta *55* (2010) 8953–8959
29. L. Zhang, X. Jiang, J. Electroanal. Chem. 583 (2005) 292 -299
30. H. J. Qiu, G. P. Zhou, G. L. Ji, Y. Zhang, X. R. Huang, Y. Ding, *Colloids and Surfaces B:* Biointerfaces 69 (2009) 105–108
31. A. I. Gopalan, K. P. Lee, K. M. Manesha, P. Santhosh, J. H. Kim, J. S. Kang, ,Talanta 71 (2007) 1774–1781
32. S. Senthil Kumar, J. Mathiyarasu, K. Lakshminarasimha Phani, J. Electroanal. Chem 578 (2005) 95–103
33. A. Stoyanova, S. Ivanova, V. Tsakovaa, A. Bund, Electrochimica Acta 56 (2011) 3693–3699
34. T. Liu, M. Li, Q. Li, Talanta 63 (2004) 1053–1059
35. J.D. Qiu, M. Xiong, R. P. Liang, H. P. Peng, F. Liu, Biosensors and Bioelectronics 24 (2009) 2649–2653
36. J. B. Raoof, A. Kiani, R. Ojani, R. Valiollahi, S. Rashid-Nadimi, J Solid State Electrochem (2010) 14:1171–1176
37. S. Yixin, S. F. Wang, Microchim Acta 154, (2006), 115–121
38. P. Ghosh, G. Han, M. De, C. K. Kim, V. M. Rotello, *Advanced Drug Delivery Reviews*, 2008, **60**, 1307-1315.
39. G. F. Paciotti, D. G. I. Kingston, L. Tamarkin, *Drug Dev. Res.*, 2006, **67**, 47-54.
40. G. F. Paciotti, L. Myer, D. Weinreich, D. Goia, N. Pavel, R. E. McLaughlin, L. Tamarkin, *Drug Deliv.*, 2004, **11**, 169-183

41. J. Larminie, A. Dicks, "Fuel Cell Systems Explained", 2nd Edn., John Wiley&Sons, USA, 2003.
42. H. K. Lee, J. H. Park, D. Y. Kim, T. H. Lee, J. Power Sources 131 (2004) 200-206
43. http://www.eere.energy.gov/hydrogenandfuelcells/fuelcells/types.html
44. H. S. Wroblowa, Y. C. Pan, G. Razumney, *J. Electroanal. Chem* **69**, 195 (1976).
45. A. Stassi, C. D'Urso, V. Baglio, A. Di Blasi, V. Antonucci, A. S. Arico. J Appl Electrochem 2006;36:1143–9.
46. K. Kinoshita, *Electrochemical Oxygen Technology*, John Wiley & Sons, New York 1992.
47. L. J¨orissen, J. Power Sources 155 (2006) 23–32
48. H.A. Gasteiger, J.E. Panels, S.G. Yan, J. Power Sources 127 (2004) 162–171
49. US Department of Energy (Fuel Cell Technologie Record,2013) http://www.hydrogen.energy.gov/pdfs/13012_fuel_cell_system_cost_2013.pd
50. N. M. Markovic, H. A. Gasteiger, P. N. Ross, J. Phys. Chem. 1995, 99, 3411
51. X. Yu, P.G. Pickup, J. Power Sources 182 (2008) 124-132
52. Y.W. Rhee, S.Y. Ha, R.I. Masel, J. Power Sources 117 (2003) 35-38
53. C. Rice, S. Ha, R. I. Masel, A. Wieckowski,. J. Power Sources 2003, 115, 229
54. S. Uhm, H. J. Lee, J. Lee, Phys. Chem. Chem. Phys. 2009, 11,9326.
55. R. Dillon, S. Srinivasan, A.S. Arico, V. Antonucci, J. Power Sources 127 (2004) 112–126.
56. J. S. Spendelow, J. D. Goodpaster, P. J. A. Kenis, A. Wieckowski, *Langmuir, Vol. 22, No. 25, 2006 10457* -10464
57. R. Manoharan, J. Prabhuram, J. Power Sources 96 (2001) 220–225
58. E.H. Yu, K. Scott, J. Power Sources 137 (2004) 248–256.
59. J.S. Spendelow, A. Wieckowski, Phys. Chem. Chem. Phys. 9 (2007) 2654– 2675.
60. B. Beden, F. Kadirgan, C. Lamy, J.M. Leger, J. Electroanal. Chem. 142 (1982) 171–190.
61. C. Nishihara, T. Okada, J. Electroanal. Chem. 577 (2005) 355–359
62. H. S. Liu , C. J, Song, L. Zhang, J. J. Zhang, H. J. Wang, D. P. Wilkinson, J. Power Sources 155 (2006) 95–110
63. W.P. Zhou, A. Lewera, R. Larsen, R.I. Masel, P.S. Bagus, A. Wieckowski, J. Phys. Chem. B 110 (2006) 13393e13398.

64. J.M. Feliu, E. Herrero, in: W. Vielstich, H.A. Gasteiger, A. Lamm (Eds.), Handbook of Fuel Cells, vol. 2, Wiley, New York, 2003, p. 679.
65. N.M. Markovic, H.A. Gasteiger, P.N. Ross Jr., X. Jiang, I. Villegas, M.J. Weaver, Electrochim. Acta 40 (1995) 91e98.
66. S. Ye, in: J. Zhang (Ed.), CO Tolerant Catalysts in PEM Fuel Cell Electrocatalysts and Catalysts Layers, Fundamentals and Applications, Springer-Verlag, 2008, pp. p759e834.
67. J. Greeley, J.K. Norskov, M. Mavrikakis, Annu. Rev. Phys. Chem. 53 (2002) 319e 348.
68. B. Hammer, J.K. Norskov, Adv. Catal. 45 (2000) 71e129.
69. A. Ruban, B. Hammer, P. Stoltze, H.L. Skriver, J.K. Norskov, J. Mol. Catal. A: Chem. 115 (1997) 421e429.
70. N. Hoshi, K. Kida, M. Nakamura, M. Nakada, K. Osada, J. Phys. Chem. B 110 (2006) 12480e12484.
71. J.H. Choi, K.J. Jeong, Y. Dong, J. Han, T.H. Lim, J.S. Lee, Y.E. Sung, J. Power Sources 163 (2006) 71e75.
72. J.B. Xu, T.S. Zhao, Z.X. Liang, J. Power Sources 185 (2008) 857e861.
73. J.K. Lee, J. Lee, J. Han, T.H. Lim, Y.E. Sung, Y. Tak, Electrochim. Acta 53 (2008) 3474e3478.
74. S. Wang, N. Kristian, S. Jiang, X. Wang, Electrochem. Commun. 10 (2008) 961- 964.
75. Y. Yu, Y. Hu, X. Liu, W. Deng, X. Wang, Electrochim. Acta 54 (2009) 3092e 3097.
76. Z. Peng, H. Yang, Nano Res. 2 (2009) 406e415.
77. S. Zhang, Y. Shao, G. Yin, Y. Lin, J. Power Sources 195 (2010) 1103e1106.
78. C. Xu, R. Wang, M. Chen, Y. Zhang, Y. Ding, Phys. Chem. Chem. Phys. 12 (2010) 239e246.
79. S. Zhang, Y. Shao, G. Yin, Y. Lin, Angew. Chem. Int. Ed. 49 (2010) 2211e2214.
80. R. Wang, C. Wang, W.B. Cai, Y. Ding, Adv. Mater. 22 (2010) 1845e1848.
81. C.V. Rao, C.R. Cabrera, Y. Ishikawa, J. Phys. Chem. C 115 (2011) 21963e21970.
82. S. Zhang, Y. Shao, H.G. Liao, J. Liu, I.A. Aksay, G. Yin, Y. Lin, Chem. Mater. 23 (2011) 1079e1081.
83. Liu, L. Cao, W. Huang, Z. Li, ACS Appl. Mater. Interfaces 3 (2011) 3552e3558.
84. S. Chen, M. Malig, M. Tian, A. Chen, J. Phys. Chem. C 116 (2012) 3298e3304.

85. Y. Kim, H.J. Kim, Y.S. Kim, S.M. Choi, M.H. Seo, W.B. Kim, J. Phys. Chem. C 116 (2012) 18093e18100.
86. I.S. Park, K.S. Lee, J.H. Choi, H.Y. Park, Y.E. Sung, J. Phys. Chem. C 111 (2007) 19126e19133.
87. D. Pletcher, V. Solis, J. Electroanal. Chem. 131 (1982) 309e323.
88. J. Clavilier, A. Fernandez-Vega, J.M. Feliu, A. Aldaz, J. Electroanal. Chem. 258 (1989) 89e100.
89. T. H. M. Housmans* and M. T. M. Koper**,** J. Phys. Chem. B 2003**,** 107, 8557-8567
90. W. Li, X. Wang, Z. Chen, M. Waje, Y. Yan, J. Phys. Chem. B 2006, 110, 15353-15358 f
91. E.H. Yu, K. Scott, J. Power Sources 137 (2004) 248–256.
92. J.S. Spendelow, A. Wieckowski, Phys. Chem. Chem. Phys. 9 (2007) 2654– 2675.
93. B. Beden, F. Kadirgan, C. Lamy, J.M. Leger, J. Electroanal. Chem. 142 (1982) 171–190.C. Nishihara, T. Okada, J. Electroanal. Chem. 577 (2005) 355–359
94. H. S. Liu , C. J, Song, L. Zhang, J. J. Zhang, H. J. Wang, D. P. Wilkinson, J. Power Sources 155 (2006) 95–110
95. N. P. Lebedeva, M. T. M. Koper, J. M. Feliu, and R. A. van Santen, J. Electroanal. Chem. 524- 525 (2002) 242.
96. M. T. M. Koper, N. P. Lebedeva, and C. G. M. Hermse, Faraday Discuss. 121 (2002) 301.
97. T. H. M. Housmans, J. M. Feliu, and M. T. M. Koper, J. Electroanal. Chem. 572 (2004) 79.
98. R. S. Jayashree, D. Egas, J. S. Spendelow, D. Natarajan, L. J. Markoski and P. J. A. Kenis, Electrochem. Solid-State Lett., 2006, 9, A252–256.
99. E. R. Choban, J. S. Spendelow, L. Gancs, A. Wieckowski and P. J. A. Kenis, Electrochim. Acta, 2005, 50, 5390–5398.
100. J. V. Barth, Surf. Sci. Rep. 40 (2000) 75.
101. D.P. Quan, D. P. Tuyena, T. D. Lamb, P. T. N. Trama, N. H. Binhb, P. H. Viet, Colloids and Surfaces B: Biointerfaces 88 (2011) 764– 770
102. A. Safavi, N. Maleki, O. Moradlou, F. Tajabadi, Anal. Biochem. 359 (2006) 224–229
103. A. Galal, N. F. Atta, E. H. El-Ads, Talanta 93 (2012) 264– 273

104. T. Selvaraju, R. Ramaraj, Electrochemistry Communications 5 (2003) 667–672

105. M. Mallesha, R. Manjunatha a, C. Nethravathi, G. S. Suresh, M. Rajamathi, J. S. Melo, T. V. Venkatesha, Bioelectrochemistry 81 (2011) 104–108

106. R.K. Shervedani, M. Bagherzadeh, S. A. Mozaffari, Sensors and Actuators B 115 (2006) 614–621

107. H.S. Wang, T. H. Li, W-L Jia, H.Y. Xu, Biosensors and Bioelectronics 22 (2006) 664–669

108. Y. Zhang, L. Lin, Z. Feng, J. Zhou, Z. Lin, Electrochimica Acta 55 (2009) 265–270

109. J. Li, X. Lin, Sensors and Actuators B 124 (2007) 486–493

110. N. Jia, Z. Wang, G. Yang, H. Shen, L. Zhu, Electrochemistry Communications 9 (2007) 233–238

111. M. Zhang, K. Gong, H. Zhang, L. Mao, Biosensors and Bioelectronics 20 (2005) 1270–1276

112. N.F. Atta, M.F. El-Kady, Sensors and Actuators B 145 (2010) 299–310

113. J. Breczko, M. E. Plonska-Brzezinska, L. Echegoyen, Electrochimica Acta 72 (2012) 61– 67

114. https://umm.edu/health/medical/altmed/supplement/vitamin-c-ascorbic-acid

115. A. Maines, D. Ashworth, P. Vadgama, Food technology and biotechnology, **34,** (1996), 31-37.

116. S.P. Perone, W.J. Kretlow..Analytical Chemistry, 38, (1966), 1760-1763.

117. I.-F. Hu, T. Kuwana, Analytical Chemistry, 58, (1986), 3235-3239.

118. I.G. Casella, M.R. Guascito, Electroanalysis, 9, (1997), 1381-1386.

119. A. Sivanesan, P. Kannan, S. Abraham John, Electrochimica Acta 52 (2007) 8118–8124

120. C.R. Raj, T. Okajima, T. Ohsaka, J. Electroanal. Chem. 543 (2003) 127_ 133

121. M. Reuda, A. Alda, f. Sanchex-Burgos, Electroch1mica Acta, 29 (1978), 419-424

122. M. Brezina, J. Koryta, T. Loucka, D. Marsfkova, J. Electroanal. Chem., 40 (1972) 13 - 17

123. X. Xing, I. T. Bae, M. Shao, C. C. Liu, J. Electroanal. Chem., 346 (1993) 309 – 321

124. M. A. Climent, A. Rodes, M. J. Valls, J. M. Perez, J. M. Feliu, A. Aldaz, J. CHEM. SOC. FARADAY TRANS., 1994, 90(4), 609-615

125. J.S. Yoo, S. M. Park, Anal. Chem. **2005**, 77, 3694-3699.

126. H. Bi, Y. Li, S. Liuc, P. Guoa, Z. Weia,b, C. Lva, J. Zhanga, X.S. Zhao, Sensors and Actuators B 171– 172 (2012) 1132– 1140

127. Y. Lin, Y. Hu, Y. Long, J. Di, Microchim Acta (2011) 175:259–264

128. F. Zuo, C.H. Luo, Z.H. Zheng, X.B. Ding, Y.X. Peng, Electroanalysis 8 (2008) 894–899

129. A. Sivanesan, P. Kannan, S. Abraham John, Electrochim. Acta 52 (2007) 8118–8124

130. J. Zhang, D. N. Oko, S. Garbarino, M. Chaker, A. C. Tavares, D. Guay, D. Ma, J. Phys. Chem. C (2012), 116 (24), 13413–13420

131. D.Mott, J. Luo, P. N. Njoki, Y.Lin, L.Wang, C. Zhong Catal Today 122, (2007) 378–38

132. R. A. A. Muñoz, R. C. Matos, L. Angnes . Talanta 55, (2001) 855–860

133. S. Thiagarajan, S.M. Chen / Talanta 74 (2007) 212–222

134. P. Ramesh, G.S. Suresh, S. Sampath, J. Electroanal. Chem. 561 (2004) 173–180.

135. D. N. Oko, J. Zhang, S. Garbarino, M. Chaker, D. Ma, A. C. Tavares, D. Guay, J. Power Sources xxx (2013) 1e10

136. H. Lang, S. Maldonado, K. J. Stevenson, B. D. Chandler, J. AM. CHEM. SOC. 20**04**, 126, 12949-12956

137. M. Haruta, M. Date, Appl. Catal. A 222 (2001) 427–437

138. C. Mihut, C. Descorme, D. Duprez, M. D. Amiridis,, *J. Catal*. **212,** 125–135 (2002).

139. C. Mihut, C. Descorme, D. Duprez, M. D. Amiridis,, *J. Catal*. **212,** 125–135 (2002).

140. M. M. Esfahani, M. Mostafavi, B. Keita, L. Nadjo, P. Kooyman, H. Remita, Gold Bulletin Volume 43 No 1 2010

141. D. Mott, J. Luo, P. N. Njoki, Y. Lin, L. Wang, C. J. Zhong, Catalysis Today 122 (2007) 378–385

142. Y. Yu, Y. Hu, X. Liu, W. Deng, X. Wang, Electrochim. Acta 54 (2009) 3092 3097.

143. S. Thiagarajan, S.M. Chen, Talanta 74 (2007) 212–222

144. J.H. Choi, K.J. Jeong, Y. Dong, J. Han, T.H. Lim, J.S. Lee, Y.E. Sung, J. Power Sources 163 (2006) 71-75.

145. J.B. Xu, T.S. Zhao, Z.X. Liang, J. Power Sources 185 (2008) 857-861.

146. J.K. Lee, J. Lee, J. Han, T.H. Lim, Y.E. Sung, Y. Tak, Electrochim. Acta 53 (2008) 3474-3478.

147. S. Wang, N. Kristian, S. Jiang, X. Wang, Electrochem. Commun. 10 (2008) 961-964

148. Z. Peng, H. Yang, Nano Res. 2 (2009) 406-415.

149. S. Zhang, Y. Shao, G. Yin, Y. Lin, J. Power Sources 195 (2010) 1103-1106.

150. C.V. Rao, C.R. Cabrera, Y. Ishikawa, J. Phys. Chem. C 115 (2011) 21963-21970.

151. J. Liu, L. Cao, W. Huang, Z. Li, ACS Appl. Mater. Interfaces 3 (2011) 3552-3558.

152. S. Chen, M. Malig, M. Tian, A. Chen, J. Phys. Chem. C 116 (2012) 3298-3304.

153. Y. Yu, Y. Hu, X. Liu, W. Deng, X. Wang, Electrochim. Acta 54 (2009) 3092-3097

154. R. Wang, C. Wang, W.B. Cai, Y. Ding, Adv. Mater. 22 (2010) 1845-1848

155. C. Xu, R. Wang, M. Chen, Y. Zhang, Y. Ding, Phys. Chem. Chem. Phys. 12 (2010) 239-246.

156. J. Xu, C. Zhang, X. Wang, H. Ji, C. Zhao, Y. Wang, Z. Zhang, Green Chem. 13 (2011) 1914-1922

157. Z. Zhang, Y. Wang, X. Wang, Nanoscale 3 (2011) 1663e1674.

158. S. Zhang, Y. Shao, G. Yin, Y. Lin, Angew. Chem. Int. Ed. 49 (2010) 2211-2214

159. Y. Kim, H.J. Kim, Y.S. Kim, S.M. Choi, M.H. Seo, W.B. Kim, J. Phys. Chem. C 116 (2012) 18093-18100

160. S. Zhang, Y. Shao, H.G. Liao, J. Liu, I.A. Aksay, G. Yin, Y. Lin, Chem. Mater. 23 (2011) 1079-1081

CHAPTER TWO

Experimental Procedures

This Chapter introduces the materials, synthesis and physical characterization and electrochemical characterization techniques employed in this dissertation along with a brief overview of the techniques.

2.1 Materials and Chemicals

Platinum (≥ 99.9%, 0.5-1.2 μm) and gold (≥ 99.9%, < 10 μm) powders, sodium hydroxide (NaOH (99. 8% purity) and hydrochloric acid (HCl) were purchased from Sigma-Aldrich and used without further purification. Nafion solution (5 wt %, Dupont), sulfuric acid (H_2SO_4, OmniTrace Ultra), and Amicon Ultra-4 Ultracel-50K centrifuge filters (Millipore) were obtained from Fisher Scientific.

Formic acid (HCOOH, 99.9 % purity) and Methanol (CH_3OH, 99.9 % purity) were purchased from Fisher Scientific. Water was purified by a Millipore Ultra-pure water system and has a resistivity of 18.2 MΩ·cm at 25 °C.

Dopamine (DA) and ascorbic acid (AA), were supplied by Aldrich Chem. Co. (Milwaukee, WI, USA). Na_2HPO_4 and NaH_2PO_4 were also purchased from Fisher Scientific Inc. All other reagents were of analytical quality. In this dissertation, all chemicals were used as received without any further purification.

2.2 Synthesis of PtAu colloids by Pulsed laser ablation in liquid

For the preparation of PtAu alloy NPS, Pt and Au powders mixtures with different ratios (Pt_xAu_{100-x}, x = 0, 30, 50, 70, 100) were mechanically mixed for 30 minutes before being compression molded into a disk. In a typical process, 500 mg of Pt+Au powder mixture with the right composition was placed into a steel die with a diameter of 8 mm and pressed (CARVER Press, maximum pressure = 12 tons, during 10 minutes) to form a compact disk with a thickness of *ca* 1.5 mm. Then, this disk was used as a target to perform pulsed laser deposition in liquid [1]. All the operations were performed at room temperature.

Neutron Activation Analysis (NAA) was used to assess the concentrations of the various elements (that is Au to Pt weight ratios in the alloys). The analysis was performed on 1 mL of as-prepared colloidal solution using a SLOWPOKE nuclear reactor (École Polytechnique de Montréal, Montréal, Canada).

The mixtures of Pt and Au NPs were prepared by physical mixing of pure Pt NPs and pure Au NPs that were obtained from pulsed laser deposition in liquid using pure Pt and pure Au targets, respectively. Mixtures of Pt_x and Au_{100-x} NPs with the following nominal ratios (x=0, 30, 50, 700, 100 at %) were prepared by taking the right amount of Pt and Au NPs based solution using a micropipette. The mixed solution was then sonicated for at least 20 min to form a uniform suspension which was drop-cast onto the surface of the supporting glassy carbon electrode.

2.3 Materials Characterization Techniques

Several qualitative and quantitative methods were employed to characterize the structural, morphological and compositional properties of the PtAu alloys catalysts produced.

2.3.1 X-ray diffraction

X-ray powder diffraction is a technique used to study the phase structure and crystallite size of powdered polycrystalline samples. Since the wavelength of X-rays (~ 1 Å) is comparable to the size of atoms, it is suitable to examine the crystal structure and the atom positions in a crystalline solid. The technique is contingent on the scattering of X-rays by rows of atoms. The evaluation of crystal structure employs Bragg's law, which can be modeled as constructive interference by two waves reflected from rows of atoms [2]. Fig. 2.1 shows the model of reflection from two planes of atoms in a solid. If the wavelength (λ) of the incident X-rays and the incident angle (θ) are known then the interplanar spacing (d) can be determined by Bragg‟s equation as:

$$2d \sin(\theta) = n\lambda \tag{2.1}$$

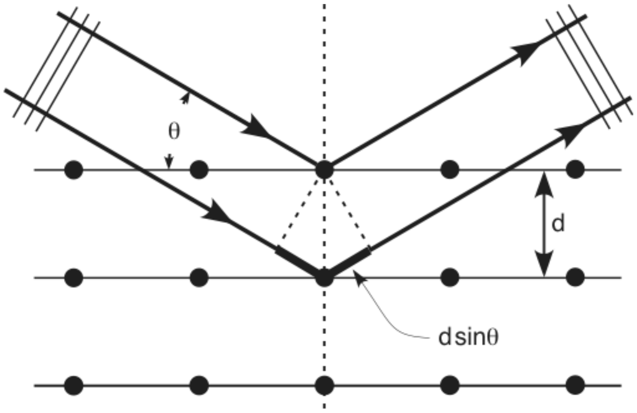

Fig 2.1: Diffraction of X-ray by rows of atoms in a crystal lattice [3]

In this thesis, the X-ray diffraction studies were carried out with a Panalytical XRD X-pert Pro diffractometer (Cu K_α radiation) at a grazing incidence angle of 0.5° with a step size of 0.1° and counting time of 15 s per step. The diffraction patterns were recorded in the 2θ range extending from 30° to 90°.

2.3.2 Transmission Electron Microscopy (TEM)

Transmission Electron Microscopy (TEM) images were obtained by using a high resolution JEOS-2100F TEM (École Polytechnique de Montréal, Montréal, Canada) with an accelerating voltage of 200 kV. The samples for the TEM analysis were prepared by placing a small drop of the colloidal solution onto a coated copper-carbon grid and the excess solution was wicked away by a filter paper. Meanwhile, the selected area electron diffraction (SAED) pattern and energy dispersive spectroscopy (EDS) spectra were measured at different locations on the sample. The particle size was determined by measuring more than 100 individually dispersed particles identified in TEM images.

High Resolution Transmission Electron Microscopy (HRTEM) is a direct visualization of structures and defects at a resolution of 0.1 nm. HRTEM is based on electron diffraction which is a collective elastic scattering phenomenon with electrons being scattered by atoms in a regular array (crystal). The incoming plane electron wave interacts with the atoms, and secondary waves are generated which interfere with each other. This occurs either constructively (reinforcement at certain scattering angles generating diffracted beams) or destructively (extinguishing of beams). As in XRD, the scattering event can be described as a reflection of the electron beam from planes of atoms (lattice planes) [4]. The Bragg law gives the relation between interplanar distance d and diffraction angle θ. Since the wavelength of the electrons is known, d can be calculated from electron diffraction (ED) patterns. Information regarding lattice parameter, crystal orientation and crystal symmetry can be obtained simultaneously which aid phase identification analysis in the sample.

2.3.3 Scanning Electron Microscopy (SEM)

Scanning Electron Microscopy (SEM) is a technique that utilizes back scattered and secondary electrons to construct an image. In a scanning electron microscope, a tiny electron beam is scanned across the sample. Simultaneously, the generated signals are being recorded, and an image is formed pixel by pixel. In SEM, the signals are observed on the same specimen site as the incoming electron beam on the specimen. In contrast to TEM methods needing very thin samples, compact samples can thus be investigated by SEM. Valuable information about morphology, surface topology and composition can be obtained. The use of SEM for the study of sensitive electrodes may need the use of special transfer systems [5]. A Scanning Electron Microscope (FEI, Model: Quanta 200) was used to observed the surface morphology and composition of the perovskites catalysts. The sample powders were dispersed on a carbon tape before mounting on a sample holder.

2.3.4 Energy dispersive X-ray spectroscopic analysis (EDX)

Energy dispersive X-ray spectroscopy (EDX) was used to determine the atomic ratios of the constituent elements in the perovskite electrocatalysts synthesized. The method depends on measuring the characteristic X-rays energies emitted when a transition of the outer shell electrons to inner shell occurs. A high energy incident electron beam creates an electron hole in the inner shell and causes the transition of an outer shell electron. As the energy of the X-rays emitted is characteristic of the element, an accurate estimation of elemental compositions can be obtained using th is technique [5]. EDX analysis was conducted with a FEI, Model Quanta 200 scanning electron microscope having an Oxford instruments EDX attachment. The incident electron energies were kept constant at 20 keV for all the samples.

2.4 Electrochemical measurements

The electrochemical behavior of synthesized Pt_xAu_{100-x} alloys NPs was investigated using cyclic voltammetry, chronoamperometry, differential pulse voltammetry and rotating disk electrode techniques. The electrochemical set-up for carrying out these experiments is illustrated in Fig. 2.2 All electrochemical measurements were done in a conventional three electrode electrochemical cell using a glassy carbon electrode (GCE) (5 mm diameter, PineChem Inc) as the working electrode substrate, platinum gauze as the counter electrode and different reference electrodes such as Mercury-Mercury Oxide (Hg/HgO), Reversible Hydrogen Electrode (RHE) and Saturated Calomel Electrode (SCE) depending on the system (probe molecule and pH) under investigation. This section will describe the electrode preparation and experimental techniques used in the determination of the electrochemical characteristics of the Pt_xAu_{100-x} alloy system. All electrochemical studies were performed with an AUTOLAB (Eco Chemie) potentiostat a at room temperature.

Fig. 2.2: The electrochemical cell set up arrangement

2.4.1 Electrode Materials

The electrode materials that were electrochemically evaluated were the Pt_xAu_{100-x} alloy NPs and Pt_x+Au_{100-x} mixture NPs electrodes made from Pt, Au, and Pt_xAu_{100-x} (x: atomic %) catalyst suspensions prepared by pulsed laser ablation in liquid (PLAL). The physical properties of the distinct Pt_xAu_{100-x} NPs electrodes with varying particle sizes are summarized in Table 1.1 in chapter 1 of this thesis.

2.4.2 Working Electrode Preparation

The working electrodes used in this work were prepared from Pt_xAu_{100-x} colloidal suspension. An adequate volume of the Pt_xAu_{100-x} colloidal suspension, corresponding to various metal loadings (*ca*. 10 ± 0.3 $\mu g_{catalyst}$ cm^{-2} for FAOR and the MOR and 18 ± 2 $\mu g_{catalyst}$ cm^{-2} for dopamine (DA) and ascorbic acid (AA) oxidation) was deposited onto the GC disk. After evaporation of the solvent, 3 µl of Nafion solution (5 wt.%) was pipetted onto the electrode and allowed to dry overnight. It is worth mentioning that preceding every electrode preparation, the GC disk substrates were polished with alumina slurries (1.0 µm and 0.05 µm diameters) and ultrasonically cleaned in pure water for 5 min.

2.4.3 Electrolyte, reference and counter electrodes

De-ionized water (18 mΩ cm^{-1}) was used to prepare all aqueous solutions and rinsing. The electrolyte solutions consisting of 0.5 mol dm^{-3} H_2SO_4 and 0.5 mol dm^{-3} HCOOH were prepared with de-ionized water for formic acid oxidation.

An electrolyte solution of 0.5 mol dm^{-3} NaOH +0.5 mol dm^{-3} CH_3OH prepared with de-ionized water was used for methanol oxidation experiments in alkaline medium, while 0.5 mol dm^{-3} H_2SO_4 + 0.5 mol dm^{-3} CH_3OH was used as electrolyte for methanol oxidation experiments in acidic medium.

In the case of Dopamine (DA) and ascorbic acid (AA) oxidation, 0.1 mol dm^{-3} phosphate buffer solution prepared from (0.1 mol dm^{-3} Na_2HPO_4 and 0.1 mol $dm^{-3}$$NaH_2PO_4$) was used as the supporting electrolyte. The pH was adjusted using 1.0 mol dm^{-3} HCl or 1.0 mol dm^{-3} NaOH. 1.0 mmol dm^{-3} DA and 5.0 mmol dm^{-3}AA solutions were prepared in 0.1 mol dm^{-3} PBS.

All potentials reported in the alkaline medium were referred to the Hg/HgO reference electrode immersed in NaOH solution of the same concentration as the experimental electrolyte. A Hg/Hg_2SO_4 reference electrode immersed in H_2SO_4 solution of the same concentration as the electrolyte was used in acidic medium. In the case of DA and AA oxidation, a saturated calomel electrode (SCE) was used as reference electrode.

2.4.4 Electrochemical Characterization Techniques

In this section a brief overview of the electrochemical characterization techniques employed in the electrocatalysis of the small organic molecules under study here is presented, including the kind of information that were obtained from these techniques.

2.4.4.1 Cyclic voltammetry (CV)

Cyclic voltammetry is perhaps the most useful technique in electrochemistry. It can rapidly provide qualitative information about materials and electrochemical reactions, such as the electrochemical response of catalysts and their catalytic activity with respect to the electrochemical reactions under study. The concept of this method is that a potential is varied back and forth between half wave potential values with time and the current response of the system is recorded (see Fig. 2.3a). This technique is similar to linear sweep voltammetry (LSV). However, unlike linear sweep voltammetry, the potential is reversed after a maximum/minimum set potential is attained. The inversion gives useful information about the species present in the solution. Usually, the current response of a system is dependent on the concentration of the species, scan rate, diffusion coefficient, and the reaction rate [6 - 8]. For surface processes such as adsorption of electroactive species from bulk solution to the electrode surface; O is being reduced to another adsorbed species R with the fraction of surface coverage being θ, the electrochemical charge transfer reaction can be written as:

$$O_{ads} + e^- \rightarrow R_{ads} \qquad (2.2)$$

$$\theta \qquad\qquad (1-\theta)$$

If the electron transfer reaction is fast enough, the Nernst equation for the surface process can be expressed as

$$E = E^{O} + \frac{RT}{F}\ln\frac{(1-\theta)}{(\theta)} \qquad (2.3)$$

where E^o is the standard thermodynamic potential for adsorbed species, R is the gas constant, T is temperature in Kelvin, and F is the Faraday constant.

If the redox peak potential change occurs with pH change on the electrochemical reaction mechanism of the surface adsorbed species. For a reaction involving either a proton or OH^-, e.g.,

$$O_{ads} + mH^{+} + ne^{-} \rightarrow R_{ads} \qquad (2.4)$$

Then the change in the formal potential (the average of the anodic potential and cathodic potential) vs. pH follows Equation 2.5:

$$E^{f} = E^{O} - 2.303\frac{mRT}{nF}pH \qquad (2.5)$$

where E^f is the formal potential, E^o is the Nernst potential, and the other terms have their usual significance [6, 7].

The current response of such a system will be given by

$$i = FA\frac{d\theta}{dt} \qquad (2.6)$$

where A is the electrode area. The peak current is given by

$$i_p = \frac{n^2F^2}{4RT}\upsilon A \qquad (2.7)$$

where, υ is the scan rate (V s^{-1}) and the other symbols have their usual meaning [9].

However, a typical cyclic voltammogram of a diffused species obeying Nernst equation is shown in Fig. 2.3. For a reversible reaction, the peak current is related to the bulk concentration of the electroactive species given by the Randles–Sevcik equation [6] (at 25 °C):

$$i_p = 2.686 \times 10^5 n^{3/2} A C_O D^{1/2} \upsilon^{1/2} \qquad (2.8)$$

where i_p is the peak current in amperes, A is the electrode area (cm^2), D is the diffusion coefficient (cm^2 s^{-1}), C_0 is the bulk concentration in mol cm^{-3}, and υ is the scan rate in V s^{-1}.

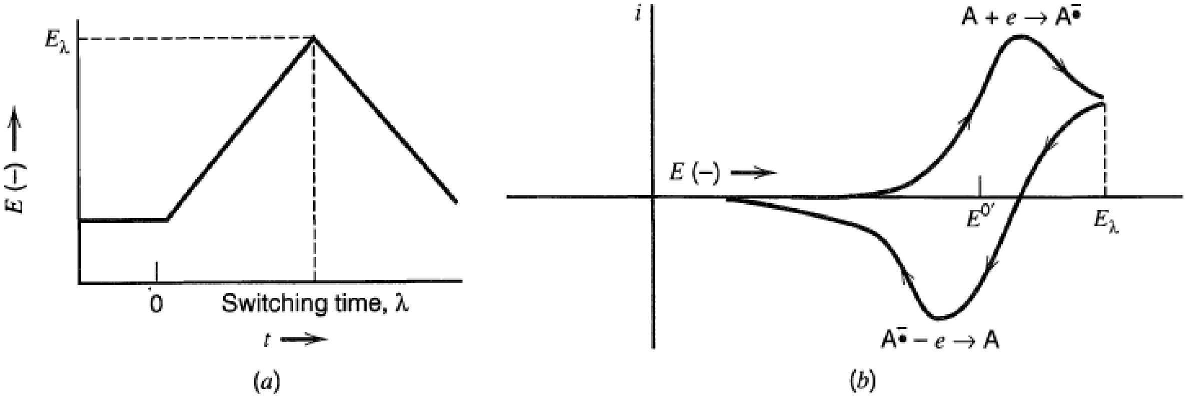

Fig. 2.3**:** (a*)* cyclic potential sweep, (b) Resulting cyclic voltammogram [6]

It is important to mention that the exact potential range and scan rate used are given in the respective Chapters.

Several information was obtained from the CVs curves derived from the oxidation of each organic molecule studied in this dissertation. Common to all the molecules, the CV curves provide information concerning the redox behavior of the electro-oxidation process on the PtAu MPs. Prior to the electro-oxidation of the molecules on the PtAu NPs, the PtAu NPs were cycled in the supporting electrolyte for each molecule and the CV curves provided information concerning the surface atoms and the electrochemical surface areas of these catalysts. However, specific information was obtained from the CVs curves of these small organic molecules oxidation.

For instance the reaction mechanisms were obtained from the CVs curves of formic acid oxidation at the PtAu NPs. With respect to DA and AA oxidation, the CVs curves helped us to analyze the information regarding the surface coverage of DA molecules on PtAu NPs. The way the different CVs were analyzed to gain information on the electrochemical processes occurring during the oxidation of the different small organic molecules will be discussed in the following chapters.

2.4.4.2 Differential Pulse Voltammetry (DPV)

Differential pulse voltammetry (DPV) is one of the few sensitive and selective electroanalytical tools for studying redox properties of extremely small amounts of chemicals because of the following two features: (1) In these measurements, the effect of the charging current can be minimized, so high sensitivity is achieved; (2) Only faradaic current is extracted, so electrode reactions can be analyzed more precisely [10]. Differential pulse voltammetry has these characteristics: (1) Reversible reactions show symmetrical peaks, and irreversible reactions show asymmetrical peaks. (2) The peak potential is equal to $E_{1/2}^{r}$-ΔE ($E_{1/2}^{r}$ is half wave potential of the reaction and ΔE is the potential between the start and end potentials of the pulse) in reversible reactions, and the peak current is proportional to the concentration. (3) The detection limit is about 10^{-8} M.

This technique relies on the principle of applying small pulses of constant amplitude (10 to 100 mV) superimposed on a staircase wave form with a slowly increasing base potential (see Fig. 2.4). The current is measured at two points for each pulse, the first point (1) just before the application of the pulse and the second (2) at the end of the pulse. These sampling points are selected to allow for the decay of the nonfaradaic (charging) current. The difference between current measurements at these points for each pulse is determined and plotted against the base potential.

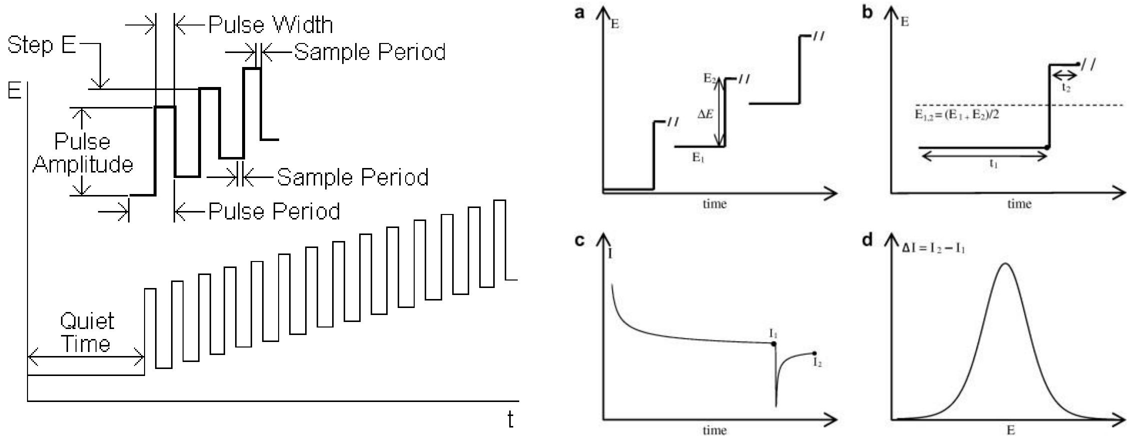

Fig 2.4: Potential wave form for differential pulse voltammetry [10]

In this dissertation, the selective and sensitive determination of DA and AA concentrations is carried out by employing DPV experiments. The exact DPV conditions are as follows: scan rate (20 mV s^{-1}), pulse amplitude (50 mV), pulse rate (200 ms) and pulse width (50 ms). These conditions give a sharp and well-defined peak signal.

2.4.4.3 Steady-state polarization curves

Polarization means that the potential of the electrode surface shifts away from its equilibrium value, leading to an electrochemical reaction. A steady-state polarization curve describes the relationship between the electrode potential and the current density, which is recorded by either holding the electrode potential and recording the stable current response, or holding the current density and recording the stable potential response [6]. The criteria to evaluate a polarization curve depend on its application. Chronoamperometry is a typical kind of steady state polarization technique used for quantitative analysis of electrooxidation process. In that case, the electrode potential is held at a constant value and the current is recorded over time. This technique provides information about the oxidation mechanisms and the kinetic of the system under study. Additionally, the amount of charge for deposition (dissolution) can be determined. Also, this method can be applied for the determination of a poisoning rate and an adsorption isotherm.

With the chronoamperometry, the current is measured versus time as a response to a potential pulse. The recorded current can be analyzed and the reactions responsible for it can be identified from the variations with time. For example: at short times the capacitive current is dominant ($\propto e^{-t/RC}$, with R = solution resistance and C = capacitance), while at longer time scales, the diffusion limited faradaic current might prevail ($\propto t^{-1/2}$).

The principle underlying chronoamperometry is that, at the beginning of the transient experiment, the potential of the working electrode is held at E_i (Fig. 2.5A). At $t = 0$ the potential is instantaneously changed to a new value E_1, and corresponding current time response is recorded as shown in Fig. 2.5B.

In general, for an elementary electrochemical reaction, $O + e^- \rightarrow R$, the most useful equation in chronoamperometry is the Cottrell equation, which describes the observed current of a reversible redox reaction at a planar electrode at any time following a large forward potential step (or to large overpotential) assuming a linear diffusion control at the planar electrode surface [6].

$$i = \frac{nF\sqrt{D_O}C_O}{\sqrt{\pi t}} \tag{2.9}$$

where i is the current density, D_O and C_O is the diffusion coefficient and bulk concentration for the reduction of the electroactive species respectively, and other symbols have their usual meanings.

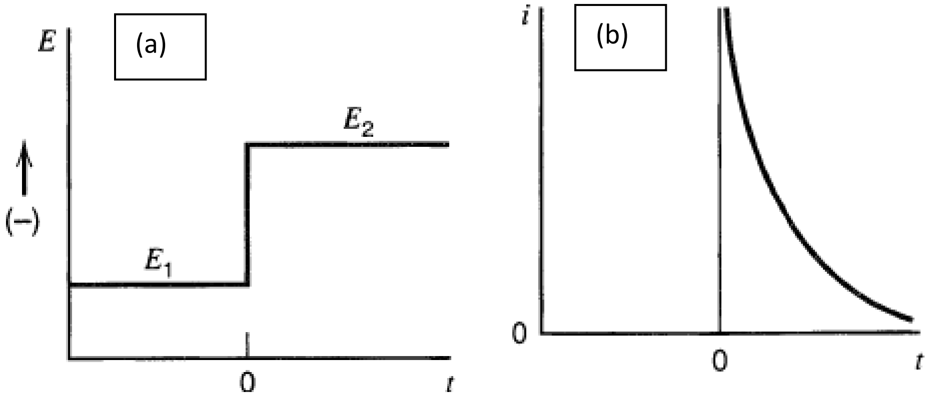

Fig 2.5: **(a)** The potential-time profile applied during experiment, E_i is initial value and E_1 is the potential of interest. (**b)** The corresponding response of the current due to changes of the potential. [6]

In this dissertation, chronoamperometric characterizations were carried out for FAO and MOR (in both acidic and alkaline media) with the aim of determining the steady state catalytic stability and the catalyst tolerance to CO poisoning.

2.4.4.4 Rotating disc electrode (RDE) experiments

Rotating disc electrode (RDE) experiments are hydrodynamic techniques, where the working electrode is rotated to induce forced convection and obtain diffusion limited current (i_L) [6]. The limiting current is a function of the rotation speed under diffusion control regime is given by Levich equation as:

$$i_L = 0.62nFAD^{\frac{2}{3}}\chi^{\frac{-1}{6}}C_o\omega^{\frac{1}{2}} \tag{2.10}$$

where, i_L is the limiting current in A, n is the total number of electrons transferred, F is the Faraday constant (96485 C mol^{-1}), A is the area of the electrode, D is the diffusion coefficient of the species in cm^2s^{-1}, C_o is the bulk concentration in mol cm^{-3}, γ is the kinematic viscosity in cm^2 s^{-1}, and ω is the rotation rate in rad s^{-1}. Under mixed-diffusion-kinetic condition, the determination of the limiting current (i_L) allows an easy evaluation of the kinetic currents (i_k) and measured current (i) is given by the Koutecy-Levich equation {6}:

$$\frac{1}{i} = \frac{1}{i_l} + \frac{1}{i_K} \tag{2.11}$$

Additionally, a plot of $1/i$ and $1/\omega^{1/2}$ yields a straight line that gives information on the total number of electrons transferred. Fig. 2.6 shows oxygen reduction reaction (ORR) LSV plot obtained for Pt NPs electrode in 0.5 mol dm^{-3} H_2SO_4.

RDE experiments were conducted with a glassy carbon disk electrode (5 mm dia.) mounted onto an interchangeable RDE holder (Pine Instruments, USA) in O_2 saturated 0.5 mol dm^{-3} H_2SO_4 for PtAu alloy NPs. This experiment was conducted to determine whether the direct four electron pathway or indirect 2-electron pathway is present on the PtAu NPs.

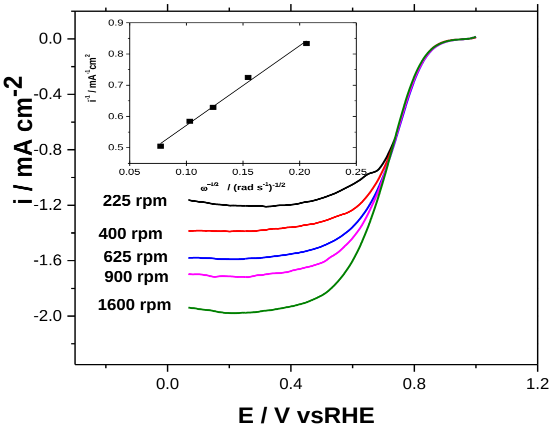

Fig. 2.6: Hydrodynamic polarization curves for Pt NPs electrode in 0.5 mol dm^{-3} H_2SO_4 in oxygen saturated medium at various rotation rates. The inset shows the variation of $1/i_l$ with $1/\omega^{1/2}$ at 0.6 V

References

1. J. Zhang, D. Oko, S. Garbarino, R. Imbeault, M. Chaker, A. C. Tavares, D. Guay, D. Ma, J. Phys. Chem. C, 2012, 116 (24), 13413–13420
2. B. D. Cullity, Elements of X-ray diffraction, 2nd Eds. Addison-Wesley, Reading, 1978
3. X-ray crystallography, http://en.wikipedia.org/wiki/X-ray_crystallography, site accessed on 10th July 2009.
4. Z. I. Wang, J. Phys. Chem. B 2000, 104, 1153-1175
5. Bogner, P.-H. Jouneau, G. Thollet, D. Basse, C. Gauthier, Micron 38 (2007) 390–401
6. A. J. Bard and L. R. Faulkner, Electrochemical methods: Fundamentals and Applications, John Wiley, New York, 2001
7. C. G. Zoski (eds.), Handbook of Electrochemistry, Elsevier, Boston, 2007.
8. J. Wang, Analytical Electrochemistry, Wiley-VCH, Hoboken, 2006.
9. E. G. Compton and C. E. Banks, Understanding voltammetry, World Scientific Publishing Company
10. http://www.basinc.com/mans/EC_epsilon/Techniques/Pulse/pulse.html

CHAPTER THREE

Optimization of Catalyst ink, Cyclic voltammetry and Electrocatalytic Oxygen Reduction Reaction in Acidic Medium at PtAu alloy Nanoparticles

Summary

In this work, we report on how the catalyst electrodes (i. e. catalyst and Nafion loading of the Pt nanoparticles) were optimized. The voltammetric profile of Pt_xAu_{100-x} alloy NPs (x= 0, 30, 50, 70, 100) synthesized by pulsed laser ablation in liquid (PLAL) was investigated in nitrogen-saturated 0.5 mol dm^{-3} $H_2SO_{4.}$ The results of the surface properties probed by voltammetric measurements demonstrated that the surface content of the PtAu NPs is not modified by the electrochemical procedure and that de-alloying is not occurring at the surface of the catalysts as long as electrochemical active surface area of Pt is determined from CVs recorded up to 1.5 V. The catalytic activity of these optimized Pt_xAu_{100-x} alloy NPs electrodes was also tested towards the oxygen reduction reaction (ORR) and the findings are reported in this chapter. The results of the voltammetric experiments were analyzed and compared to those obtained in the literature.

3.1 Catalyst Optimization

As electrocatalytic activity is dominated by nanoparticle surface composition, we use the well-established cyclic voltammetry (CV) methods, since it is a powerful surface sensitive tool for monitoring electrochemical surface properties of the catalysts [1 - 3].

As a first step to optimize the PtAu NPs electrodes for electrocatalytic studies, metal and Nafion loadings were varied to obtain the optimum value which is the electrochemical surface area of Pt catalyst necessary for the catalytic studies. As first, we fixed the Nafion content at 3 ul and monitored the Coulombic charge under the Pt-oxide reduction peak by cyclic voltammetry on electrodes with different Pt loadings. The metal loading with optimum Coulombic charge and catalyst utilization efficiency was then fixed and, as second step, the influence of Nafion loading on the electrochemically active surface area (ECSA), oxygen reduction reaction (ORR) activity and stability of the catalyst was also investigated by recording cyclic voltammograms..

3.1.1 Effect of the Metal loading on the Coulombic Charge

Fig. 3.1A shows the cyclic voltammograms recorded for Pt NPs electrodes with different metal loadings in N_2-purged 0.5 mol dm^{-3} H_2SO_4 at 50 mV s^{-1}. The voltammograms of Pt NPs (Fig. 3.1A) show all features characteristic of the electrochemical behavior of bulk polycrystalline Pt with three main potential regions: (i) from 0.05 to 0.35 V, a pair of anodic (cathodic) peaks attributed to hydrogen desorption (adsorption); (ii) from 0.35 to 0.65 V, a featureless potential region attributed to double layer capacitive current; and (iii) Pt oxide formation/removal potential region at values higher than 0.65 V.

It is worth mentioning that there is an increase of the hydrogen desorption and metal oxide reduction peak currents with increasing catalyst loading up to Pt metal loading of *ca.* 20 µg cm^{-2} and then the oxide reduction peak reduces with further increase in metal loading. The total voltammetric charge in the metal-oxide reduction region is estimated by integrating the area of the reduction peak in the reverse scan of the voltammograms assuming that 440 µCcm^{-2} is needed to reduce a monolayer of Pt-oxide on polycrystalline platinum [4-6].

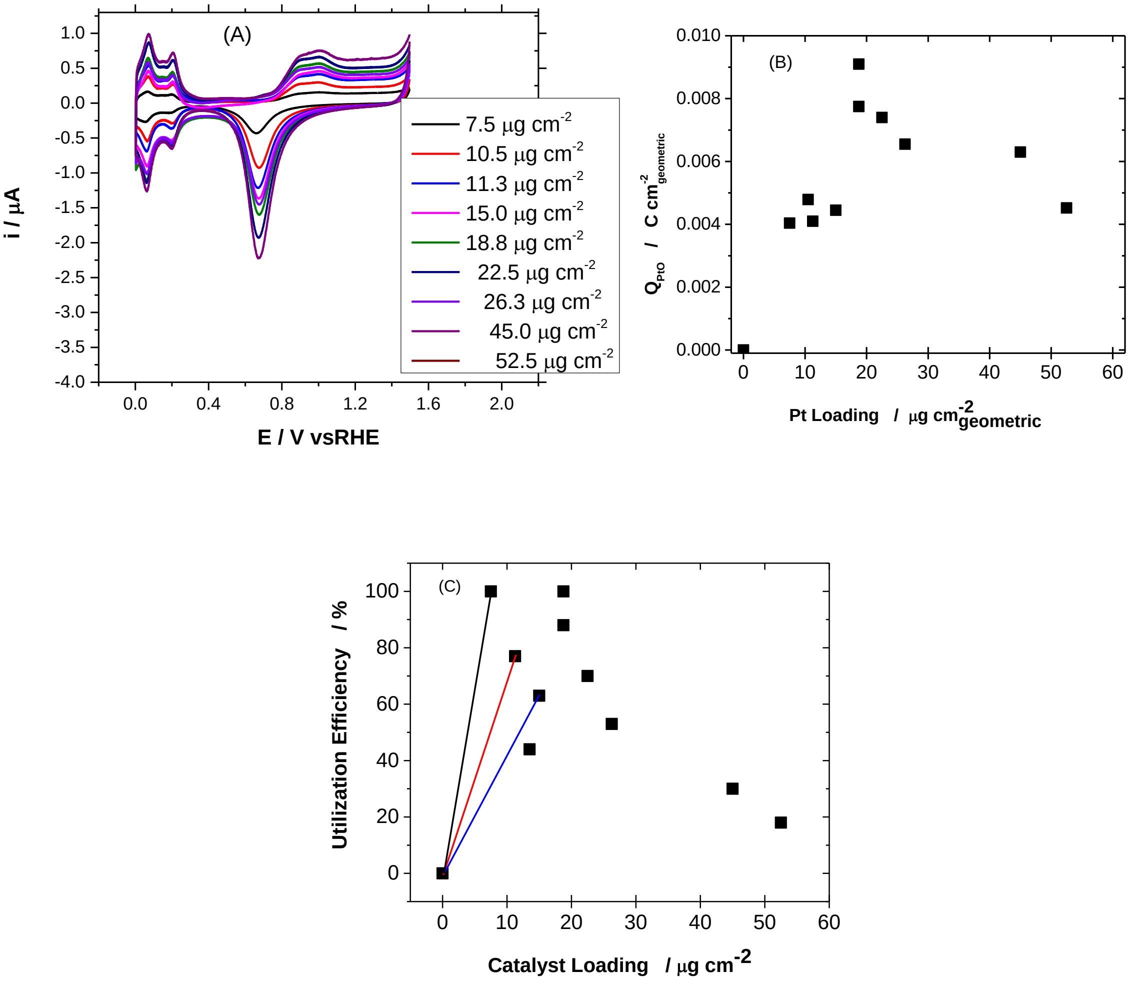

Fig 3.1: (a) CVs responses (50 mV s^{-1}) for Pt NPs with different metal loading of 7.5, 10.5, 11.3, 15.0, 18.8, 22.5, 26.3, 45.0 and 52.5 µg cm^{-} in N_2 purged 0.5 M H_2SO_4 up to 1.5V vs. RHE at a fixed Nafion Loading of 3 µl (5 wt % DUPONT), (b) total Coulombic charge of the Pt-oxide reduction region, and (c) utilization efficiency as function of catalyst loading calculated from (b)

As shown in Fig. 3.1B, the electric charge increases linearly with the catalyst loading up to 20±2 µg cm^{-2} and then decreased steadily with further increase in Pt-metal loadings. This is due to the fact that some Pt sites become not accessible as the mass of the catalyst is increased above a certain value and also possible agglomeration of the Pt NPs.

To select the optimum metal loading for electrocatalytic reaction, we estimated the utilization efficiency of Pt, taking into account the particle sizes of NPs, by employing the equation below:

$$\% \, Utilization = \frac{ECSA \times \rho \times d}{6 \times 1000} \times 100\% \tag{3.1}$$

where ρ is the density of the bulk active material (g cm^{-3}) and d the diameter of the Pt NPs (nm) determined by TEM.

This simple calculation demonstrates that the Pt utilization efficiencies vary with different particle sizes. For example, the utilization efficiency was estimated to be 80% (red line) and 100 % (black line), when the diameter is 2.5 nm. However, when the diameter of the Pt NPs was 3.0 nm, the utilization efficiency was 60 % (blue) 3.0 nm. These results are clear shown in Fig 3.1C. This indicates high utilization efficiency of Pt NPs varies between 60 to 100 % for Pt NPs with particle size varying from 2.5 to 3.0 nm. . The lowest metal loading range to giv8e the optimum sites for efficient catalysis is 10-15 µg cm^{-2}.

Similar work was conducted by Paganim and co-workers [7] on the effect of Pt loading on their thin-film cell for development and electrochemical studies of gas diffusion electrodes for polymer electrolyte fuel cells. They compared loadings of 0.1 and 0.4 mg cm^{-2} in the anode and found that the performance was better for catalyst with lower metal loading. A similar work on low Pt loading high performance cathodes for PEM fuel cells was conducted by Qi and co-worker [8]. They found that Pt catalyst with low metal delivered the highest performance.

From the above literature results, it is obvious that the best performance of a catalyst is related to metal loading with optimum utilization efficiency. Therefore, Pt-metal loading of *ca.* 10 µg cm^{-2} was chosen for catalytic activity towards ORR, formic acid and methanol electrooxidation. However, for DA and AA oxidation, the catalyst loading was optimized again and this will be discussed in an appropriate subsequent chapter of this dissertation.

3.1.2 Effects of the Nafion loading on the electroactive surface area

Addition of Nafion onto a catalyst film makes the film active in three dimensions because proton transport throughout the entire film is improved. It was reported that the ionic conductivity of the catalyst layer is proportional to the amount of Nafion in the catalyst film [9]. However, since Nafion is an electronic insulator, it decreases the electronic conductivity of the catalyst film, and may cause some catalyst particles to be electronically isolated. These isolated particles will not be able to participate in any electrochemical reactions. Therefore, the Nafion content on the catalyst film needs to be precisely controlled in order to achieve the best balance among all these influencing factors [10–13].

In order to optimize these pressing factors, we fixed the Pt metal loading at 10 µg cm^{-2} and the influence of Nafion loading on the electrochemically active surface area (ECSA) of Pt NPs was investigated in 0.5 H_2SO_4 mol dm^{-3} nitrogen saturated solution at 50 mV s^{-1}. Fig. 3.2A presents the CVs of Pt electrodes with varied Nafion loadings. Again the CVs reflect the surface chemistry of the Pt electrode for adsorption/desorption processes of hydrogen and oxygen on platinum at its interface. The calculated Pt ECSA is presented in Fig. 3.2B. As can be seen, the increase in Nafion loading from 0.72 to 1.82 µg cm^{-2} led to increase in the ECSA of Pt NPs. This indicates an increase in utilization of Pt NPs. However, when the Nafion concentration was further increased to 2.34 µg cm^{-2}, there was a sharp drop in the ECSA of Pt NPs. This is because additional Nafion loading blocked the reactant species and likely covered active sites in the catalyst layer. Thus, limited active sites of Pt NPs for the electrocatalytic activity are available.

To conclude the optimization of the Pt NPs ink and ascertain its efficacy as an electrode for catalytic activity for various molecules, we investigated the influence of the Nafion loading on the ORR activity and electrochemical stability of the Pt NPs in oxygen saturated electrolyte.

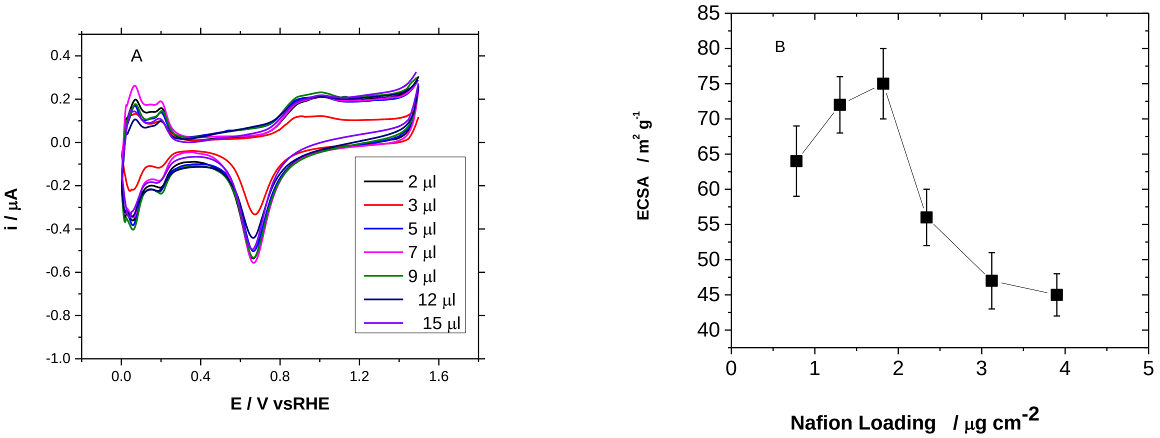

Fig 3.2: (a) CV responses (50 mV s^{-1}) for Pt NPs with varying Nafion loadings in N_2-saturated 0.5 mol dm^{-3} H_2SO_4 up to 1.5V vs. RHE and (b) ECSA calculated from the Pt-oxide reduction region as a function of the Nafion loading.

3.1.3 Effect of Nafion loading on ORR activity

Fig. 3.3A shows RDE voltammograms on the Pt NPs electrodes with various Nafion loadings between 2 µl (0.52 µg cm^{-2}) to 15 µl (3.9 µg cm^{-2}) at 10 mV s^{-1} with rotation speed of 1600 rpm in O_2 saturated 0.5 mol dm^{-3} H_2SO_4 solution. The RDE voltammograms did not overlap very well with a common baseline. This might be due to the different activities of Pt NPs towards ORR with various Nafion loadings. This could also be due to the difference in accessible Pt sites. The ORR performance for Pt NPs electrodes, estimated from the current at 0.2 V, and normalized to ECSA is shown as a function of the Nafion loadings in Fig. 3.3B. The current was evaluated at 0.2V since it is limited by the diffusion of O_2 in that potential region. It can be seen that the normalized diffusion-limited current for the ORR slightly increases and then decreases drastically with increase of Nafion content. This maximal current is 0.32 mA $cm^{-2}{}_{Pt}$ and occurs at 7 µl (1.82 µgcm^{-2}) Nafion loading on the Pt NPs electrodes (Fig. 3.3B). It is interesting to note that this value coincide with that found earlier based on the optimization of the ECSA alone (see Fig. 3.2). This behavior, is related to opposite contributions of Nafion which involves an increase of the ECSA of Pt NPs covered with Nafion and an easier migrations of protons through the electrolyte to catalyst sites (positive contribution) and an increased hindrance of O_2-diffusion by the thick Nafion layer on the sites of the catalyst (negative contribution) [7, 8]. Therefore, the effect of Nafion loading on ORR performance is clearly depicted by the results of Pt NPs in this work.

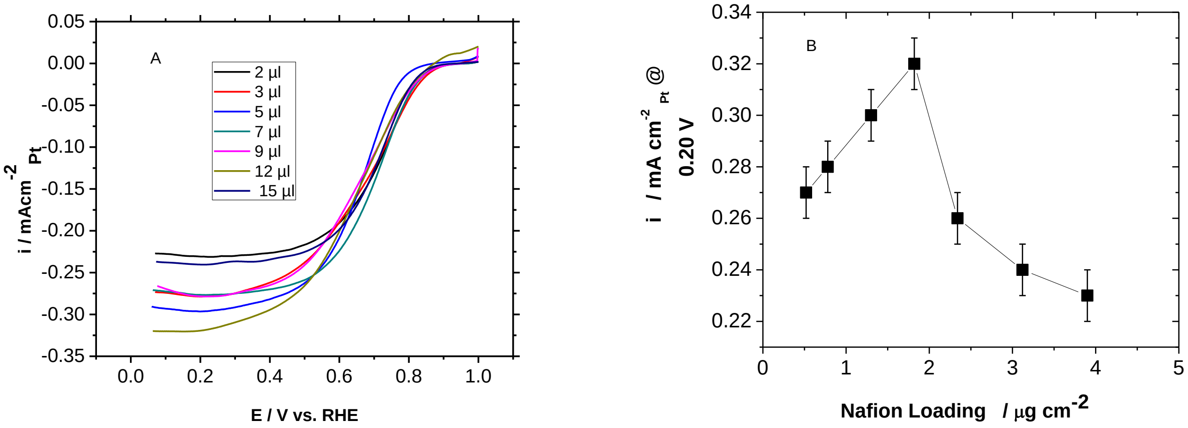

Fig 3.3: (a) RDE Voltammetric responses (10 mV s^{-1}) for Pt NPs in O_2-saturated 0.5 mol dm^{-3} H_2SO_4 at 1600 rpm as a function of Nafion loading and (b) current density in mA cm^{-2} $_{Pt}$ at 0.2 V as a function of the Nafion loading.

3.1.4 Effect of Nafion loading on catalyst stability

For any electrode material used in fuel cells, long-term stability is critical. In order to test the practical feasibility of the synthesized NPs material, a CV test was conducted in 0.5 mol dm^{-3} H_2SO_4 nitrogen atmosphere (50 mVs^{-1}) on all the Pt NPs with metal loading of 10 µg cm^{-2} and at different Nafion loadings before and after ORR test described above. The amount of materials loss, estimated from the fractional change of metal oxide reduction before and after ORR is studied as a function of the Nafion loading on the Pt NPs. Fig. 3.4A shows the representative CVs of the optimum Pt NPs catalyst electrode before and after ORR experiment with Pt-metal loading of 10 μgcm^{-2} and Nafion loading of 1.82 μgcm^{-2}. It is evident from the two voltammograms that the metal-oxide reduction peak in the reverse scan remains virtually unchanged and the amount of materials loss is less than 10 % after ORR. This suggests that the catalyst is quite stable under the ORR activity experiment.

The amount of charge involved in the metal-oxide reduction peaks before and after ORR was converted into percentage loss of materials, andthe results are shown as a function of Nafion loadings in Fig. 3.4B. It is evident from Fig.3.4 B that the materials loss decreased gradually as the Nafion loading is increased, before remaining constant at *ca.* 1 % of the original material at Nafion loading of 1.82 µg cm^{-2}, indicating that this Pt NPs catalyst were reasonably stable. This suggests that the electrode stability increases steadily with increase of Nafion loading.

These potentiodynamic results demonstrate that large amounts of Nafion content may help to increase the electrode activity, but may make the access of the Pt NPs sites difficult, leading to more significant stability of the electrodes. Therefore, to obtain good stability while still have better performance of the electrodes, an optimum Nafion loading of not more ca. 1.82 µg cm^{-2} is selected for all the PtAu NPs experiments in this thesis work.

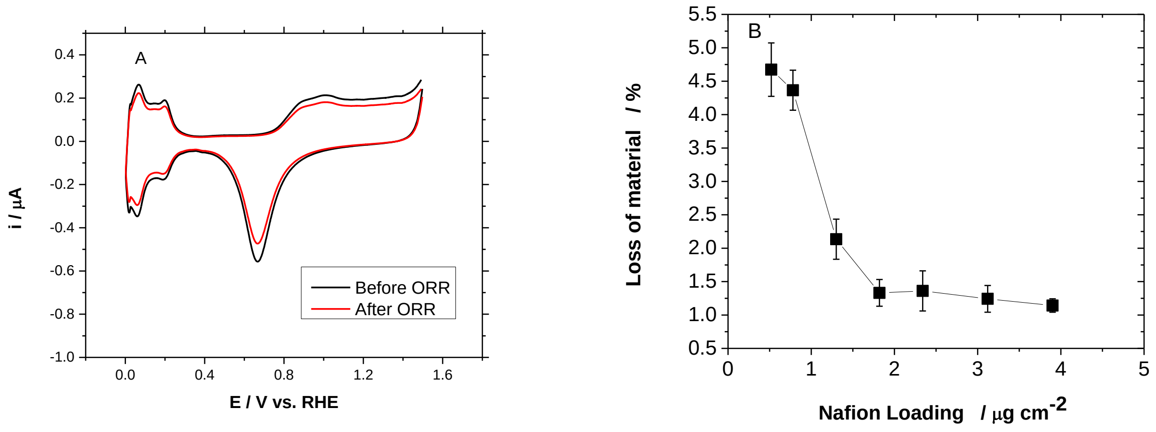

Fig 3.4: (a) Cyclic Voltammetric responses (50 mV s^{-1}) for Pt NPs before and after ORR in N_2-saturated 0.5 mol dm^{-3} H_2SO_4 up to 1.5V vs. RHE (b) percentage loss of materials as a function of the Nafion loading.

Thus, the choice of catalyst and Nafion Loading was based on the ECSA of the Pt NPs, although an optimization of the catalyst and Nafion loading would be necessary in a later stage (e.g. fabrication of gas diffusion electrodes, GDE). As such an optimum electrode composition with metal and Nafion loadings of 10 and 1.82 µg cm^{-2}, respectively, is selected at this point to study the electrocatalytic activity of the NPs for ORR, formic acid and methanol oxidation reactions on all the PtAu NPs. As a preliminary objective of this thesis, we probe the electrochemical properties of these PtAu alloy NPs and their activity towards ORR. The results obtained in these studies are discussed in the following sections.

3.2 Electrochemical Properties of Pt_xAu_{100-x} alloy NPs

Fig. 3.5 shows the cyclic voltammograms (CV) of PtAu alloy NPs in Ar-saturated 0.5 mol dm^{-3} H_2SO_4 up to 1.5 V (panel A) and 1.8 V (panel B). On one hand, voltammograms of Pt NPs (in panel A of Fig. 3.5) show features similar to the well-known electrochemical behavior of bulk Pt as discussed in previous sections. On the other hand, CV of Au NPs in panel B of Fig. 3.5 displays the characteristic features of bulk Au, i.e., a wide potential region corresponding to the double layer charging current from 0.05 to 1.15 V, followed by Au monolayer oxide formation which starts at 1.30 V during the forward sweep, and the gold oxide reduction peak in the backward potential sweep occurred at ca 1.13 V. The electrochemically active surface area of gold (Au ECSA) was determined by integrating the charge associated with the Au oxide reduction peak and by using a factor of 400 µC cm^{-2} for the reduction of Au α-oxide film grown up to 1.8 V in sulfuric acid [13]. In the case of PtAu alloy NPs, a linear combination of the features of both metals is observed, i.e., well-defined hydrogen peaks at 0.12 and 0.26 V and Pt oxide reduction peak at 0.75 V in the case of Pt-rich alloys, while an ill-defined hydrogen sorption peak region and a more pronounced Au oxide reduction peak around 1.17 V are observed for Au-rich alloys.

Another interesting aspect correlated with the PtAu alloy NP stoichiometry is the upper potential region of panel B of Fig. 3.5 ($E \geq 1.6$ V), in which the drastic anodic current increase is attributed to water oxidation, i.e., oxygen evolution reaction (OER) [1]. The onset potential for the OER is shifted toward higher values with increasing Au content and eventually vanishes for pure Au NPs, which is attributed to the formation of monolayer of Au oxide at such potential values and to the fact that the overpotential for the OER is larger than on Pt. It is therefore obvious that surface electrochemistry for alloy NPs displayed in Fig. 3.5 corresponds to the voltammetric characteristics of both Pt and Au surface atoms.

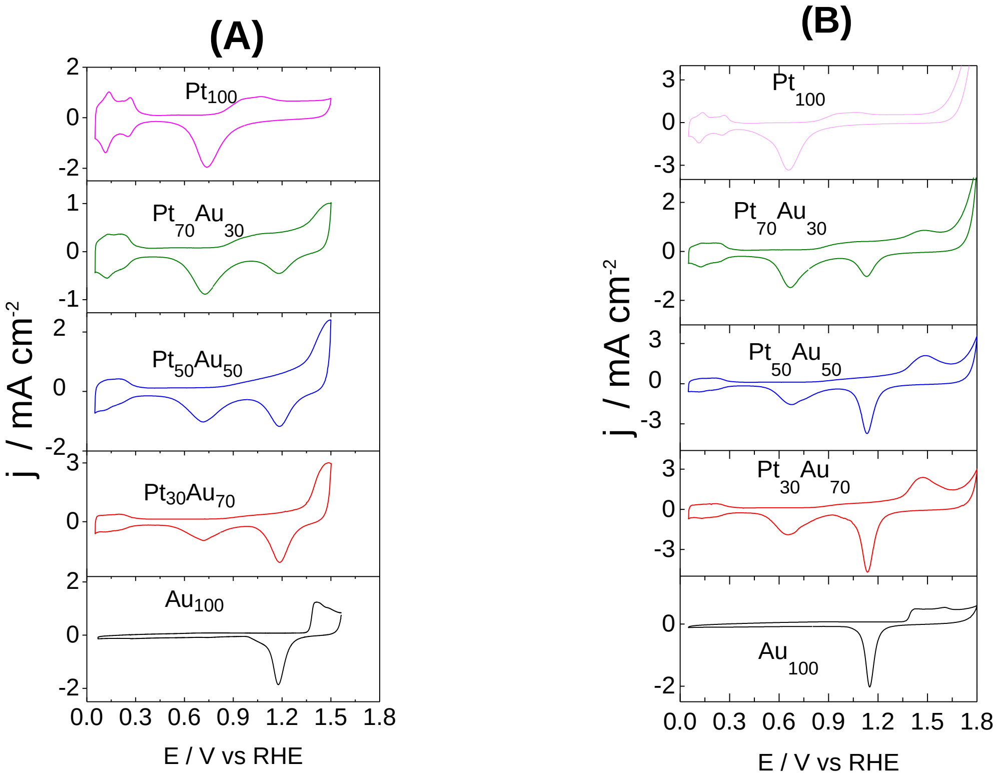

Fig 3.5: Cyclic Voltammetric responses (50 mV s^{-1}) for Pt$_x$Au$_{100-x}$ nanoparticles in Ar-saturated 0.5 M H_2SO_4 up to (a) 1.5V and (b) 1.8V vs RHE.

A detailed investigation of the CVs in panel B of Fig. 3.5 reveals that the peak potential value for Au oxide reduction remained constant at ~1.17 V for the whole range of PtAu alloy NPs. On the other hand, in panel A of Fig. 3.5, the peak potential values for Pt oxide reduction were found to shift toward negative values from 0.74 V for pure Pt NPs to E = 0.73 V for Pt$_{70}$Au$_{30}$ and further to E = 0.71 V for Pt$_{30}$Au$_{70}$. This shift reflects a slightly enhanced Pt oxide reduction hindrance as compared to pure Pt and was already observed at reported PtAu surface alloys [14, 15]. The negative shift of the Pt oxide reduction peak for the Au-rich alloys reveals the stronger Pt−O binding energies as compared with Pt-rich alloy electrodes. This is related to the increase of lattice parameter of PtAu alloys with Au content, which has been correlated to the stabilization of oxygen-type adsorbates, such as −O and –OH species, on an expanded lattice [16]. The above-mentioned voltammetric features reinforce the formation of alloys on the NP surface for the whole stoichiometry range of PtAu NPs.

As catalytic properties are largely affected by the surface chemistry, it is also necessary to examine whether these PtAu alloy NPs have a uniform composition on the surface and in the bulk. To this end, the Pt surface content ([Pt] surface) of the PtAu NPs with nominal Pt content of 30%, 50%, and 70% was estimated by analyzing their corresponding CVs displayed in Fig. 3.5, viz.

$$[\mathrm{Pt}]_{\mathrm{surface}} = \mathrm{ECSA}_{\mathrm{Pt}} / (\mathrm{ECSA}_{\mathrm{Pt}} + \mathrm{ECSA}_{\mathrm{Au}}) \tag{3.2}$$

where ECSA $_{\mathrm{Pt}}$ and ECSA $_{\mathrm{Au}}$ are the Electrochemically Active Surface Areas (cm^2) of Pt and Au, respectively. ECSA $_{\mathrm{Pt}}$ was determined as discussed previously. From the charge of the Au oxide reduction peak, centered at *ca* 1.17 V in the reverse scan of panel B in Fig. 3.5, ECSA $_{\mathrm{Au}}$ was determined using a conversion factor of 400 $\mu C\ cm^{-2}{}_{\mathrm{Au}}$ [17, 18].

Fig. 3.6 shows a plot of $[\mathrm{Pt}]_{\mathrm{surface}}$ against $[\mathrm{Pt}]_{\mathrm{Overall}}$ (bulk Pt atoms). It is clearly seen that there is a one-to-one correspondence between $[\mathrm{Pt}]_{\mathrm{surface}}$ and $[\mathrm{Pt}]_{\mathrm{overall}}$ for all alloy samples, which indicates that the surface composition of the NPs is identical to that of the target used during the synthesis of the NPs. This observation supports the view that there is no surface enrichment. In general, these findings verify that the composition control of the PtAu alloy NPs can be successfully achieved by varying the composition of the target [1]. This indicates that the surface content of the films is not modified by the electrochemical procedure and that dealloying is not occurring at the surface of the catalysts as long as Pt ECSA is determined from CVs recorded up to 1.5 V.

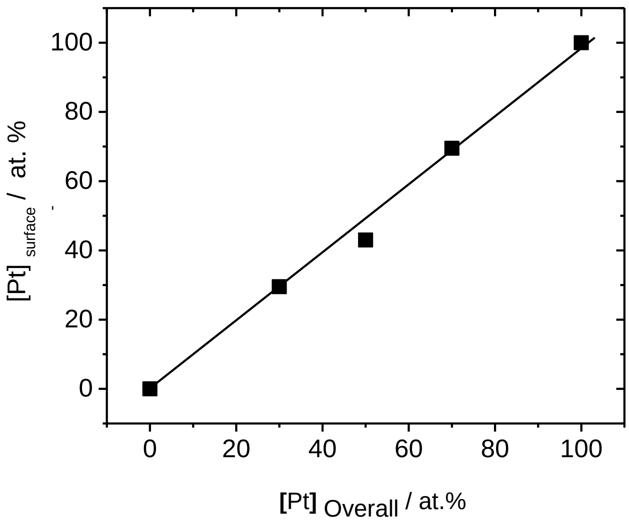

Fig 3.6: Pt surface content of PtAu alloy NPs prepared by PLAL with respect to their Pt bulk content.

3.3 ORR Kinetics by RDE of Pt_xAu_{100-x} alloy NPs

The RDE technique was employed to determine the electrocatalytic activity of Pt_xAu_{100-x} alloy NPs electrodes, in O_2 saturated 0.5 mol dm^{-3} H_2SO_4 solutions. RDE voltammograms of negative going scans for ORR with rotation speeds varying between 225 to 1600 rpm at 10 mV s^{-1} sweep rate for the Pt_xAu_{100-x} alloy NPs (x= 0, 30, 50, 70, 100) are presented in Figs 3.7A, 3.7B, 3.7C, 3.7D and 3.7E. The corresponding Levich plots are displayed as inset.

For each Pt_xAu_{100-x} alloy NPs electrode, the ORR operates under three ranges: the kinetics controlled regime in the potential range of 1.0 to 0.8 V vs. RHE (low current regime); the mixed kinetics and diffusion controlled regime in the potential range of 0.8 to *ca.* 0.5 V vs. RHE (middle current range); and at potential values more negative than *ca.* 0.5 V, current plateau seems to prevail indicating the domination of diffusion-limiting regime.

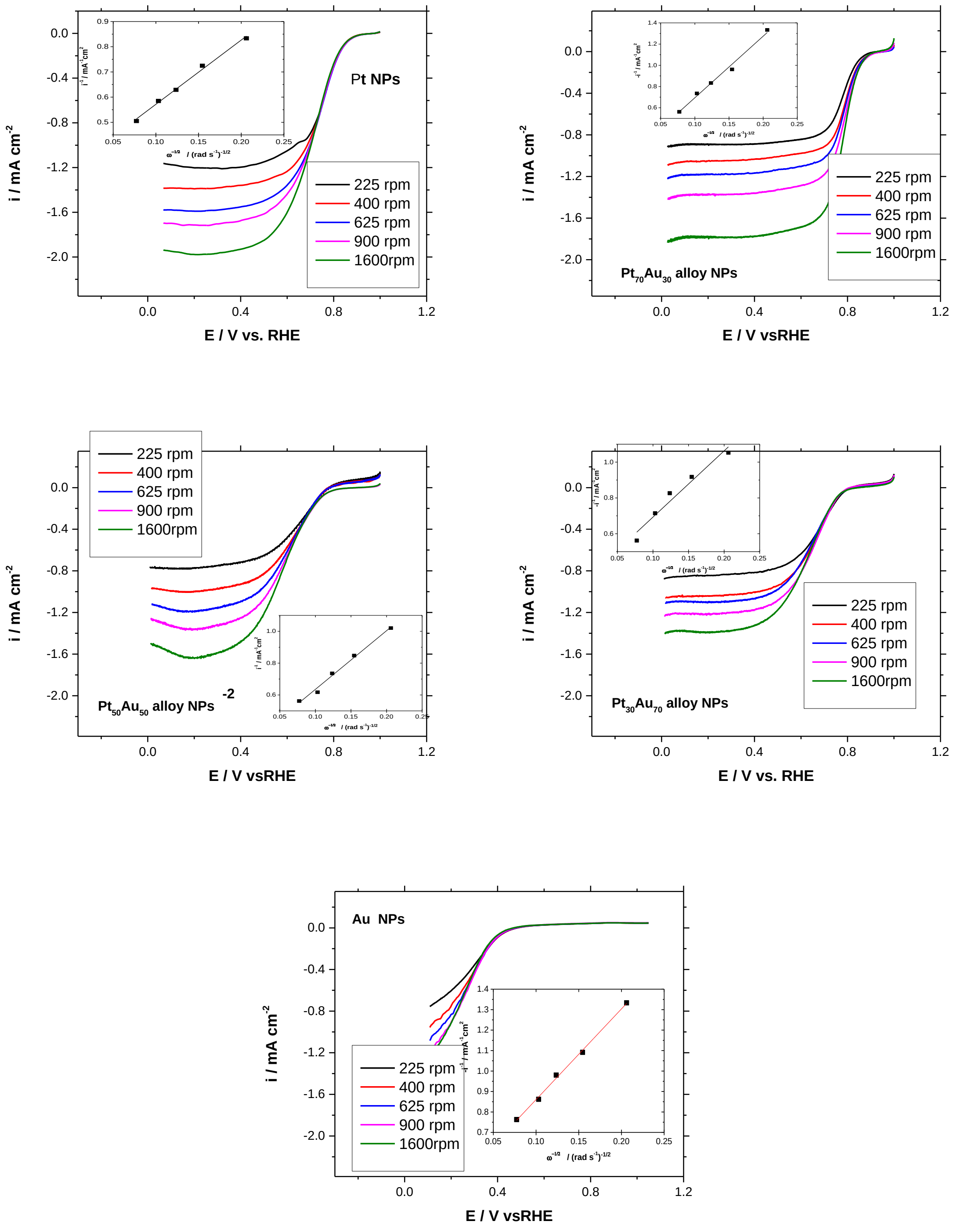

Fig. 3.7: Hydrodynamic voltammograms of positive to negative-going scans in O_2 saturated 0.5 M H_2SO_4 with rotation speeds varying between 225 to 1600 rpm at 10 mV s^{-1} sweep rate for the Pt_xAu_{100-x} alloy NPs (x= 0,30, 50, 70, 100). Inset: Levich plot determined at 0.2V for each catalyst NPs.

The limiting current densities decrease with increasing Au content in PtAu NPs with pure Pt NPs demonstrated the highest limiting current density from 1.2 to *ca.* 2.0 mA cm^{-2} as rotation speeds increased from 225 to 1600 rpm. High rotational speeds lead to faster oxygen flux to electrode surface and consequently larger currents.

The rotation-rate dependent current-potential data can be applied to construct Levich curves accordingly to equation (3.3) that has been widely used to analyze the ORR reaction kinetics [19, 20]

$$i_L = 0.62nFAD^{\frac{2}{3}}\nu^{\frac{-1}{6}}C_o\omega^{\frac{1}{2}} \tag{3.3}$$

where i_L correspond to the diffusion limiting currents, n is the overall number of electron transferred per O_2 molecule, F is Faraday constant (96485 C mol^{-1}), A is the geometric electrode area (cm^2), C_0 is the saturated bulk concentration of oxygen in 0.5 mol dm^{-3} H_2SO_4 ($1.18x10^{-6}$ mol cm^{-3}), D is the diffusion coefficient of oxygen ($1.9x10^{-5}$ cm^2 s^{-1}), υ is the kinetic viscosity of solution (0.01 cm^2 s^{-1}), and ω is the rotation rate (rad s^{-1}) [20].

The inset Fig. 3.7 shows the Levich curves for the as-prepared PtAu alloy NPs electrodes. The linearity of the plots indicate that the rotation speeds used in this study are large enough that the number of electrons transferred per oxygen molecule (n) is independent of rotation speed and therefore a first-order dependence of O_2 kinetics on all PtAu alloy NPs electrodes as reported also on all Pt-based catalysts [19, 20]]. The Levich constant (B) obtained from the slope of the Levich plots, was used to calculate the number of electrons transferred per O_2 molecule which is an important parameter for evaluating the catalyst performance. The number of electrons transferred was calculated as 3.9, 3.4, 3.1, 2.8 and 2.5 for Pt NPs, $Pt_{70}Au_{30}$ alloy NPs, $Pt_{50}Au_{50}$ alloy NPs, $Pt_{30}Au_{70}$ alloy NPs and Au NPs respectively.

The oxygen reduction reaction is a multi-electron-transfer which includes several elementary steps [21] and can follow either the 2 e^- or 4 e^- pathway, which leads to hydrogen peroxide formation or complete water formation reactions, respectively. The high number of electrons transferred per O_2 molecule calculated for Pt NPs here (close to 4) is an indication of low H_2O_2 formation and an almost complete reduction of O_2 to H_2O. Otherwise these values close to 2 indicate H_2O_2 formation.

Figs 3.8A presents a comparison of the activities of selected Pt_xAu_{100-x} alloy NPs electrocatalyst for the ORR in O_2 saturated 0.5 mol dm^{-3} H_2SO_4 at 10 mV s^{-1} at 1600 rpm. From the RDE voltammetric curves as shown in Fig. 3.8A, it is evident that as the Au content in the alloy increased, the activity of the PtAu alloy NPs significantly decreases. In the case of $Pt_{70}Au_{30}$ alloy NPs, the onset potential for ORR was found to be 0.85 V and the limiting current was close to that observed for as-synthesized Pt NPs (1.95 mA/cm^2). The onset potential of $Pt_{70}Au_{30}$ alloy NPs is more positive compare to Pt NPs (0.78 V) which is suggestive of higher catalytic activity towards ORR.

As discussed already in chapter one of this thesis, one critical strategy to reduce the use of Pt without compromising ORR activity and stability is to alloy Pt with other transition metals. This strategy has proven very efficient in reducing Pt metal use, as well as enhancing catalytic ORR activity and stability. Indeed, it has been reported elsewhere that some Pt-alloys can achieve at least two to four times greater ORR activity compared to Pt/C catalysts [22]. This huge activity enhancement was related to a positive shift of onset potential for OH_{ads} formation on the alloy. However, the activity of the $Pt_{70}Au_{30}$ alloy NPs is lower than of pure Pt NPs. This might be due to several contrasting parameters such as particle size, morphology and composition of the PtAu NPs with Au content. Also, increasing the Au content in Pt Au NPs has an adverse effect on activity as can be seen for $Pt_{50}Au_{50}$ alloy NPs and $Pt_{30}Au_{70}$ alloy NPs. It is well-known that ORR is strongly dependent on the particle size, composition and morphology of the NPs. These parameters are connected to each other. For instance as the composition varies from pure Pt NPs to pure Au NPs, both the particle size and morphologies of the NPs changes (e.g. the particle size varies with ORR activity of these PtAu NPs and would be affected with increasing Au content in the PtAu NPs). This is in close agreement with those reported by Luo et al work on activity-composition correlation of AuPt alloy nanoparticle catalysts in the electrocatalytic reduction of oxygen [23]. The current densities profiles (Fig. 3.8A) at 0.20 V at 1600 rpm were compared for all the PtAu NPs. The results demonstrate a decreasing order as shown: Pt NPs> $Pt_{70}Au_{30}$ > $Pt_{50}Au_{50}$ > $Pt_{30}Au_{70}$ and Au NPs

The electrocatalytic activities in terms of mA $cm^{-2}{}_{disk}$ and mA mg-$^{1}{}_{metal}$ for these catalysts with different bimetallic compositions were evaluated from current profiles in Fig. 3.8A at 0.8V and the data presented in Fig 3.8B and C. From the plot, it can be concluded that $Pt_{70}Au_{30}$ alloy

NPs demonstrated significantly higher activities towards ORR in terms of both mA $cm^{-2}{}_{disk}$ and mA $mg^{-1}{}_{metal}$ than those of Pt NPs and the other PtAu alloy NPs. However, the activity decreased drastically with further increase of the Au content in PtAu alloy NPs with virtually no activity for Au NPs towards ORR. This suggests that alloying Pt with Au beyond a certain limit is not beneficial for ORR. Also, at 0.9 V, the currents obtained on the PtAu alloy NPs was positive indicating that these catalysts were not suitable for ORR studies. Therefore, the research was then switched to the studies of small organic molecules oxidation on these PtAu alloys for fuel cells and electrochemical biosensing application.

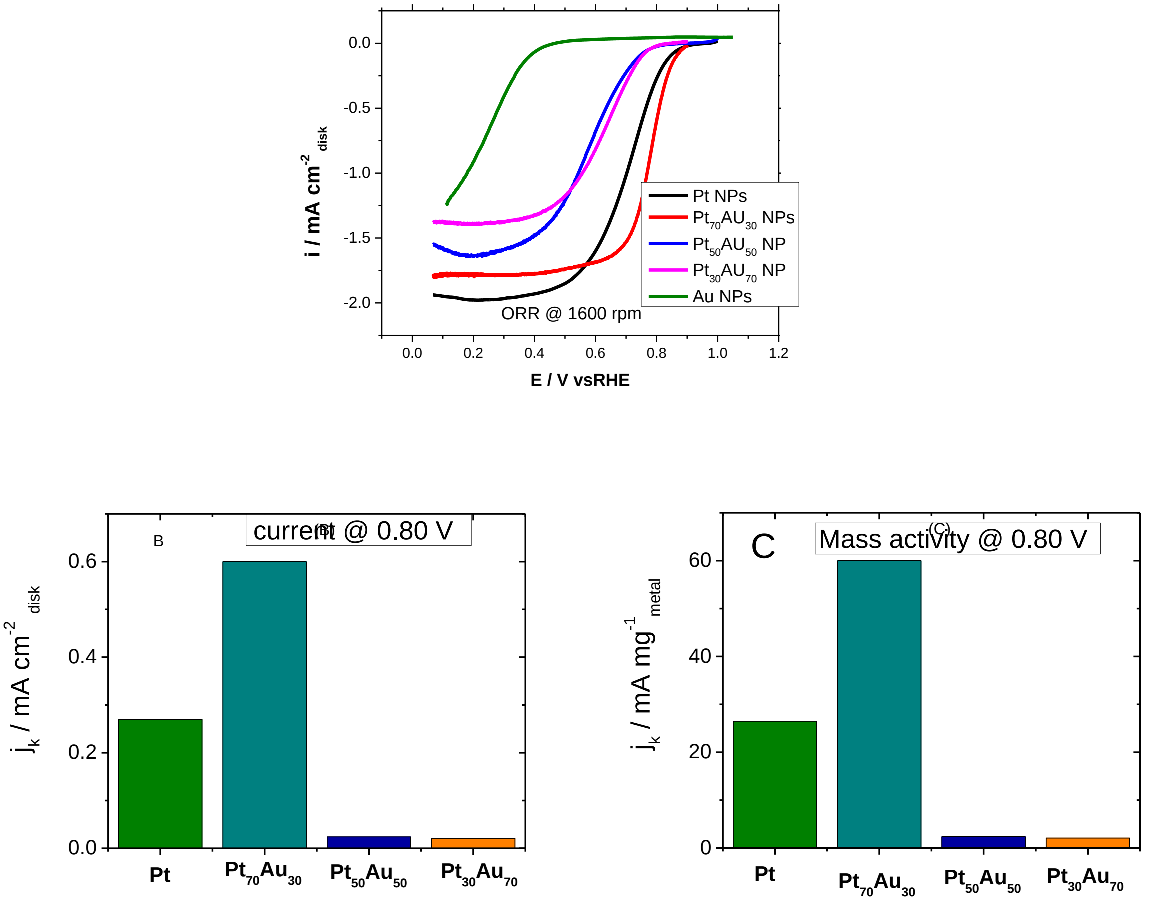

Fig 3.8: (a) RDE voltammetric curves of Pt_xAu_{100-x} alloy NPs. The ORR curves were obtained in O_2 saturated 0.5M H_2SO_4 with a rotation speed of 1600 rpm at room temperature (the current density refers to geometric area). (b) the measured kinetic currents at 0.8 V vs. RHE at various compositions for Pt_xAu_{100-x} alloy NPs.

3.4 Conclusions

In summary, the metal and Nafion loading were successfully optimized for Pt NPs prepared by PLAL. Both metal and Nafion loadings affected the EASA and the utilization efficiency of the nanoparticles, but the variation of Nafion loading affected in addition the stability of the catalyst.

The surface composition of the PtAu alloy NPs as determined by cyclic voltammetry in 0.5 mol dm^{-3} H_2SO4 was very close to the bulk composition. The ORR activity is dependent on the NPs composition, and the ORR activity of the PtAu alloy NPs were less than Pt NPs. Also, the current on the PtAu alloy NPs at 0.9 V was positive suggesting that these catalysts were not suitable for ORR studies. As a result, PtAu NPS can not be used as effective and efficient NPs electrodes for the oxygen reduction reaction in fuel cells.

References

1. J. Suntivich, Z. Xu, C. E. Carlton, J. Kim, B. Han, S. W. Lee, N. Bonnet, N. Marzari, L. F. Allard, H. A. Gasteiger, K. Hamad-Schifferli, Y. Shao-Horn, J. Am. Chem. Soc. 2013, 135, 7985−7991.
2. Y. C. Lu, Z. Xu, H. A. Gasteiger, S. Chen, K. Hamad-Schifferli, Y. Shao-Horn, J. AM. CHEM. SOC. 2010, 132, 12170–12171.
3. Z. Xu, C. E. Carlton, L. F. Allard, Y. Shao-Horn, K. Hamad-Schifferli, J. Phys. Chem. Lett. 2010, 1, 2514–2518.
4. A.-Kozlowska, H.; Conway, B. E.; Hamelin, A.; Stoicoviciu, L. J. Electroanal. Chem. 1987, 228, 429−453.
5. D. V. Heyd, D. A. Harrington, J. Electroanal. Chem. 1992, 335, 19−31.
6. M. D. Obradović, J. R. Rogan, B. M, Babić, A. V. Tripković, A. R. S. Gautam, V. R. Radmilović, S. Gojković, S. Lj. J. Power Sources 2012, 197, 72−79.
7. V.A. Paganin, E.A. Ticianelli, E.R. Gonzalez, , J. Appl. Electrochem. 26 (1996) 297–304.
8. Z. Qi, A. Kaufman, J. Power Sources 113 (2003) 37–43.

9. C. Boyer, S. Gamburzev, O. Velev, S. Srinivasan, A.J. Appleby, Electrochim. Acta 43 (1998) 3703.
10. Y.-G. Chun, C.. S. Kim, D.- H. Peck, D.-R. Shin, J. Power Sources 71 (1998) 174.
11. E. Passalacqua, F. Lufrano, G. Squadrito, A. Patti, L. Giorgi, Electrochim. Acta 43 (1998) 3665.
12. E. Antolini, L. Giorgi, A. Pozio, E. Passalacqua, J. Power Sources 77 (1999) 136.
13. E. Passalacqua, F. Lufrano, G. Squadrito, A. Patti, L. Giorgi, Electrochim. Acta 46 (2001) 799.
14. R. Woods, Electrochim. Acta 1971, 16, 655−659.
15. M. W. Breiter, J. Phys. Chem. 1965, 69, 901−904.
16. M. P. Hyman, J. W. Medlin, J. Phys. Chem. C 2007, 111, 17052−17060.
17. K. J. J. Mayrhofer, B. Blizanac, M. Arenz, V. R. Stamenkovic, P. N. Ross, P. N.; Markovic, . J. Phys. Chem. B 2005, 109, 14433− 14440.
18. K.A. Friedrich, F. Henglein, U. Stimming, W. Unkauf, Electrochim. Acta 2000, 45, 3283−8293
19. A. J. Bard, L. R. Faulkner, Electrochemical Methods: Fundamentals and Applications; Wiley: New York, 2000
20. U.A. Paulus, T.J. Schmidt, H.A. Gasteiger, R.J. Behm, Journal of Electroanalytical
21. N. M. Markovic, T. J. Schmidt, V. Stamenkovic, P. N. A. Ross, Fuel Cells 1 (2001) 105-116.
22. H. A. Gasteiger, S. S. Kocha, B. Sompalli, F. T. Wagner, Appl.Catal. B, 56 (2005), 9
23. J. Luo, P. N. Njoki, Y. Lin, L. Wang, C. J. Zhong Electrochemistry Communications 8 (2006) 581–587

CHAPTER FOUR

Formic Acid Electro-oxidation of PtAu Alloy versus PtAu Mixture Nanoparticles

Summary

In the present chapter, a systematic study of the influence of the composition and structure of PtAu bimetallic catalysts on the electrocatalytic activity for the formic acid oxidation was performed. Accordingly, Pt, Au, PtAu alloy nanoparticles (NPs) and mixture of Pt and Au NPs with controlled size and composition was also investigated. Through a detailed study of the NPs' electrochemical properties involving both cyclic voltammetry and chronoamperometry, a correlation is established between the surface composition of the PtAu alloy NPs and their electrocatalytic activity towards formic acid oxidation. Also, it will be shown that the surface structure and surface composition of physically mixed Pt and Au NPs was modified through electrochemical aging, and that the activity and poisoning tolerance of the resulting materials approach that of PtAu alloy NPs, although the latter still exhibits larger mass specific electrocatalytic activity for the FAOR.

4.1 Electro-oxidation of formic acid

To evaluate the electrocatalytic activity towards FAO, the whole range of Pt_xAu_{100-x} alloy and Pt_x + Au_{100-x} mixture NPs catalysts were investigated by cyclic voltammetry (CV) and some representative results for $Pt_{50}Au_{50}$ alloy NPs and Pt_{70} + Au_{30} nominal mixture NPs are displayed in this thesis. The CV curves displayed are the 20th cycle performed in 0.5 M H_2SO_4 and 0.5 M HCOOH solution (between 0.0 and 1.2 V). The shape of the CVs remained the same from the first to the 20th cycle, with the maximum current varying by less than 20%.

Fig. 4.1 displays the CVs in 0.5 M H_2SO_4 + 0.5 M HCOOH of electrochemically aged to activate the electrodes (50 cycles, between 0.05 and 1.80 V at 100 mV s^{-1}) of pure Pt NPs (Fig. 4.1A) and pure Au NPs (Fig. 4.1B). For electrochemically aged Pt NPs, two different anodic contributions are observed in the forward scan with a first current peak (peak 1) located at ca 600±20 mV, which is related to the direct oxidation of HCOOH to CO_2 via a dehydrogenation pathway. The second peak (peak 2) occurs at ca 920±20 mV, and is associated with the oxidation of CO-type surface intermediates (CO_{ads}) that are concomitantly generated with the oxidation of formic acid via the dehydration pathway (as cited in equation 1.19 in chapters 1).

For pure Au NPs, a single oxidation current contribution is observed at ca 520 mV (peak 1). However, this peak current is quite low, confirming the poor electrocatalytic activity of Au NPs for FAO [13].

It is well known from the literature that the ratio between the maximum current reached at peak 1 and peak 2 can be used to assess the degree of tolerance with respect to CO_{ads} formation and the relative importance of the dehydrogenation and dehydration pathways. On Pt NPs, the peak current density of peak 2 (ip2) is higher than that of peak 1(ip1) and the ratio ip1/ip2 is ca 0.33. This ip1/ip2 value is in the range of (ca 0.2-0.7) found elsewhere for Pt black and various other forms of pure Pt catalysts [7,14]. This is clear indication that the FAO occurs mainly through the indirect pathway on Pt NPs, independently of the preparation procedure

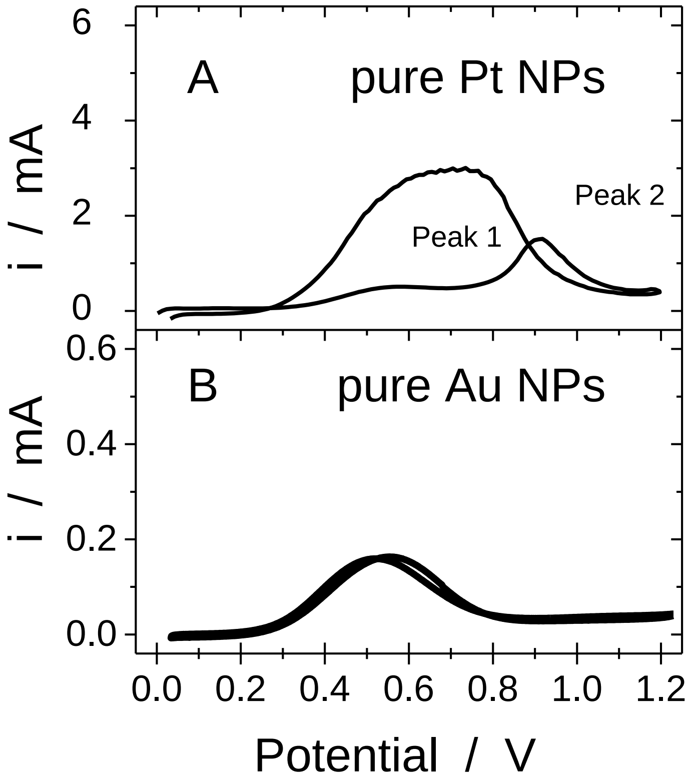

Fig. 4.1 Stable CVs of electrochemically aged (A) pure Pt and (B) pure Au NPs catalysts recorded at 50 mV s^{-1} in 0.5 M H_2SO_4 +0.5 M HCOOH. The twentieth cycle is depicted. The samples were electrochemically aged by performing 50 cycles in 0.5 M H_2SO_4 (between 0.05 and 1.80 V at 100 mV s^{-1}) prior to the CV measurements

It was found that electrochemical aging is critical in influencing the electrocatalytic activity of Pt_x + Au_{100-x} mixture NPs. Accordingly, CV profiles of freshly prepared Pt_{70} + Au_{30} mixture NPs (nominal composition) in formic acid solution are shown in Fig. 4.2A, and after electrochemical aging in Fig. 4.002B-D. The aging consisted in potential cycling between 0.05 and 1.80 V (at 100 mV s^{-1}) in 0.5 M H_2SO_4 for 2 cycles (Fig. 4.2B), 10 cycles (Fig. 4.2C) and 50 cycles (Fig. 4.2D) solution prior to the CV in formic acid.

As seen in Fig. 4.2A, the shape of the CV and the ip1/ip2 value of as prepared Pt_{70} + Au_{30} mixture NPs catalysts are similar to that of pure Pt NPs, suggesting that the dehydration pathway is dominant. This is not surprising considering that this sample is made by physically mixing both Pt and Au NPs. However, following electrochemical aging, the value of ip1 (ip2) increases (decreases) steadily, resulting in a steady increase of the ratio ip1/ip2 with the number of potential cycles in H_2SO_4. For example, the ratio ip1/ip2 is 0.8 after 2 CVs in H_2SO_4 and 1.7 after 10 CVs. This effect levels off and the ratio ip1/ip2 does not increase significantly if the electrochemical aging process is prolonged up to 50 cycles, in which case the ratio ip1/ip2 reaches 1.9. Clearly, the surface of the catalysts made of a physical mixture of Pt and Au NPs is altered and this modification favors the dehydrogenation pathway.

As noted in Fig. 4.2A-D, this modification of mechanisms is also accompanied by an increase of the electrocatalytic activity of the materials for the FAO, as evidenced by the gradual increase of the maximum current reached on the reverse scan. Indeed, the maximum current on the reverse scan increases from 1.5 to 4.6 mA as a result of the electrochemical aging process. A similar phenomenon was observed for all the Pt_x + Au_{100-x} mixture NPs catalysts. These results suggest that potential cycling in sulfuric acid prior to FAO is crucial to increase the electrocatalytic activity towards the FAO and to alter the reaction mechanisms governing the FAO.

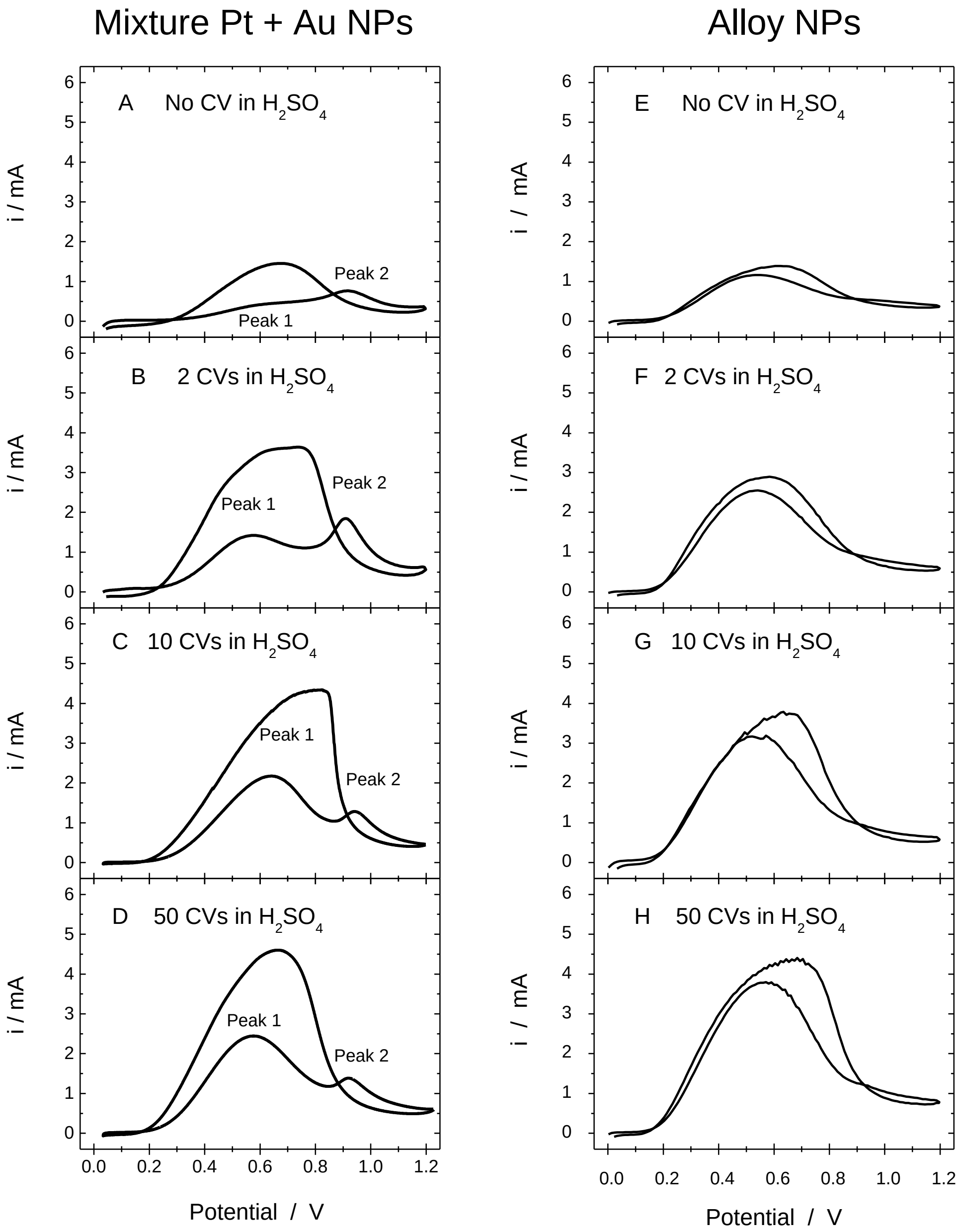

Fig. 4.2: Stable CVs (50 mV s^{-1}) of (A-D) a nominal (70:30) mixture of Pt and Au NPs, and (E to H) a nominal $Pt_{50}Au_{50}$ alloy NPs in 0.5 M H_2SO_4 + 0.5 M HCOOH. An electrochemical aging process was previously applied which consists in cycling the material in 0.5 M H_2SO_4 between 0.05 and 1.80 V for a fixed number of cycles (A and E) 0 cycle, (B and F) 2 cycles, (C and G) 10 cycles, and (D and H) 50 cycles.

The CV profiles in formic acid of as-prepared $Pt_{50}Au_{50}$ alloy NPs and after electrochemical aging (2, 10 and 50 cycles) are displayed Fig. 4.2E-H, respectively. It is observed that:

(i) The CV of as-prepared $Pt_{50}Au_{50}$ alloy NPs is strikingly different from that of as-prepared Pt_{70} + Au_{30} mixture NPs catalysts. Indeed, on the forward scan, the current of peak 1 is higher than the current of peak 2, resulting in a ip1/ip2 ratio of 2.2, several times larger than that found for the mixture of Pt and Au NPs. This is strong evidence that the FAO proceeds mainly through the dehydrogenation mechanism at the surface of as-prepared $Pt_{50}Au_{50}$ alloy NPs, unlike what was observed previously on as-prepared mixtures of Pt and Au NPs. This conclusion is reinforced by the fact that the forward and the backward scans are almost superimposed on each other, indicating that oxidation of the catalyst at the upper potential limit of the scan does not cause any drastic change, essentially because the amount of CO_{ads} is minimal. This is in clear contrast with the as-prepared Pt_{70} + Au_{30} mixture NPs catalysts, where a large hysteresis is observed between the forward and backward scans. In that case, this is indicative that removal of CO_{ads} at the upper potential limit freed the surface from its contaminants.

(ii) There is no change in the shape of the CVs with electrochemical aging. Indeed, the current associated with peak 1 is always larger than that of peak 2. After 50 cycles in H_2SO_4, the ip1/ip2 ratio for $Pt_{50}Au_{50}$ alloy NPs is 3.78. The value is in close agreement with the ip1/ip2 ratio value of 3.57 independently reported elsewhere for PtAu alloy NPs [15]. This indicates that the FAO occurs through the more desirable dehydrogenation pathway on PtAu alloy NPs, whether or not the catalyst has been electrochemically aged. This is radically different from the previous case (mixture of Pt and Au NPs), where it was observed that the shape of the CV evolves dramatically with electrochemical aging.

(iii) The current maximum of the CVs increases steadily from ca 1.3-4.3 mA with electrochemical aging.

It is interesting to note that the CV profiles of electrochemically aged mixture of Pt and Au NPs (Fig. 4.2D) and PtAu alloy NPs (Fig. 4.2H) are quite similar (although not identical). For example, in Fig. 4.2H, the current contribution at 920 mV (dehydration path) is hardly discernible, whereas that current contribution is still present for the electrochemically aged mixtures of Pt and Au NPs (Fig. 4.2D). The absence of this feature in the case of the PtAu alloy NPs suggests a more homogenous surface repartition of the Pt-Au ensemble catalytic sites, giving rise to a single current peak at 560 mV that indicates that the FAO occurs almost exclusively through the dehydrogenation pathway. It is clear that electrochemical aging of mixtures of Pt + Au NPs drastically changed the composition and structure of the catalyst surface but the presence of a non-negligible current at 920 mV (peak 2) in the CV profile of electrochemically aged mixture of Pt and Au NPs indicates that some Pt-like surface domains remained present and that the FAO still proceeds to a certain extent via the partial dehydration pathway.

A series of additional experiments were performed to get further insights on the effect of electrochemical aging on the surface properties of the Pt + Au mixture NPs and on their activity towards FAO. First, a similar series of measurements were realized by decreasing the upper potential limit of the CV during the electrochemical aging procedure. Thus, two freshly prepared (70:30) mixtures of Pt and Au NPs were subjected to potential cycling (50 cycles in 0.5 M H_2SO_4) between 0.05 V and 1.50 V, and between 0.05 V and 1.20 V. In the first case (1.5 V upper potential), the CV of the resulting material recorded in 0.5 M H_2SO_4 + 0.5 M HCOOH (see Fig. 4.3A) is similar to the one obtained previously for an upper potential of 1.80 V (Fig. 4.2D). This is in striking contrast to what happen when the upper potential is reduced to 1.20 V. In that later case, the shape of the CV of the resulting material recorded in 0.5 M H_2SO_4 + 0.5 M HCOOH (see Fig. 4.4B-E) does not evolve with the number of cycles (up to 50 cycles were performed), indicating that the FAO occurs mainly through the indirect pathway as on pure Pt NPs.

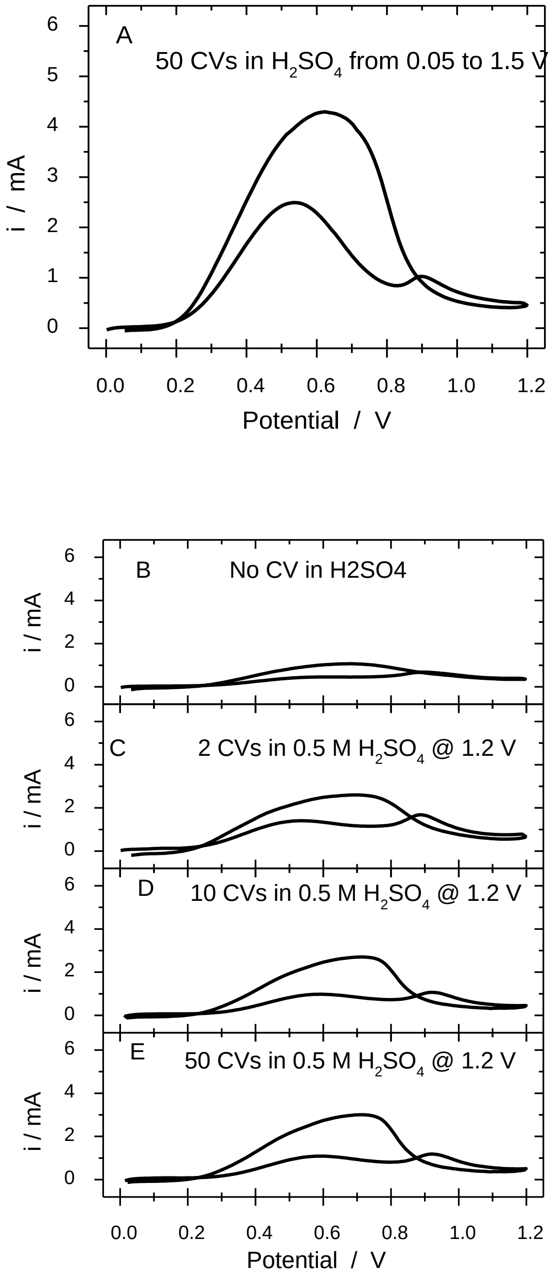

Fig. 4.3 Stable CVs of electrochemically aged (70:30) nominal mixture of Pt and Au NPs catalysts recorded at 50 mV s^{-1} in 0.5 M H_2SO_4 +0.5 M HCOOH. The sample was electrochemically aged by performing cycles in 0.5 M H_2SO_4 (between 0.05 and 1.50 V and 0.05 and 1.20 V) prior to the CV measurements.. (A) 50 cycles in 0.5 M H_2SO_4 (between 0.05 and 1.50 V) prior to the CV measurements. The effect of (A) 0, (B) 2, (C) 10 and (D) 50 cycles prior to FAO is depicted.

Finally, the effect of conducting the electrochemical aging process by holding the potential at a constant value (instead of cycling it between a lower and an upper limit) was investigated. Thus, two freshly prepared (70:30) mixtures of Pt and Au NPs were polarized at 1.50 and 1.80 V in 0.5 M H_2SO_4 during 30 min before being transferred to a HCOOH + H_2SO_4 solution where CVs were recorded. As seen in Fig. 4.4A and B for 1.50 and 1.80 V, respectively, the shape of the CVs resemble closely to those recorded for Pt (see Fig. 4.2A), with an ip1/ip2 value of ca 0.5. These potential limits are the same as those used previously in Fig. 4.3A and Fig. 4.2. Obviously, holding the electrode potential at the upper potential limit is not enough to change the mechanisms responsible for the FAO on the Pt + Au mixture NPs. The reasons for this will become clear in the next section.

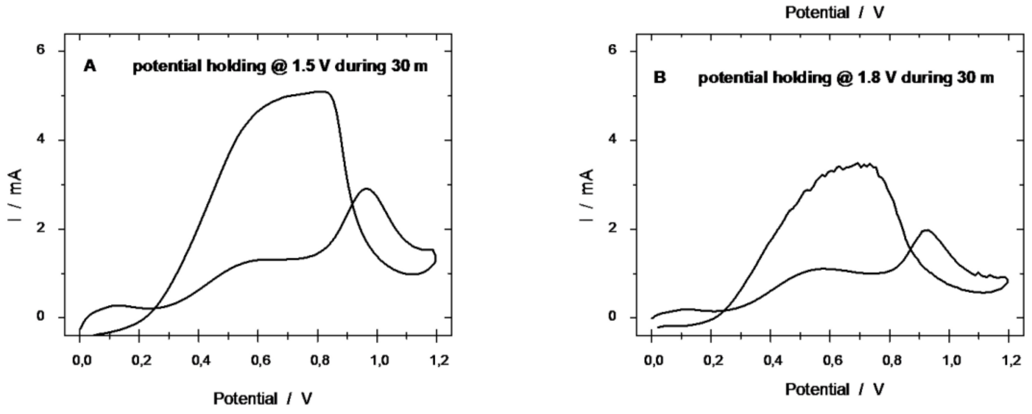

Fig 4.4: Stable CVs of electrochemically aged (70:30) nominal mixture of Pt and Au NPs catalysts recorded at 50 mV s^{-1} in 0.5 M H_2SO_4 +0.5 M HCOOH. The sample was electrochemically in 0.5 M H_2SO_4 by holding the electrode potential (A) at 1.50 V and (B) at 1.80 V during 30 minutes prior to the CV measurements

4.2 Surface properties of the nanocatalysts

Fig. 4.5 shows a typical cyclic voltammogram (CV) of pure Pt NPs and pure Au NPs electrode in 0.5 M H_2SO_4 with upper potentials were set to (A) 1.5 V, (C) 1.2 V, (D) 1.8 V and (F) 1.5 V and their associated ECSAs as a function of electrochemical ageing. The CVs of Pt NPs cycled up to 1.5 V exhibits a steady decrease of current associated with the various features of the CV and a concomitant decrease of the Pt ECSA (see Fig. 4.5A and B, respectively. In contrast, there is almost no change in the CVs if the upper potential is reduced to 1.2 V (see Fig. 4.5C), indicating there is no change of the ECSA with potential cycling.

In the case of pure Au NPs, the same observations can be made except that a more positive potential limit is required to observe a significant change of the Au ECSA. As shown in Fig. 4.5D and E, there is an appreciable decrease of the Au ECSA for a potential limit of 1.8 V, while CVs remain unchanged when the potential limit is 1.5 V (see Fig. 4.5F).

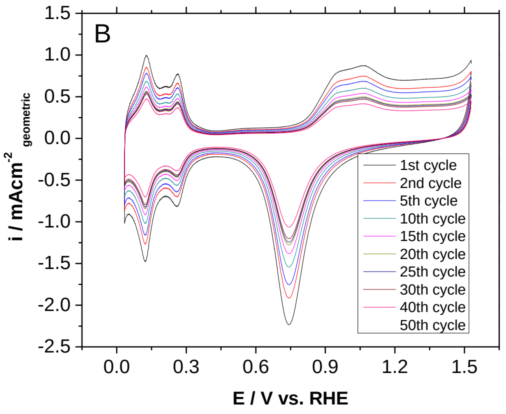

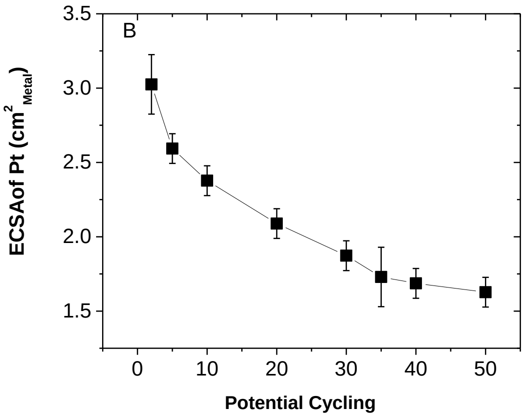

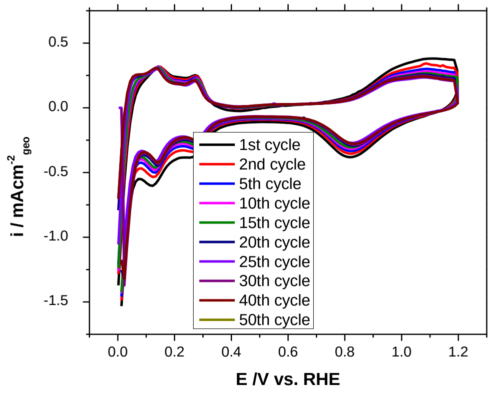

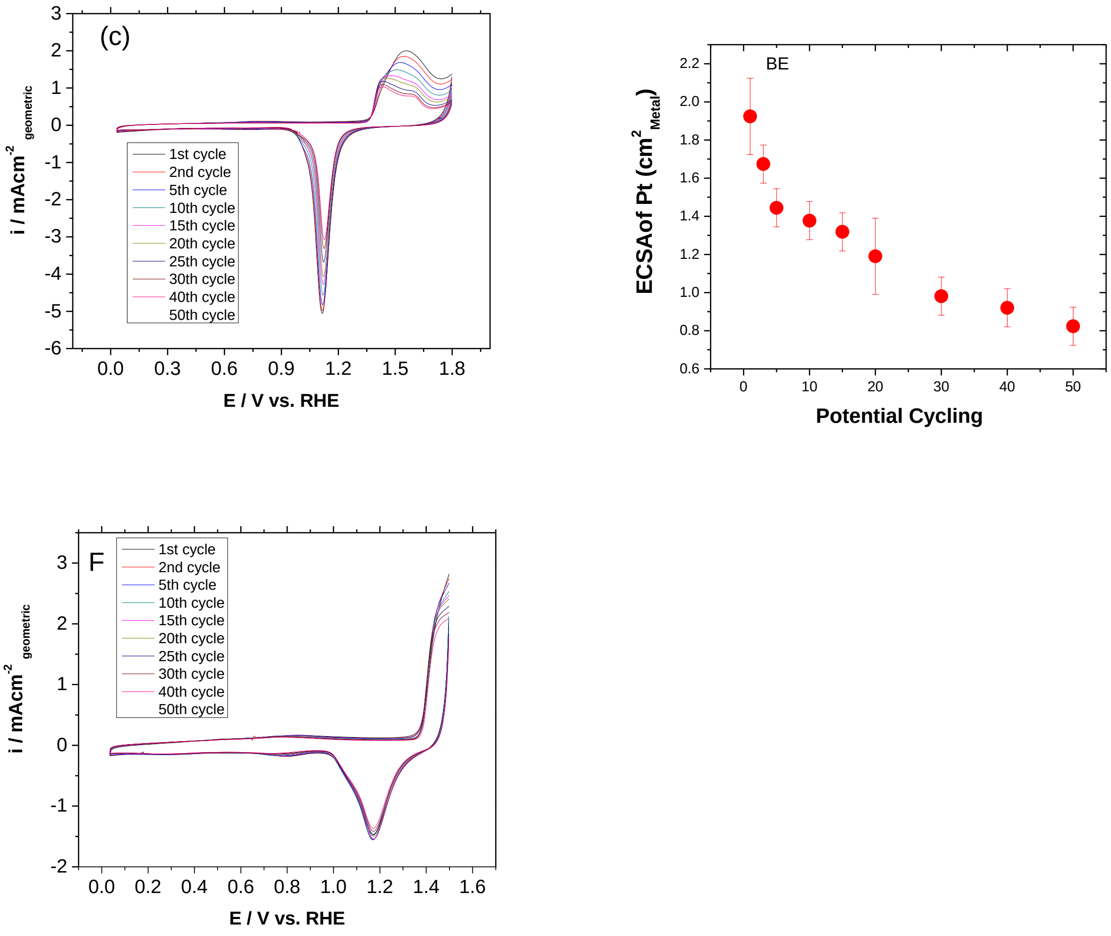

Fig. 4.5: A few representative examples of (A, C, D and F) CVs used to evaluate the (A and C) Pt and (D and F) Au ECSAs as a function of electrochemical ageing. These CVs were performed in 0.5M H_2SO_4 and the upper potentials were set to (A) 1.5 V, (C) 1.2 V, (D) 1.8 V and (F) 1.5 V. In each case, a freshly prepared Pt and Au NPs sample was used. (B) And (E) are the ECSA of Pt and Au NPs as a function of potential cycling.

The ECSA and the surface composition of the samples at their different states of electrochemical aging were assessed through a detailed analysis of the CVs recorded in 0.5 M H_2SO_4. CVs in 0.5 M H_2SO_4 of a nominal (70:30) mixture of Pt + Au NPs and nominal $Pt_{50}Au_{50}$ alloy NPs are depicted in Fig. 4.6. The CVs show fingerprints of both Pt and Au surface features as described in the previous chapter (3) for Pt-Au bimetallic systems.

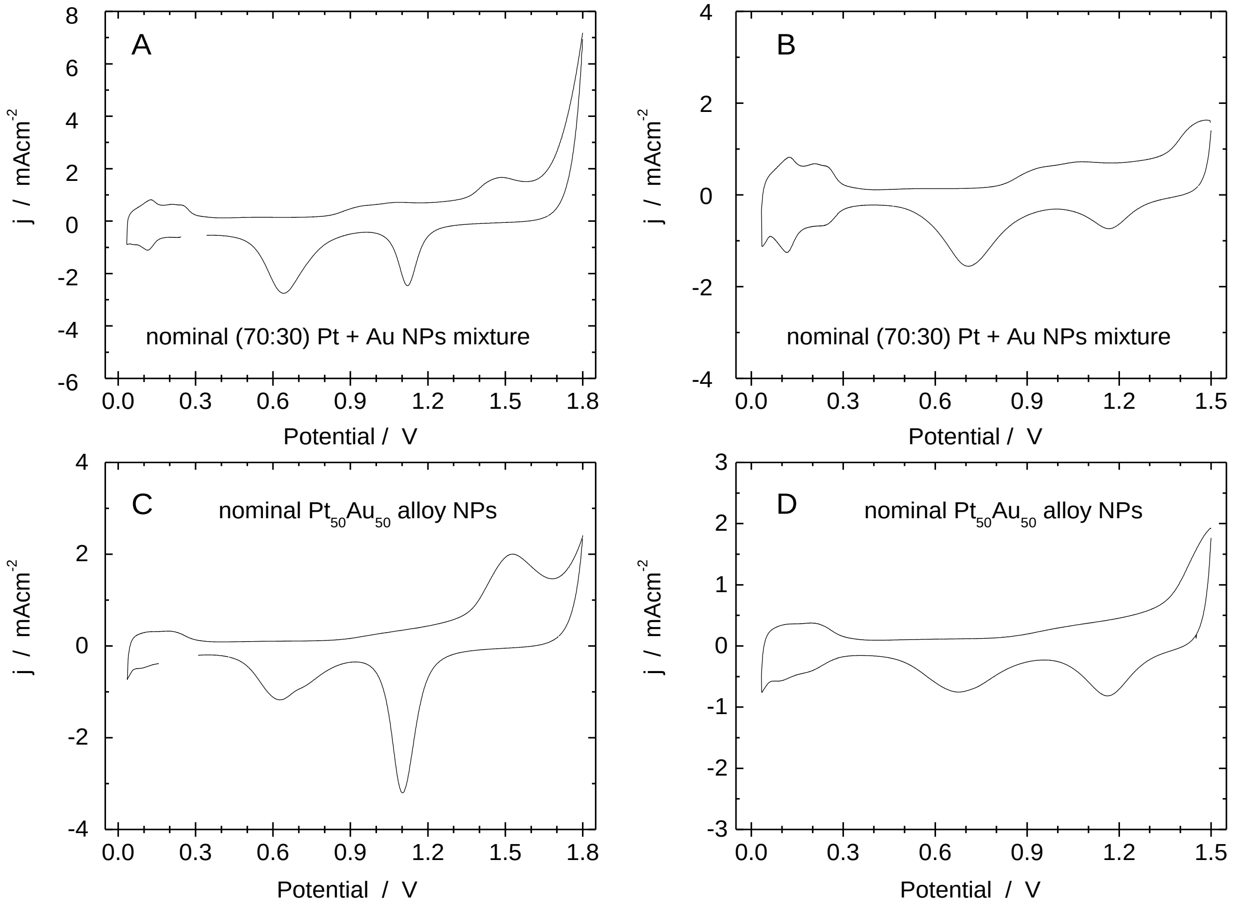

Fig. 4.6: Typical CVs that were used to evaluate (A and C) the Au and (B and D) the Pt ECSAs as the catalysts were electrochemically aged. These CVs were performed in 0.5M H_2SO_4 and the upper potential was set to 1.8 and 1.5 V to evaluate the Au and the Pt ECSAs, respectively. In this example, the CVs used to evaluate the Au and the Pt ECSAs after 20 cycles of electrochemical ageing are shown

The evolution of the Pt and Au ECSAs with electrochemical aging is depicted in Fig. 4.7A and C for a nominal (70:30) mixture of Pt + Au NPs and $Pt_{50}Au_{50}$ alloy NPs, respectively. As seen in Fig. 4.7A, both Pt and Au ECSAs decreased with potential cycling from 1.32 to 0.56 $cm^2{}_{Pt}$ and from 0.76 to 0.55 $cm^2{}_{Au}$, respectively. In comparison, the Pt and Au ECSAs decrease from 1.12 to 0.51 cm^2 $_{Pt}$ and from 1.21 to 0.71 cm^2 $_{Au}$, respectively, in the case of the nominal $Pt_{50}Au_{50}$ alloy NPs. This decrease is more drastic at the beginning of the aging process and levels off with the number of cycles.

In Fig. 4.7A and C, the decrease of the Pt and Au ECSAs is similar to that observed when pure Pt NPs and pure Au NPs are cycled in the same conditions (Fig. 4.5).

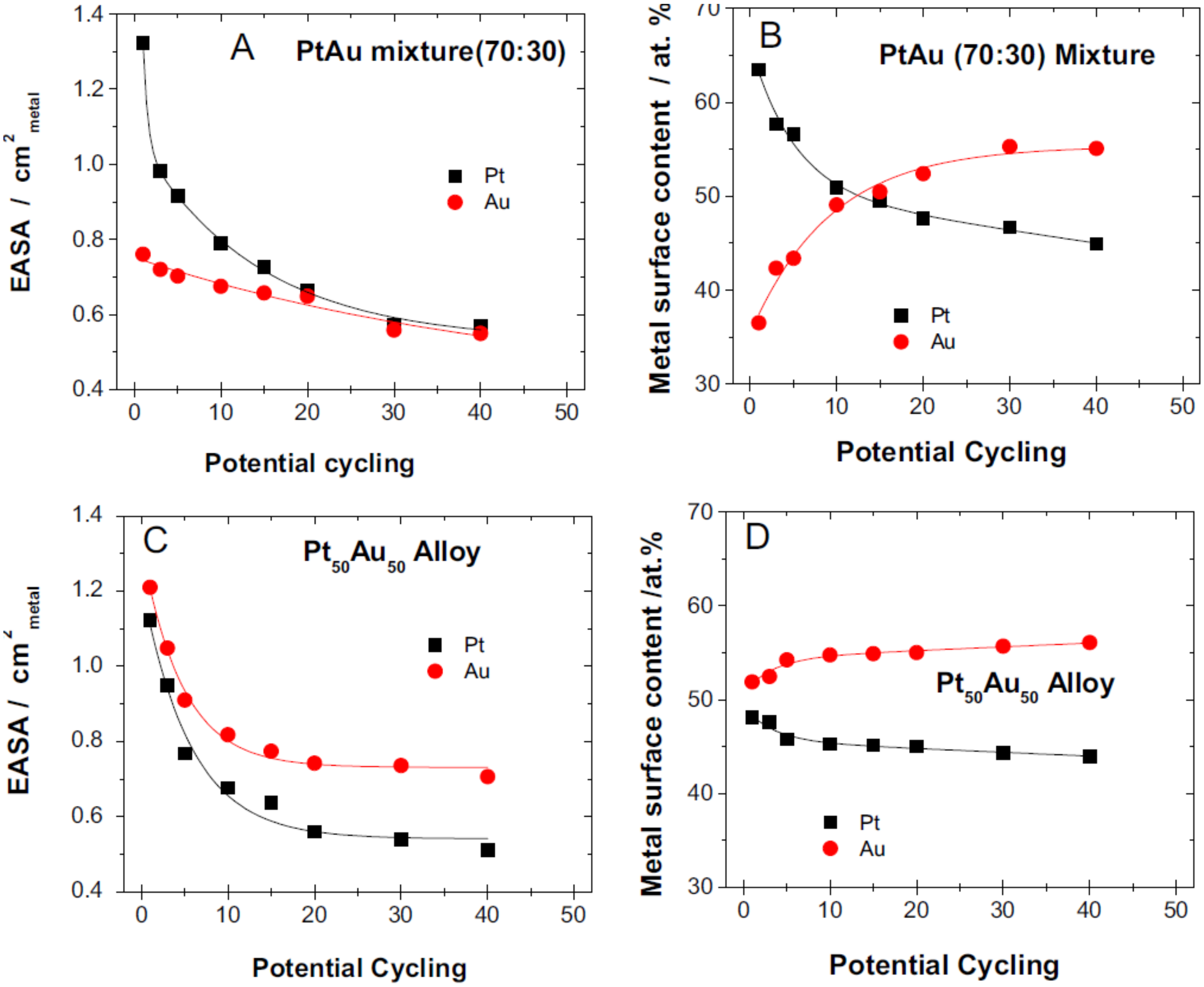

Fig. 4.7: Effect of potential cycling on (A and C) the electrochemically active surface area (EASA) and (B and D) the surface composition of (A and B) a nominal (70:30) mixture of Pt and Au NPs, and (B and D) nominal Pt_50Au_{50} alloy NPs. The potential cycling was performed in

0.5 M H^2SO_4 and between 0.05 and 1.80 V for a fixed number of cycles.

The EASA loss for Pt [20] and Au [21, 22] NPs under potential cycling conditions was extensively studied in previous reports. The suggested mechanisms include interface processes such as sintering, dissolution, coalescence and Ostwald ripening. However, the mechanisms responsible for the decrease of the EASA cannot be unequivocally identified from curves like those shown in Fig. 4.7 since all of them leads to a diminution of the EASA. It is beyond the scope of this study to give a detailed account of the mechanisms responsible for the decrease of the EASA. Nevertheless, it is important to emphasize that Pt atoms re-organization, which is indicated by a decrease of the Pt EASA, occurs only for potential cycling up to 1.5 and 1.8 V, which are the upper potential of the electrochemical aging process at which the Pt-like behavior disappears and the alloy-like behavior appears during the FAO on mixtures of Pt and Au NPs (see Figs. 4.2 and 4.3).

The value of the upper potential during the CV performed in 0.5 M H_2SO_4 is not the sole determining factor for the development of the alloy-like behavior during FAO on mixtures of pure Pt and pure Au NPs. Indeed, as shown in Fig. 4.4, holding the electrode potential at 1.5 or 1.8 V for an extended period of time (30 min) does not lead to the appearance of the alloy-like behavior. This observation emphasizes the fact that the excursion of the potential to value lower than 1.5 and 1.8 V (potential cycling) is critical to achieve the atomic surface re-arrangement responsible for the change in the mechanisms responsible for the FAO in the mixture of Pt + Au NPs.

All these observations can be reconciled if one considers that Pt and/or Au dissolution and re-deposition could occur during potential cycling if the value of the upper potential is sufficiently large. This hypothesis is consistent with a recent study by Mayrhofer et al. [23] that measured the dissolution rates (mg cm^{-2} $cycle^{-1}$) of extended surfaces of Au and Pt with potential cycling in sulfuric acid solution. Thence, for cycling up to 1.50 V and 1.80 V (RHE), the dissolution rates of Pt are 5.8 and 9.0 ng cm^{-2} $cycle^{-1}$, respectively, while that of Au are 4.4 and 20.0 ng cm^{-2} $cycle^{-1}$, respectively. In the present case, the dissolution rates of both Pt and Au nanoparticles might even be higher than these values since the dissolution rate of metal nanoparticles increases as the particle size decreases due to the larger specific surface energy [24]. The hypothesis is also consistent with the fact that electrochemical deposition of platinum and gold occurs readily at potential as large as 0.7 V (NHE) [25,26] and 1.0 V (NHE) [27], respectively, well above the lower potential of the CV performed during the electrochemical aging process. Electrochemical Quartz Crystal Microgravimetry studies already mentioned dissolution and redeposition of both Au [28] and Pt [25] during cyclic voltammetry experiments in sulfuric acid solution. It is worth mentioning that this behavior was only observed if the upper potential limit of the CV was set up in the oxide potential region.

Thus, it is hypothesized that the change in the mechanisms responsible for the FAO on the mixtures of Pt + Au NPs occurs as a result of the dissolution and re-deposition of both Pt and Au atoms during the electrochemical aging process if the upper potential is 1.5 and 1.8 V. During this process, re-deposition must occur in such a way that Pt and Au atoms become intimately mixed. The exact structure (Pt deposited on gold NPs, Au deposited on Pt NPs, code position of Pt and Au to form an alloyed NP) of the catalysts at the end of the electrochemical aging process is difficult to assess from the present results. However, data from the literature have shown that suppression of the formation of poisoning intermediate CO is observed in the following cases: (i) deposition of Pt on Au nanorods and nanoparticles [13, 29], (ii) deposition of Au on a Pt surface [30], and electrodeposition from a solution containing a mixture of Pt and Au salts [6]. Moreover, as recently pointed out, the surface of the Pt-on-Au system is not frozen and potential dependent surface exchange occurs between Pt and Au atoms, allowing both atoms to migrate onto the surface [31]. Considering the similitude between the experimental conditions of that study and those of the present study, this aging process might contribute to the development of a catalyst surface composed of an intimate mixture of Pt and Au atoms. Indeed, it was shown elsewhere that the presence of both Pt and Au atoms at the surface of the catalysts are needed to favor the dehydrogenation over the dehydration pathway [13,32]. These two studies showed that FAO proceeds mostly through the dehydrogenation pathway when the coverage of Pt on the Au substrate is low, but then changes to the dehydration pathway as the Pt coverage is increased beyond a monolayer and gold atoms are not accessible to the electrolyte.

As it can be qualitatively assessed from a visual inspection of the curves shown in Fig. 4.7A and C, the rate of decrease of the Pt and Au EASAs varies from one type of catalyst to the other, causing a change in the surface composition of the catalysts with respect to the nominal surface composition. Therefore, to assess the effect of the electrochemical aging process on the surface composition of the materials, the sPt surface content ([Pt]surface) of the Pt_xAu_{100-x} mixture and Pt_xAu_{100-x} alloy NPs was evaluated through the following equation

$$s[Pt]_{surface} = EASA_{Pt} / (EASA_{Pt} + EASA_{Au}) \qquad (4.1)$$

where $EASA_{Pt}$ and $EASA_{Au}$ are the electrochemically active surface areas (cm^2) of platinum and gold, respectively. As seen in Fig. 4.7B and D, the Pt surface content of the (70:30) nominal mixture of Pt + Au NPs decreases from 65 to 44 at.% upon potential cycling, while the Au surface increases from 35 to 56 at.%. Thus, the surface composition of the physically mixed Pt + Au NPs samples is drastically changed by the electrochemical aging process. In comparison, the surface composition of the PtAu alloy NPs is hardly modified during the same electrochemical aging process and the Pt surface content decreases from 48 to 45 at.%, while the Au surface content increases from 52 to 55 at.%. The final surface composition on the nominal $Pt_{50}Au_{50}$ alloy electrode remains very close to the composition of the as-prepared catalyst, even if there is a significant decrease of the Pt and Au EASAs.

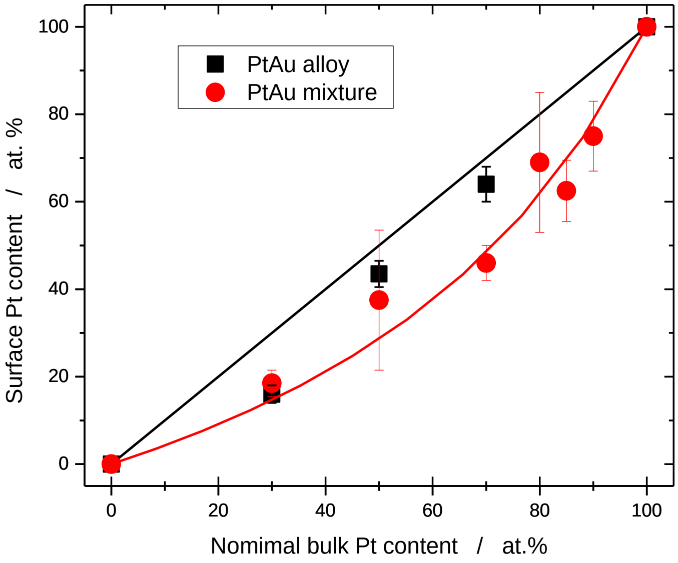

Fig. 4.8: Variation of the Pt surface content as a function of the Pt bulk content following electrochemical aging of catalysts that consists in potential cycling between 0.05 and 1.80 V in 0.5 M H_2SO_4 (50 mV s^{-1}).

Fig. 4.8 summarizes the evolution of the Pt surface content versus the nominal Pt content of Pt_xAu_{100-x} alloys and Pt_x + Au_{100-x} mixtures NPs after electrochemical aging (upper potential of 1.8 V) in 0.5 M H_2SO_4. The CVs that were used to assess the final surface composition of $Pt_{30}Au_{70}$ and $Pt_{70}Au_{30}$ alloy NPs, and nominal (30:70) and (50:50) Pt + Au NPs mixtures are shown in Fig. 4.9 and 4.10, respectively in appendix A. In all cases, there is a depletion of Pt atoms at the surface of the catalysts compared to the nominal Pt content. This effect is more pronounced on the mixtures of Pt and Au NPs. In the following, the different catalyst materials will be designated by their actual surface composition.

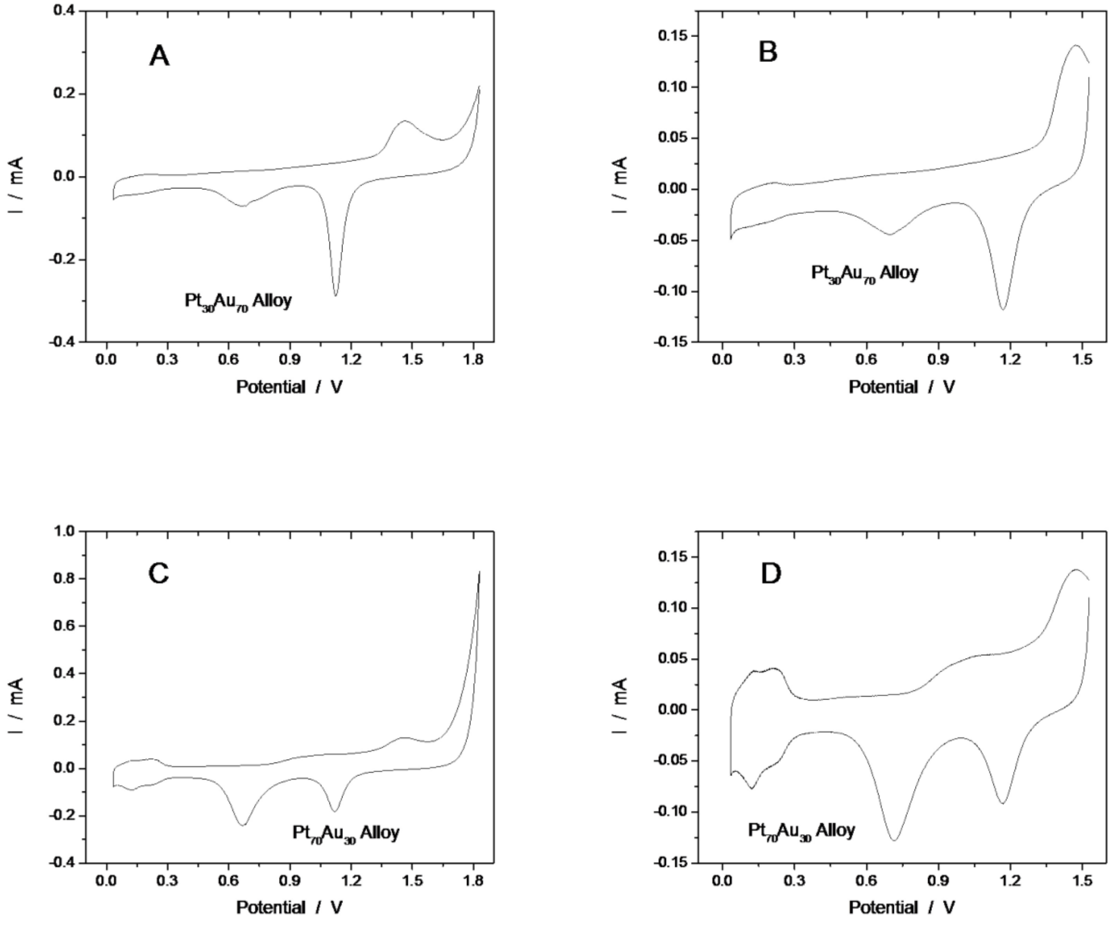

Fig. 4.9 CVs that were used to evaluate (A and C) the Au and (B and D) the Pt EASAs as the catalysts were electrochemically aged. These CVs were performed in 0.5M H_2SO_4 and the upper potential was set to 1.8 and 1.5 V to evaluate the Au and the Pt EASAs, respectively. The CVs used to evaluate the Au and the Pt EASAs after 50 cycles of electrochemical ageing are shown.

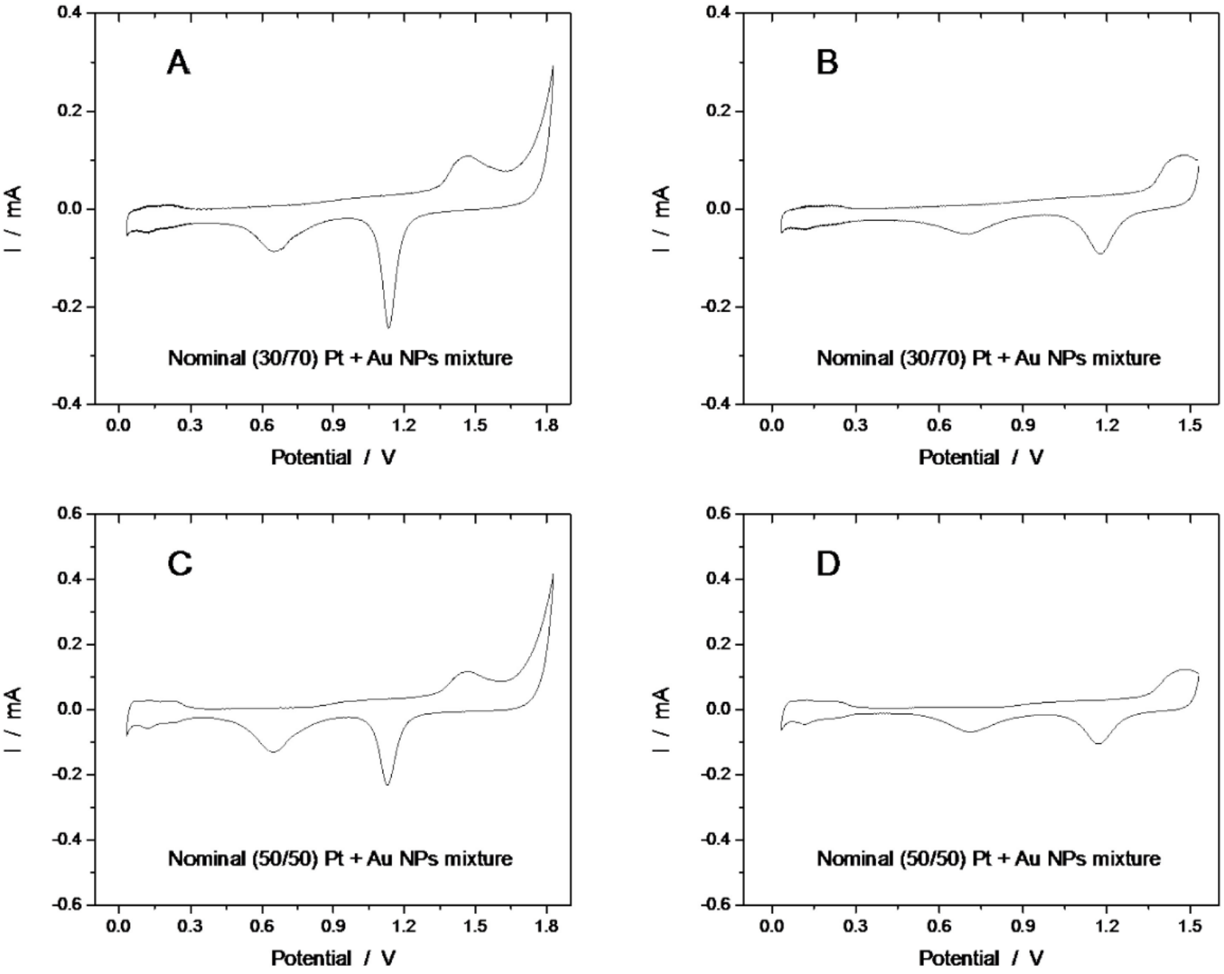

Fig. 4.10 CVs that were used to evaluate (A and C) the Au and (B and D) the Pt EASAs as the catalysts were electrochemically aged. These CVs were performed in $0.5MH_2SO_4$ and the upper potential was set to 1.8 and 1.5 V to evaluate the Au and the Pt EASAs, respectively. The CVs used to evaluate the Au and the Pt EASAs after 50 cycles of electrochemical ageing are shown.

4.3 Steady-state activity towards formic acid oxidation

The chronoamperometric technique was used to further probe the steady-state activity of the Pt_x + Au_{100-x} mixtures and Pt_xAu_{100-x} alloys NPs after electrochemical aging in H_2SO_4 (50 cycles, potential limit of 1.8 V). As representative examples, the chronoamperometric curves of pure Pt NPs, $Pt_{45}Au_{55}$ alloy NPs, Pt_{44} + Au_{56} mixture NPs and pure Au NPs electrodes in 0.5 M H_2SO_4 + 0.5 M HCOOH are displayed in Fig. 4.11 A-D, respectively. This series of measurements were realized by first holding the electrode potential at 0.25 V (10 s) and then stepping it up to 0.56 V (600 s). At the end of the electrolysis period (t = 600 s), low current values (ca 0.01 A $mg^{-1}{}_{metal}$) are observed for pure Au NPs and pure Pt NPs, reflecting the fact that these materials exhibit a poor intrinsic activity and a fast poisoning, respectively. In comparison, the current density after 600 s on the $Pt_{45}Au_{55}$ alloy NPs is 0.84 A $mg^{-1}{}_{metal}$, a factor of 80 larger than on pure Pt NPs, and ca 0.44 A $mg^{-1}{}_{metal}$ on the electrochemically aged mixture of Pt_{44} + Au^{56} NPs. This improvement over the performance of pure Pt NPs clearly indicates that the introduction of Au atoms endows the catalyst with a much higher steady-state current density. A similar improvement of the electrocatalytic activity for the FAO resulting from the mixing of Pt and Au atoms was already demonstrated elsewhere. For example, graphene-supported bimetallic $Pt_{50}Au_{50}$ nanoparticles have been shown to exhibit a much higher current density than pure graphene-supported Pt nanoparticles [7, 33].

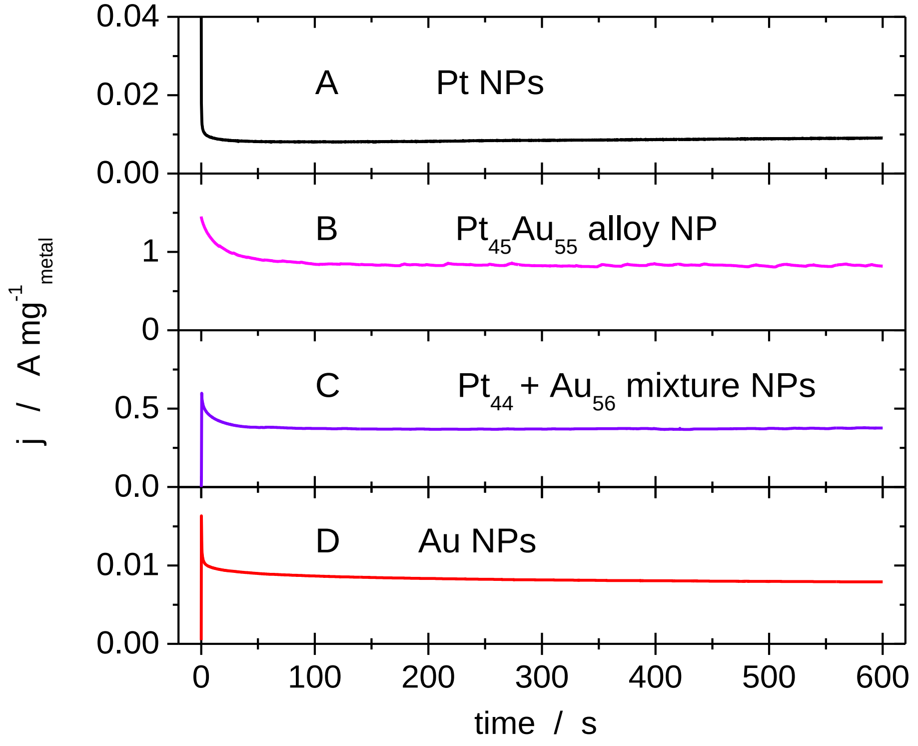

Fig. 4.11: Chronoamperometric curves (E_{appl} = 0.56 V in 0.5 M H_2SO_4 + 0.5 M HCOOH) of electrochemically aged (A) pure Pt NPs, (B) $Pt_{45}Au_{55}$ alloy NPs, (C) Pt_{44} + Au_{56} mixtures of Pt and Au NPs, and (D) pure Au NPs. The actual composition of materials was used for their identification.

The value of the steady-state current density recorded after 600 s of polarization is plotted in Fig. 4.12 with respect to the actual surface composition of the materials. In that figure, the current densities are expressed with respect to the experimentally determined total EASA (Pt + Au) (mA $\text{cm}^{-2}{}_{\text{metal}}$, see Fig. 4.12A), and with respect to the total initial mass of metal deposited on the electrode (A $\text{mg}^{-1}{}_{\text{metal}}$ see Fig. 4.12B). In both cases, an optimal current value with a maximum close to ca. 50 at.% Pt is found.

When the electrocatalytic activity of both types of materials is normalized with respect to the total EASA (Fig. 4.9A), the two curves are close to each other with a difference less than 20%. This suggests that, despite the fact that the structure of the catalysts is radically different in the as-prepared states (mixture of Pt and Au NPs versus PtAu alloy NPs), the electrochemical aging process tends to alleviate these differences as a result of the atomic re-arrangement taking place during the CVs in H_2SO_4.

The above consideration does not hold true if the mass activity is used to compare the electrocatalytic activity of the materials for the FAO. For example, the mass activity of $Pt_{45}Au_{55}$ alloy NPs is 0.84 A mg^{-1}, as compared to 0.44 A mg^{-1} for Pt_{44} + Au_{56} mixture NPs. There is a factor of 2 differences between the two materials that would point to a higher activity of PtAu alloy NPs compared to Pt + Au mixture NPs. As discussed previously, it is suspected that the organization of the Pt and Au atoms is such that the surface of the alloys and mixtures resembled closely to each other (compare the CV of Fig. 4.3D and H) at the end of the electrochemical aging process. So, although some subtle differences might remain between the Pt and Au atomistic organization at the surface of the two types of materials (the CV recorded in the presence of formic acid are not formally identical), it is suspected that another reason is responsible for this difference by a factor of 2. Indeed, it should be remembered that the initial mass of the catalyst is used to compute the mass activities and the residual mass of catalysts left at the electrode surface as a result of the electrochemical aging process might differ from the initial one. Unfortunately, the amount of catalysts left at the surface of the electrode following the electrochemical aging process cannot be easily assessed. And it can be assumed that the dissolution rate of Pt and Au atoms from a mixture of Pt and Au NPs is identical to that of PtAu alloy NPs under potential cycling conditions.

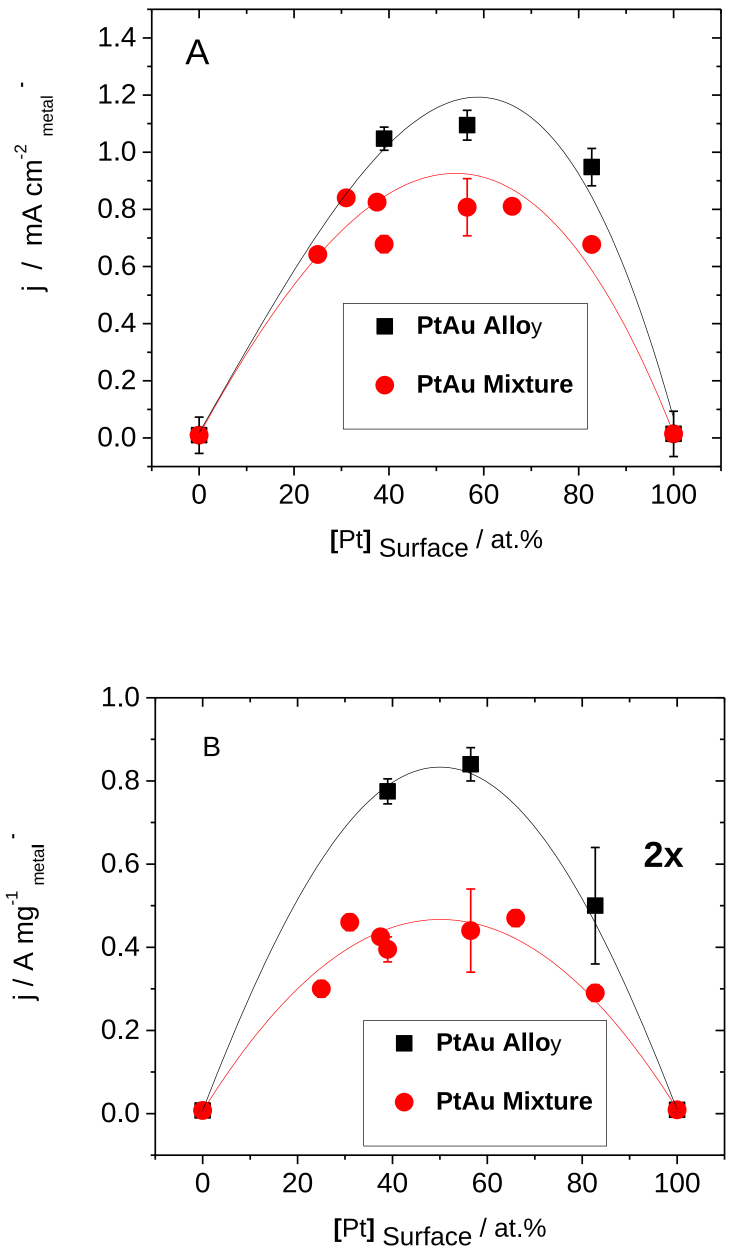

Fig. 4.12: Potentiostatic current densities ($E_{app}l$ = 0.56 V) in 0.5 M H_2SO_4 + 0.5 M HCOOH as a function of the Pt surface content. The current was read after 600 s of electrolysis. In (A), the current is normalized with respect to the total (Pt + Au) electrochemically active surface area. In (B), the current is expressed in terms with respect to the initial mass of catalysts (A mg^{-1} $_{metal}$).

4.4 The Poisoning rate as a function of potential

Fig. 4.13 shows a representative sample of potentiostatic current-time profiles measured on Pt NPs electrode in 0.5 M H_2SO_4 + 0.5 M HCOOH at room temperature. At short time the current densities of the electrodes decrease rapidly, whereas at long time and for all potentials, the rate of current decay becomes linear with time. It worth mentioned that, the rate of current decay is potential dependent. At 0.38 and 0.43 V the current density quickly reaches a steady-state and even increases slightly with time (see Fig. 4,11). At higher potentials a gradual decrease in oxidation current with time is observed.

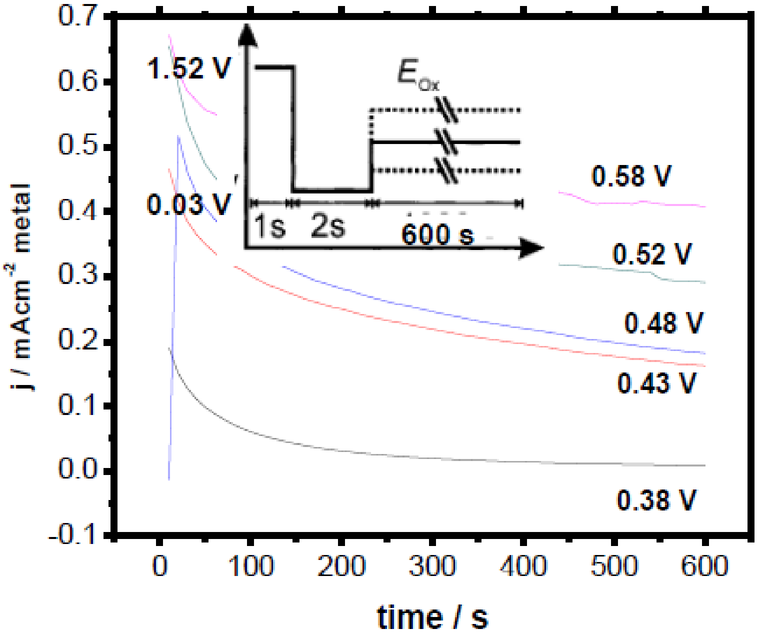

Fig 4.13: Potentiostatic current-time profiles measured on Pt electrode in 0.5 M H_2SO_4 + 0.5 M HCOOH at room temperature. Inset: schematic of the pre-treatment sequence applied to the electrode

The current decay appears quite linear with time after the first 300 s of polarization. A measure of the variation of current with time is obtained by determining the slope of the linear section of the current variation, i.e. for times greater than 300 s. The current decay, δ, was normalized to the current determined from the intercept of the linear current decay line with the y-axis, $j_{t=0}$. The linear decay of the current at times greater than 300 s may be characterised by the long-term poisoning rate, δ [34]:

$$\delta = -\frac{100}{j_{j=0}}\left(\frac{dj}{dt}\right)_{t>300}\left(\% \min^{-1}\right)................(4.2)$$

where $\left(\frac{dj}{dt}\right)_{t>300}$ is the slope of the linear portion of the current decay, and $j_{j=0}$ is the current at the start of polarisation back extrapolated from the linear current decay;

Thus, we prefer to utilise the linear relationship in Eq. (4.2) as indicative of an effective poisoning rate.

The poisoning rate as a function of applied potential for Pt, $Pt_{45}Au_{55}$ alloy and $Pt_{44}Au_{56}$ mixture NPs are displayed in Fig. 4.14. The poisoning rate decreased continuously with potential for all the electrodes. This is because CO adoption on the catalyst surface is oxidized to CO_2 (g) at high potential in the indirect pathway during FAO. The rate of current decay was rapid on the Pt electrode than the $Pt_{45}Pt_{55}$ alloy and $Pt_{44}Au_{56}$ mixture NPs which is an evident of the fact that Pt is easily poisoned and that the addition of Au NPs endowed the catalysts tolerance to CO poisoning via the direct pathway of FAO. These results and observations were consistent with the CVs behaviors of the PtAu systems already discussed in (see Fig. 4.2). For instance, at 0.38 V, the Pt electrode is easily poisoned with the rate of current-loss of 6.5 % $\min^{-1}$. This is an evident that Pt NPs is easily poisoned at low potential due the high adsorption capacity of CO on the surface. However, reasonably stable current decay sis achieved at E>0.43 V due to facile removal of poisoning species at high potential.

In contrast to the Pt electrode, the poisoning rate of $Pt_{45}Pt_{55}$ alloy and $Pt_{44}Au_{56}$ mixture NPs the current decay at 0.38 V were 3.5 % $\min^{-1}$ and 4.9 % $\min^{-1}$ respectively as compared to Pt (6.5 % $\min^{-1}$) and attained stability at ca. 2% $\min^{-1}$ for $Pt_{45}Pt_{55}$ alloy and ca. 3% $\min^{-1}$ for $Pt_{44}Au_{56}$ mixture. This confirms that PtAu proceeds through the direct pathway with low CO adoption on the catalyst surface.

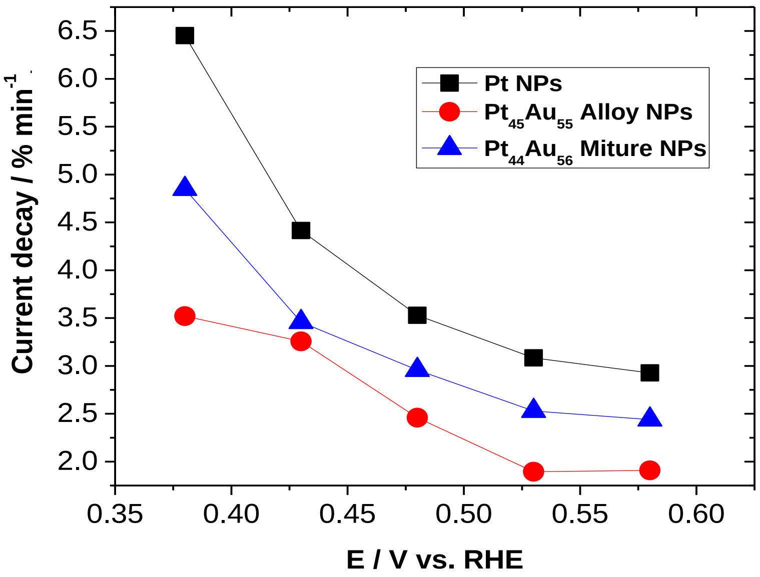

Fig 4. 14**:** Variation of poisoning rate with applied potential. Data from Fig. 4.11. See text for a description of the method used to determine the poisoning rate.

4.5 Conclusion

In this chapter, we conclude the following on the PtAu NPs for FAOR.

1. The oxidation of formic acid proceeds was mostly according to the direct pathway on these alloy NPs that involves the dehydrogenation of the molecule.
2. In comparison, the as-prepared mixtures of Pt and Au NPs with the same composition exhibit very little activity for the FAOR that proceeds through the indirect pathway (dehydration of formic acid).
3. However, a change in the composition and structure of the as-prepared mixtures of Pt and Au NPs occur during an electrochemical aging process that consist in performing CV in 0.5MH2SO4 between 0.05 and an upper potential limit that should not be lower than 1.5 V.

4. It is hypothesized that Pt and Au dissolution and re-deposition occurs during the potential cycling to transforms the Pt + Au mixture NPs catalysts surface so that it adopts a structure close to that of alloy NPs. As a consequence, there is a change of mechanisms and the FAO proceeds also according to the direct pathway.
5. The mass activity of electrochemical aged mixtures of Pt and Au NPs is only a factor of two lower than that of PtAu alloy NPs owing to different dissolution rates of pure Pt and pure Au NPs on one side, and PtAu alloy NPs, on the other side.
6. The mass activity of these alloy NPs for the FAO is maximal for a surface composition close to 50 at.% and reaches ca 0.8 A mg^{-1} after 600 s of electrolysis at 0.56 V vs RHE.

References

[1] J. Zhang, D.N. Oko, S. Garbarino, R. Imbeault, M. Chaker, A. Tavares, D. Guay, D. Ma, J. Phys. Chem. C 116 (2012) 13413-13420.

[2] B.N. Wanjala, J. Luo, R. Loukrakpam, B. Fang, D. Mott, P.N. Njoki, M. Engelhard, H.R. Naslund, J.K. Wu, L. Wang, O. Malis, C.J. Zhong, Chem. Mater. 22 (2010) 4282-4294.

[3] E. Irissou, F. Laplante, D. Garbarino, M. Chaker, D. Guay, J. Phys. Chem. C 114 (2010) 2192-2199.

[4] J.K. Lee, J. Lee, J. Han, T.H. Lim, Y.E. Sung, Y. Tak, Electrochim. Acta 53 (2008) 3474-3478.

[5] C. Xu, R. Wang, M. Chen, Y. Zhang, Y. Ding, Phys. Chem. Chem. Phys. 12 (2010) 239-246.

[6] J. Liu, L. Cao, W. Huang, Z. Li, ACS Appl. Mater. Interfaces 3 (2011) 3552-3558.

[7] Y. Kim, H.J. Kim, Y.S. Kim, S.M. Choi, M.H. Seo, W.B. Kim, J. Phys. Chem. C 116 (2012) 18093-18100.

[8] Z. Xu, C.E. Carlton, L.F. Allard, Y. Shao-Horn, K. Hamad-Schifferli, J. Phys. Chem. Lett. 1 (2010) 2514e2518.

[9] J. Luo, P.N. Njoki, Y. Lin, L. Wang, C.J. Zhong, Electrochem. Commun. 8 (2006) 581-587

[10] B. Fang, B.N. Wanjala, X. Hu, J. Last, R. Loukrakpam, J. Yin, J. Luo, C.J. Zhong, J. Power Sources 196 (2011) 659.

[11] Z. Zhang, Y. Wang, X. Wang, Nanoscale 3 (2011) 1663e1674.

[12] S. Xiao, W. Hu, W. Luo, Y. Wu, X. Li, H. Deng, Eur. Phys. J. B 54 (2006) 479-484.

[13] S. Wang, N. Kristian, S. Jiang, X. Wang, Electrochem. Commun. 10 (2008) 961e

964.

[14] J.H. Choi, K.J. Jeong, Y. Dong, J. Han, T.H. Lim, J.S. Lee, Y.E. Sung, J. Power Sources 163 (2006) 71-75.

[15] S. Trasatti, O.A. Petrii, Pure Appl. Chem. 63 (1991) 711-734.

[16] D.F. van der Vliet, C. Wang, D. Li, A.P. Paulikas, J. Greeley, R.B. Rankin, D. Strmcnik, D. Tripkovic, N.M. Markovic, V.R. Stamenkovic, Angew. Chem. Int. Ed. 51 (2012) 3139-3142.

[17] S.J. Xia, V.I. Birss, Electrochim. Acta 44 (1998) 467-482.

[18] K.A. Friedrich, F. Henglein, U. Stimming, W. Unkauf, Electrochim. Acta 45 (2000) 3283-3293.

[19] J.P. Hoare, J. Electrochem. Soc. 131 (1984) 1808-1815.

[20] S. Garbarino, A. Pereira, C. Hamel, E. Irissou, M. Chaker, D. Guay, J. Phys. Chem. C 114 (2010) 2980-2988.

[21] E. Pichardo-Pedrero, M. Giesen, Electrochim. Acta 52 (2007) 5659-5668.

[22] M. Giesen, G. Beltramo, S. Dieluweit, J. Müller, H. Ibach, W. Schmickler, Surf. Sci. 595 (2005) 127-137.

[23] S. Cherevko, A.A. Topalov, I. Katsounaros, K.J.J. Mayrhofer, Electrochem.

Commun. 28 (2013) 44e46.

[24] C.T. Campbell, S.C. Parker, D.E. Starr, Science 298 (2002) 811-814.

[25] G. Inzelt, B.B. Berkes, A. Kriston, Pure Appl. Chem. 83 (2011) 269-279.

[26] G. Inzelt, B.B. Berkes, A. Kriston, Electrochim. Acta 55 (2010) 4742-4749.

[27] M. Tian, W.G. Pell, B.E. Conway, Corros. Sci. 50 (2008) 2682-2690.

[28] Z. Jusys, S. Bruckenstein, Electrochem. Sol. State Lett. 1 (1998) 74-76.

[29] Y. Yu, Y. Hu, X. Liu, W. Deng, X. Wang, Electrochim. Acta 54 (2009) 3092-3097.

[30] R. Wang, C. Wang, W.B. Cai, Y. Ding, Adv. Mater. 22 (2010) 1845-1848.

[31] B.L. Abrams, P.C.K. Vesborg, J.L. Bonde, T.F. Jaramillo, I. Chorkendorff, J. Electrochem. Soc. 156 (2009) B273-B282.

[32] J. Kim, C. Jung, C.K. Rhee, T.H. Lim, Langmuir 23 (2007) 10831-10836.

[33] S. Zhang, Y. Shao, H.G. Liao, J. Liu, I.A. Aksay, G. Yin, Y. Lin, Chem. Mater. 23 (2011) 1079-1081.

[34]] J. Jiang, A. Kucernak, J. Electroanal. Chem. 520 (2002) 64

CHAPTER FIVE

Electro-oxidation of Methanol on PtAu alloy Nanoparticles in Acidic and Alkaline Media

Summary

In this chapter, the electrocatalytic activity of Pt_xAu_{100-x} alloys towards methanol oxidation in both acidic and alkaline media was investigated by cyclic voltammetry and chronoamperometry. Different trends on the activity with the Pt_xAu_{100-x} alloy composition were found for the two electrolytes. The ensemble mechanism dictates the activity of the NPs in acid environment. For alkaline medium the results suggest a strong effect of adsorbed CO and OH species on the electro-oxidation of methanol on the Pt_xAu_{100-x} alloy surfaces, in addition to electronic effect due to alloying Pt with Au.

5.1 Methanol Electro-Oxidation on PtAu NPs in Acid Medium

It is generally known that Au is a material with a surprising activity for most catalytic oxidation reactions [1 - 6]. However, Au is not a good catalyst for methanol electro-oxidation in acidic medium. But since most of the PEM-based fuel cells employ an acidic medium, we considered it important to study the methanol electro-oxidation on PtAu alloys in this medium due to its carbonation free reactions, and to compare it to the reaction in alkaline medium.

Fig. 5.1 shows a typical set of CV curves obtained for methanol oxidation (MOR) at Pt_xAu_{100-x} alloy NPs of different bimetallic compositions in acid electrolyte (0.5 M H_2SO_4+ 0.5 M CH_3OH at 50 mV s^{-1}). Data collected from the methanol free environment (0.5 M H_2SO_4 at 50 mV s^{-1}) is also presented. In the absence of methanol (dashed lines), all samples exhibit the features of polycrystalline Pt and polycrystalline Au surface chemistry as discussed in chapter 3 of this thesis. It is important to state the electrochemical surface compositions will be used to denote the bimetallic alloy NPs since it was demonstrated in chapter 4 of this thesis that it is different from the nominal composition in acidic medium.

Fig. 5.1A-E shows the typical CV curves obtained for methanol oxidation at the Pt NPs, $Pt_{64}Au_{36}$, $Pt_{44}Au_{56}$, $Pt_{16}Au_{84}$ alloy and Au NPs in the acidic electrolyte. By comparing these CVs with those from the control experiment (dashed line), the following observations can be done:

i) the oxidation current on Au NPs electrode is small and no peak for MOR is observed. This behavior indicates that the Au NPs have no catalytic activity toward MOR.

ii) in the 0.3–1.0 V potential range for Pt and PtAu alloy NPs, an anodic wave at 0.8 V is evident on the forward scan (i_f), which corresponds to the oxidation of methanol [1]. In the reverse sweep (i_b), another anodic wave is observed at a less positive potential (+0.6 V), arising from the oxidation of methanol on re-activated catalyst surface [1, 2].

The magnitude of the anodic peak current represents the electrocatalytic activity toward methanol oxidation. Thus, the catalytic activity is found to be highly dependent on the alloy composition. For example, while the Au-rich alloy NPs (Fig. 5.1D) demonstrated little activity, the Pt-rich alloy NPs (Fig. 5.1B) showed clear catalytic activity.

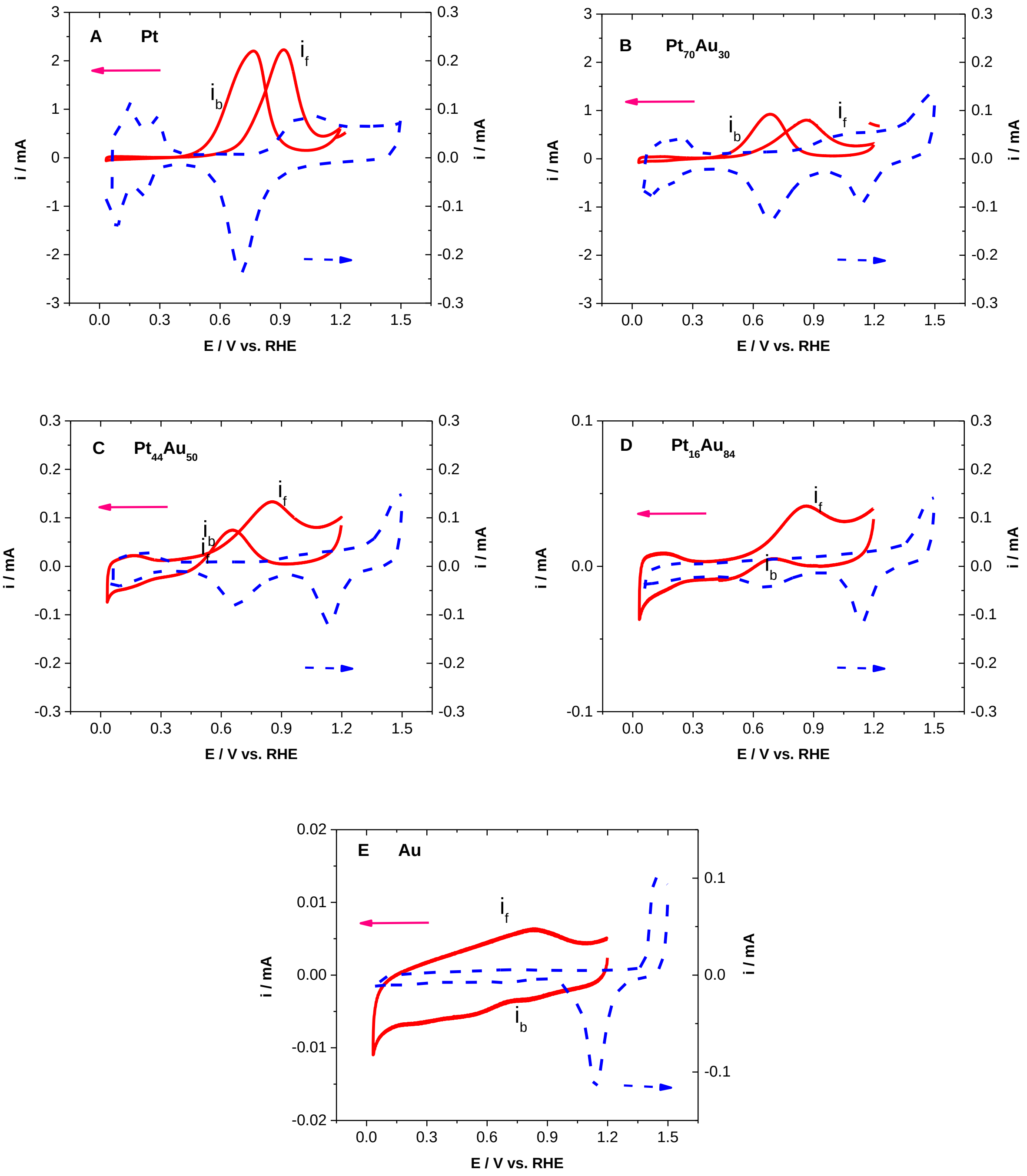

Fig. 5.1: CVs (20th cycle) of Pt NP (A), $Pt_{64}Au_{36}$ alloy (B) $Pt_{44}Au_{56}$ alloy (C) $Pt_{16}Au_{84}$ alloy (D) and Au NPs (E) electrodes in 0.5 M H_2SO_4+ 0.5 M CH_3OH (solid lines) and in 0.5 M H_2SO_4 (dashed lines) at 50 mV s^{-1}.

Fig. 5.2 summarizes a representative set of results displaying the dependence of the MOR peak current for both the forward scan (i_{pf}) and backward scan (i_{pb}) on the electrochemical Au content in the bimetallic composition. From Fig. 5.2, it can be observed that the peak current of Pt_xAu_{100-x} NPs catalyst in both directions decreases with increase Au content. The monotonic decrease in the MOR peak current is suggestive that the number of Pt sites which is responsible for the methanol dehydrogenation determines the magnitude of the MOR peak current of the PtAu alloy NPs. The methanol oxidation activity(forward scan) for Pt catalyst is higher than all Pt_xAu_{100-x} catalysts. Among the PtAu catalysts, $Pt_{44}Au_{56}$ and $Pt_{16}Au_{84}$ alloy NPs exhibit the lowest MOR current. It is known that the methanol adsorption-dehydrogenation process in acidic medium requires at least three neighboring Pt atoms with appropriate crystallographic orientation [3]. In the Pt_xAu_{100-x} catalysts, with a disordered structure, the probability of finding three neighboring Pt atoms on the surface is lower if no Pt enrichment on the surface takes place. In this work, the surface composition of PtAu NPs synthesized from a single metal target made from a mixture of pure Pt and pure Au NPs via PLAL (as cited in chapter 1 and 2) demonstrated a depletion of Pt atoms from the surface as indicated by the notations in Fig. 5.1 and cited in chaper 4. The depletion of the Pt atoms from the surface may be attributed to atomic-level mixing during the prior electrochemical aging process of the PtAu NPs in sulphuric acid. This surface composition change effect explains the behavior that the bimetallic PtAu alloy NPs prepared with this method result in a lower peak current for the MOR .

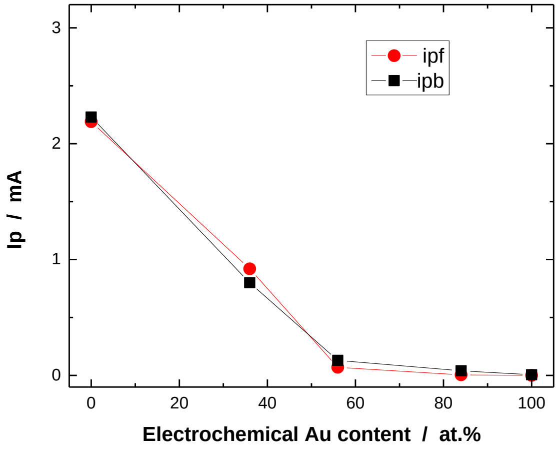

Fig. 5.2: Dependence of the MOR Forward and backward peak current as a function of electrochemical Au content in bimetallic PtAu catalysts.

For the MOR electro-catalyst, another critical parameter for evaluating the catalytic activity is its resistance to carbonaceous species accumulation. In MOR, the anodic peak during the backward scan is principally attributed to the removal of intermediate carbonaceous residues formed on the catalyst during the forward scan. Therefore, the ratio of two anodic currents, I_f/I_b, is commonly used to describe catalyst susceptibility to poisoning [4]. The ratio of the forward to backward peak current was calculated to be 1.02, 0.87, 1.86, 4 and 6 for Pt NPs, $Pt_{64}Au_{36}$, $Pt_{44}Au_{56}$, $Pt_{16}Au_{84}$ and Au NPs electrode's respectively. These ratios increase with increasing Au content, suggesting an increase catalyst tolerance to carbonaceous species.

Even though the potentiodynamic curves may provide some fundamental data regarding the electrocatalytic performance of MOR, the activities observed from these work are transient in behaviour. For this reason, steady state chronoamperometry is used to further probe the electrocatalytic activity of the Pt_xAu_{100-x} NPs for MOR. Fig 5.3 shows the chronoamperometric profiles of Pt_xAu_{100-x} NPs in 0.5 M H_2SO_4+ 0.5 M CH_3OH at 0.60 V vs. RHE. The current profiles exhibited a high initial current and then decrease with time due to the deactivation of Pt sites by strongly bound intermediates (CO-like species) produced during the MOR [4].

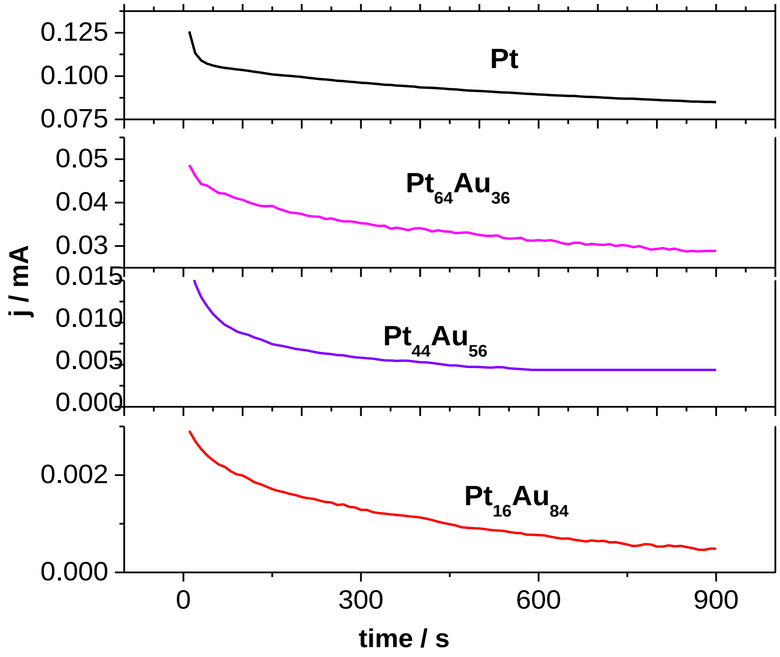

Fig. 5.3: Chronoamperometric curves of Pt, $Pt_{64}Au_{36}$, $Pt_{44}Au_{56}$ alloy and $Pt_{16}Au_{84}$ alloy NPs electrodes in 0.5 M H_2SO_4 + 0.5 M CH_3OH measured at 0.60 V..

As anticipated by the voltammetric studies, the electrocatalytic activity at the end of the polarization studies was higher on the Pt NPs than on any other PtAu bimetallic catalysts as shown in Figure 5A. The electrochemical data for Pt and PtAu catalysts were compared in terms of the intrinsic activity (mA $cm^{-2}{}_{Pt}$) and mass activity (cA $mg^{-1}{}_{Pt}$). We noted that both intrinsic (Fig. 5.4B) and mass activities (Fig. 5.4C) were found to be strongly dependent on the bimetallic composition (Pt_xAu_{100-x}) with a decrease in activity from Pt NPs to the Au-rich PtAu catalysts by a factor of 5 from Pt to $Pt_{16}Au_{84}$ alloy (Fig. 5.4B) and by 53 times from Pt to $Pt_{16}Au_{84}$ alloy (5.4 C) respectively.

In acidic solution, Au is not capable of providing adsorption sites for –OH in this range of potential and the electrocatalytic activity of the alloy NPs is thus rather low. Also, in the PtAu alloy NPs, Au affects the adsorption of methanol on Pt particles via Pt dilution. These results are consistent with CVs data reported in Fig. 5.1.

Thus to improve the electrocatalytic activity of PtAu NPs toward MOR we have to switch to alkaline medium where Au is known to be active for MOR (see next section).

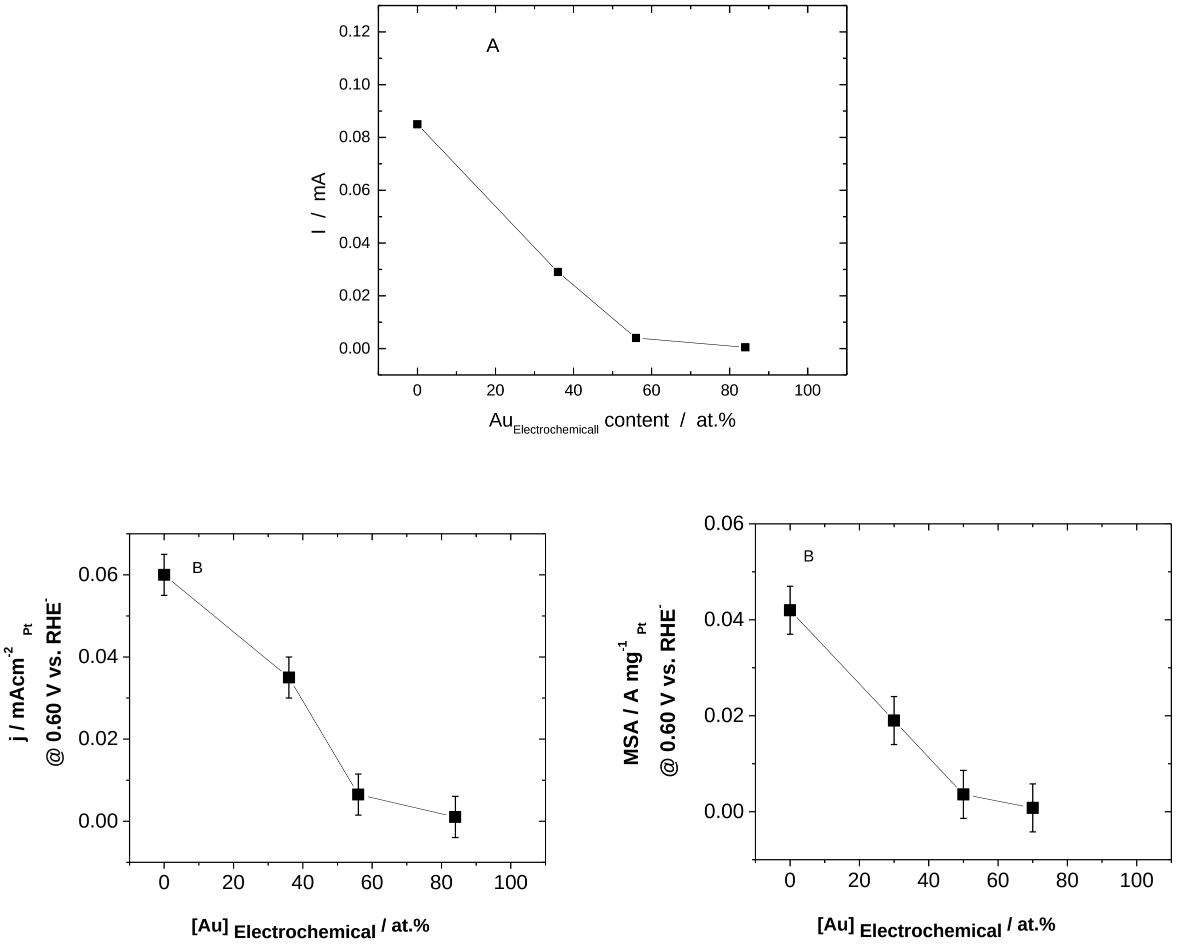

Fig. 5.4. The electrochemical composition dependence of (A) steady state current in mA (B) intrinsic activity in mA cm^{-2} $_{Pt}$ and (C) mass activities in A mg^{-1} $_{Pt}$ determined for different Pt_xAu_{100-x} catalysts in 0.5 M H_2SO_4 + 0.5 M CH_3OH.

5.2 Methanol Oxidation in Alkaline Medium

In this section, all potential values were reported versus Hg/HgO reference electrode.

5.2.1 Potentiodynamic Polarization Curves for different Electrodes in Alkaline Medium

Representative voltammograms of Pt_xAu_{100-x} alloy electrodes in nitrogen-purged 0.5 M NaOH solution at 50 mV s^{-1} are given in Fig. 5.5. The Au content (atom %) varied from 30 % in Fig. 5.5B to 70 % in Fig. 5.5D. For the sake of comparison, the CV curves of pure Pt NPs and pure Au NPs are also presented in Fig. 5.5A and Fig. 5.5E respectively. All CVs displayed the well-known voltammetric features of Pt and Au in NaOH solution. For pure Pt NPs, hydrogen adsorption-desorption region can be distinguished below -0.68 V, followed by the reversible OH^- anion adsorption up to -0.17, V and then by the irreversible Pt-oxide monolayer formation at more positive potential ($E > -0.17$ V). The PtO layer is reduced during the backward scan and exhibited a cathodic peak centered at ca. $E = -0.38$ V [7, 8]. For pure Au NPs, double layer pseudo-capacitive current up to $E < -0.05$ V is observed. This corresponds to a partial charge-transfer due to the chemisorption of OH^- anions on the Au surface [9, 10]. The formation of gold surface oxides commences at more positive potential (E > -0.05 V), resulting in a well-defined peaks of the different monolayers of Au-oxides with different oxidation states [10]. In the cathodic sweep, gold oxides are reduced, leading to a large reduction peak centered at E = -0.05 V, followed by desorption of OH^- at more negative potentials. The generation of an $Au\text{-}OH_{ads}$ (oxide precursor) in the potential region prior to the gold oxide formation is an important property of Au electrodes which plays a key role in enhancing the catalytic activity of Au methanol in alkaline solutions [4, 5, 9, 10].

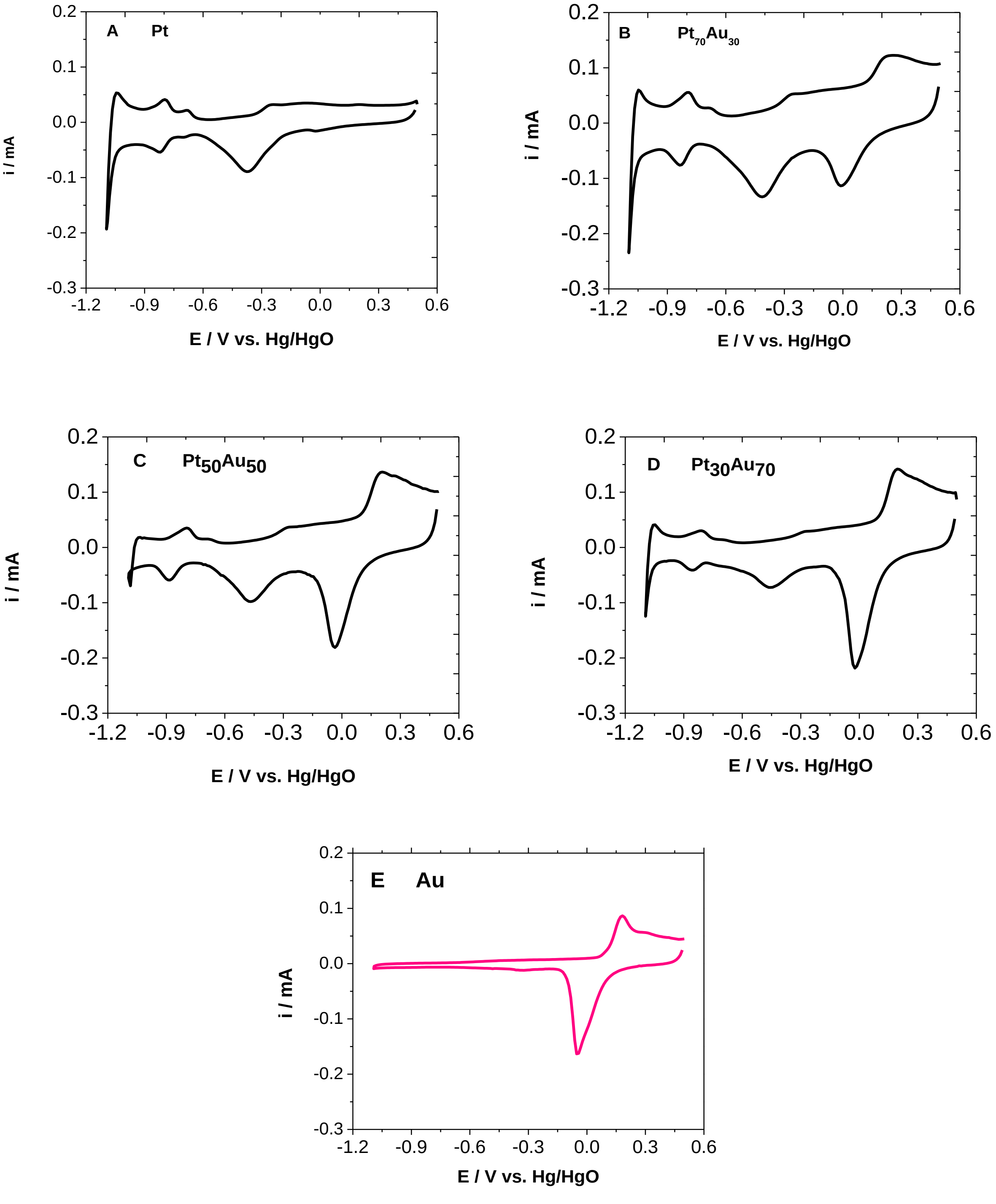

Fig. 5.5: CVs (20th cycle) of Pt (A), $Pt_{70}Au_{30}$ (B), $Pt_{50}Au_{50}$ (C), $Pt_{30}Au_{70}$ (D) and Au (E) NPs electrodes in 0.5M NaOH at 50 mVs^{-1}.

Hence, CVs for PtAu alloys appear as a linear combination of the CVs for both pure metals in good agreement with previous voltammetric studies of PtAu alloys [29, 32]. During the reverse sweeps, fingerprints of both metals are observed as well-defined cathodic peaks, that is, around ca. -0.02 and -0.44 V for gold and platinum oxide reduction peaks, respectively. The peaks in the hydrogen region are related to hydrogen adsorption at Pt-surface sites of the alloy electrode [11]. The OH chemisorption region on the PtAu NPs extends from ca. -0.6 to -0.3V.

It is important to remark that the peak intensity at E <-1.05 V was higher in Pt and Pt-rich alloy NPs compared to Au-rich alloy NPs. This peak intensity is related with H adsorption. Also, the higher the peak intensity, the larger the adsorption-desertion density and the smaller is the coverage by OH_{ad} species on the catalyst surface as reported in literature [12]. Both the hydrogen and OH^- anion adsorption are influenced by surface density of the active sites as suggested in literature [12] and this play an important role in methanol oxidation reaction in alkaline medium. It has also been suggested that he co-habitation of OH_{ad} with H_{ad} species in this potential region is assigned to the surface process (such as atomic rearrangement) on Pt based catalysts [13]. Since the Au-rich alloy NPs have lower intensity hydrogen adsorption-desorption density, the OH anion adsorption coverage is expected to be higher and therefore will affect the MOR as will be discussed in later section. Metal oxide species are generated at potentials E > -0.02 V.

It is well recognized that surface composition of metals affects considerably the electrocatalytic activity of MOR under potentiodynamic conditions [14 - 19]. This is usually achieved by: (i) changing the electronic properties of the metal surface via surface processes such as metal dissolution, atomic rearrangement, etc; (ii) affecting the energetics of the reaction; (iii) influencing the adsorption behavior of reaction intermediates and/or products at the catalytic surface [14, 15, 16, 19]. Similar phenomenon such as metal dissolution, change of reaction mechanism were observed in acidic medium as discussed in chapter 4 of this thesis in which potential cycling of PtAu NPs in sulphuric acid prior to FAOR resulted in change of reaction mechanism. Therefore, in the light of this, the surface composition under potentiodynamic conditions at the Pt_xAu_{100-x} alloy electrodes prior to MOR are assessed from the corresponding voltammograms in the alkaline medium (0.5 M NaOH) at 50 mV s^{-1} at room temperature.

The surface atomic content of the Pt_xAu_{100-x} alloy electrodes was deduced as follows:

$$[Au]_{electrochemical} = ECSA_{Au} / (ECSA_{Pt} + ECSA_{Au}) \quad (5.1)$$

where $[Au]_{electrochemical}$ represents the Au surface content, $ECSA_{Au}$ and $ECSA_{Pt}$ are the electrode active surface area of gold and platinum NPs, respectively. The $ECSA_{Au}$ and $ECSA_{Pt}$ were determined by integrating the electric charge involved in both metal oxides reduction waves and using a conventional factor of 386 $\mu Ccm^{-2}{}_{Au}$ and 420 $\mu Ccm^{-2}{}_{Pt}$ for monolayer formation of gold and platinum oxides in alkaline media respectively [11, 19]. The surface composition of Pt_xAu_{100-x} electrodes is presented in Figure 5.6 in terms of Au surface content as a function of bulk Au composition. It is clear from these results that $[Au]_{electrochemical}$ and $[Au]_{bulk}$ values are quite close for all Pt_xAu_{100-x} alloys, which indicates that the surface composition of the alloy NPs is nearly identical to the average bulk composition of alloy NPs. This observation supports the viewpoint that, there is very little surface enrichment and that the PtAu NPs have virtually uniform composition from the surface to the bulk. It is important to state that, since the these two compositions are very close to each other, we will therefore report all the electrodes in this section by their nominal compositions.

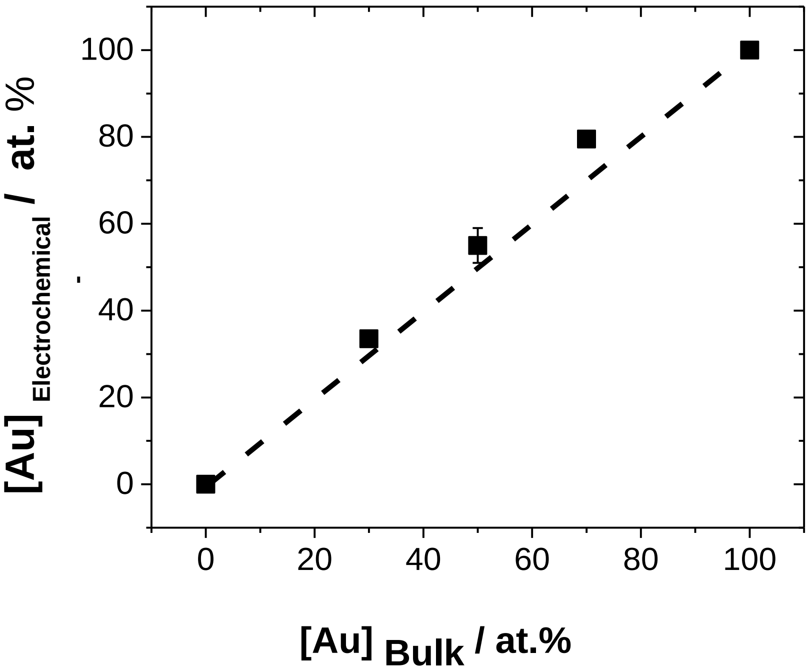

Fig. 5.6 Variation of the electrochemical surface composition vs. the bulk composition of $Pt_{100-x}Au_x$ NPs.

A closer inspection of the CVs in Fig. 5.5 reveals that the peak potential value for gold oxide reduction remained constant at ca. -0.02 V for the whole range of alloy composition, whereas a significant potential shift is observed for the platinum oxide reduction peak, from *E* = -0.38 V for Pt, - 0.42 V for $Pt_{70}Au_{30}$, - 0.44 V for $Pt_{50}Au_{50}$ and *E* =- 0.46 V for $Pt_{30}Au_{70}$ alloy (Fig. 5.7). Therefore, the potential peak of the PtO reduction wave appears at slightly less positive potential in the PtAu alloy than on the pure metal. The slightly larger oxide reduction hindrance as compared with the pure metal was already shown to reflect the higher reactivity of PtAu surface alloys towards the oxidation of small organic molecules [20, 21]. It worth mentionning that the lattice parameter increased linearly with respect to $[Au]_{bulk}$, indicating that Pt-Au alloy formation had occurred [17]. The increased in lattice parameter with increasing Au content resulted in a negative shift of PtO reduction potential in the same trend. This might be due to the expansion of Pt surfaces as reported in literature [22]. Oxygen-type adsorbates, such as O and OH species, were also recently found to be stabilized at the surface of expanded Pt as compared to bulk Pt [23]. It must be mentioned that an increase in the oxophilicity of platinum was also recently correlated to a size effect, and a 130 mV cathodic shift of the Pt oxide reduction peak was observed as the particle size is decreased from 30 to 1 nm [22]. In this study, the size effect can be rule out, since we observed only a cathodic potential shift of about 80 mV with the particle size varying (small) from 2.5 to 5.2 nm as the Au atomic % content in PtAu NPs is increased (see Table 1.1 in chapter 1).

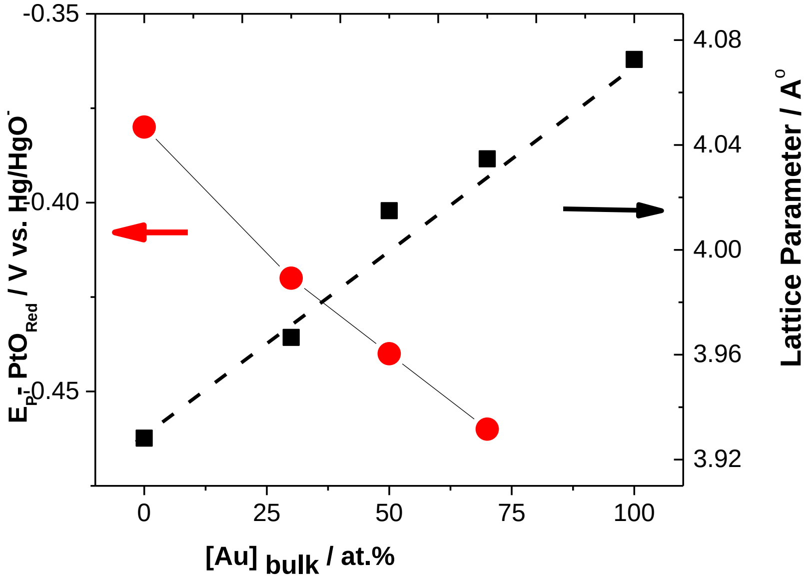

Fig. 5.7: Variation of the $E_p(PtO_{red})$ and lattice parameter vs. bulk Au composition.

The negative shift of the Pt oxide reduction peak for the Au-rich alloy reveals the stronger Pt-O binding energy as compared with Pt-rich alloy electrodes. XPS measurements of these PtAu alloy NPs reported recently in our previous work [24] revealed that the difference in binding energy, ΔBE, between $Au4f_{7/2}$ and Pt $4f_{7/2}$ increased linearly from ~12.7 eV to ~12.9 eV as the $[Au]_{bulk}$ increases from 30 % to 70 % in PtAu NPs. These observations suggest that partial charge transfer from Pt to Au could take place due to the higher electronegativity of Au (2.54) than that of Pt (2.20) which induces the BE shift [24]. This may be related to the fact that the lattice parameter of PtAu alloys increases with the Au content as summarized in Figure 5.6. Recent density function theory (DFT) computations [25] on PtAu alloy indicated that the d-band shift for Pt in a Pt-Au alloy on Au(111) differs from that for a Pt-Au alloy on Pt(111). The modeling results suggested that the change in the binding energy was proportional to the shift of the d-band center of the metal over layer. Also the adsorption of CO showed an increased binding energy in comparison with that of Pt(111), due to the larger lattice constant of Au, leading to an expansion of Pt [26].

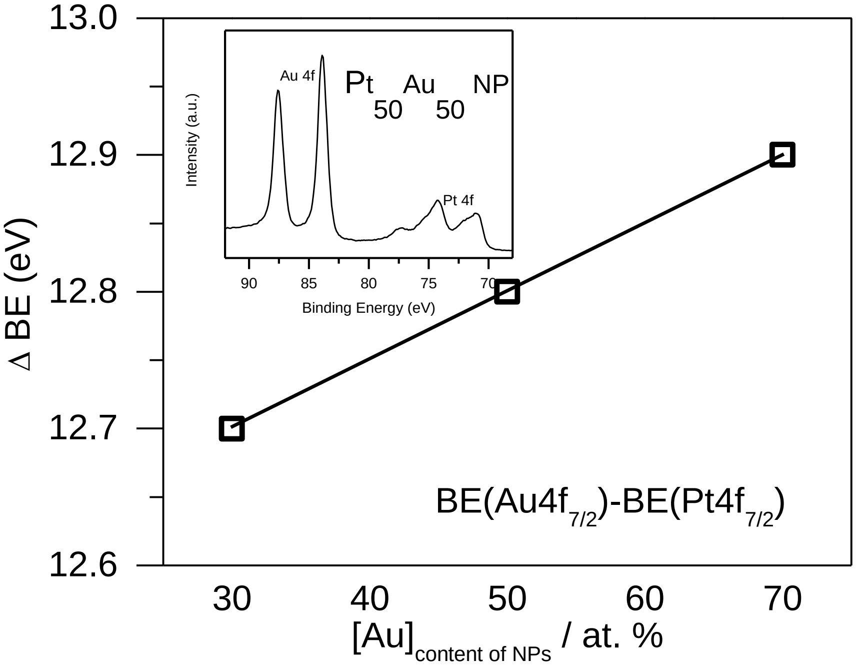

Fig. 5.8: XPS core electron binding energy difference, ΔBE, defined as Au $4f_{7/2}$-Pt $4f_{7/2}$, of alloy samples as a function of Au content of NPs (Inset: XPS spectrum of $Pt_{50}Au_{50}$) [24].

5.2.2 Methanol oxidation at Pt_xAu_{100-x} alloy electrodes by potentiodynamic measurements

The voltammograms for methanol oxidation under potentiodynamic conditions on a Pt_xAu_{100-x} surface in 0.5 M NaOH + 0.5 M MeOH at 50 mV s^{-1} are presented in Fig. 5.9. The CVs recorded in NaOH alone (dashed lines) are included for comparison.

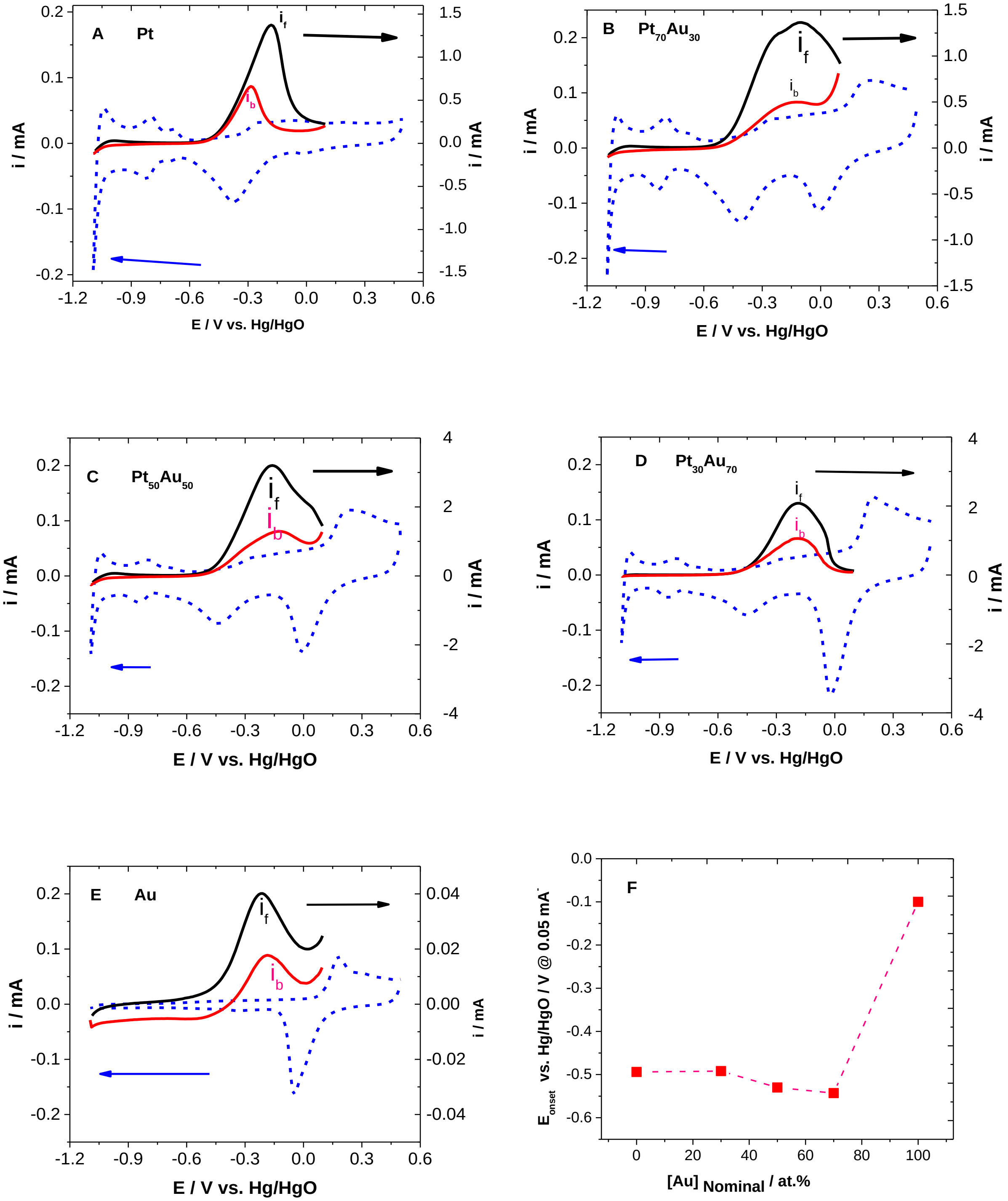

Fig.5.9: CVs of Pt NP (A), Pt$_{70}$Au$_{30}$ (B) Pt$_{50}$Au$_{50}$ (C), Pt$_{30}$Au$_{70}$ (D), Au (E) NPs electrodes in 0.5 M NaOH + 0.5 M CH$_3$OH (solid line) and 0.5 M NaOH (dashed line) at 50 mVs^{-1}; (F) Variation of the potential at fixed current of 0.05 mA with the NPs composition.

The CV displayed in Figure 5.9A is characteristic of methanol oxidation on Pt surfaces. During the forward scan, the current increases gradually registering a maximum current with a single anodic peak at -0.18 V. The maximum current attained at this peak potential is attributed to the higher coverage of OH^- anion adsorption on the Pt surface coming from the greater availability of OH^- anions in solution [7]. Also, at this peak potential, the maximum current is due to a balance between the rate of methanol dehydrogenation and the rate of oxidation of dehydrogenated products with OH_{ad} species **[**8, 12, 13]. After the peak potential, the current profile decreased gradually until $E = 0.15$ V. The exponential decline of the current profile is due the generation of less active carbonaceous intermediate species such as CHO which are adsorbed on the catalyst surface rendering the catalytic sites of Pt inactive [7, 8]. Also, within this potential region, an irreversible of PtO film is formed which is less active than the OH adsorbed and therefore inhibits the MOR.

During the backward scan, another oxidation peak is recorded at -0.28 V which is within the potential region where the PtO film is reduced (Fig. 5.9A, blue dash curve). The anodic peak at the reverse can corresponds to the oxidation of residual weakly bonded carbonaceous intermediate species that remain at the end of the forward sweep, as well as oxidation of freshly chemisorbed methanol molecules [7, 8]. The relative peak current of the forward wave to backward wave of Pt NPs towards MOR was calculated to be 2.07. This gives the magnitude of the catalytic tolerance of Pt NPs to carbonaceous species generated during MOR in alkaline medium. This value is higher than that calculated for MOR in acidic medium suggesting that OH anion are critical species in MOR to oxidize all carbonaceous species.

The CVs of methanol oxidation on Au NPs electrode is represented in the Fig. 5.9E. It has been reported previously that methanol oxidation on Au electrode proceeds independently in two potential regions, with different mechanisms [9]. At lower potentials, methanol was mainly oxidized to formate via an overall 4-electron transfer reaction as shown by equation 5. 2:

$$CH_3OH + 5OH^- \rightarrow HCOO^- + 4\,H_2O + 4e^- \qquad (5.2)$$

whereas at higher potentials, the methanol molecules were oxidized to carbonate with the exchange of six electrons, according to the reaction given below:[9]

$$CH_3OH + 8OH^- \rightarrow CO_3^{2-} + 6\,H_2O + 6e^- \qquad (5.3)$$

We focused on the electro-oxidation of methanol in the low potential region where only formate is formed but not the carbonated species [9]. The oxidation currents recorded on Au NPs at this lower potential are similar to those reported by Borkowska et al. [9] for rough gold surfaces.

During the forward scan, the current profile increased steadily reaching a maximum value at -0.1V with a single peak. Since the commencement of OH^{-} adsorption in the absence of methanol occurred at ca. -0.74V, a significant fraction of OH_{ads} might have already covered the surface at -0.1 V. After this point, MOR current decreases rapidly from a maximum of 0.05 mA at -0.1 V to less than 0.02 mA at same potential. During the reverse potential scan, the MOR current increased again to reach a peak maximum centered at -0.1 V, which coincides with the OH^{-} adsorption region on Au electrode in the methanol-free NaOH solution. The reverse scan also leads to removal of the gold surface oxides, resulting in regeneration of Au-OH_{ads} species on the Au surface, thereby re-initiating methanol oxidation [9]. The relative peak current of the forward wave to backward wave of Au NPs towards MOR was calculated to be 2.4 indicating the high active nature of Au NPs towards MOR in alkaline medium [5, 6, 9].

The CVs for the three studied alloys, Figures 5.9 B to D, also show an anodic peak during the forward scan and another anodic peak during the reverse scan, as expected. However, the following was observed on varying the bimetallic compositions in the electrode:

i. the onset of MOR occurred at more negative potentials relatively to those of Au and Pt electrodes;
ii. an increase in the magnitude of the oxidation current, accompanied by a change in the general shape of the voltammogram;
iii. the relative peak current of the forward/backward wave was dependent on the bimetallic composition of the PtAu NPs.
iv. the peak potentials of the forward and backward waves are also contingent on Au % content in the bimetallic nanoparticles.

Onset potential: By fixing the current at 0.05 mA for all the electrodes, the onset potential for the whole spectrum of Pt_xAu_{100-x} alloy NPs were estimated and the results presented in Fig. 5.9F. We have defined the potential at 0.5 mA to be the onset potential for MOR. It is clearly seen that, the onset MOR potential on the Pt_xAu_{100-x} alloy electrodes decreases slightly as the Au content increased displaying V-shape behavior presenting a minimum of -0.54 V at approximate electrochemical Au content of 70 at%. In addition, the onset potential of MOR on the Pt and Au NPs catalysts were -0.49 V and -0.10 V, while those on the Pt_xAu_{100-x} alloy catalysts are negatively shifted to lower values. For example, the onset potential of MOR values was -0.49, -0.53 and -0.54 V for $Pt_{70}Au_{30}$, $Pt_{50}Au_{50}$, $Pt_{30}Au_{70}$ alloy electrodes, respectively.

This shift of the MOR onset potential on the Au-rich alloy (Fig. 5.9D) reveals the stronger Pt-O and Pt-CO binding energies as compared with Pt-rich alloy (Fig. 5.9B) and Pt electrodes (Fig. 5.9A). This shift is consistent with what was reported recently by Kopper and co-workers [5] who reported that that adsorbed CO on Au surface in alkaline medium acts as a promoter for dehydrogenation of alcohol shifting the potential to more negative values and thereby facilitating MOR in alkaline medium. This shift is also attributed to the expansion of lattice constant with increase Au content of the alloy. A similar conclusion was reached by Mott et al. who investigated the adsorption of gaseous CO at SiO_2-supported PtAu nanoparticles by FT-IR [24]. They concluded that the participation of CO or OH adsorption on Au sites result in shifting the onset potential of the AuPt NPs to more negative with high catalytic activity of AuPt alloys with relatively high Au concentration.

Peak current: Another critical parameter which was influenced by PtAu bimetallic composition is the peak current due to MOR. Therefore, the peak current of the above PtAu bimetallic catalysts were collected and used to assess their electrocatalytic activity. Fig. 5.10 displays a representative set of results showing the dependence of MOR peak current on the bimetallic composition. It is noteworthy that the peak current presents a volcano shape with a maximum at 50 % Au, and the current is doubled in for $Pt_{50}Au_{50}$ alloy (3.1 mA) compared to Pt NP (1.5 mA) as seen in Fig. 5.10. This agrees well with the occurrence at the range of minimal onset potential at fixed current of 0.02 mA (-0.58 to -0.60 V) observed at 30-50 % Au in the PtAu bimetallic catalysts. It is interesting to note that the trend found for the MOR peak current in the alkaline electrolyte contrasts to the continuous decrease from high activity of Pt to low activity of PtAu alloy and Au NPs in the acidic electrolyte. This might be due to a couple of reasons:

1. For MOR in alkaline medium, the highest peak current on Pt_xAu_{100-x} catalyst with 50 % Au is suggestive of the operation of bifunctional mechanism [5, 8, 12, 15, 17]. Such a bifunctional mechanism will be discussed in detailed later.

2. While the presence of Au in Pt increases the lattice distance of Pt, the higher electronegativity of Au than Pt cause an increase of the amount of charge being transferred from Pt to Au, which was in fact supported by shift of Pt-oxide reduction peak potential as indicated in Fig. 5.7. Thus, the presence of Au in Pt may alter the electronic structure of Pt changing the equilibrium process of MOR on PtAu NPs in alkaline medium as suggested by Kopper and co-workers [5].

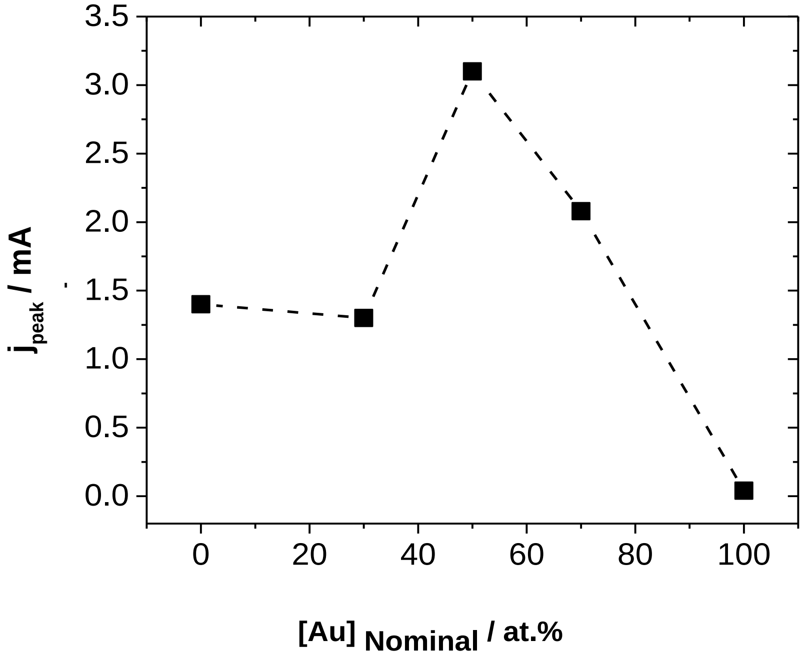

Fig. 5.10: The nominal composition dependence of MOR peak current determined for different Pt_xAu_{100-x} catalysts in 0.5 M NaOH + 0.5 M CH_3OH.

Relative Forward to backward Peak currents: The magnitude of the relative anodic peak currents for both the forward and backward waves represents the catalytic activity toward MOR. The relative peak current of the forward wave to backward wave is dependent on Au% in the bimetallic nanoparticles. The values of the forward to backward peak currents calculated were found to 2.07, 2.8, 2.5. 1.99 and 2.0 for Pt, $Pt_{70}Au_{30}$, $Pt_{50}Au_{50}$, $Pt_{30}Au_{70}$ and Au NPs respectively. These results demonstrate that the catalytic tolerance to carbonaceous products increases with increasing Au content up to 50 at Au and thereafter decreasing with further increase in Au content. This decrease in the catalytic ratio after 50 %at confirms the bifunctional mechanism on 50-50 PtAu NPs.

Forward and backward peak potentials: The forward and backward peak potentials were plotted against the electrochemical nominal composition presented in Fig. 5.11. The peak potentials of the forward and backward waves are dependent on the Au content in the bimetallic PtAu systems. For the Au NP, both the backward and forward peak occurred at almost the same potential. However, for Pt NP, the backward wave occurs at a less positive potential and differ from the forward wave by 110 mV. However, a small difference resulted from the peak potential locations of the forward and the backward waves of Pt_xAu_{100-x} alloy catalysts. Such behaviours differed from those of individual metal NPs. This is probably due to the combined bimetallic effect of the individual metals NPs in the PtAu alloy on the MOR [16, 17, 27]. It is insightful to state that the difference on the relative peak potentials of the PtAu NPs should be related qualitatively to the OH_{ads} layer and PtO formation which plays a critical role in MOR. Unfortunately, the vivid relationship between activity and OH coverage on the PtAu alloy NPs studied is not possible to obtain since the adsorption of Pt-OH $_{ads}$ and Au-OH $_{ads}$ species superimposed on each other. However, since OH adsorption is more facile on Au sites than on Pt sites, we can assume that the amount of adsorbed OH species is pronounced on PtAu alloy with greater amount of Au content and that may be the reason for the highest activity of $Pt_{50}Au_{50}$ and $Pt_{30}Au_{70}$ alloy NPs compared to the Pt NPs. Also, the observation may be due to the re-activation of the catalyst surface after the anodic scan which modifies the catalyst surface by the presence of Au in the catalyst [as a result of the oxidation of the carbonaceous species generated during the forward scan of MOR17, 28].

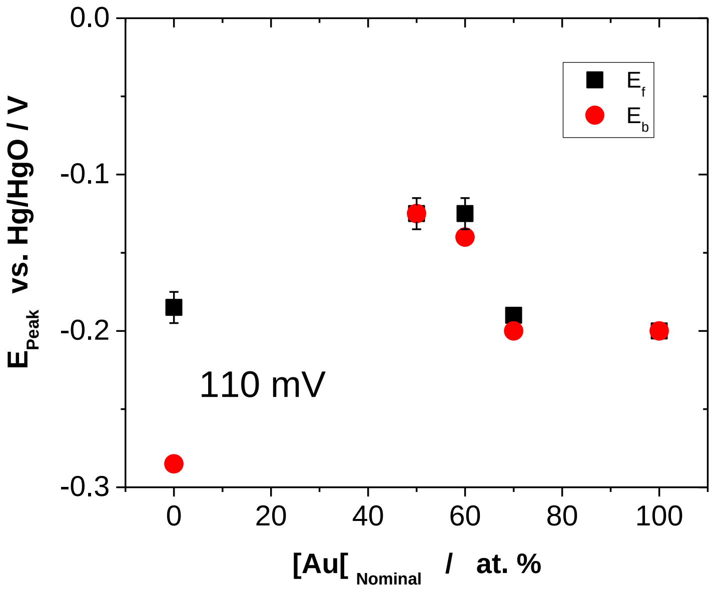

Fig 5.11: The dependence of forward and backward peak potentials as a function of bimetallic composition for PtAu alloy electrodes.

5.2.3 Potentiostatic curves for Methanol Oxidation

We have carried out chronoamperometry to determine steady state performance and poisoning rate of Pt_xAu_{100-x} NPs as anode catalysts, in 0.5 M CH_3OH in 0.5 M NaOH solution. Fig. 5.12 shows the current–time curves obtained during the oxidation of methanol recorded for 30 minutes at $E=-0.45$ V which is close to the practical operating voltage of DMFCs . The initial conditioning voltage was -1.05 V for 10 s. The current profile exhibited a high initial current and then decreases steadily with time. The high initial current is attributed to the double-layer charging [29] and abounding active sites initially available for methanol oxidation. While the exponential current decay with time was attributed to surface poisoning of Pt sites by CO-like species formed during the reaction [4]. However, the reversible OH_{ads} coverage from the solution also plays the role of an active intermediate in the methanol oxidation, but decreases with an increasing time by holding a potential at $E=-0.45$. A pseudo-steady state is reached in approximately 500 s.

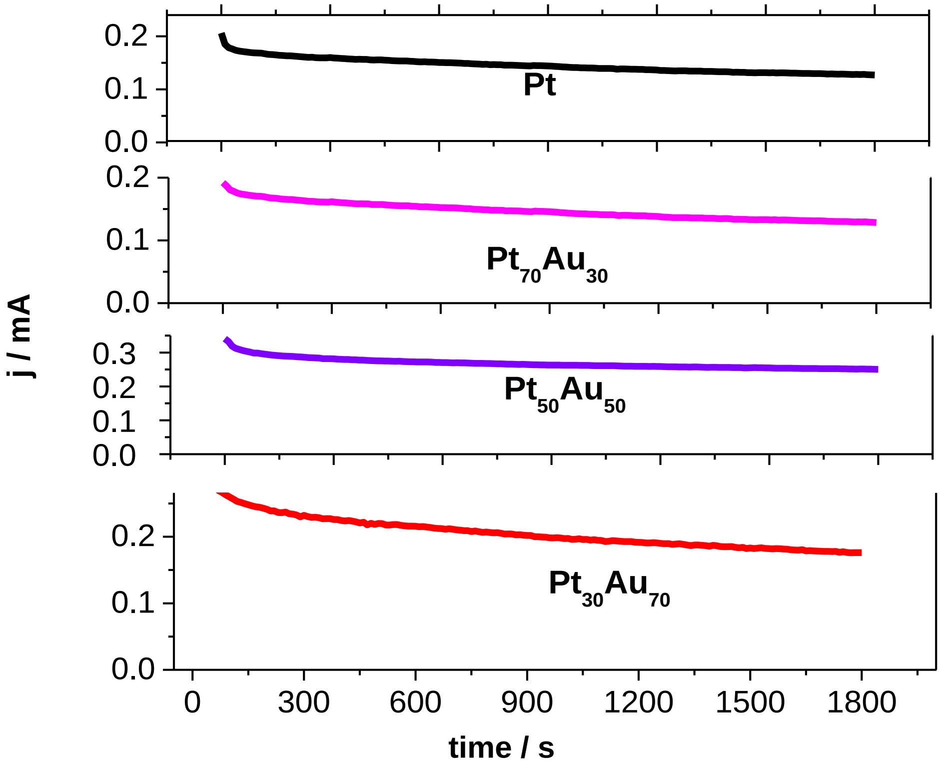

Fig. 5.12: Potentiostatic current in mA in 0.5 M NaOH + 0.5 M CH_3OH at -0.45 V for 1800s.

The steady current at the end of 1800s is collected and plotted against the nominal Au content of the PtAu NPs as presented in Fig5.13A. The steady current showed a volcano shape behavior with a maximum current activity at 50 % Au content in the bimetallic suggesting a bi-functional mechanism on the PtAu NPs towards MOR in alkaline medium. This result is consistent with the compositional-peak current dependence curve shown in Fig 5.10 in which the same trend was observed for PtAu NPs with maximum activity at 50 % Au content.

The true activities from the potentiostatic data of the whole spectrum of Pt_xAu_{100-x} alloy catalysts investigated were collected at the end of 1800s and assessed in detail. The data was normalized to the electrochemical surface area of Pt (cm^2_{Pt}) and Pt (mg_{Pt}). The Pt atoms provide the most active sites for the dehydrogenation of MOR due to the high reactivity of Pt in an aqueous media [14, 15]. The dependence of the potentiostatic current densities in cm^2_{Pt} and mg

$_{Pt}$ against the nominal Au content in the bimetallic composition for the above catalysts is plotted in Fig. 5.13 (It was impossible to test Au NPs at -0.45 Due to the very low oxidation current). The two plots showed a similar behavior with the highest current densities for the MOR at nominal composition of 70 at% Au in PtAu alloy. Inspection of Fig. 5.13B and Fig. 5.13C revealed that both Pt and $Pt_{70}Au_{30}$ catalysts have lower intrinsic and mass activities than the $Pt_{50}Au_{50}$ and $Pt_{30}Au_{70}$ electrodes. $Pt_{30}Au_{70}$ alloy appeared to be the most active electrode by factors of 8 and 5 in terms of cm^2_{Pt} and mg $_{Pt}$. respectively, with respect to Pt. The highest intrinsic and mass activities for the bimetallic catalyst with 70 % Au to those of pure Pt catalyst is suggestive of the participation of Au in the catalytic reaction of MOR in alkaline medium. The Pt atom for an AuPt alloy with 70 % Au would be practically surrounded by Au atoms as proposed by Mott et al [17]. These results are consistent with what was reported on synergistic activity of gold-platinum alloy NPs catalysts by Mott et al [17]. They concluded that the mass activity for the MOR exhibits a maximum around 65–85% Au, which is relatively close to the composition range (70 %Au) observed for the PtAu NPs (see Fig. 5.13).

However, the data presented in Fig. 5.10 and Fig. 5.13A (current intensity vs composition) is in apparent contradiction with Figures 5.13B and C (current density vs composition). According to Figures 5.13B and C we could not have a bi-functional mechanism as suggested by Figure 5.10 and Figure 5.13A, since the maximum activity is not recorded on 50-50 composition but on 70 at % Au content. .

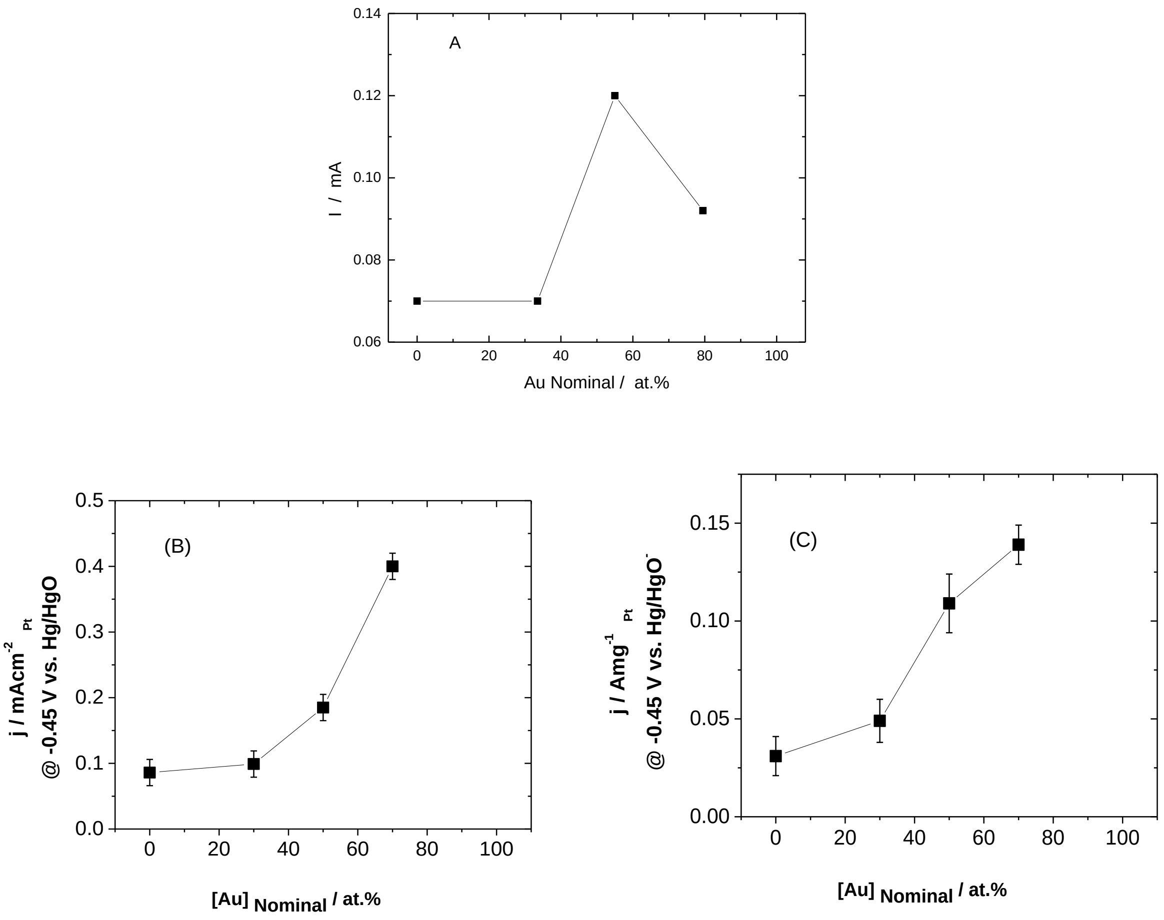

Fig. 5.13: The dependence of potentiostatic current density as a function of bimetallic composition of PtAu NPs for the (a) raw activity in mA (b) intrinsic activity in mA cm^{-2} $_{Pt}$ and (c) mass activity in A mg^{-1} $_{Pt}$

The poisoning rate (δ) was calculated by measuring the linear decay of the current for a period of more than 500 s from Fig. 5.12 by using equation (5.2). The current decay remains quite linear with time after the first 500 s of polarization. A measure of the variation of current with time is obtained by determining the slope of the linear section of the current profile, for times greater than 500 s. The current decay, δ, was normalized to the current determined from the intercept of the linear current decay line with the y-axis, $j_{t=0}$. The linear decay of the current at times greater than500 s may be characterized by the long-term poisoning rate, δ [30]:

$$\delta = -\frac{100}{j_{j=0}}\left(\frac{dj}{dt}\right)_{t>500}\left(\%\min^{-1}\right)................(5.4)$$

where $\left(\frac{dj}{dt}\right)_{t>500}$ is the slope of the linear portion of the current decay, and $j_{j=0}$ is the current at the start of polarization back extrapolated from the linear current decay. The poisoning rate as a function of nominal Au bulk composition for Pt_xAu_{100-x} alloy NPs is displayed in Fig. 5.14. The poisoning rate is found to be dependent on the bimetallic composition, decreasing with increasing Au content. Pt NPs demonstrated the highest poisoning rate while $Pt_{30}Au_{70}$ is the least poisoned electrode. The results demonstrated that the rate of poisoning of Pt NPs is minimized using bimetallic Pt_xAu_{100-x} alloy catalyst with higher Au content.

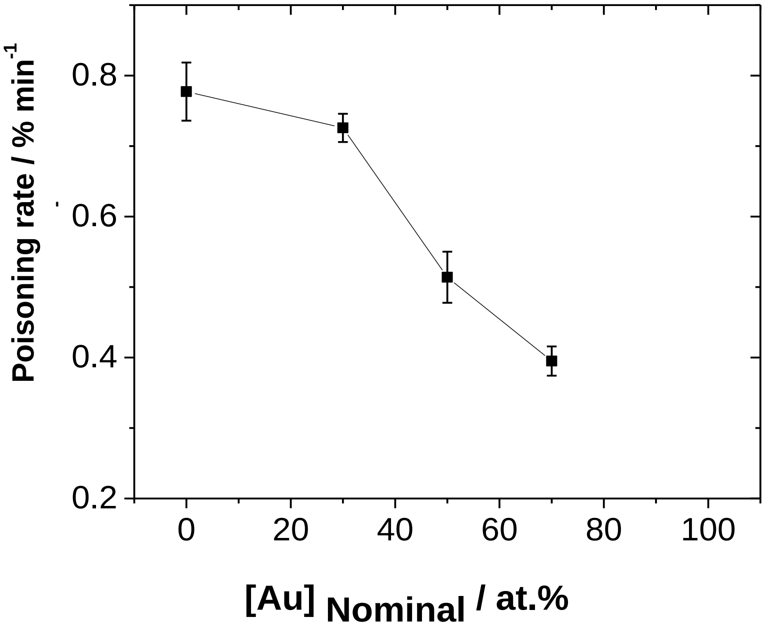

Fig. 5.14: Rate of Poisoning from potentiostatic curves in mA in 0.5 M NaOH + 0.5 M CH_3OH at 0.45 V at the end 1800s.

The MOR on Pt had been widely investigated over the years. However, the definite mechanistic reactions and the kinetic parameters are still debated. Based on the existing results in literature [5, 7, 8. 12, 15, 17, 31, 32], the bifunctional mechanism may be operational in alkaline medium. Such a bifunctional mechanism involves the following reactions:

$$2CH_3OH + 2Pt + 2H_2O \Rightarrow 2Pt\text{-}CO_{\mathrm{ad}} + \mathrm{CO_2} + 12\mathrm{H}^+ + 12\mathrm{e}^- \quad (5.5)$$

CO_2 and CO-like species were formed by direct methanol oxidation. Pt sites were deactivated by CO-like species, resulting in the initial current decrease in the chronoamperometric test.

$$Au + H_2O \Rightarrow Au\text{-}OH_{\mathrm{ad}} + H^+ + e^- \quad (5.6)$$

At the same time, abundant Au-OH $_{\mathrm{ads}}$ groups were formed

$$Pt\text{-}CO_{\mathrm{ads}} + Au\text{-} OH_{\mathrm{ads}} \Rightarrow CO_2 + Pt + Au + H^+ + e^- \quad (5.7)$$

And reaction occurred between Pt-CO $_{\mathrm{ads}}$ and Au-OH $_{\mathrm{ads}}$ releasing CO_2

$$Pt\text{-}CO_{ads} + Au \Rightarrow Au\text{-}CO_{\mathrm{ads}} + \mathrm{Pt} \quad (5.8)$$

Formation of Au-CO $_{\mathrm{ads}}$ reactivated a majority of the Pt sites, resulting in an enhanced MOR *I*p on PtAu electrodes as shown in the CVs, where Au works as the synergistic catalyst in a bifunctional system.

The enhancement of MOR activity in alkaline medium at the Pt_xAu_{100-x} alloy catalyst could also be explained on the basis of a decrease of electrode poisoning of Pt sites due to introduction of Au NPs to form PtAu NPs. Recent XPS measurements on PtAu binary systems [17, 32, 33] support this assertion that the Pt particles are more sensitive and the main sites for the oxidation process which could be improved by using a co-catalyst such as Au [32, 33]. The transfer of the intermediate CO_{ads} species from Pt-sites to neighboring Au-sites is possible in view of the favorable adsorption of CO on Au NPs is known from both experimental measurements [5, 17] and theoretical calculations [125, 26]. The formation of Au-OH_{ad} or surface oxides on gold in alkaline medium was in fact proposed to explain some of the electrocatalytic properties observed for a gold electrode [9].

As already mentioned above the onset of MOR coincides with the initiation of OH $_{ads}$ layer formation and the reaction is pronounced at where the highest coverage of OH $_{ads}$ layer is fully formed on PtAu alloy. The oxide layer formation is shifted to more positive potentials due to the presence of adsorbed Au-OH $_{ads}$, and it would have been interesting to correlate activity with the degree of OH $_{ads}$ coverage. Unfortunately, the vivid relationship between activity and coverage on the PtAu alloy studied is not possible to obtain since the adsorption of Pt-OH $_{ads}$ and Au-OH $_{ads}$ species superimposed on each other. However, since OH adsorption is facile on Au sites than Pt sites, we assumed that the amount of adsorbed OH species is pronounced on PtAu alloy with greater amount of Au content and that may be the reason for the highest activity of $Pt_{50}Au_{50}$ and $Pt_{30}Au_{70}$ alloy NPs compared to the Pt NPs.

Some relevant results published on PtAu binary systems [14, 15, 16, 17, 22, 23, 25, 26] also support the assumption that CO_{ads} and OH $_{ads}$ species participate in the MOR. As far as electronic effect on Pt_xAu_{100-x} alloy is concerned, CO and OH adsorption on Au sites may shift the oxidation potential of MOR in alkaline medium to more negative direction enhancing the activity of the PtAu NPs [4, 5,17]. This electronic effect is important, since the current densities ($P_{t30}Au_{70}$ alloy NPs) are up to 8 times greater than Pt NPs catalysts (Fig. 5.13B) and their mass activity is also 5 times higher than Pt NPs catalyst (Fig. 5.13 C).

5.3 Conclusions

The reactivity of PtAu NPs toward the electrooxidation of methanol was assessed in both acidic and alkaline medium. The electrocatalytic activity of the PtAu catalysts did not only depend on the bimetallic compositions but also strongly contingent on the electrolyte medium employed.

In the acidic medium, the MOR electrocatalytic activities in terms of peak current and steady current decreases continuously with Au content in the PtAu bimetallic catalyst. In alkaline solution, OH formation on Au sites enhances the activity and decreases the poisoning rate of Pt for the MOR.

Pt_xAu_{100-x} alloy NPs with 50-70 % Au content showed the best electrocatalytic activity for methanol electro-oxidation in the alkaline electrolyte. The highest activity for this range of compositions was explained in terms of bi-function mechanism and/or electronic effect. The studies also suggested key insights into the participation of CO_{ad} and OH_{ad} on Pt and Au sites respectively in the catalytic reaction of Pt in the PtAu alloys for MOR and their relationship between electronic structures such as the lattice constant and binding energy.

The insights from this work are useful for understanding the correlation of the electronic and/or bifunctional electrocatalytic activity of the bimetallic NPs catalysts with different *compositions.*

References

1. **J. Wang, G. Yin, G. Wang, Z. Wang, Y. Gao,** Electrochem. Commun**.** 2008, ***10*****, 83.**
2. T. Page, R. Johnson, J. Hormes, S. Noding, B. Rambabu, J. Electroanal. Chem. 485 (2000) 34
3. P. H. Fernandez, S. Rojas, P. Ocon, A. de Frutos, J. M. Figueroa, P. Terreros, M. A. Pena, J. L. G. Fierro, J. Power Sources 2008, 177, 9.
4. J. . Zhang, H. Y. Ma, D.J. Zhang, P. P. Liu, F. Tian, Y. Ding,. Phys Chem Chem Phys 2008, 10, 3250-3255.
5. P. Rodriguez, Y. Kwon, M. T. M. Koper, Nature Chemistry, 4 (2012), 177 – 182
6. . Kwon, S. C. S. Lai, P. Rodriguez, M. T. M. Koper,J. Am. Chem. Soc. 2011, 133, 6914–6917
7. B. Beden, F. Kadirgan, C. Lamy, J.M. Leger, J. Electroanal. Chem. 142 (1982) 171–190.
8. C. Nishihara, T. Okada, J. Electroanal. Chem. 577 (2005) 355–359
9. Z. Borkowska, A. Tymosiak-Zielinska, G. Shul, Electrochimica Acta 49 (2004) 1209–1220
10. L. D. Burke, P. F. Nugent, Gold Bulletin 1997, 30(2)
11. P. Iotov, S. Kalcheva, A.M. Bond. J. Electroanal. Chem, 638 (2010) 275–279
12. A.V. Tripkov c, K. D. Popovic, J. D. Lovic, Electrochim. Acta 46 (2001) 3163

13. T.J. Schmidt, P.N. Ross, N.M. Markovi, J. Phys. Chem. B 105 (2001) 12082 -12086
14. J. Luo, P.N. Njoki, Y. Lin, D. Mott, L.Y. Wang, C.J. Zhong, Langmuir 22 (2006) 2892–2898
15. L. Yang, W. Yang, Q. Cai, *J. Phys. Chem. C* 2007, 111, 16613-16617
16. M. M. Esfahani, M. Mostafavi, B. Keita, L. Nadjo, P. Kooyman, H. Remita, Gold Bulletin Volume 43 No 1 2010
17. D. Mott, J. Luo, P. N. Njoki, Y. Lin, L. Wang, C. J. Zhong, Catalysis Today 122 (2007) 378–385
18. K. Yahikozawa, Y. Fujii, Y. Matsuda, K. Nishimura, Y. Takasu, Electrochim. Acta, 1991, 36, 973–978
19. J. Luo, M. M. Maye, N. N. Kariuki, L. Wang, P. Njoki, Y. Lin, M. Schadt, H. R. Naslund, C. H. Zhong, Catalysis Today 99 (2005) 291–297
20. R. Woods, Electrochim. *Acta* 1971, *16*, 655
21. M. W. Breiter, *J. Phys. Chem.* 1965, *69*, 901
22. J. J. Mayrhofer, B. B. Blizanac, M. Arenz, V. R. Stamenkovic, P. N. Ross, and N. M. Markovic, *J. Phys. Chem. B* 2005, *109*, 14433-14440
23. M. P. Hyman, J. W. Medlin, *J. Phys. Chem. C* 2007, *111*, 17052 – 17060
24. J. Zhang, D. Oko, S. Garbarino, R. Imbeault, M. Chaker, A. C. Tavares, D. Guay, D. Ma, J. Phys. Chem. C, 2012, 116 (24), 13413–13420
25. M. O. Pedersen, S. Helveg, A. Ruban, L. Stensgaard, E. Lægsgaard, J.K Nørskov, F. Besenbacher, *Surf. Sci.* 1999, *426*, 395 =409.
26. J. W. A. Sachtler, G. A. Somorjai, *J. Catal.* 1983, *81*, 77 - 94.
27. M. M.Esfahani, M. Mostafavi, B. Keita, L. Nadjo, P. Kooyman, H. Remita, Gold Bulletin Volume 43 No 1 2010, 49-55
28. C. J. Naslund, Catalysis Today 99 (2005) 291–297
29. D. Chu, S. Gilman, J. Electrochem. *Soc.* 1996, *143*, 1685 - 1690.
30. J. Jiang, A. Kucernak, J. Electroanal. Chem. 543 (2003) 187 – 199
31. M. Watanabe, S. Motoo, J. Electroanal. Chem. 60 (1975) 259–266.
32. A.V. Tripkovic, K.D. Popovic, J.D. Lovic, V.M. Jovanovic, A. Kowal J. Electroanal. Chem 572 (2004) 119–128
33. M. Morita,Y. Iwanaga, andY. Matsuda, *Electrichim. Acta* 36, 947– 951 (1991).

CHAPTER SIX

Electro-oxidation of Dopamine and Ascorbic Acid on AuPt alloy Nanoparticles

Summary

This chapter describes results of an investigation of the electrocatalytic oxidation of dopamine (DA) and ascorbic acid (AA) on Au_xPt_{100-x} alloy nanoparticles catalysts prepared by pulsed laser ablation in water. The electrochemical sensing and properties of the Au_xPt_{100-x} alloys were studied by differential pulse voltammetry (DPV) and by cyclic voltammetry in neutral phosphate buffer solution, respectively. First a study on the optimization of some experimental parameters on the intensity of DPV current on Au for DA and AA is presented, followed by the study of the effect of alloying Au with Pt on the selectivity and sensitivity for detecting the two analytes (DA and AA). The influence of the NPs composition on the rate of AA and DA oxidation is studied by cyclic voltammetry.

6.1 Optimization of solution pH, immersion time and catalyst loading

In differential pulse voltammetry (DPV), the current is measured at two points for each pulse, the first point just before the application of the pulse and the second at the end of the pulse. These sampling points are selected to minimize the non-faradic current; therefore, DPV technique is considered more sensitive and to give better resolution than CV [1]. So DPV method was used for the optimization of the experimental parameters on Au NPs electrodes. The solution pH, the electrode immersion time, as well as the catalyst loading were optimized for the DA electro-oxidation. In addition, the effect of Au NPs loading was studied toward both DA and AA oxidation. The electrodes were first cycled in PBS between -0.65 to 0.85 V at 50 mV s^{-1} prior their use for DA and/or AA oxidation.

6.1.1 Effect of Solution pH on electro-oxidation of DA

DA usually exists in cationic form at pH less than 8.92, which is the first pKa value of DA at 25 ^{o}C [2, 3]. Fig. 6.1A shows the differential pulse voltammograms (DPVs) of 20 µM DA in 0.1 M phosphate buffer solution (PBS) with pH varying from 2.0 to 8.0. The voltammograms show similar features with a single oxidation potential peak attributed to DA oxidation to o-dopaminoquinone (DAQ), according to the reaction mechanism presented in Chapter 1 (section 1.2.2). As expected, changing the pH of the supporting electrolyte altered both the peak potentials and the peak currents of DA oxidation. It is interesting to note that the anodic peak potential varied with solution pH from neutral to acidic values, with a linear relationship of R^2 = 0.9899 between the oxidation peak potential and pH as shown in Fig. 6.1 B.

$$E_p = -53.7\,pH + 493 \qquad (6.1)$$

The slope of 53.7 mV per pH is close to the anticipated Nernstian value (59 mV per pH) for a two electrons/two protons reaction process during the DA oxidation [2-4].

A deeper investigation of Fig. 6.1 B revealed a deviation from linearity at pH 8.0 due to the deprotonation of DA at pH 8.0 (implying that DA is no longer a two-proton, two-electron process at higher pH) [2–4].

The actual current response current during the oxidation process is estimated by subtracting the baseline current from the apex of the peak height. As shown in Figure 6.1B, the anodic peak current increased with pH presenting a maximum at pH 7. The pH of maximum activity is close to the physiological one (pH 7.4). Therefore, pH 7.0 PBS was chosen for all experiments in this work. The pH response of the DA electro-oxidation on Au NPs is similar to that observed in the literature for electrodes based on Au NPs and other carbon materials [2-4] and consistent with the general mechanism presented in Chapter 1.

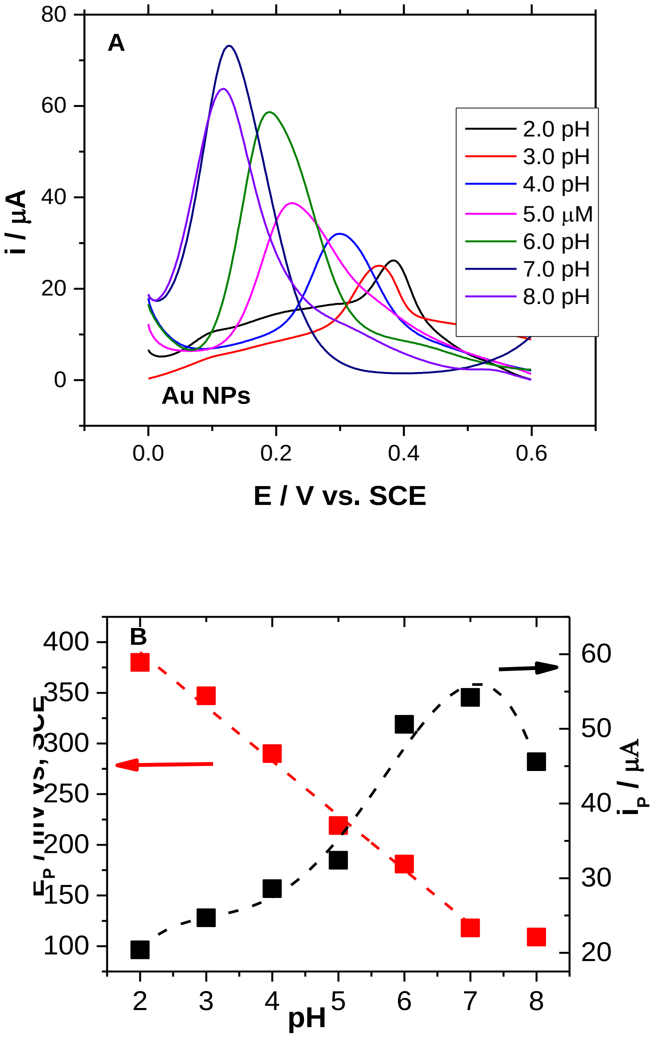

Fig. 6.1: (A) DPVs obtained on Au NPs in the presence of 20 µM DA in 0.1 M PBS at different pH varying between 2.0 to 8.0. (B) plot of peak potential and anodic peak current for oxidation of DA vs. pH in the range of 2 -8. The DPV conditions are: Au NPs electrode (10 µg), scan rate 20 mV s^{-1}, pulse amplitude 50 mV, pulse width 50 ms and pulse period 200 ms.

6.1.2 Effect of immersion time on DA oxidation

Since DA oxidation on the electrodes is a surface-controlled process (c.f. section 6.5 and reference [5]) the adsorption time will definitely influence the DA oxidation current response. Thus, the effect of the equilibration time of the electrode in the DA solution was examined. DPVs of 20 µM DA in 0.1 M PBS at varying immersion time at Au NPs electrodes are presented in Fig. 6.2A. The voltammograms show similar features with a single oxidation potential peak at ca. 0.13 V attributed to DA oxidation reaction. It can be clearly seen that the peak potential for oxidation of DA does not shifts significantly with immersion time. However, the response current showed a dependence with this parameter.

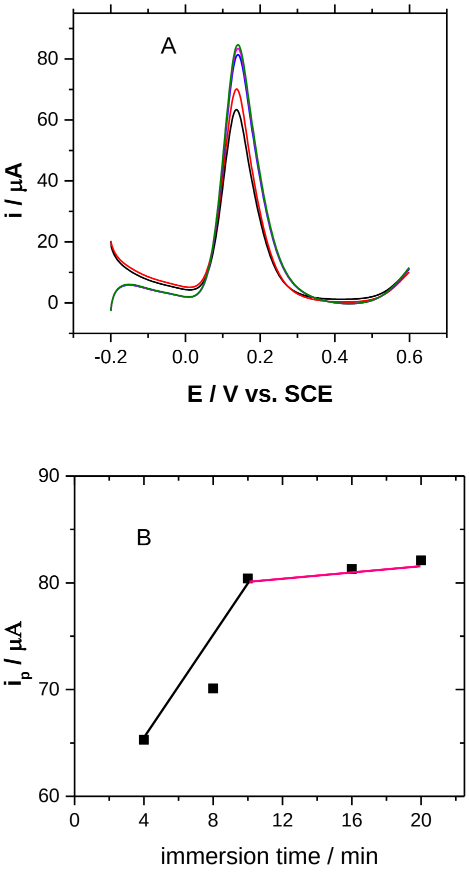

Fig. 6.2: (A) DPVs at Au NPs in 20 µM DA in PBS pH 7 at various conditioning time (B) Dependence of peak current on the conditioning time of Au NPs electrodes. The DPV conditions are: Au NPs electrode (10 µg), scan rate 20 mV s^{-1}, pulse amplitude 50 mV, pulse width 50 ms and pulse period 200 ms.

Fig. 6.2B displays the dependence of the peak current on the adsorption time, and shows that the current for DA oxidation at the Au NPs electrodes increased almost linearly with the equilibration time up to 10 min (black line) and then achieving a steady maximum afterwards (pink line). This was attributed to the saturation of DA adsorbed on the surface of the NPs due to the strong interaction of Au NPs with DA molecules [5]. This could also be that semi-equilibrium is reached after 10 min. For practical purposes, 10 min pre-concentration time was chosen for all experiments in this work.

6.1.3 Effect of metal loading on DA and AA oxidation

Fig. 6.3A and B show representative DPVs of Au NPs electrodes with different metal loadings in 0.1 mol dm^{-3} PBS at pH 7 at 20 mV s^{-1} for both DA and AA oxidation respectively. The voltammograms of Au NPs (Fig. 6.3A) showed similar features with a single oxidation potential peak recorded at 0.12 V attributed to DA oxidation reaction. Similar behavior was shown by AA oxidation with varying metal loadings of Au NPs (Fig. 6.3B). The DPVs contain a single peak at -0.02 mV attributed to the oxidation of AA to dehydro ascorbic acid (c.f. Chapter 1, Fig. 1.7) [6 -10]. There was very little or no shift of peak potential of the DA and the AA oxidation with increasing Au loading. It is worth mentioned that there is an increase of the oxidation peak currents for both DA and AA with increasing metal loadings from 9 to 18 μg as shown in Fig. 6.3C. This indicates that the catalyst utilization is the same in this linear region and therefore the current response increases. However, the current response increases less rapidly with further increase in metal loadings (beyond 18 μg), suggesting a decrease in the catalyst utilization. Therefore, metal loading of ca. 18 μg was chosen for catalytic activity towards DA and AA oxidation in this work.

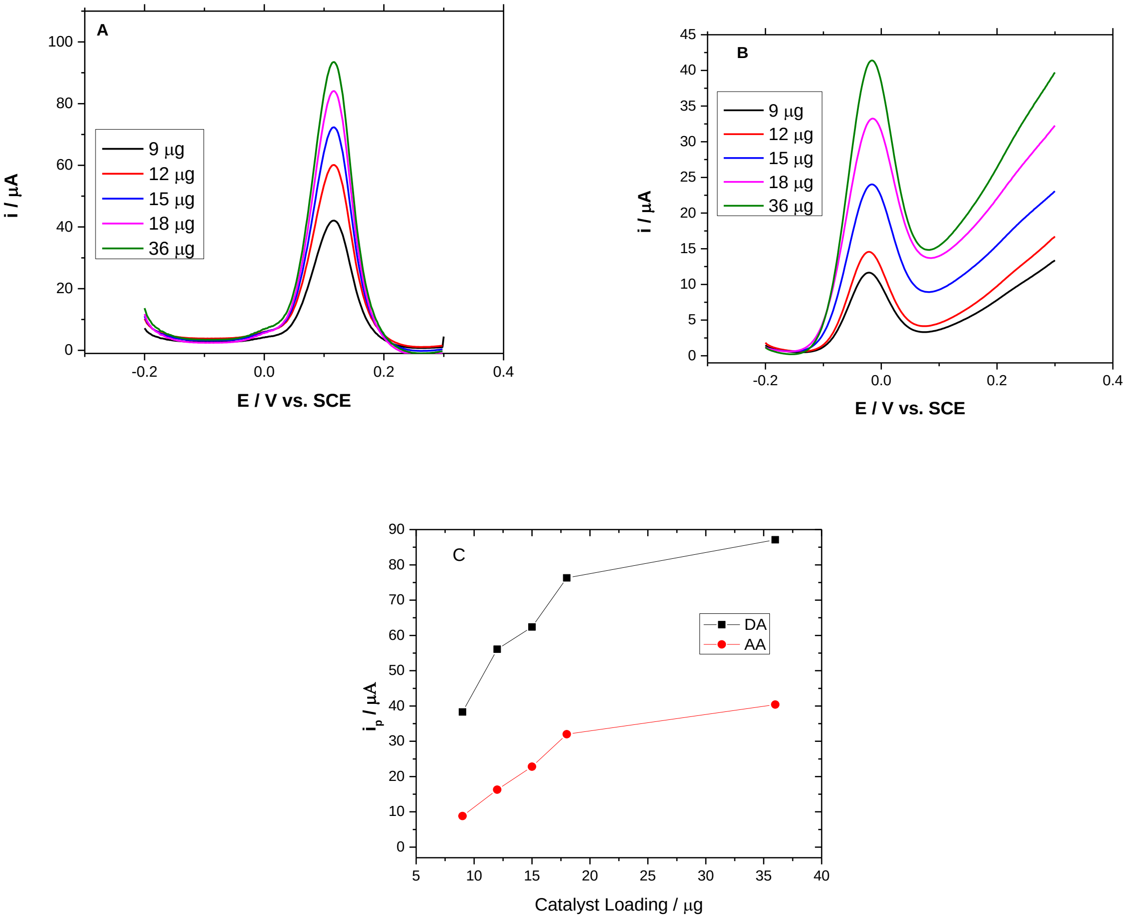

Fig 6.3: DPV responses for Au NPs with different metal loadings in 0.1 M PBS for (A) 20.0 μM DA oxidation, (B) 2.0 mM AA oxidation and (C) variation of the peak current as a function of Au loading. The DPV conditions are: scan rate 20 mV s^{-1}, pulse amplitude 50 mV, pulse width 50 ms and pulse period 200 ms.

6.2 Dopamine and Ascorbic acid oxidation on Au_xPt_{100-x} NPs

AA coexists with DA in most biological fluids and therefore always influences the determination of DA, so it is important to determine DA sensitively and selectively in the presence of AA. Since the concentration of AA is much higher than that of DA, AA is a major interference for DA detection.

6.2.1 Dopamine oxidation

The oxidation of 20 µM DA in 0.1 M PBS at pH 7.0 at Au_xPt_{100-x} NPs (x=0, 30, 50, 70 and 100) is shown in Fig. 6.4. As expected, the DA oxidation exhibits a single anodic peak at these electrodes. At the Au NPs electrodes the oxidation peak was well-shaped and relatively intense indicating the excellent catalytic activity of Au NPs to the electrochemical oxidation of DA. When compared with Au NPs electrode, the oxidation current of DA decreases by 15 and 14, % at $Au_{70}Pt_{30}$ and $Au_{50}Pt_{50}$, respectively, which suggests a lower catalytic activity of the alloyed NPs for DA oxidation. The decrease in the oxidation current was huge on $Au_{30}Pt_{70}$ and Pt NPs electrodes. In fact, for these NPs the oxidation peak current is by 83 % lower of the value measured for the Au NPs confirming the poor catalytic activity of Pt to electrochemical oxidation of DA [11]. It is also interesting to note that, while the anodic peak of DA oxidation remain virtually constant at 110 mV at Au and $Au_{70}Pt_{30}$ alloy, the peak potential at $Au_{50}Pt_{50}$ alloy shifted to more positive values to 140 mV and 120 mV for Pt NPs and $Au_{30}Pt_{70}$ alloy NPs electrodes, respectively. The decrease in activity with increasing Pt content can be attributed to a lower number of Au adsorption sites on the surface of the NPs. However, these results also suggest that alloying Au with Pt does not have a positive effect on DA oxidation. A more detailed cyclic voltammetric study on the effect of the nanoparticles composition and particle size on the DA oxidation is presented at the end of this chapter (section 6.5).

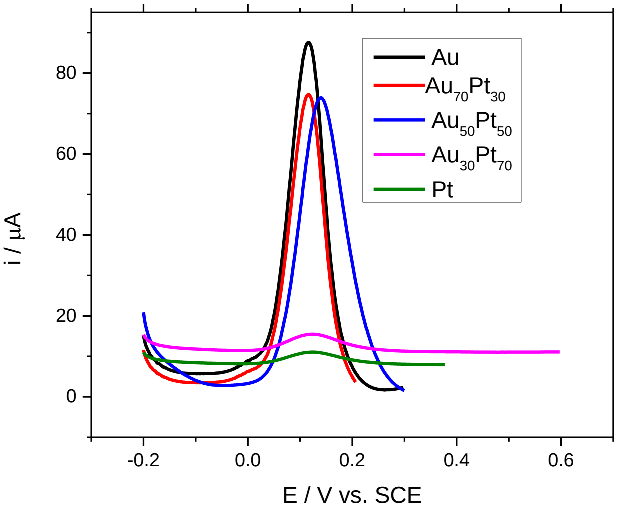

Fig. 6.4: DPV of Au_xPt_{100-x} alloy NPs in 20 µM DA in 0.1 M PBS at pH 7.0. DPV conditions: scan rate, 20 mVs^{-1}; amplitude, 50 mV; pulse width, 50 ms; pulse period, 200 ms.

6.2.2 Ascorbic acid oxidation

The differential pulse voltammograms for the oxidation of 2.0 mM AA in 0.1 M PBS at pH7.0 at Au_xPt_{10-x} NPs are displayed in Fig. 6.5. It can be seen that AA oxidation also exhibited a single anodic peak at these electrodes, but the peak potential and peak current are largely different and dependent on the Au-Pt bimetallic composition.

At the Au NPs electrode the anodic peak of AA oxidation was well-defined and the peak potential occurred at about -0.027 V. The oxidative peak current at $Au_{70}Pt_{30}$ alloy electrode was enhanced by 15 % with respect to Au NPs, but the peak potential almost did not change (-0.033 V). As the Pt content in the AuPt bimetallic NPs increased to 50 at %, the AA oxidation peak at $Au_{50}Pt_{50}$ alloy electrode shifted positively to about -0.02 V, and the peak current decreased to a value similar to that of Au NPs. As the Pt content in the bimetallic NPs was increased further to 70 at %, the AA oxidation peak shifted to more positive potential at about 0.01 V, and the peak current was smaller ca. (50 %) compared to the other bimetallic NPs. This was even more drastic at the pure Pt NPs electrodes, where the intensity of the peak, centered at 0.11V, was very small suggestive of poor catalysis of Pt and Pt-rich bimetallic NPs [6, 7, 12, 13].

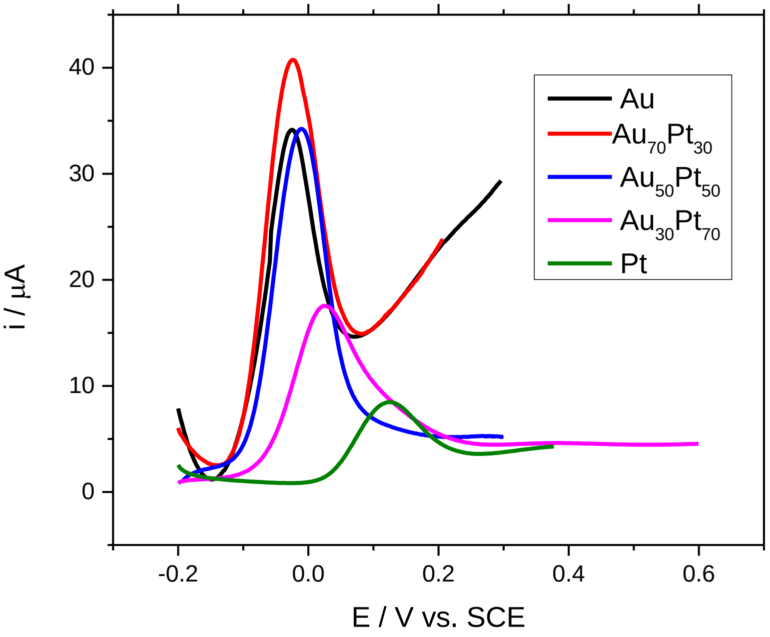

Fig. 6.5: DPV of Au_xPt_{100-x} alloy NPs in 2.0 mM AA in 0.1 M PBS at pH 7.0 DPV conditions: scan rate, $20mVs^{-1}$; amplitude, 50mV; pulse width, 50 ms; pulse period, 200ms.

It is important to remark that Au and Au rich based bimetallic NPs showed excellent electrocatalytic activity for AA oxidation, with the alloyed $Au_{70}Pt_{30}$ NPs demonstrating higher activity. This suggests a synergistic effect between Pt and Au in the alloy. Many papers reported on bimetallic Au-Pt NPs of controllable composition that serve as a synergistic catalyst system for electrochemical oxidation of methanol [14] and glucose [15] and reduction of nitrite [16] oxygen [17] and dopamine [18]. This effect is also consistent with our previous work on FAO and MOR on AuPt NPs in chapters 4 and 5, but apparently it contrast with the results on DA oxidation (Figure 6.4). As for DA, a more detailed investigation on the effect of the NPs composition on the AA oxidation was carried out by cyclic voltammetry and it will be presented at the end of this chapter.

6.2.3 Simultaneous oxidation of dopamine and ascorbic acid

The above results clearly show that the electrochemical responses of AA and DA at the Au_xPt_{100-x} NPs occur at different potential windows, which means that the electrochemical responses of these compounds could be well resolved when mixed in solution. The oxidation of coexisting AA and DA at the Au_xPt_{100-x} NPs was thus carried out.

Fig. 6.6 shows the DPV curves of 20.0 µM DA and 2.0 mM AA mixture at different Au_xPt_{100-x} alloy NPs electrodes (x=0, 30, 50, 70, 100). Pure Au NPs showed two clearly distinct peaks at -0.027 V and 0.129 V corresponding to AA and DA oxidation respectively. As Au NPs is being alloyed with 30 at% Pt, a single broad peak is observed. This indicates that $Au_{70}Pt_{30}$ alloy NPs is not able to separate DA and AA in the mixture. In fact, the unseparated broad anodic peak was centered at 0.101V with a huge current peak response of 114.3 µA could be due to the superimposition of oxidation currents of the two analytes in solution. As the Pt content in the $Au_{100-x}Pt_x$ alloy NPs increases to 50 at%, the electrodes were able to resolve the AA and DA oxidation reactions into two well-defined peaks at -0.04 V and 0.15 V respectively.

Similar DPV profiles were recorded for Au, $Au_{70}Pt_{30}$ and $Au_{50}Pt_{50}$ NPs in 20 mM DA and AA concentration gradually increased from 1 to 2 mM (data not shown). Once again a single wave was recorded for $Au_{70}Pt_{30}$. It is noteworthy that $Au_{50}Pt_{50}$ alloy NPs demonstrated a wide peak separation of 190 mV and Au NPs showed 156 mV peak separation which should be large enough for the determination of DA in AA/DA mixed solution. Moreover, this peak – to – peak separation compares very well to those reported in the literature for simple electrodes' structures based on Au nanoparticles. For example, 170 mV in 50 µM AA and 50 µM DA solution for Au NPs immobilized on amine terminated self-assembled monolayers [9]; ca. 200 mV on dendritic Au nanorods in 0.2 mM AA and 10 µM DA [19]; and 150 mV in AA up to 1.4 mM + DA up to 440 µM (pH=4) at PtAu hybrid films modified with L-Cysteine [20].

As the Pt content is increased further to 70 at% as in the $Au_{30}Pt_{70}$ alloy, the electrode showed again one single broad peak at 0.13 V and a very small current response (30.3 µA). Pure Pt NPs could also not resolve DA and AA oxidation peaks either, presenting a single broad and small anodic peak at about 0.21 V. Nevertheless, as compared to$Au_{70}Pt_{30}$ NPs, the pure Pt NPs electrode showed a 25 % enhancement in the response current (40.6 µA). Thus Pt NPs and $Au_{30}Pt_{70}$ alloy NPs are not potential candidates for separating AA and DA analytes in solution.

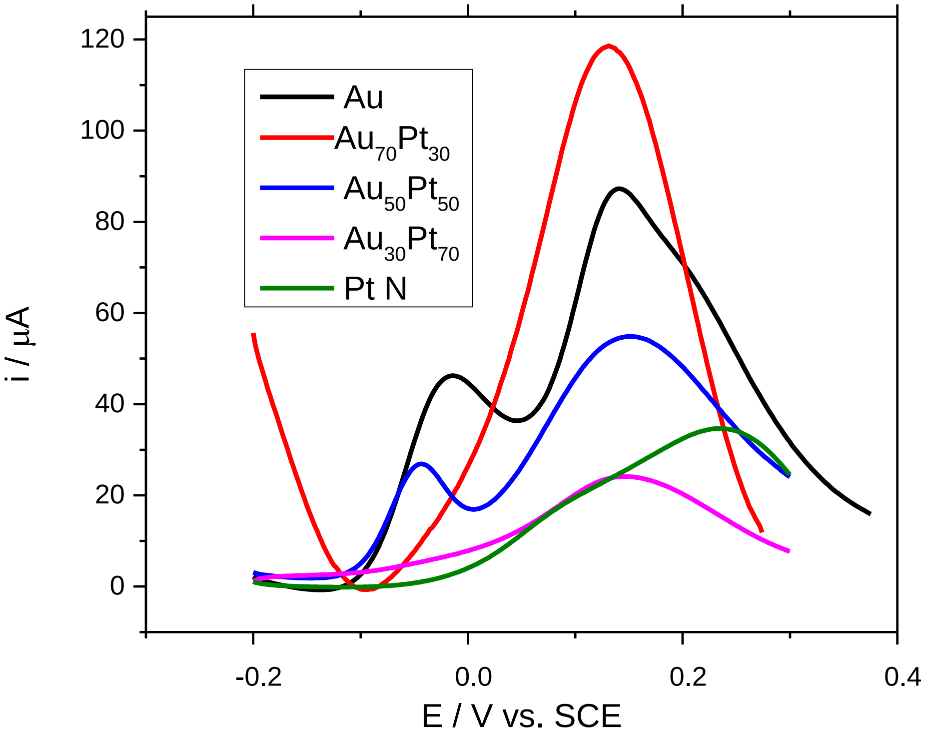

Fig. 6.6: DPV of Au_xPt_{100-x} alloy NPs in 20 µM DA + 2.0 mM AA in 0.1 M PBS at pH 7.0 DPV conditions: scan rate, $20mVs^{-1}$; amplitude, 50mV; pulse width, 50 ms; pulse period, 200ms.

From the above results, we hypothesize that the Au and $Au_{50}Pt_{50}$ alloy NPs combine the biosensing properties of Au NPs for DA and AA and the synergistic effect of alloying Au with Pt to promote a fast electron transfer reaction for AA oxidation.

Since both the sensitivity and the selectivity are two critical parameters in simultaneous detection of DA in the presence of AA, Au and $Au_{50}Pt_{50}$ alloy were selected to proceed with the analytical determination of DA and AA. $Au_{70}Pt_{30}$ alloy was also included in this study to gather more information on the synergetic effect of Pt on Au for AA oxidation.

6.3 Detection of dopamine and ascorbic acid for selected Au_xPt_{100-x} NPs catalysts

6.3.1 Detection of DA alone at physiological pH

Fig. 6.7 shows the typical DPV voltammograms of DA at the (A) Au, (B) $Au_{70}Pt_{30}$ alloy and (C) $Au_{50}Pt_{50}$ alloy NPs with increasing concentration (by successive addition) from 0.50 µM to 20.0 µM. It can be found that the DPV peak height was linearly related to the DA concentration over the entire concentration intervals, viz., 0.50–20.0 µM as presented in Fig.6.7D.

The limit of detection (LOD) for all the selected catalysts (Au**,** $Au_{70}Pt_{30}$, and $Au_{50}Pt_{50}$ NPs electrodes) could be estimated by employing the equations (6.2) [3, 21]:

$$LOD = \frac{3s}{b} \tag{6.2}$$

where s is the standard error on the slope value and b is the slope of the calibration curve. The standard error as well as the analytic parameters namely sensitivity, limit of detection and regression coefficients are shown in Table 6.1.

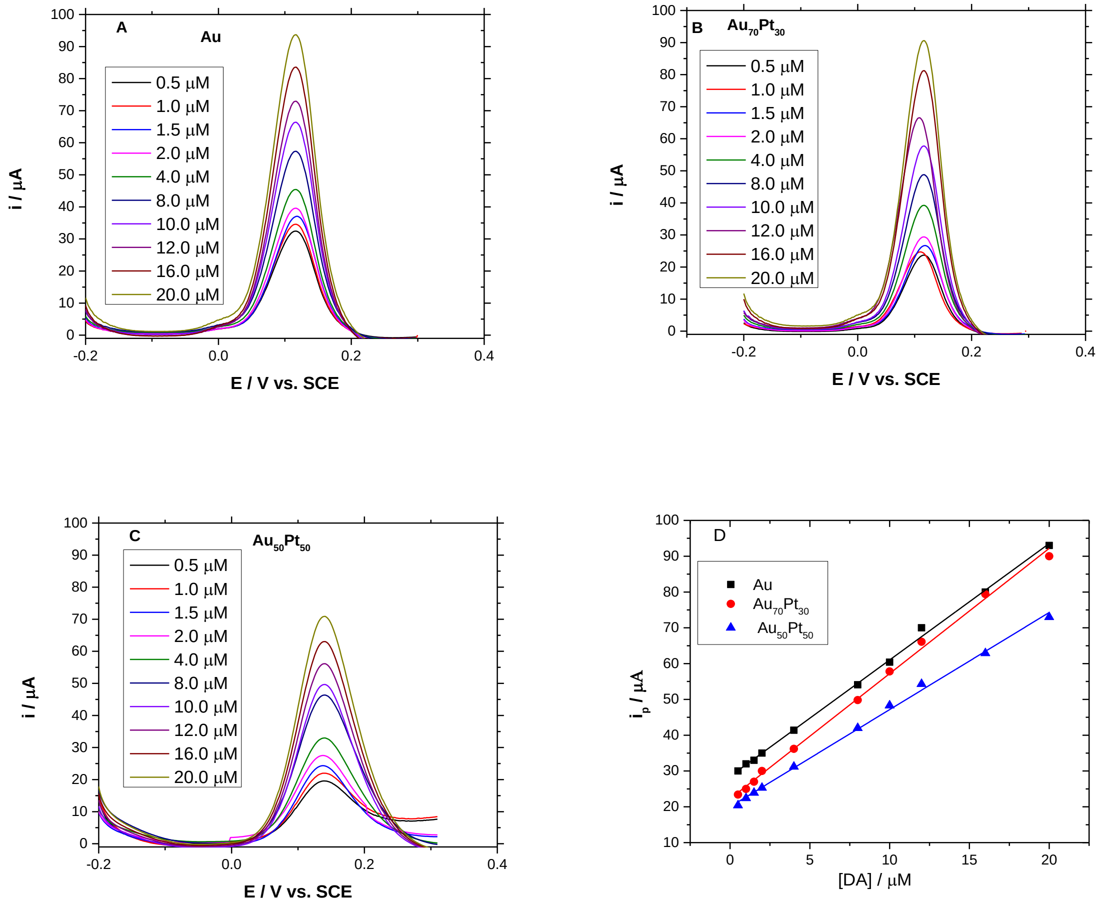

Fig 6.7**:**DPV responses with various concentrations of DA from 0.5, 1.0, 1.5, 2.0, 4.0, 8.0, 10.0, 12.0, 16.0, and 20.0 µM DA (0.1 M PBS/pH 7) for (A) Au NPs, (B) $Au_{70}Pt_{30}$, and (C) $Au_{50}Pt_{50}$ NPs electrodes and (D) calibration curves for DA electro-oxidation on the electrodes. Other conditions are the same as in Fig. 6.1.

Table 6.1. Analytical parameters obtained for the electrochemical quantification of DA from the respective calibration plots (Figure 6.7D).

Catalysts	**Slope / µA µM^{-1}**	**R^2**	**Standard Error**	**LOD/ µM**
Au	3.25	0.9981	0.0469	0.04
$Au_{70}Pt_{30}$	3.50	0.9974	0.0595	0.05
$Au_{50}Pt_{50}$	2.71	0.9973	0.0470	0.05

The slope of the calibration curve represents the sensitivity of the electrode towards DA oxidation. The Au NPs showed a sensitivity of 3.25 µA µM^{-1}. When Au was alloyed with 30 at % Pt, the $Au_{70}Pt_{30}$ alloy NPs showed sensitivity of 3.5 µA µM^{-1} representing a slight increase of 8 % over the pure Au NPs electrodes. However, with increasing Pt content in the alloyed NPs to 50 at %, the $Au_{50}Pt_{50}$ alloy NPs demonstrated a sensitivity 2.71 µA µM^{-1}, suggesting a reduction of 17 % of sensitivity over the pure Au NPs.

The Au NPs showed detection limit of 0.04 µM towards DA oxidation. When the Au was alloyed with 30 at % Pt, the detection limit was 0.05 µM. Also, with increasing Pt content in the alloyed NPs to 50 at %, the $Au_{50}Pt_{50}$ alloy NPs demonstrated a detection limit of 0.05 µM (same as $Au_{70}P_{t30}$) indicating that alloying Au with Pt does not improve the detection limit of AuPt NPs towards DA oxidation.

6.3.2 Detection of AA alone at physiological pH

The analytical detection of AA was carried out on the selected Au_xPt_{100-x} alloy NPs electrodes using DPV by successive addition of AA (from 1.0 to 2.0 mmol dm^{-3}) to the phosphate buffer solution at pH 7. As shown in Fig. 6.8, the peak current increased with the AA concentration and the peak height was linearly related to the AA concentration over the studied interval. The analytical parameters values, namely sensitivity and coefficient of regression, determined from the linear plot of the peak current response as a function of the AA concentration are shown in Table 6. 2.

The sensitivity of the electrodes is very small (<0.02 µA/µM) probably due to the fouling of the electrode surface by the oxidized products of ascorbic oxidation [22]. In fact, the concentration of AA used in this study is quit high (1 to 2 mM). Because of such small slope values and consequently the standard deviation associated with, the calculated LOD values are also very small and vary between 0.06 and 0.09 µM. It is noteworthy that both, Au NPs and $Au_{70}Pt_{30}$ alloy NPs showed detection limit of 0.06 µM towards AA oxidation. However, with increasing Pt content in the alloyed NPs to 50 at %, the $Au_{50}Pt_{50}$ alloy NPs demonstrated a detection limit of 0.06 µM (30 % appreciation of LOD as against pure Au and $Au_{70}Pt_{30}$ alloy NPs)$^{\cdot}$ The LOD is largely overestimated under the current experimental conditions.

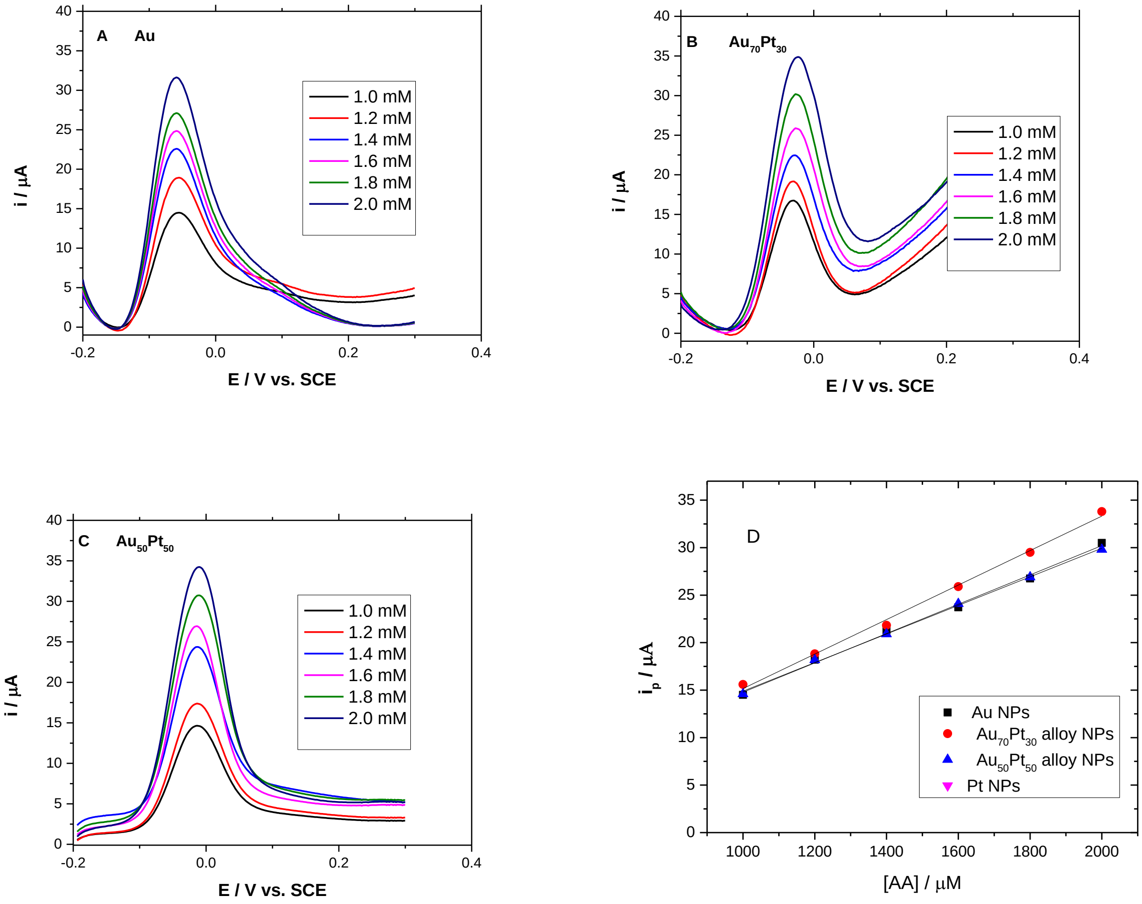

Fig 6.8: Differential pulse voltammograms for AA electro-oxidation in 1.0, 1.2, 1.4, 1.6, 1.8 and 2.0 mM in 0.1 M PBS/pH 7 at (A) Au NPs**,** (B) $Au_{50}Pt_{50}$, and (C) $Au_{70}Pt_{30}$ NPs electrodes; (D) calibration curves for ascorbic acid oxidation on the electrodes. Other conditions are the same

Table 6.2. Analytic parameters obtained for the electrochemical quantification of AA from the respective calibration plots (Figure 6.8D).

Catalysts	**Slope / μA μM^{-1}**	**R^2**	**StD Error x10^{-4}**	**LOD / μM**
Au NPs	0.0154	0.9952	4.7927	0.09
$Au_{70}Pt_{30}$ alloy NPs	0.0182	0.9955	5.4684	0.09
$Au_{50}Pt_{50}$ alloy NPs	0.0151	0.9984	2.7741	0.06

6.3.3 Determination of dopamine in the presence of ascorbic acid

The determination of DA in the presence of AA on the Au_xPt_{100-x} NPs was carried out. In these measurements, the DA was step wise added to a fixed concentration of AA (2.0 mmol dm^{-3}) solution starting from 0.5 and up to 20 μmol dm^{-3}. It can be seen from DPVs in Fig. 6.9 that upon the addition of DA, the height and amplitude of the peak corresponding to DA increased proportionally to the DA concentration. For all the concentrations of DA studied, the signal of the AA was about 200 mV away from that of DA on Au NPs and $Au_{50}Pt_{50}$ alloy NPs; but this was far smaller on $Au_{70}Pt_{30}$ alloy NPs (AA was about 70 mV away from that of DA).

In general, the peaks were very well separated at low concentration of DA up to about 4.0 μM. But, upon successive additions of DA, the peaks were less well separated and this was more evident on $Au_{70}Pt_{30}$ NPs electrode in which the peaks almost completely overlapped. This is notably due to the fouling of the electrodes with the oxidation products of AA, and this seems to be more severe in the case of $Au_{70}Pt_{30}$ NPs.

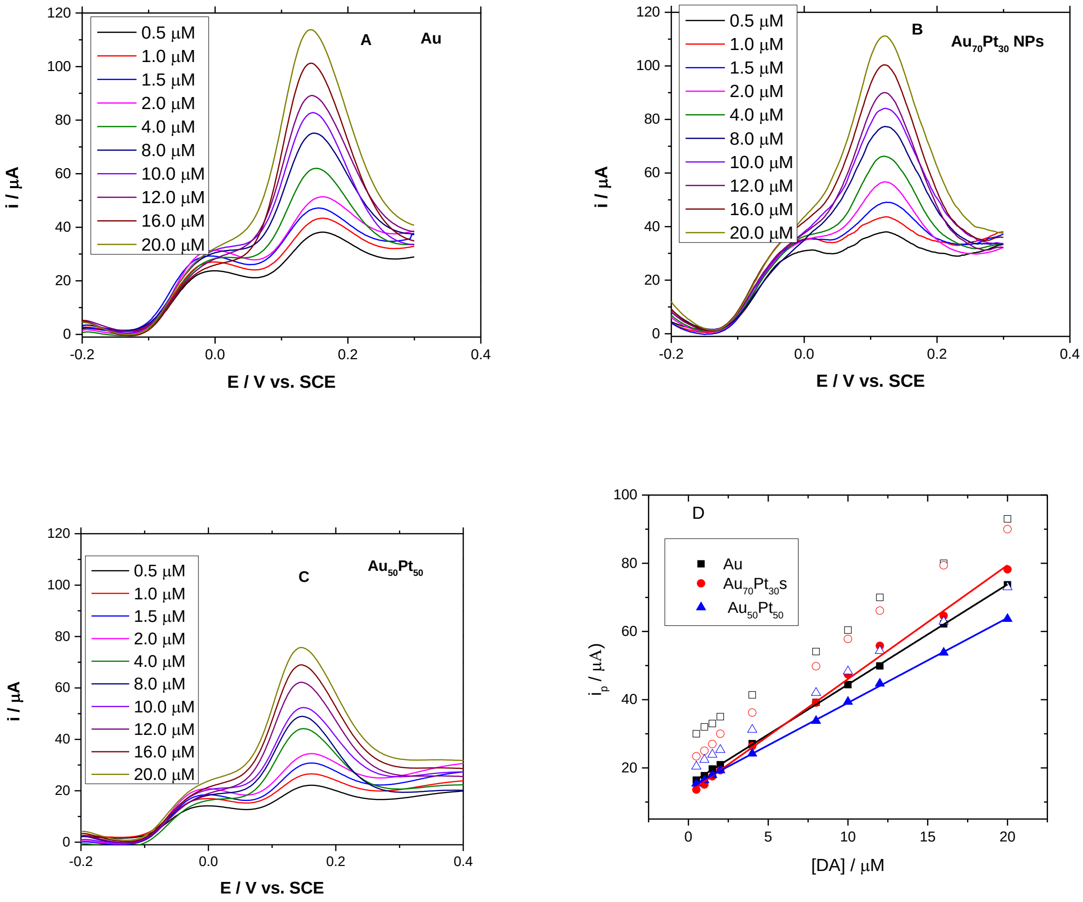

Fig 6.9: DPV responses with various concentrations of DA from 0.5, 1.0, 1.5, 2.0, 4.0, 8.0, 10.0, 12.0, 16.0 and 20.0 µM DA (0.1 M PBS/pH 7) in the presence of fixed concentration of 2.0 mM AA for (A) Au, (B) Au$_{70}$Pt$_{30}$ and (C) Au$_{50}$Pt$_{50}$ electrodes; (D) calibration curves for DA alone (open symbols) and DA in the presence of AA (solid symbols) Other conditions are the same as in Fig. 6.1.

Fig. 6.9D shows the DA oxidation peak current values recorded in the presence of AA (solid symbols) as a function of DA concentration. As a comparison, the calibration curve of DA alone (open symbols) is also added for all the electrodes studied. It can be seen from the calibration curves that there is an apparent drop of the current response for DA oxidation in the presence of AA compared to the values recorded for DA oxidation alone. This drop is an artifact because the DA peak current depends on how the base line (after the AA peak) is considered. This might also be due to competitive adsorption of AA (or oxidation products) and DA, so adsorbed AA molecules occupy some electrode surface area, and the surface conc of DA is thus lower than in the absence of AA in the solution As evidenced in Figure 6.8, the AA peak shape varies between the various catalysts, which complicate the determination of the base line for the DA oxidation peak. In the present study, the base line was taken from the inflexion point between the AA and DA peaks.

The regression parameters for both DA alone and DA in the presence of AA derived from the calibration plots are presented in Table 6.1 and Table 6.3 respectively. It is interesting to note that the sensitivity of the electrodes for DA in the presence of AA depreciates by less than 10% compared to DA alone on these catalysts. This confirms that these Au and Pt-Au alloyed NPs can detect DA in solutions in highly concentrated AA (1000-fold more concentrated) solution. This result is very good considering that the electrodes used here consist only of the NPs and Nafion thin film and that no attempt was done to optimize its structure and composition in order to maximize the electrostatic interaction with DA ions, to repel the AA anions from the electrodes' surface and to minimize the fouling of the electrodes with AA's oxidation products.

Table 6.3. Analytic parameters obtained at low concentration region for both DA alone and DA in the presence of 2.0 mM AA from the calibration plots for all the AuPt NPs

Catalysts	Slope / μA μM^{-1}	StD Error	R^2	LOD / μM
Au	2.93	0.0158	0.9999	0.02
$Au_{70}Pt_{30}$	3.34	0.0699	0.9961	0.06
$Au_{50}Pt_{50}$	2.49	0.0156	0.9998	0.02

Comparison of the performance of the AuPt NPs electrodes towards DA oxidation in the presence of AA with some previous results is listed in Table 6.4. The limit of detection estimated using equation 6.2 was the same for Au and $Au_{50}Pt_{50}$ NPs and higher for $Au_{70}Pt_{30}$ NPs. It could be noticed that the performance of both Au NPs and $Au_{50}Pt_{50}$ NPs electrodes for DA detection are superior to the electrodes based on single metal such as Au [19, 23, 24, 25] and Pt [26]. In particular, both Au NPs and $Au_{50}Pt_{50}$ NPs results exhibits significantly lower LOD (about 5 times) than those reported results on dendritic Au rod modified with Nafion [19] and N-acetylcysteine SAM Au electrode [24] which showed a limit of detection of 0.1 µM and 0.8µM, respectively. Also, it is noteworthy that the LOD for DA in the presence of AA for these AuPt NPs electrode are significantly higher than that of hybrid mixture of PtAu/Nafion reported recently for selective detection of DA in the presence of AA and UA [20]. Furthermore, these results demonstrated that both Au NPs and $Au_{50}Pt_{50}$ NPs exhibited comparable sensitivities with the previously reported electrodes such as PtAu hybrid film modified electrodes [20]. Therefore, it can be concluded that a synergetic effect of Pt and Au play a vital role in electrocatalysis of small organic molecules of our AuPt NPs as cited in chapter 2 and 4 of this thesis.

Although the fabrication of the Au-based electrodes capable of in vivo applications is still recommended for further studies in our group, the high sensitivity and selectivity against DA and AA oxidation strongly suggest the potential application of the as-fabricated AuPt NPs electrodes for selective and sensitive determination of DA and AA, which is believed to find some interesting biological applications.

Table 6.4: Comparison of Au$_x$Pt$_{100-x}$ NPs for DA oxidation in presence of AA to various systems

Electrode	Analyte	pH	LOD (µM)	Sensitivity (µA/µM)	Reference
Dendritic Au rod/Nafion	DA in presence of 0.1 mM AA	7.0	0.1	13.8	19
Nanostructured Au with packed spikes	DA in presence of 1.0 mM AA	7.4	5	0.139	23
N-acetylcysteine SAM Au electrode	DA	6.5	0.8	0.474	24
self-assembled Au NPs films	DA in 0.1 mM AA	5.0	90	0.0035	25
Nafion/Pt/GCE	DA in presence of 0.1 mM AA	7.4	0.01	N/A	26
Hybrid PtAu/GCE	DA in 1.mM AA and 1.033 Mm UA	4.0	24	0.05	20
Au NPs	DA in presence of 2.0 mM AA	7.0	0.02	2.93	this work
Au5$_0$Pt$_{50}$ alloy NPs	DA in presence of 2.0 mM AA	7.0	0.02	2.49	this work
Au$_{70}$P$_{t30}$ alloy NPs	DA in 2.0 mM AA	7.0	0.06	33.34	this work

6.4 Surface Properties Au_xPt_{100-x} NPs

Cyclic voltammetry has proven to be a powerful sensitive tool for probing surface atoms and properties of NPs [27, 28]. Therefore, cyclic voltammograms were recorded in 0.1 M PBS and analyzed in terms of catalyst' electrochemical surface area, metal surface content and catalyst utilization. In section 6.5, cyclic voltammetry will be used to study the influence of the NPs composition on the reaction mechanism of DA and AA electro-oxidation.

Fig. 6.10 shows the cyclic voltammograms of Au_xPt_{100-x} NPs in N_2-saturated 0.1 mol dm^{-3} PBS at pH 7 up to 0.85 V and 1.15 V. On the Au NPs (Fig. 6.10A), Au oxide formation starts at $E > +0.7$ V and a well-defined cathodic peak, attributed to the reduction of surface gold oxide, appears centered at +0.48 V on the reverse scan. For pure Pt NPs (Fig.6.10D), hydrogen adsorption-desorption region can be distinguished below -0.30 V, followed by the narrow double layer region up to $E < -0.15$ V, and then by the Pt-oxide monolayer formation at more positive potential ($E > -0.15$ V). The PtO layer is reduced during the backward scan and exhibits a cathodic peak centered at ca. $E = -0.12$ V.

The CVs for AuPt alloys appear as a linear combination of the CVs for both pure metals in good agreement with previous voltammetric studies of PtAu alloys reported in acidic and alkaline media (Chapters 4 and 5). During the reverse sweeps, fingerprints of both metals are observed around ca. -0.02 and +0.44 V for platinum and gold oxide reduction peaks, respectively. The peaks in the hydrogen region are related to hydrogen adsorption at Pt-surface sites of the alloy electrode.

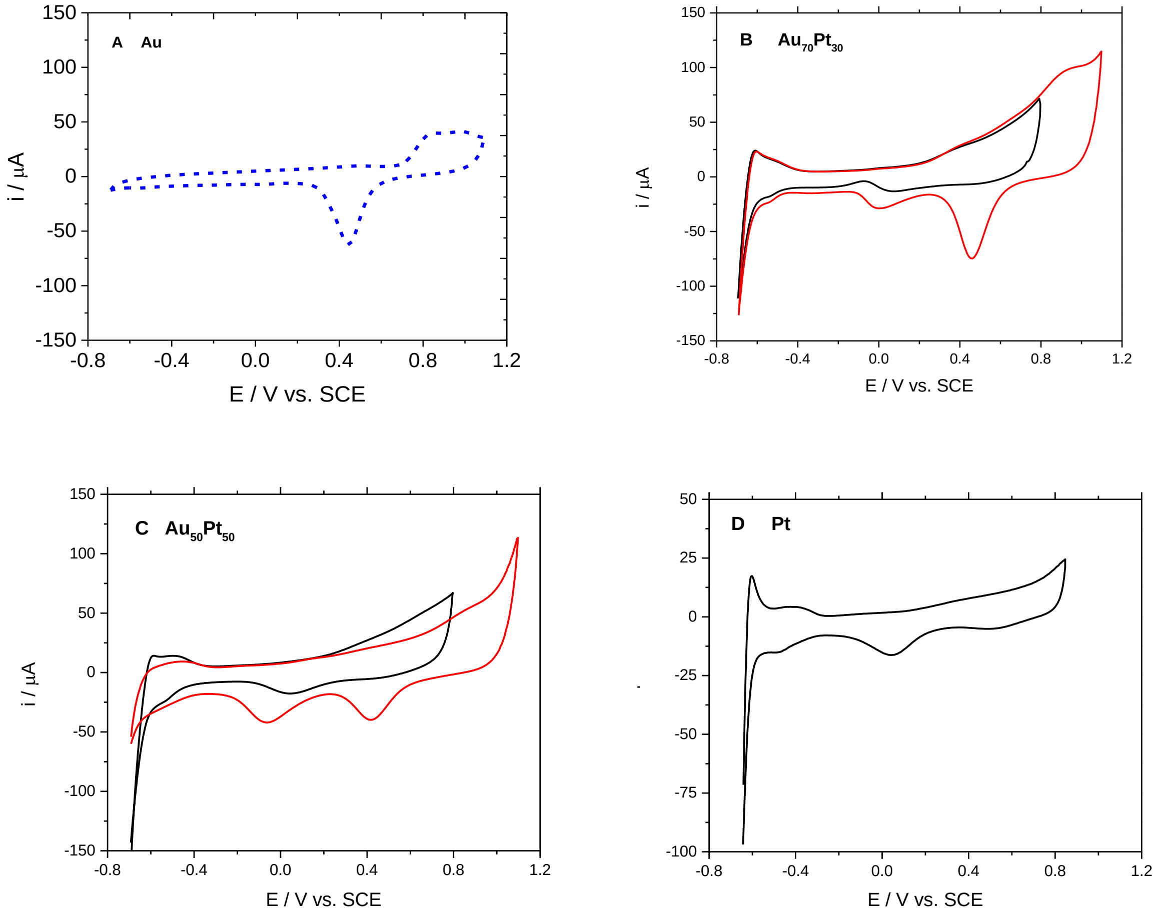

Fig. 6.10: CVs response of (a) Au, (b) $Au_{70}Pt_{30}$ (c) $Au_{50}Pt_{50}$ and (d) Pt NPs electrodes in 0.1 mol dm^{-3} PBS pH7, at 50 mV s^{-1} (10th Cycle)

The electrochemically active surface area of gold ($ECSA_{Au}$) was determined by integrating the charge associated with the Au oxide reduction peak and by using a factor of 400 µC cm^{-2} for the reduction of Au α-oxide film grown up to 1.15 V in PBS [29, 30]. The electrochemically active surface area of platinum ($ECSA_{Pt}$) was determined by integrating the charge associated with the Pt oxide reduction peak and by using a factor of 440 µC cm^{-2} for the reduction of Pt α-oxide film grown up to 0.85 V in PBS. The charge values are reported in Table 6.5. The surface Au composition could then be derived from equation 6.3:

$$[Au]_{surface} = ECSA_{Au} / (ECSA_{Pt} + ECSA_{Au}) \tag{6.3}$$

The surface composition of Au_{70} Pt_{30} is $Au_{74}Pt_{26}$ which is very close to the nominal composition of the as-prepared catalyst. However, the surface composition of $Au_{50}Pt_{50}$ is $Au_{62}Pt_{38}$. These values were quite different from those reported for acid and alkaline media. For example in acidic medium, $Au_{50}Pt_{50}$ becomes $Au_{57}Pt_{43}$ and $Au_{70}Pt_{30}$ becomes $Au_{84}Pt_{16}$; and in alkaline medium $Au_{50}Pt_{50}$ becomes $Au_{55}Pt_{45}$ and $Au_{70}Pt_{30}$ becomes $Au_{80}Pt_{20}$ as cited in chapters 4 and 5 of this thesis. This might be due to different rate of metal dissolution in these media.

The amount of surface atoms available for electrocatalytic oxidation of DA and AA can also be calculated from the integrated charges (Q) of the cathodic reduction peaks in PBS as follows [27]:

$$r_{Au_x Pt_{100-y}} = \frac{Q_{total}}{F} \tag{6.4}$$

where r is the mole of surface atoms, F is Faraday's constant and Q is equal to sum of the integrated charge involved in the reduction peaks of AuO and PtO of the Au_xPt_{100-x} alloy NPs. The number of surface atoms is determined by considering the Avogadro's number of $6.02*10^{23}$ atoms per mole, and the results obtained on Au, $Au_{70}Pt_{30}$, $Au_{50}Pt_{50}$ and Pt NPs in PBS are listed in Table 6.5. It is important to state that this procedure is useful to combine the effects of surface composition and particle size on the oxidation of the analytes (as will be discussed in section 6.5).

Table 6.5: Monolayer charges for platinum and gold oxide reduction and their corresponding surface atoms at Au_xPt_{100-x} NPs electrodes from PBS medium.

Catalysts	**QPtO /C**	**Pt surface atoms**	**QAuO /C**	**Au surface atoms**	**$Q_{PtO} + Q_{AuO}$ /C**	**Total surface Atoms**
Au s	-	-	$7.04*10^{-4}$	$4.39*10^{15}$	$7.04*10^{-4}$	$4.39*10^{15}$
$Au_{70}Pt_{30}$	$1.85*10^{-4}$	$1.15*10^{15}$	$5.25*10^{-4}$	$3.28*10^{15}$	$7.10*10^{15}$	$.4.43*10^{15}$
$Au_{50}Pt_{50}$	$2.25*10^{-4}$	$1.40*10^{15}$	$4.52*10^{-34}$	$2.82*10^{15}$	$6.77*10^{-34}$	$4.22*10^{15}$
Pt	$4.49*10^{-4}$	$2.80*10^{15}$	-	-	$4.49*10^{-4}$	$2.80*10^{15}$

It is interesting to remark that the number of surface atoms of Au NPs was almost 2 times larger than that estimated for pure Pt NPs electrodes in PBS. Also, the total surface metal atoms values obtained on the AuPt alloy NPs and Au NPs were higher than that of the Pt NPs. For example the total surface atoms were estimated to $4.39x10^{15}$, $4.43x10^{15}$, $4.22x10^{15}$ and $2.80x10^{15}$ for Au NPs, Au_{70} Pt_{30}, $Au_{50}Pt_{50}$ alloy NPs and Pt NPs respectively. Therefore, the total surface atoms increased with increased Au content in the AuPt NPs as illustrated in Fig. 6.11. This difference between the alloy and the pure monometallic Pt NPs suggests that surface catalyst utilization of the alloy NPs is higher than Pt NPs, as it will be show next, the number of surface metals atoms could also be influenced by the degree of catalyst utilization in PBS.

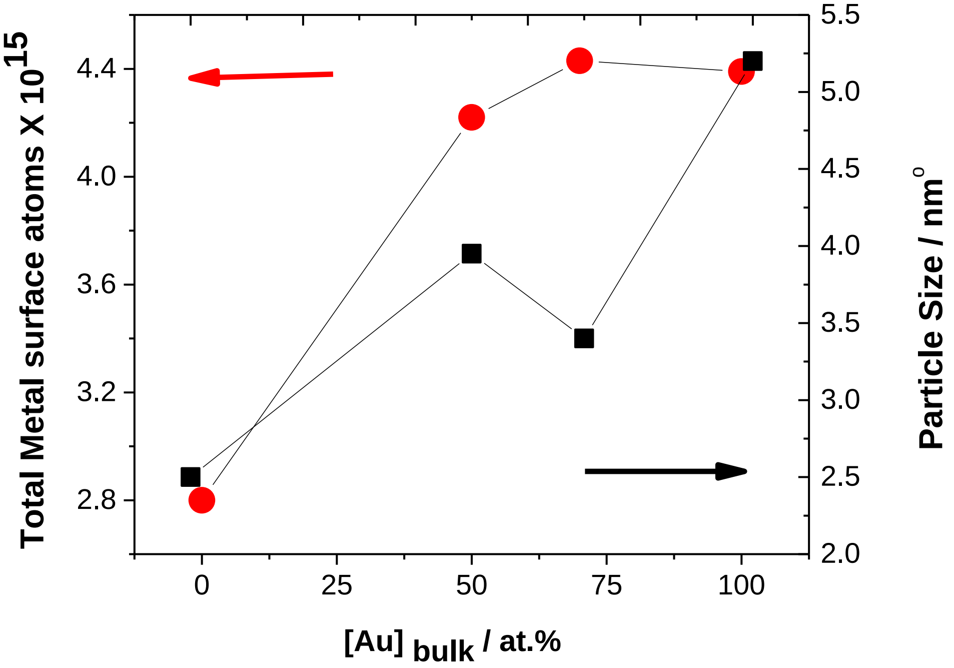

Fig. 6.11: The evolution of the total surface metal for Au_xPt_{100-x} NPs catalysts as a function of the atomic Au content in both PBS medium

It is generally known that the catalyst utilization efficiency is a critical parameter in determining the electrochemical activity of a catalyst. The better the dispersion of the catalysts' NPs on the electrodes, the higher is the utilization factor and hence more active are accessible. Therefore the catalyst utilization efficiency (%) in PBS was estimated using Eq. 6.5 [29]:

$$\vartheta = \frac{ECSA}{S} \times 100\% \tag{6.5}$$

where S is the specific surface area ($m^2\ g^{-1}$) of the corresponding NPs estimated using Eq. 6.6

The specific surface area of the Au_xPt_{100-x} NPs catalysts can be estimated from the density of the catalyst material and particle diameter estimated from the TEM analysis using the equation below [30]:

$$S_{Au_xPt_{100-y}} = \frac{6000}{d \times \rho_{Au_xPt_{100-x}}} \tag{6.6}$$

where $S_{AuxPt100-x}$ is the global specific surface area ($m^2\ g^{-1}$) of Au_xPt_{100-x} NPs, d the average particle diameter (nm) estimated from TEM analysis.

As a comparison and control, CVs of the NPs in 0.5 mol dm^{-3} H_2SO_4 were also recorded and analyzed because the catalyst loading used in this part of the work is almost the double of the one used in Chapters 3 to 5. The evolution of the utilization efficiency values (ϴ) for Au_xPt_{100-x} NPs catalysts as a function of the atomic Au content is presented in Fig. 6.12 for both PBS and sulphuric acid media.

It is important to note that the utilization efficiency for the Pt catalyst in the acid medium is far lower compared to the other catalysts. This low value found for the Pt catalyst utilization in sulphuric acid is consistent with the data on catalyst utilization with the loading presented in Chapter 3. The utilization efficiency increases with the increasing Au content, presenting maximum catalyst utilization efficiency at 50 % Au content in acid media. However, the utilization efficiency in the acidic medium is far greater (ca. 8 times) for Au and alloyed NPs than in the neutral medium. In fact, the utilization degree lies somewhere in the range of 5 – 20 % and 30 – 90 % for BPS and sulphuric acid media respectively. Elsewhere, it was reported that the degree of adsorption of phosphate species on Pt [31] and Au [27, 28] is much stronger than adsorption of sulphate species on those catalysts surfaces. Since the utilization efficiency of the catalyst is less than 50 %, it implies that the majority of the active sites are not available for catalysis in PBS medium compared to sulphuric acid medium. This is due to the strong adsorption of phosphate ions as compared to sulphate ions.

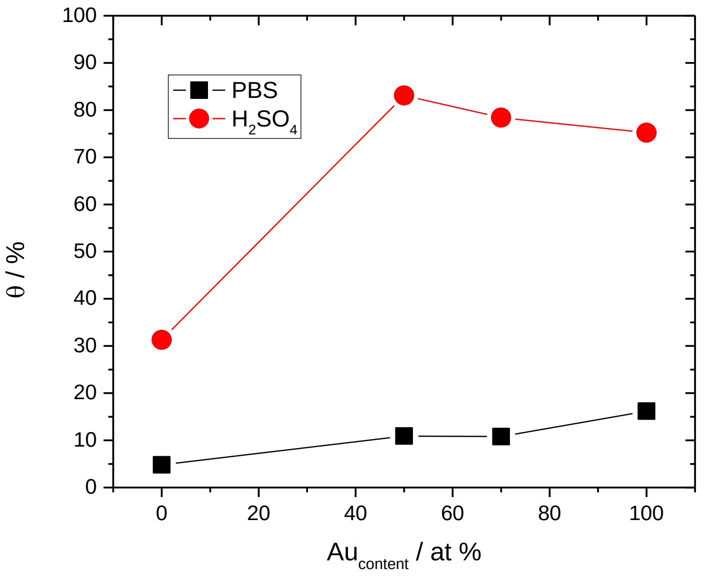

Fig. 6.12: The evolution of the catalyst utilization (ϴ) for Au_xPt_{100-x} NPs catalysts as a function of the atomic Au content in both PBS and sulphuric acid media.

6.5 Electrochemistry of DA and AA and their mechanistic study on Au_xPt_{100-x} NPs

Cyclic voltammetry was used to study the influence of the nanoparticle composition on the mechanisms of AA and DA electro-oxidation. Fig. 6.13 shows the typical cyclic voltammograms for the oxidation of 20 µM DA in PBS pH 7.0 at 50 mV s^{-1} at the Au, $Au_{70}Pt_{30}$, $Au_{50}Pt_{50}$ and Pt NPs electrodes. The CVs showed a pair of roughly symmetric anodic and cathodic peaks at ca. 155 mV and 100 mV, respectively, with almost equal peak heights (current) for Au and AuPt alloyed NPs as commonly observed for the quasi-reversible oxidation of DA [2-4]. Under identical conditions, ill-defined CV peaks can be observed at Pt NPs electrode around 0.2 V and 0.08 V for the forward and backward directions, respectively, with a much lower current response due to the poor catalysis of Pt NPs for DA oxidation [26, 32]. The separation between anodic and cathodic peak potentials, ΔE_P, at the Pt NPs and Au NPs electrode was found to be 115 and 70 mV, respectively, and 51 and 40 mV at $Au_{70}Pt_{30}$ and $Au_{50}Pt_{50}$ alloy NPs electrodes, respectively. The variation of ΔE_P with the Pt content suggests that alloying Au with Pt facilitates nevertheless the electron transfer step.

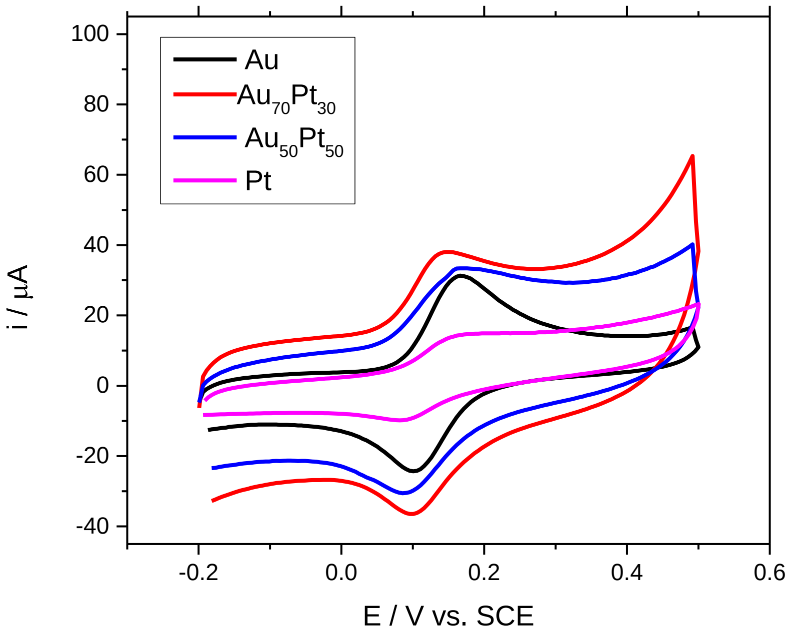

Fig.6.13: CVs of 20 µM DA at Au_xPt_{100-x} alloy NPs electrode and in pH 7.0 0.1 M PBS at a scan rate 50 mVs^{-1}.

The total peak current for the oxidation of DA at the $Au_{70}Pt_{30}$ alloy NPs and $Au_{50}Pt_{50}$ alloy NPs is about 22 % and 7 % larger than that at the Au NPs respectively. However, these response currents are made up of both the capacitive and faradaic current. Therefore, by subtracting the capacitive current from the total response current, a faradaic current of 27.6, 24.4, 23.8 and 12.9 µA was found for Au, $Au_{70}Pt_{30}$, $Au_{50}Pt_{50}$ and Pt NPs, respectively, indicating that the DA current decreases from Au NPs to Pt NPs. This clearly demonstrates that Au sites are the most active sites for DA electro-oxidation in the alloys.

It can also be noted that the variation of the capacitive current for the gold-based nanoparticles (Au < $Au_{50}Pt_{50}$ < $Au_{70}Pt_{30}$) is inversely proportional to their particle size (Au > $Au_{50}Pt_{50}$ > $Au_{70}Pt_{30}$) as expected. Pt does not follow this trend, probably due to the much lower catalyst utilization and/or adsorption of anions. Moreover, for the Pt containing catalysts, the after peak current also includes a contribution of the PtO formation. This was evidenced by overlapping the CVs recorded at 50 mV/s for DA oxidation and PBS alone.

Fig.6.14 shows the cyclic voltammograms recorded at different scan rates (from 200 mVs^{-1} to 20 mV s^{-1}) at (A) Au (B) $Au_{70}Pt_{30}$, (C) $Au_{50}Pt_{50}$ and (D) Pt NPs electrodes. As the scan rate increases, the anodic peak potentials shifts slightly positively and the cathodic peak shifts slightly towards negative potentials as shown in Figure 6.14. For example, the anodic peak shifts about 23 mV for Au NPs, 17 mV for $Au_{50}Pt_{50}$ and for $Au_{70}Pt_{30}$ and 20 mV for Pt NPs. The smaller shift from Au to $Au_{50}Pt_{50}$ and to $Au_{70}Pt_{30}$ reinforces the hypothesis that alloying Au with Pt facilitates the electron transfer step.

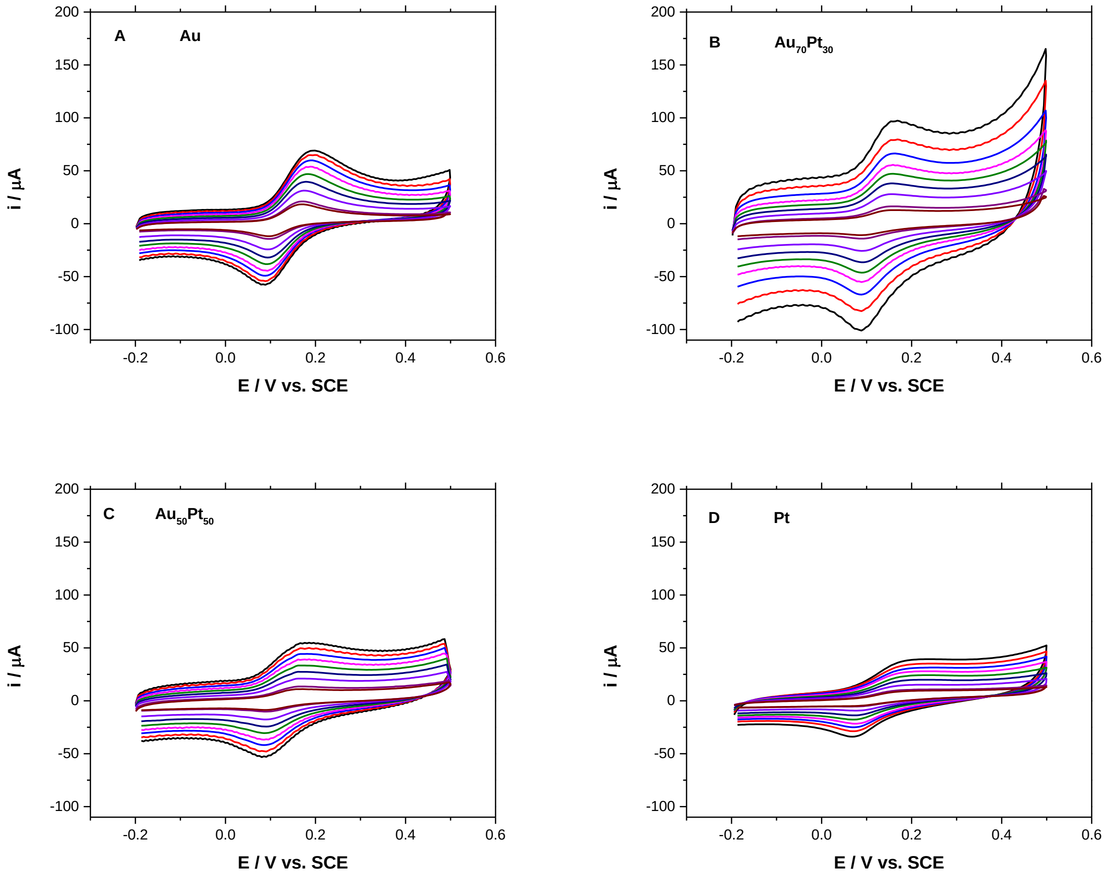

Fig.6.14: Cyclic voltammograms obtained for the oxidation of DA 20 µM in 0.1M PBS pH 7.2 at the (A) Au, (B) $Au_{70}Pt_{30}$, and (C) $Au_{50}Pt_{50}$ and (D) Pt NPs electrodes. Scan rate: 25, 50, 75, 100, 125, 150 and 175 and 200 mV s^{-1}.

The relationship between the potential and scan rate can be described through the following equations by Laviron assuming charge transfer rate determining step [33, 34]

$$Epa = Eo + \frac{2.3\,RT}{(1-\alpha_{c)}n_\alpha F}\log v \qquad (6.7)$$

$$Epa = Eo - \frac{2.3\,RT}{\alpha_c n_\alpha F}\log v \qquad (6.8)$$

where α is the electron transfer coefficient, n is the number of transfer electrons, R, T and F have their usual meanings, E_{pa} is the oxidation peak potential and E_{pc} is the reduction peak potential. Fig 6.15 showed the evolution of the peak potential with the logarithm of the scan rate. It is evident that the peak potential of the DA oxidation is almost independent of the scan rate..

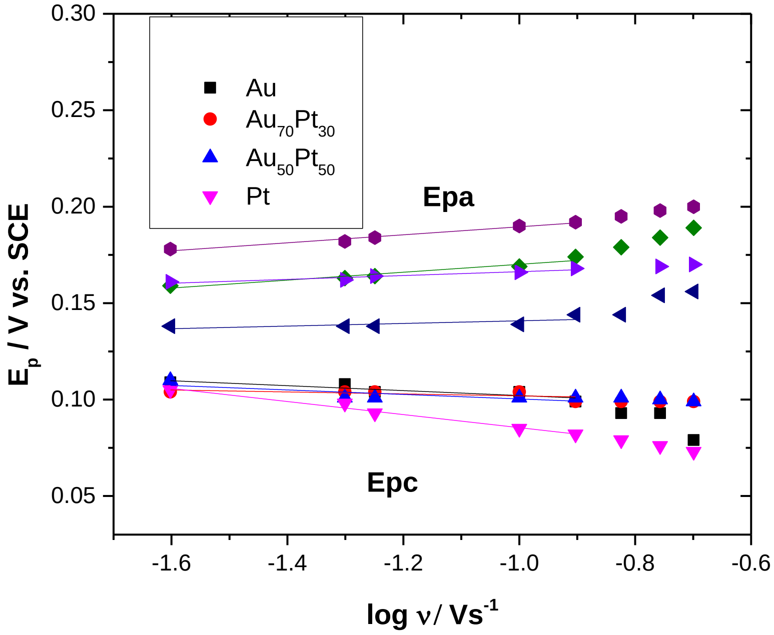

Fig. 6.15: Variation of E_{pa} and E_{pc} with log υ.

Fig. 6.16 presents the plot of the peak current of DA vs. scan rate. It is seen that the anodic and cathodic peak currents were proportional to the scan rate for all Au_xPt_{100-x} NPs, as expected from a surface adsorption controlled process [14, 35, 36]. This is consistent to reported results in the literature for selective determination of dopamine in the presence of high concentration of ascorbic acid using nano-Au self-assembly glassy carbon electrode [37].

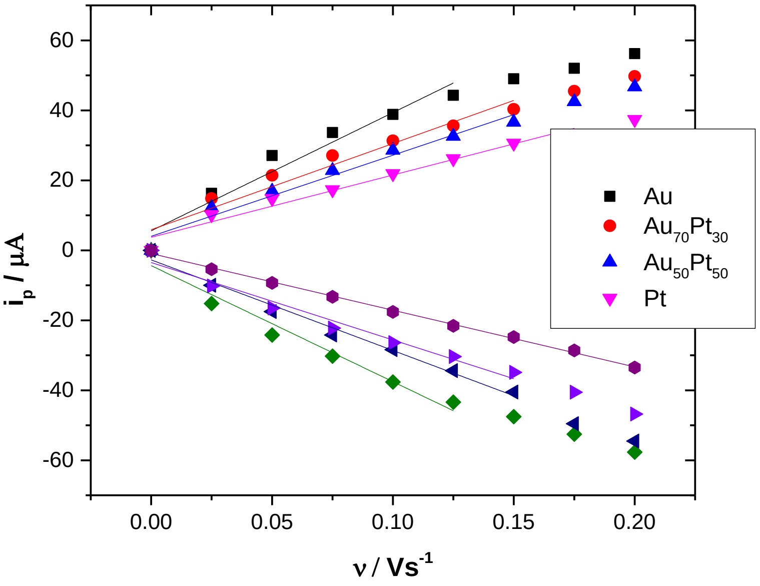

Fig 6.16: Dependence of DA oxidation with the scan rate in 20 µM DA in 0.1 M PBS/pH 7 at Au NPs**,** Pt NPs, $Au_{70}Pt_{30}$, and $Au_{50}Pt_{50}$ alloy NPs electrodes.

According to the model of surface controlled processes [35, 36], the dependence of the anodic peak current (I_{pa} µA) on the scan rate can been used for the estimation of the surface concentration of analyte molecules (mol cm^{-2}) on electrodes. According to this method, the peak current is related to the surface concentration of the electroactive species "r", by the following equation (Eq. (6.9):

$$I_p = n^2 F^2 \frac{rA\upsilon}{4RT} \qquad \text{Eq. (6.9)}$$

where *n* represents the number of electrons involved in the reaction, *A* represents the geometric surface area of the electrode (cm^2), *v* is the scan rate (V s^{-1}) and other symbols have their usual meanings [35].

Table 6.6: Comparison of anodic and cathodic slopes and their correlation coefficients for DA oxidation on Au_xPt_{100-x} NPs electrodes

Catalysts	**Anodic Slope / μA V^{-1} s**	**R^2**	**Cathodic Slope / μA V^{-1} s**	**R^2**
Au	337.9	0.9268	-331.7	0.9569
$Au_{70}Pt_{30}$	246.3	0.9273	-258.9	0.9826
$Au_{50}Pt_{50}$	231.9	0.9600	-221.4	0.9642
Pt	178.0	0.9654	-161.9	0.9974

Using the anodic slope of the line in the Fig. 6.15, the surface concentration of DA molecules was calculated as 4.50×10^{-10}, 3.28×10^{-10}, 3.05×10^{-10} and 2.40×10^{-10} mol cm^{-2} at Au NPs, $Au_{70}Pt_{30}$, $Au_{50}Pt_{50}$ NPs and Pt NPs electrodes respectively. These results were comparable with what is reported elsewhere for selective determination of dopamine in the presence of high concentration of ascorbic acid using nano-Au self-assembly glassy carbon electrode (1.15×10^{-10} mol cm^{-2}) [37] which was concluded to be a surface adsorption controlled process.

This emphasizes the role of the exposed metal surface sites responsible for the electrochemical oxidation of DA. We expressed the DA surface coverage as % adsorbed DA molecules, which is the ratio of the number of adsorbed DA molecules to the number of total metal (Au+Pt) surface metal atoms exposed (measured by CV in PBS in the absence of DA).

$$\theta = \frac{Number\ of\ adsorbed\ DA\ molecules}{Number\ of\ Au+Pt\ metal\ surface\ atoms\ exposed} \qquad \text{Eq. (6.10)}$$

Where θ is DA surface coverage

The variation of DA surface coverage as a function of Au at % content is shown in Fig. 6.17. Only 0.8 to 1.2 % of the surface of the NPs is covered by DA. It has been reported elsewhere that the adsorption of DA on metal NPs surfaces such as Au changes the NP morphology from isolated domains to aggregated domains [38]. They observed that the particle size of Au clusters increased due to adsorption of DA on the NPs surface. These aggregated Au NPs are generated due to dipole–dipole coupling between the plasmon of neighboring Au NPs. The aggregation behavior of metal NPs in the presence of DA molecules can be interpreted by the electric double layer (EDL) balance breaking and/or molecular bridging effects. The amine group binding to the surface of metal NPs via electrostatic interactions would break the electronic balance of the NPs. Thus, the stability of the NPs would be decreased and the resulting NPs tend to aggregate due to the disturbance of electric double layer (EDL). Thus, the weakened stability of the metal NPs due to these modifications on the catalyst surface may account for the low DA molecules coverage that we observed.

For the AuPt alloyed NPs there is V-shape dependence of surface coverage degree of DA molecules and the catalysts composition presenting a minimum value of 1.2 % at pure Au content confirming that Au sites are the most active element as discussed before.

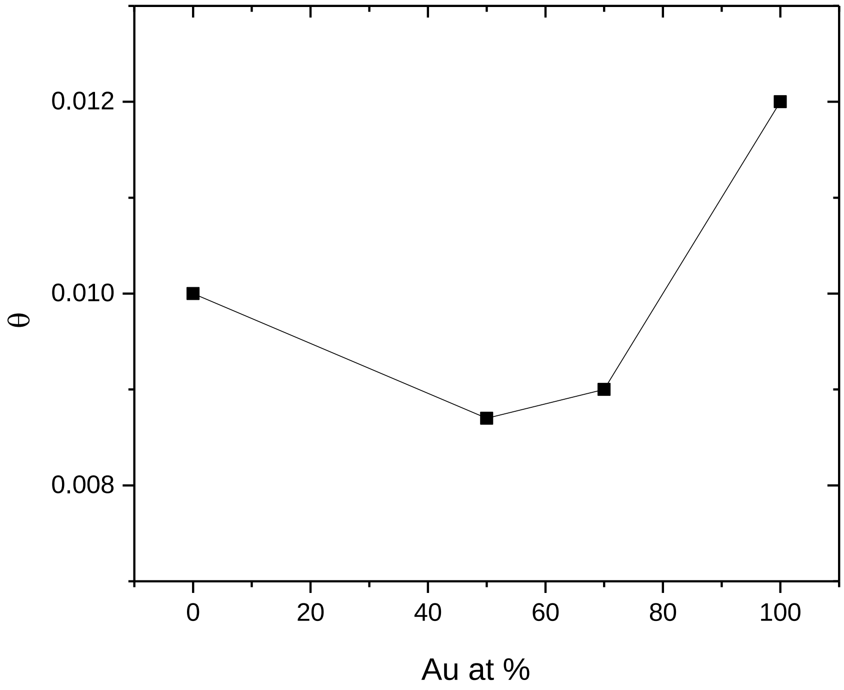

Fig 6.17: Dependence of DA molecules surface coverage as a function of Au content in thAu$_x$Pt$_{100-x}$ NPs

We will now focus on AA electro-oxidation. The cyclic voltammograms recorded in 2.0 mM AA in 0.1 M PBS at pH 7 at 50 mV s^{-1} on Au$_x$Pt$_{100-x}$ alloy NPs electrodes are shown in Fig. 6.18. An anodic peak attributed to the irreversible oxidation reaction of AA was always observed. The Au NPs showed a voltammetric peak at 0.03V, and the peak shifts of ca. -15 and -45 mV for

$Au_{70}Pt_{30}$ and $Au_{50}Pt_{50}$ alloy NPs, respectively. Moreover, the peak current of the alloyed NPs is 54.3 µA for $Au_{50}Pt_{50}$ and 115.1 µA on $Au_{70}Pt_{30}$ which are about two-times and four times higher than that of Au NPs (29.8µA) respectively. In addition, the variation of the peak current between NPs is independent of the degree of catalyst utilization (Figure 6.12) and does not follow either the total surface metal atoms (Table 6.5). Therefore, this negative shift in the oxidation peak potential and the substantial increase in the peak current indicate a favorable electronic effect of alloying Au with Pt on the electro-oxidation of AA. In other words, the catalytic activity of $Au_{70}Pt_{30}$ alloy NPs is enhanced greatly due to the synergic effect of Pt and Au in the alloyed nanoparticles. This contrasts with the Pt NPs where only a very weak current response can be seen at a more positive potential (ca. 0.40 V, i.e., in the PtO formation region) as expected from the poor catalysis of Pt towards AA oxidation [6, 7].

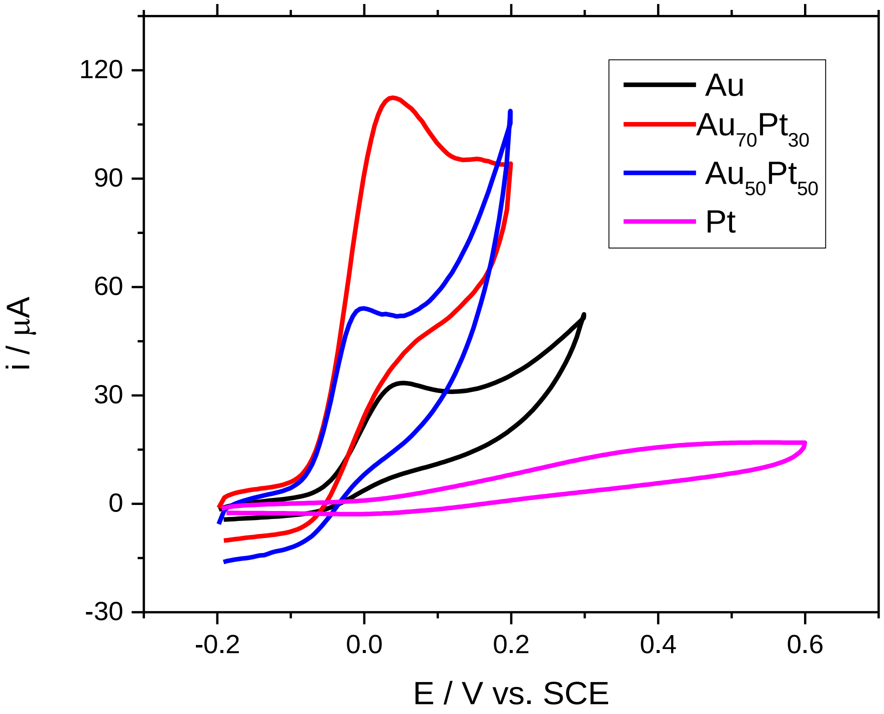

Fig.6.17: Cyclic voltammograms of 2.0 mM AA in 0.1 M PBS pH 7.0 at Au_xPt_{100-x} alloy NPs electrode at 50 mVs^{-1}.

The increment in peak current for AA on $Au_{70}Pt_{30}$ NPs and $Au_{50}Pt_{50}$ NPs compared to Au NPs is in contrast to DA in which the faradaic peak current decreases with increasing Pt content in alloy NPs. As discussed in Chapter 1 (section 1.2.2) the two reactions do not follow the same mechanism therefore their catalytic activity towards the two analytes are different.

To understand the influence of the NPs composition on the electro-chemical oxidation of AA, the effect of the scan rate on the peak current and peak potential was analyzed. Fig. 6.18 shows the cyclic voltammograms obtained for the oxidation of 2.0 mM AA at the Au_xPt_{100-x} NPs electrodes at different scan rates. The shape of the voltammograms is similar in all cases with the exception of Pt NPs where the anodic peak is not completed at high scan rate. The current increases and the peak potential shifts positively with increasing scan rate as expected for an irreversible process. However, and in spite of the very small current on Pt NPs compared to Au NPs, the presence of the cathodic peak suggests a small degree of reversibility in the case of Pt NPs. The oxidation of ascorbic acid in aqueous media is an electrochemical – chemical (EC) process [6 -10]. In an EC process the cathodic peak of the redox step is usually observed at very high sweep rates only. This is due to the totally two-electron transfer that is followed by a chemical hydration process as reported in literature [7] and cited in chapter one (section 1.1.2.2). Therefore, a contribution of the PtO reduction during the cathodic sweep cannot be excluded (c.f. Figure 6.18 and [41]). On the other hand, the CVs of alloyed NPs, especially those of $Au_{50}Pt_{50}$, show evidence of a cathodic wave below 0 V at high scan rates suggesting that AA electro-oxidation on alloyed NPs is less irreversible than on pure Au NPs. Here, we can propose a truly electronic effect for the first time due to the synergetic effect of Au NPs and Pt NPs.

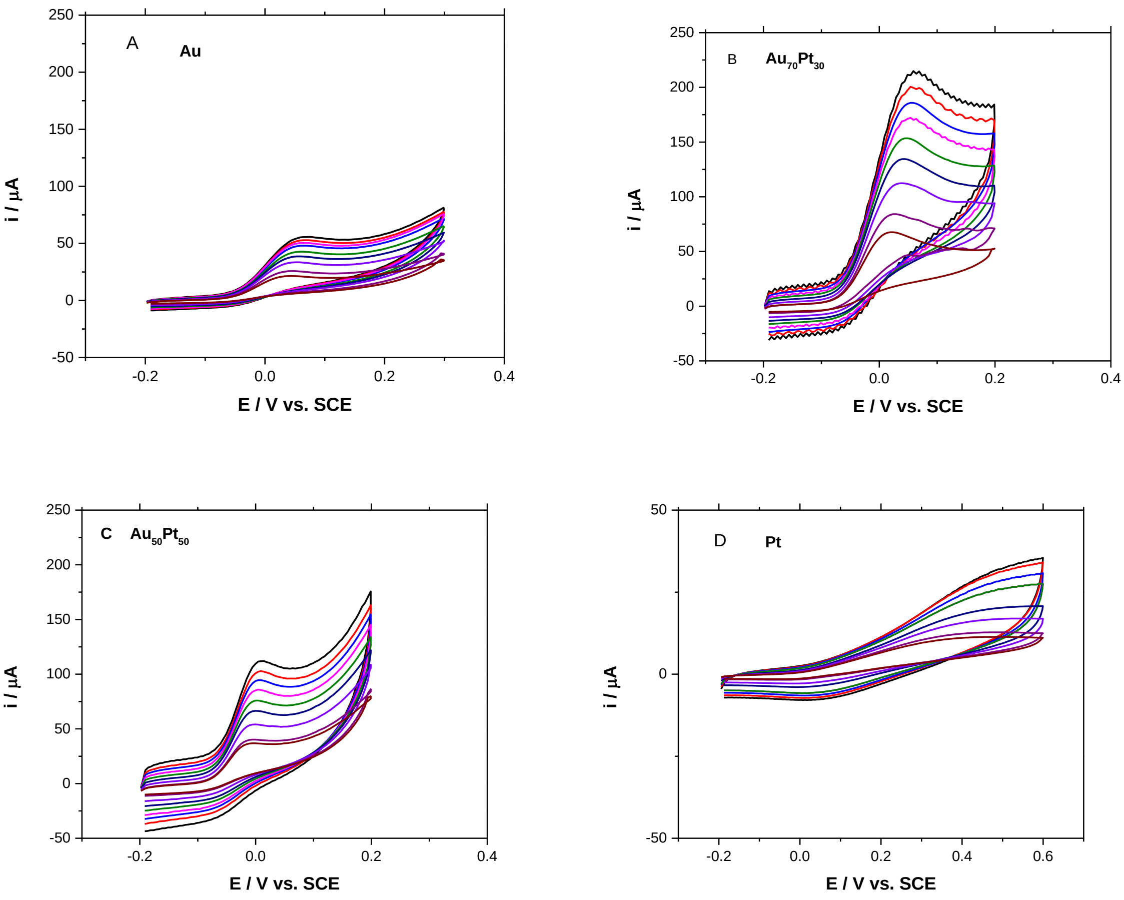

Fig. 6.19: Cyclic voltammograms obtained for the oxidation of AA (2.0 mM) at the (A) Au**,** (B) Au$_{70}$Pt$_{30}$, (C) Au$_{50}$Pt$_{50}$ and (D) Pt NPs electrodes in 0.1M PBS (pH 7.2). Scan rate: 25, 50, 75, 100, 125, 150 and 175 and 200 mV s^{-1}.

Fig. 6.20A shows the variation of the anodic peak current of AA with the square root of the scan rate. The anodic peak current increases linearly with the square root of scan rate for all the Au$_x$Pt$_{100-x}$ NPs indicating that the electrode reaction of AA was a diffusion-controlled process. This result is consistent with AA oxidation reported elsewhere on Au NPs modified electrode [8-9]. In elsewhere, AA oxidation was reported for its typical diffusion-controlled process on Au NPs modified electrode [9], showing the same mechanism of AA oxidization on both the Au NPs modified and the gold nanofilm electrode.

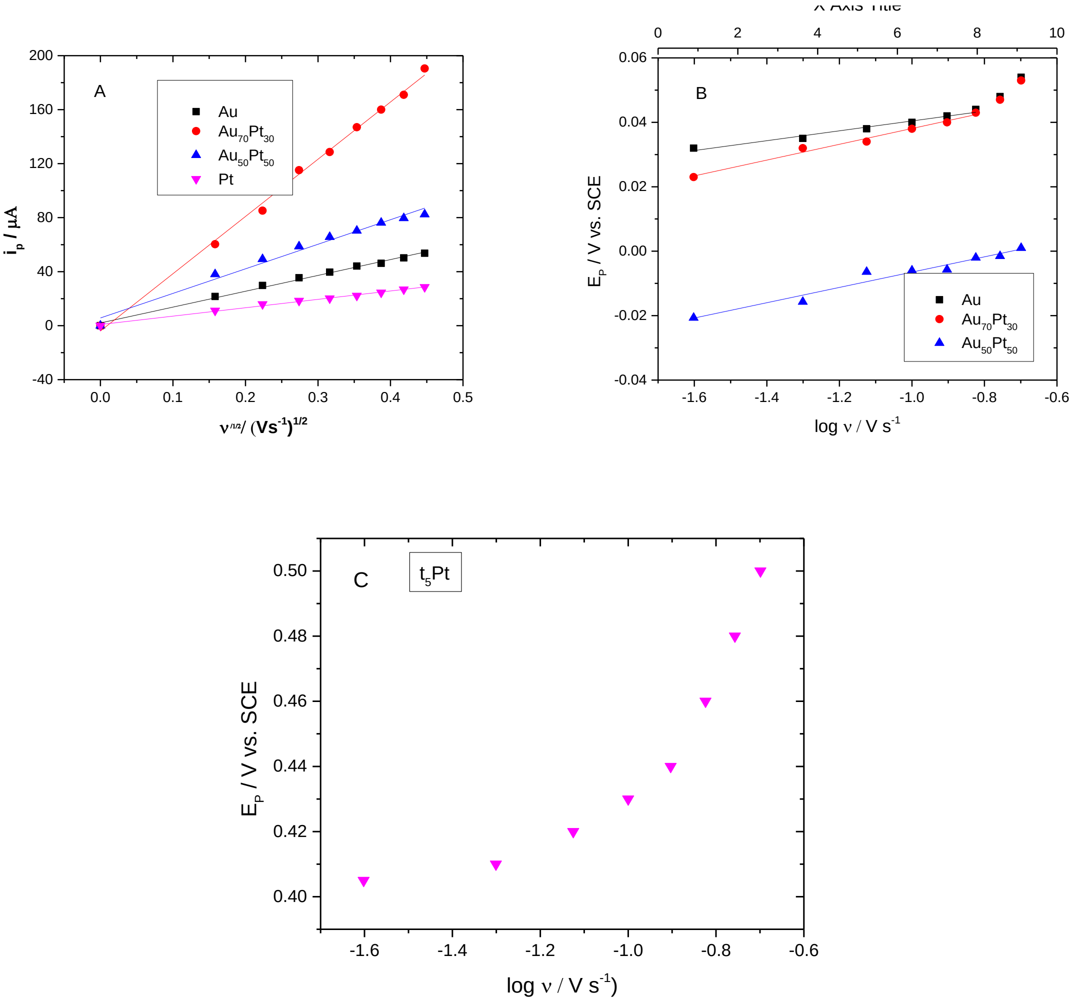

Fig 6.20: (A) The dependence of AA oxidation with square root of scan rate and (B) Ep vs. log υ and (C) Ep vs. log υ of Pt

For a diffusion-controlled process involving an irreversible charge transfer mechanism, the dependence of the anodic peak current on the square root of the scan rate is given by equation 6.11 [9]:

$$i_p = 2.99\times10^5 n^{3/2}(n_a\alpha)AC_O D^{1/2}\upsilon^{1/2} \qquad (6.11)$$

α is the transfer coefficient and n_a is the number of electrons involved in the charge-transfer step and n is the total number of electrons involved in the oxidation process. i_p is proportional to the bulk concentration of the specie being oxidized, but its intensity will vary depending upon the value of α. It is interesting to note, however, that the slopes of the I_p vs $v^{1/2}$ plots vary with the catalyst composition as shown in Figure 6.20A. As seen in Table 6.7 the slopes were ca. four and two times higher on the $Au_{70}Pt_{30}$ and $Au_{50}Pt_{50}$ alloyed nanoparticles, respectively, compared to Au NPs. Pt NPs showed the lowest slope value. The variation of the slope values indicates that the electrochemical active area of the catalysts and / or the mechanism for the AA oxidation changes with the catalyst composition.

Table 6.7: Comparison of slopes and correlation coefficients for AA oxidation on Au_xPt_{100-x} NPs

Catalysts	**Slope / µA /$(Vs^{-1})^{1/2}$**	**R^2**
Au	117.35	0.9935
$Au_{70}Pt_{30}$	424.03	0.9962
$Au_{50}Pt_{50}$	181.97	0.9797
Pt	62.15	0.9941

Fig. 6.20B shows the evolution of the anodic peak potential of AA with the logarithm of the scan rate. The anodic peak potential increases almost linearly with the logarithm of scan rate for all the Au_xPt_{100-x} NPs suggesting a charge transfer process limited by the kinetic of the reaction between AuPt NPs and ascorbic acid.

By determining the Tafel slope ‘b’ we can get the information about the rate determining step. For an irreversible diffusion controlled reaction [8], b was obtained by the Eq. (6.12)

$$Ep = K + \frac{2.3\,RT}{2\alpha_c n_\alpha F}\log v \qquad (6.12)$$

From the Eq. (6.12), the plot of Ep vs. log v gives a slope of $2.3RT/2\alpha_c n_a$F, where $2.3RT/\alpha_c n_a F$, is Tafel slope [8]. We have determined the Tafel slope of 30, 50, 48 and 98 mV for the oxidation of AA at Au, $Au_{70}Pt_{30}$, $Au_{50}Pt_{50}$ and Pt NPs electrodes, suggesting that the rate determining step in the electron transfer process is different at each type of NPs electrodes (Au vs alloyed NPs vs Pt). Elsewhere, a Tafel slope of 39 mV per decade was found for the oxidation of AA on a Au sphere electrode [10].

The overall electro-oxidation of AA at Pt [6,7] and Au [8 - 10] in solution has already been detailed in Chapter 1 of this thesis. A notable fact in this process is that the electron-transfer kinetics at a platinum electrode [6, 7] is sluggish compared with that on gold electrode [8, 10], which results in a considerable overpotential for AA oxidation at Pt [6, 7].

Two combined electrochemical and spectroscopic studies on the electro-oxidation of AA on Pt polycrystalline and single crystal electrodes in acid medium by Xing et al [7] and Climent et al [39] have demonstrated that AA undergoes a spontaneous dissociative adsorption at the Pt electrode prior to its oxidation. This dissociative adsorption probably takes place via an interaction between the side-chain of the AA molecule and the Pt surface, with CO as the adsorbate [7]. The existence of other strongly adsorbed species which are oxidized in the Pt oxide region was also demonstrated [39]. Catalytic effects on AA electro-oxidation through Bi adlayers formed on Pt were also reported [39]. It was suggested that the formation of irreversible adsorbed species was suppressed on Bi-Pt surfaces and the AA electro-oxidation become a structure-insensitive process. This effect was attributed to the suppression of the dissociative adsorption pathway.

The oxidation of AA on gold electrodes is a structure-insensitive process and does not produce adsorbed CO [10].

However, it was recently reported that adsorbed CO on Au acts as a promoter for dehydrogenation of organic molecules shifting the potential to more negative values [40]. Since CO is generated and adsorbed at the Pt surrounding atoms during AA oxidation, we propose that the adsorbed CO acts as a promoter and shifts the potential of the AA reaction to more negative value in the case of the alloyed AuPt NPs as shown in Fig. 6.19 and Fig 6.20B, where the peak potential occurs at lower values for PtAu alloy NPs. Enhancement of the AA electro-oxidation due to the presence of functional groups was also observed at glassy carbon electrodes [41]. On the unactivated electrodes the first electron transfer (ascorbate anion to radical anion $AA^{\bullet -}$on glassy carbon electrodes) is the rate determining step. An enhancement of the rate of the first electron transfer was found on thermally activated electrodes (heat treated, more acidic surface) and the second electron transfer (oxidation of the radical anion) become the rate determining step [41, 42]. The authors interpreted the change in the rate determining step in terms of unblocking of the surface with the activation of the electrode through the thermal treatment. In other words, the hydrophobic nature of the unactivated glassy carbon electrode would be responsible for slow kinetic of AA electro-oxidation [41].

Thus, alloying Au with Pt enhances the rate of the electrochemical oxidation of AA. Among the various possible factors that might contribute individually or simultaneously to this enhancement of the electron transfer, we can nominate: 1) higher active surface area or additional redox sites as manifested by the larger slope of the ip vs $v^{1/2}$ plots and 2) variation of the reaction mechanism as indicated by the Tafel slope values extracted from the Ep vs log v plots. These conclusions are also in agreement with our previous work on formic acid oxidation on PtAu alloyed NPs as cited in chapter 4, where we concluded that the mechanism of oxidation of formic acid on PtAu NPs is modified after electrochemical aging in acidic medium, favoring the dehydrogenation pathway.

As demonstrated above, the excellent catalytic activity of the AuPt NPs toward AA remarkably facilitates the electron transfer of AA (Fig. 6.5) at a potential more negative than that for DA (Fig. 6.4). Such an intrinsic property of AuPt NPs substantially differentiates the oxidation processes of AA and DA. Such demonstrations, coupled with the improved reversibility of the redox process of DA at the AuPt NPs (section 6.5) make it possible to sensitively and selectively determine DA without the interference of AA.

6.6 Conclusion

The AuPt alloy NPs electrodes show enhanced response towards the electrocatalytic detection of AA but not DA in terms of faradaic peak current for the entire compositions investigated. The following main conclusions were derived:

1. Alloying Au with Pt does not improve the faradaic current towards the electro-oxidation of DA.
2. However, alloying Au with Pt improved the electrocatalysis of AA oxidation with a negative shift in the oxidation potential and an increase of the Faradaic current. We believe that synergetic effect was the main cause for the enhancement of AA oxidation on AuPt alloy NPs.

References

1. D.P. Quan, D. P. Tuyena, T. D. Lamb, P. T. N. Trama, N. H. Binhb, P. H. Viet, Colloids and Surfaces B: Biointerfaces 88 (2011) 764– 770
2. J. Breczko, M. E. Plonska-Brzezinska, L. Echegoyen, Electrochimica Acta 72 (2012) 61– 67
3. N. F. Atta∗, A. Galal, E. H. El-Ads, Electrochimica Acta 69 (2012) 102– 111
4. M. Hosseini, M. M. Momeni, M. Faraji, J. Appl. Electrochem., 2010, 40, 1421–1427
5. C. R. Raj, T. Ohsaka, Bioelectrochemistry 53 (2001), 183–191
6. M. Brezina, J. Koryta, T. Loucka, D. Marsfkova, J. Electroanal. Chem., 40 (1972) 13 – 17
7. X. Xing, I. T. Bae, M. Shao, C. C. Liu, J. Electroanal. Chem., 346 (1993) 309 – 321
8. A. Sivanesan, P. Kannan, S. Abraham John, Electrochimica Acta 52 (2007) 8118–8124
9. C.R. Raj, T. Okajima, T. Ohsaka, J. Electroanal. Chem. 543 (2003) 127_ 133
10. M. Reuda, A. Alda, f. Sanchex-Burgos, Electroch1mica Acta, 29 (1978), 419-424
11. T. Selvaraju, R. Ramaraj, J. Electroanal. Chem. 585 (2005), 290=300
12. Y. Lin, Y. Hu, Y. Long, J, Di, Microchim Acta (2011) 175:259–264
13. Y.C. Bai, W. D. Zhang, Electroanalysis 2010, 22, No. 2, 237 – 243
14. L. Zhang, X. Jiang, J. Electroanal. Chem. 583 (2005) 292 -299
15. H. J. Qiu, G. P. Zhou, G. L. Ji, Y. Zhang, X. R. Huang, Y. Ding, Colloids and Surfaces B: Biointerfaces 69 (2009) 105–108
16. A. I. Gopalan, K. P. Lee, K. M. Manesha, P. Santhosh, J. H. Kim, J. S. Kang, ,Talanta 71 (2007) 1774–1781
17. A. Stoyanova, S. Ivanova, V. Tsakovaa, A. Bund, Electrochimica Acta 56 (2011) 3693–3699
18. S. Senthil Kumar, J. Mathiyarasu, K. Lakshminarasimha Phani, J. Electroanal. Chem 578 (2005) 95–103
19. M. Ahn, J. Kim, J. Electroanal. Chem. 683 (2012) 75–79
20. S. Thiagarajan, S.M. Chen, Talanta 74 (2007) 212–222
21. A. Galal, N. F. Atta, E. H. El-Ads, Talanta 93 (2012) 264– 273
22. M. Zhang, K. Gong, H. Zhang, L. Mao, Biosensors and Bioelectronics 20 (2005) 1270–1276

23. B.J. Plowman, M. Mahajan, A. P. O'Mullane, S. K. Bhargava, Electrochimica Acta *55* (2010) 8953–8959
24. T. Liu, M. Li, Q. Li, Talanta 63 (2004) 1053–1059
25. J. B. Raoof, A. Kiani, R. Ojani, R. Valiollahi, S. Rashid-Nadimi, J Solid State Electrochem (2010) 14:1171–1176
26. T. Selvaraju, R. Ramaraj, J. Electroanal. Chem. 2005, 585, 290-300
27. G. Hager, A.G. Brolo, J. Electroanal. Chem. 550 - 551 (2003) 291 - 301
28. A. M. Oliveira Brett, F. Matysik, M. Teresa Vieir, Electrocaatalysis, 9 (1999) 209-212
29. C.T. Hsieh, J.-Y. Lin, J.L. Wei, Int. J. Hydrogen Energy 34 (2009) 685–693
30. A. Pozio, M.D. Francesco, A. Cemmi, F. Cardellini, L. Giorgi, J. Power Sources 105 (2002) 13–19
31. S. Ye, H. Kita, J. Electroanal. Chem, 333 (1992) 299 – 312
32. S. Chumillas, M. C. Figueiredo, V.l Climent*, J. M. Feliu, Electrochimica Acta 109 (2013) 577– 586
33. E. Laviron, J. Electroanal. Chem. 101 (1979) 19–28.
34. Q. Huang, H. Zhang, S. Hua,b,n, F. Li, W. Weng, J. Chen, Q. Wang a, Y. He, W. Zhang , X. Bao, BiosensorsandBioelectronics52(2014)277–280
35. A. J. Bard and L. R. Faulkner, *Electrochemical methods: Fundamentals and Applications*, John Wiley, New York, 2001
36. P. Cappella, B. Ghasemzadeh, K. Mithchell, R.N. Adams, Electroanalysis 2 (1990) 175–182.
37. G. Z. Hu, D. P. Zhang, W. L. Wu, Z. S. Yang, Colloids and Surfaces B: Biointerfaces 62 (2008) 199–205
38. Y. Bu, S. Lee, ACS Appl. Mater. Interfaces 2012, 4, 3923−3931
39. M. A. Climent, A. Rodes, M. J. Valls, J. M. Perez, J. M. Feliu, A. Aldaz, J. CHEM. SOC. FARADAY TRANS., 1994, 90(4), 609-615
40. P. Rodriguez, Y. Kwon, M. T. M. Koper, Natue Chemistry, 4 (2012), 177 – 182
41. M.R. Deakin et al, Anal. Chem, 58 1986, 1474-1480
42. Stutts, Kenneth J. et al Anal. Chem, 55 1983, 1632-1634,

CHAPTER SEVEN

Perspectives and Future Work of this Thesis

In summary, we demonstrated and provided recent advances on how research on PtAu NPs has become exciting in the aspects of controllable synthesis, fuel cells and electro-analytical biosensing applications. These research contributions include the use of PtAu alloy NPs with varying composition as efficient electrocatalysts for fuel cells (formic acid and methanol oxidation) and for electrochemical biosensors (ascorbic acid and dopamine) applications.

Prior to electrooxidation of the small organic molecules on these catalysts, the PtAu NPs were electrochemically cycled in supporting electrolytes at the pH of investigation and the effect of alloying Au with Pt on the surface atoms and peak positions of the metal oxides reduction were correlated with the bulk composition. The surface composition of the PtAu alloy NPs were very close to the bulk composition in neutral and alkaline media but deviate slightly in acidic medium. The peak position of the Pt-oxide reduction shifted negatively with pH and with increasing Au content in all media (Figure 7.1A). However the change in the Pt-oxide peak position was more marked in the alkaline medium suggesting stronger OH adsorption on PtAu NPs in alkaline medium than the other media. The peak position of the Au-oxide reduction remains constant in all media (Fig. 7.1B). These trends reinforce the hypothesis that an electronic effect in operation during the electro-oxidation of small organic molecules, especially in neutral – alkaline solution. The advantages of pulsed laser ablation in liquid over other convention methods as a simple method for synthesizing these alloyed NPs is the formation of a stable colloid alloy solution resulting in electronic effect which is evident in the potential shift of the Pt-oxide reduction peak in the various media.

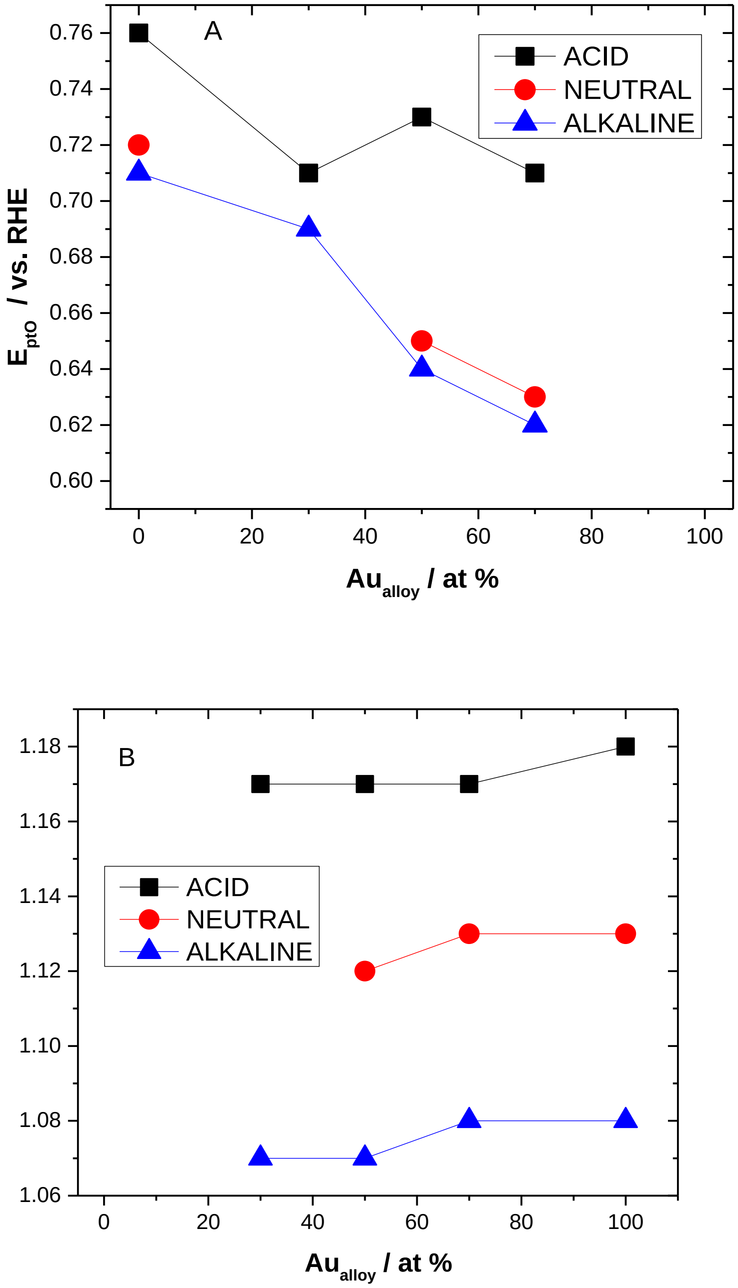

Fig. 7.1: Effect of alloying on peak positions of the metal oxide reduction of PtAu nanoparticles in acidic, alkaline and neutral environments.

Considering the goal of the kind of oxidized products produced during electro-oxidation reactions of these small organic molecules on PtAu NPs, the better understanding of oxidation reaction mechanisms may provide new ways and opportunities. Many researchers have shown that establishing the reaction mechanism is one critical unsolved question. Although spectroscopic findings on the kind of the reaction intermediates and product are available, this is certainly not enough to establish a reaction mechanism. At present, it is well known that small organic molecules oxidation undergo multistep pathways generating various insoluble and soluble species. The principal pathway involves several dehydrogenation steps via CO adsorption producing CO_2 as the final product. During these oxidation reactions, adsorbed CO [1] and hydrogenated species [2] were depicted spectroscopically as strongly bonded to the surface. On the other hand, the soluble intermediates such as formaldehyde and formate anions can either be converted to the final product or diffuse away from the electrode surface.

In this thesis, we showed that the oxidation mechanisms of small organic molecules involve generation of many oxidized products on the catalysts' surface. However, quantifying the details of these oxidized products at the level of charge and rate constants requires further theoretical and experimental work. On the theoretical side, there is no adequate theory for modelling of multistep oxidation of small organic molecules products mechanisms. Experimental studies using the rotating disk electrode, rotating ring-disk electrode and electrochemical mass spectrometry measurements could be used to quantify the mass transport parameters, the amount of charge and help to clarify the importance of the production of soluble species from a parallel path. Besides, the determination of these species requires the use of very sensitive analytical techniques. For example fluorometric techniques [3], online electrochemical mass spectrometry (DEMS) [4, 5] and liquid chromatography [6], electrochemical IRRAS facility in Montreal could be employed for identifying the oxidized products in solution during the small organic molecules oxidation. It is very challenging to find a specific efficient approach for the quantification of these various oxidized species in solution simultaneously (e.g. HCOOH and HCHO). For example, as reported elsewhere [3] infrared spectroscopy failed to measure HCHO (one of the possible species of methanol oxidation) due to the difficulty of seeing infrared active bands of the hydrated species such as $CH_2(OH))_2$ (coming from HCHO in solution). Although HCOOH was identified in the infrared spectra, very weak bands were observed which was not good for quantitative analysis. Therefore, we proposed that using High performance liquid

Chromatography (HPLC) for the quantification of these soluble species since this technique has the capacity to measure the charge balance of CO_2 which happens to be the final product of these species in solution as proposed in literature [7].

The requirement of highly active metal catalysts for fuel cell applications has attracted many interests in developing monodispersed, single component, small-size NPs of Pt and Au, as well as bimetallic PtAu alloy NPs [8]. However, the improvement for fuel cell performance provided by the majority of metal NPs and their alloy-based catalysts is limited to either activity or to stability, not to both at the same time. Pt-group metals have been extensively studied as an effective catalyst for oxidation of small organic fuels such as formic acid and methanol. However, the principal challenge is the poisoning by CO-like intermediate species during the electro-oxidation process. This is the main cause of the low activity in fuel cells. PtAu NPs catalysts possess the capacity to solve this poisoning effect on platinum electrodes. Despite this exciting progress in the fuel cell catalysis, the unsupported PtAu NPs suffers problem of stability towards the oxidation of these organic molecules upon potential cycling. A major concern with electrocatalysis of small organic molecules for fuel cell application is the long-term stability. Due to the harsh environment in fuel cells, only a few materials can withstand these conditions over the time period needed. Carbon supported metal alloys nanoparticles such as graphene [9], carbon black [10,11] as catalyst supports, covered with metal nanoparticles, have shown promising results concerning the long-term stability; therefore, the development of graphene or carbon black supported PtAu alloy NPs should also enhance the electrocatalytic activity. Besides, macroporous carbon supports could be used to eliminate the fierce aggregation of the PtAu colloid NPs over time. Also, fundamental study of the electrode processes under practical fuel cell operating conditions would give firsthand information about performance in real fuel cells and aid in the design of potential catalyst compositions. Also, the prepared unsupported binary PtAu NPs catalysts which were carbon monoxide tolerant can be tested in the fuel cell stack to determine its long term capability. The long term operation tests are important to determine the life time of the catalysts.

Electrochemical biosensors are powerful devices for detecting important substances, such as dopamine and ascorbic acid, which are two biological components that co-exist in the extracellular fluids of mammals [12-15]. The application of a novel Au-based NPs electrodes for the determination of catalytic properties of ascorbic acid and dopamine oxidation have been demonstrated in chapter 6. Additional investigations are required to fully characterize and understand the mechanism involved in the catalytic process, focusing particularly on the catalytic oxidation of Ascorbic acid where most of the results reported were interesting, for instance, the synergetic effect shown by the alloyed NPs. These significant catalytic properties of these AuPt alloyed electrodes were also demonstrated experimentally for formic acid oxidation and methanol oxidation in chapters 4 and 5 respectively. Besides, further characterizations adopting other analytical techniques would furnish precious information on the electrochemical and physical characteristics of the nanomaterials towards the small molecule oxidation under study. In fact, reviewing the electrochemical and spectroscopic differences between the oxidized products and the other forms of intermediates produced during the electro-oxidation process could explain why the electrocatalytic activity in terms of faradaic current of AA was higher for $Au_{70}Pt_{30}$ alloy NPs than Au NPs and the other alloyed NPs. Resonant Raman spectroelectrochemical (RRS) analysis have been already carried out for in situ studies of electrocatalytic reactions at conducting polymer modified electrode by Malinauskas *et al.* resulting in extremely useful information to elucidate the mechanism of the catalytic oxidation of hydroquinone and ascorbic acid [16, 17]. The application of this powerful technique could be useful to study the impact of the nanoparticle size on the observed catalytic phenomenon with particular look at the molecular interaction of DA with the Au-based electrodes interface. Another technique useful to gain structural information is the FT-IR spectroscopy which was already exploited to investigate AA oxidation on Pt metal catalysts [18, 19].

Next to the full characterization of the AuPt nanomaterial illustrated in the chapter 6, further developments could concern the investigation of catalytic properties towards other analytically important molecules. For example, electrochemical biosensing devices could be fabricated for the analysis of uric acid, urea hydroquinone, glucose, ephedrine, serotonin, etc. as these have been found to be good analytes to be detected with Au based electrodes.

A combination of the AuPt NPs with conducting polymers such as PANI, PEDOT, etc could also open up the possibility of developing biosensing devices for a wider range of analytical applications. The introduction of negatively charge polymers such as PEDOT to Au-rich alloy NPs could improve the anti-fouling effect of AA oxidation [20]. Also, it is interesting to note that while the negative conducting polymers combined with Au electrodes are useful for selective detection of DA in the presence of AA with improve activity, positive charged conducting polymers such as PANI would be a good biosensor when combine with $Au_{70}Pt_{30}$ NPs for selective detection AA.

A further strategy to enhance the performance of this electrochemical biosensor could be the use of PtAu NPs with enzymes immobilized on the surface to develop real electrochemical biosensors. This could be interesting for real sample analysis due to the selective and specific nature of enzymes towards catalysis of biological molecules. The PtAu metal NPs will not only act as platform for the immobilization of the enzymes but it also ensuring direct electron transfer between the electrode and the biomolecule. Methodologies investigated in the formation of PtAu-enzyme-conjugates and their possible application to bi-enzyme-based biosensors will be transferred to the immunosensor platform based on avidin-biotin interaction. These PtAu-enzyme biosensors have the potential to be applied in real samples such human blood and serum.

References

1. B. Beden, C. Lamy, A. Bewick, K. Kunimatsu, J. Electroanal. Chem. 121 (1981) 343.
2. X.H. Xia, T. Iwasita, F. Ge, W. Vielstich, Electrochim. Acta 41 (1996) 711.
3. C. Korzeniewski, C. Childers, J. Phys. Chem. B 102 (1998) 489.
4. H. Wang, C. Wingender, H. Baltruschat, M. Lopez, M.T. Reetz, J. Electroanal. Chem. 309 (2001) 163.
5. H. Wang, T. L€ofler, H. Baltruschat, J. Appl. Electrochem. 31 (2001) 759.
6. E.A. Batista, G.R.P. Malpass, A.J. Motheo, T. Iwasita, Electrochem. Commun. 5 (2003) 843.
7. E.A. Batista, G.R.P. Malpass, A.J. Motheo, T. Iwasita, J. Electroanal. Chem. 571 (2004) 273–282
8. V. Mazumder, Y. Lee, S. Sun, Adv. Funct. Mater. 2010, 20, 1224–1231
9. C.V. Rao, C.R. Cabrera, Y. Ishikawa, J. Phys. Chem. C, 115 (2011) 21963–21970
10. J. Luo, P. N. Njoki, Y. Lin, D. Mott, L. Wang, C. Zhong, Langmuir **2006,** 22, 2892-2898

11. J. Luo, M. M. Maye, N. N. Kariuki, L. Wang, P. Njoki, Y. Lin, M. Schadt, H. R. Naslund, C. J. Zhon, Catalysis Today 99 (2005) 291–297
12. J. Breczko, M. E. Plonska-Brzezinska, L. Echegoyen, Electrochimica Acta 72 (2012) 61– 67
13. N. F. Atta, A. Galal, E. H. El-Ads, Electrochimica Acta 69 (2012) 102– 111
14. M. Hosseini, M. M. Momeni, M. Faraji, J. Appl. Electrochem., 2010, 40, 1421–1427
15. S. Chumillas, M. C. Figueiredo, V.l Climent*, J. M. Feliu, Electrochimica Acta 109 (2013) 577– 586
16. R. Mazeikiene, G. Niaura, A. Malinauskas.. Electrochimica Acta, 51, (2006), 5761-5766.
17. R. Mazeikiene, G. Niaura, A. Malinauskas.. Electrochemistry Communications, 7, (2005), 1021-1026
18. M. A. Climent, A. Rodes, M. J. Valls, J. M. Perez, J. M. Feliu, A. Aldaz, J. CHEM. SOC. FARADAY TRANS., 1994, 90(4), 609-615
19. X. Xing, I. T. Bae, M. Shao, C. C. Liu, J. Electroanal. Chem., 346 (1993) 309 – 321
20. S. Senthil Kumar, J. Mathiyarasu, K. Lakshminarasimha Phani, J. Electroanal. Chem 578 (2005) 95–103

Résumé

La Science et la technologie « Nano » ont reçu beaucoup d'attention récemment en raison de leurs applications passionnantes dans les domaines de l'énergie propre et des dispositifs de détection biomédicale. Aussi, ce qui rend la science et la technologie « Nano » plus pertinentes en ce 21ème siècle est la préoccupation croissante de l'environnement et l'épuisement accéléré des combustibles fossiles. Cet épuisement des matières fossiles et ses implications environnementales associées ont suscité des intérêts de recherche dans le développement de sources d'énergie alternatives qui peuvent être utilisées par les piles à combustible à membrane échangeuse de protons (PEMFC). Un large éventail de nanomatériaux de tailles, de morphologies et de compositions différentes sont maintenant disponibles pour l'application des technologies de l'énergie et des biocapteurs propres. De nouvelles nanoparticules métalliques ont été étudiées dans ce travail en tant qu'électrocatalyseurs potentielles et efficaces pour les piles à combustible à membrane échangeuse de protons (PEMFC) et pour les systèmes de détection. Ces nanoparticules ont non seulement amélioré l' électrocatalyse de petites molécules organiques pour application en pile à combustible, mais aussi affichent une sélectivité améliorée et présentent une bonne sensibilité pour la détection de deux biomolécules cibles. Cette thèse contient la recherche fondamentale sur l,électrooxydation de petites molécules organiques (acide formique, **methanol, dopamine, et** acide ascorbique) sur des métaux nobles (Pt et Au) sous la forme de nanoparticules et leurs surfaces bi-métalliques. L'objectif de la recherche est de permettre de mieux comprendre les relations fondamentales structure de surface /sensibilité de ces réactions et ainsi favoriser le développement des piles à combustible à basse température (piles à combustible de méthanol direct et piles à combustible d'acide formique direct) et des biocapteurs électrochimiques .

Les objectifs spécifiques du travail de thèse étaient :

(1) étudier l'oxydation de l'acide formique et du méthanol sur des nanoparticules à base de platine en utilisant des méthodes électrochimiques classiques (voltampérométrie cyclique et chronoampérométrie) dans un milieu acide. En raison de la faible activité catalytique pour l'oxydation du méthanol en milieu acide [1], ce travail s'est aussi focalisé sur l'étude pour l'oxydation du méthanol en milieu alcalin.

(2) Utiliser des nanoparticules à base d'or pour la détection des molécules bio-organiques telles que l'acide ascorbique et la dopamine dans un milieu neutre. La voltamperométrie cyclique a été utilisée pour étudier le comportement électrochimique de l'acide ascorbique et de la dopamine sur les nanoparticules. La voltamperométrie à impulsion différentielle a été utilisée pour corréler les courants obtenus avec les concentrations des espèces à doser.

Dans ce travail, les nanoparticules à base d'alliage PtAu ont été synthétisées par l'intermédiaire de nos collègues. La méthode de l'ablation laser pulsé en milieu aqueux (PLAL) d'une cible métallique contenant des mélanges stoechiométriques de platine pur et d'or pur a été utilisée dans la préparation des nanoparticules [2]. Le tableau 1.1 résume les principales caractéristiques des nanoparticules.

Tableau 1: Description des propriétés des nanoparticules de Pt -Au préparées par PLAL et utilisées dans ce travail [2] .

Nanoparticules	**Constante de Réseau (A^0)**	**La taille de Cristal (nm)**	**La taille des Particules (TEM) (nm)**	**Structure**
Pt	3.92	2.7	2.5 ±1.1	FCC
$Pt_{70}Au_{30}$	3.96	2.9	2.8±0.8	FCC
$Pt_{50}Au_{50}$	4.015	3.9	3.9±1.7	FCC
$Pt_{30}Au_{70}$	4.03	3.7	3.4±1.6	FCC
Au	4.07	5.2	5.2 ±1.6	FCC

Dans cette thèse, l'activité electrocatalytique de nanoparticules vis-à-vis l'oxydation de l'acide formique, du méthanol (en milieu acide et alcalin), et de la dopamine et acide ascorbique en milieu neutre a été évaluée.

Toutes les mesures électrochimiques ont été effectuées dans une cellule électrochimique à trois électrodes : une électrode de carbone vitreux (de 5 mm de diamètre), une grille de platine et une électrode de référence. Un volume adéquat de la suspension colloïdale $Pt_xAu_{100-}x$, (ou des mélanges de colloïdes de Pt et de Au), correspondant à des quantités totales de 10 ± 0,3 µg catalyseur cm^{-2} pour (FAO et MOR) et 18 ± 0,5 µg catalyseur cm^{-2} pour (DA rt AA oxidation) a été déposée sur la surface du disque de carbone vitreux , ainsi que du Nafion comme liant [3].

Les caractéristiques électrochimiques des nanoparticules bi-métalliques de PtAu sont très sensibles à leur composition de surface. La voltamperométrie cyclique a été réalisée dans des solutions 0,5 M H_2SO_4 saturées en azote pour obtenir la composition de surface des nanocatalyseurs, et des voltamogrammes cycliques typiques sont présentés dans la figure 1. La figure 1a révèle des caractéristiques bien établies d'une surface de Pt polycristallin. : Une paire de pics anodiques (cathodiques) attribués à la désorption (adsorption) d'hydrogène des sites Pt (100) et Pt (110) entre 0,05 et 0,40 V; suivie d'une région de potentiel sans relief attribué à ce que l'on appelle la région de la double couche ; à des potentiels plus positifs que 0.8 V, lo'oxyde de Pt est formé puis réduit lors du balayage de retour à 0.73 V. Le voltamperogramme des nanoparticules d'or' ,figure 1b , représente également les caractéristiques de surfaces d'or polycrystallin, c'est à dire large région de potentiel correspondant à la double couche , entre 0,05 et 1,13 V , suivi par le courant d' oxydation et de réduction de - l'oxyde à environ 1,18 V. Dans le cas des nanoparticules bimetalliques PtAu (en alliage et en mélange), une combinaison linéaire des deux surfaces métalliques pures est observée , à savoir les deux pics d'hydrogène sur Pt, bien définis à 0,12 V et 0,26 V, la réduction del'oxydes de Pt à 0,72 V. ainsi que la présence du pic de la réduction de l'oxyde d'or à ca. 1.17 V.

Il est également intéressant de noter qu'aux potentiels anodiques limites (> 1.6V dans Fig. 1b), la densité de courant sur les nanoparticules de Pt a considérablement augmentée comparée aux deux alliages PtAu et aux mélanges des nanoparticules, ce qui indique la forte activité des nanoparticules de Pt pour la réaction d'évolution d'oxygène [3].

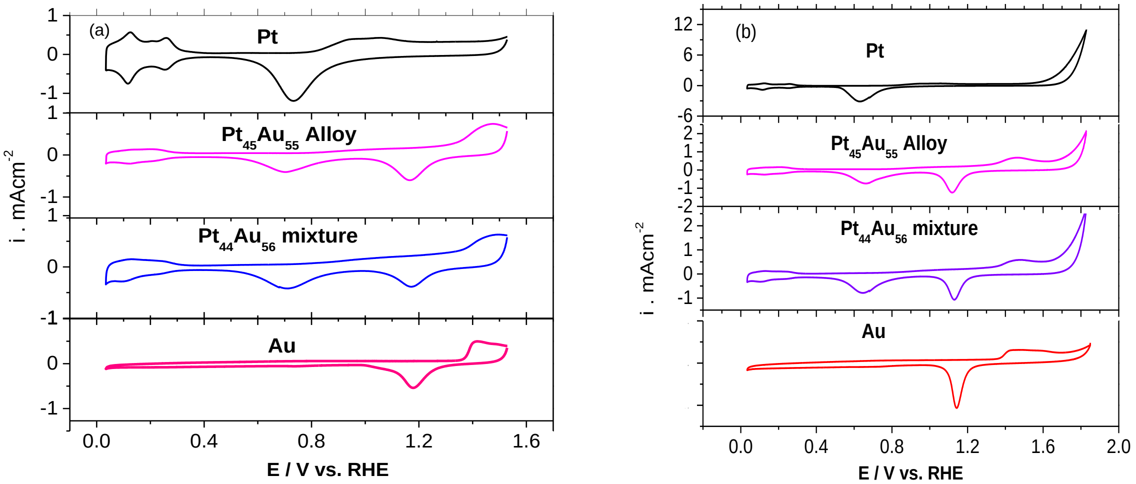

Figure 1. Réponses de VC (50 mV s-1) pour Pt. Mélange $Pt_{45}Au_{55}$ alliage $Pt_{44}Au_{56}$et Au dans Ar-saturé 0,5 M H_2SO_4 à (a) 1.5V et (b) de 1,8 V vs RHE.

Dans la plupart des cas, une étape de vieillissement électrochimique a été réalisée avant les mesures de la FAO. Ceci a été réalisé en effectuant un nombre fixe de CV dans 0,5 M de H_2SO_4 (0.05 - 1.80V, 100 mV / s). Par conséquent, l'évolution de la composition de surface des alliages et des mélanges avec le cyclage de potentiels dans 0,5 M de H_2SO_4 a été surveillée et son impact sur l'électro-oxydation de l'acide formique a également été évalué.

Comme mentionné ci-dessus, la teneur surfacique en Pt (surface de [Pt]) des alliages Pt_xAu_{100-x} et mélanges Pt_x+Au_{100-x} a été estimée par analyse de leurs CV l'équation 1 a été utilisée :

$$\lfloor Pt \rfloor_{Surface} = \frac{ECSA_{Pt}}{ECSA_{Au} + ECSA_{Pt}} \quad .....(1)$$

où ECSA $_{Pt}$ et $ECSA_{Au}$ ECSA sont les surfaces électro-chimiquement actifs (cm2) de platine et d'or, respectivement. ECSA $_{Pt}$ a été déterminée à partir de l'intégration de la charge électrique lors de la réduction de l'oxyde de et en utilisant le facteur de conversion de 440 µC cm^{-2} Pt. [4-6]. De la charge du pic de réduction de l'oxyde de l'Au, , et $ECSA_{Au}$ a été déterminée en utilisant un facteur de conversion de 400 µC cm-2 Au [7, 8]. Friedrich et al. ont insisté sur le fait que la détermination des ECSAs de la réduction de l'oxyde est plus pratique que la désorption de l'hydrogène en raison des charges plus élevées impliquées [9].

La figure 2 présente l'évolution de la concentration surfacique en Pt par rapport à la teneur massive en Pt pour les alliages Pt_xAu_{100-x} et les mélanges de nanoparticules, Pt_x+Au_{100-x} Il est évident qu'il existe une diminution du nombre d'atomes de surface de Pt pour les catalyseurs à base de mélanges de Pt + Au, (courbe rouge). Contrairement aux alliages de Pt_x Au_{100-x}, l'épuisement élevé de Pt en surface dans les mélanges pourrait être due à l'instabilité du Pt en solution acide [10 - 12]. En revanche, la structure d'alliage avec Au-renforce la stabilité du Pt à haut potentiels.

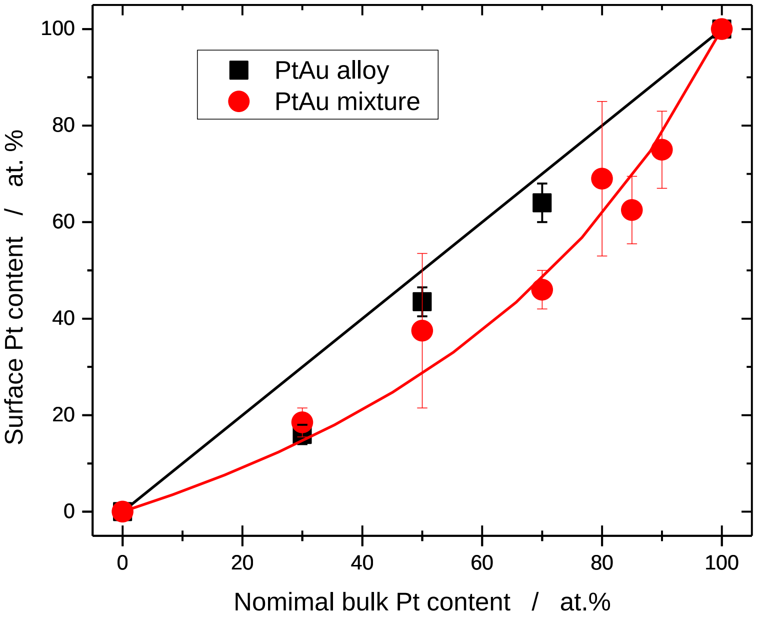

Figure 2 : Variation de la teneur en Pt de surface en fonction de la teneur en Pt total après vieillissement électrochimique de catalyseurs par cyclage entre 0,05 et 1,80 V à 0,5 M H_2SO_4 (50 mV s^{-1}, 50th cycle).

La figure 3a montre des voltamperogrammes cycliques représentatifs de l'oxydation de l'acide formique sur Pt, un alliage $Pt_{45}Au_{55}$, un mélange $Pt_{44}Au_{56}$ et Au. On peut observer deux pics anodiques lors du le balayage positif sur la surface de Pt. Il est connu que les produits d'oxydation de l'acide formique se forment par l'intermédiaire deux mécanismes parallèles impliquant l'oxydation directe en CO_2 et la déshydratation avec la formation de CO adsorbé (pic à 0.9V) [13]. Sur le Pt, la voie de déshydratation indésirable, l'emporte sur l'oxydation directe; En insérant de l’or le rapport stoechiometrique Pt: Au diminue et l’'oxydation directe domine le processus d'oxydation (pic à 0.56 V).

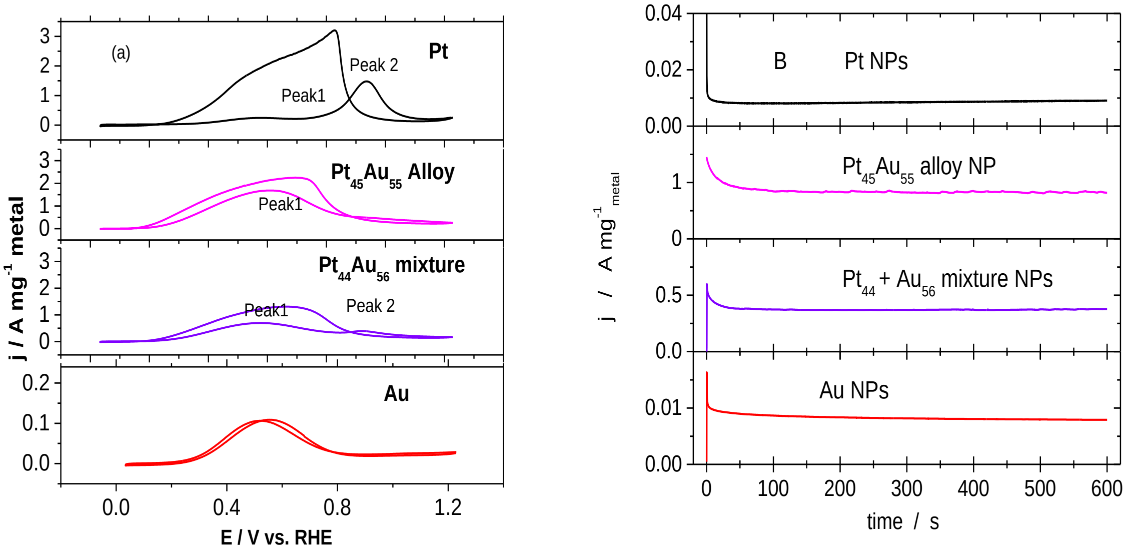

Figure 3 : (A) Voltamperogrammes cycliques à 50 mV / s et (b) chronoamperogrammes (E = 0.56V) sur des nanoparticules de Pt, d’alliage $Pt_{45}Au_{55}$, et du mélange Pt_{44} + Au_{56} et d’Au dans 0,5 M H_2SO_4 + 1 M HCOOH.

La chronoampérométrie a été utilisée pour étudier l’activité à l'état stationnaire pour l'oxydation de l'acide formique sur des nanoparticules d'alliage Pt_xAu_{100-x}. La même expérience a été réalisée sur les mélanges correspondants de nanoparticules du platine et d'or purs. Les courbes chronoampérométriques ont été enregistrées en maintenant le potentiel de l'électrode à 0,25 V pendant 10 s, puis en appliquant 0,56 V (pic 1) pendant 600 s (figure 3B). Une corrélation a été établie entre la densité de courant en A cm^{-2}_{metal} mg^{-1}_{metal} et en mA après 600s d’électrolyse et la composition de la surface bimétallique pour les alliages Pt_xAu_{100-x} et les mélanges Pt_x+Au_{100-x}. Les résultats ont montré un comportement du type volcan, avec un maximum autour de 50% de Pt pour les alliages et les mélanges, comme anticipé à partir de la prévalence de l'oxydation directe sur les catalyseurs binaires (Figure 3).

Lorsque l'activité électrocatalytique des deux types de matériaux est normalisée par rapport à la surface spécifique total (figure 4A), les deux courbes sont pratiquement superposées (la différence est inférieure à 20%). Ce n'était pas le cas pour l’activité normalisée à la masse de Pt ou en facteur de deux existe entre l'alliage et le mélange de nanoparticules correspondantes.

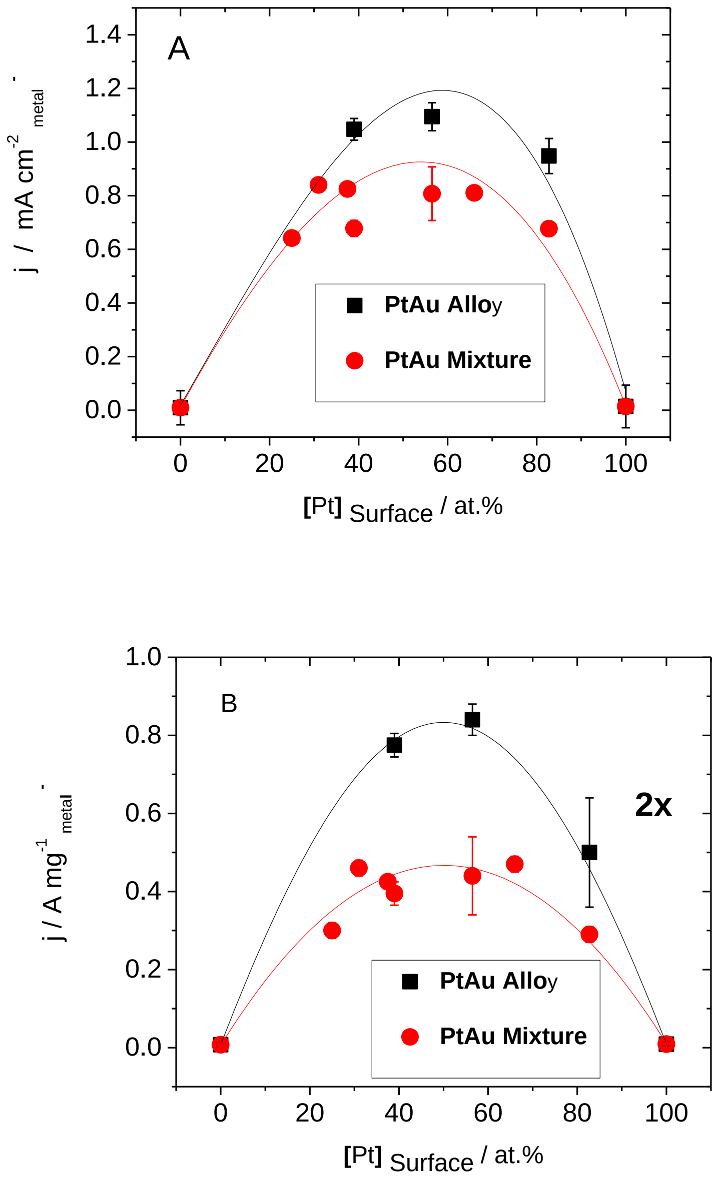

Figure 4 : densités de courant après 600 s (a) A mg^{-1}_{metal} et (b) $mAcm^{-2}_{metal}$ pour les alliages Pt_xAu_{100-x} et les mélanges Pt_x+Au_{100-x} par chronoampérométrie à 0.56 V dans 0,5 M H_2SO_4 + 0,5 M HCOOH.

La relation activité électrocatalytique / composition des nanoparticules sur l’oxydation du méthanol est également étudiée, et les résultats dans les deux milieux (acide et alcalin) mis en corrélation. Les résultats ont montré que l'activité catalytique de l'alliage PtAu diminue progressivement avec la teneur en Au en milieu acide. En milieu basique, l’activité pour l’oxydation du methanol sur les alliages PtAu suie une forme de volcano présentant un maximum d'activité à 50% de Au (figure 5). Les raisons qui affectent le comportement électrocatalytique de ces alliages PtAu ont été discutées. Par exemple, l'influence de l'adsorption d'anions OH- sur l'oxydation du méthanol dans une solution alcaline sur les alliages PtxAu100-x est analysée. La nature de l'espèce source d'oxygène ainsi que leur rôle dans l'oxydation du méthanol est proposé.

L'activité catalytique du catalyseur Pt_xAu_{100-x} NP en milieu acide a diminué de façon monotone avec l'augmentation de teneur en Au. La décroissance monotone de l'activité d'oxydation du methanol suggère que le nombre de sites de Pt qui est responsable de la déshydrogénation de methanol détermine la grandeur de l'activité d'oxydation du methanol PtAu l'alliage IP. Cependant, en milieu alcalin, l'augmentation de l'activité d'oxydation du methanol avec l'augmentation de Au présentant une teneur maximale de 50% de teneur en Au. Cette forte activité en milieu alcalin est suggestive de l'activité catalytique élevée de Au en milieu alcalin qui favorisent le mécanisme bifonctionnel dans les IP PtAu à augmenter l'activité sur celle de purs IP Pt. L'effet de l'espèce OH adsorbées à la surface de l'alliage Pt_xAu_{100-x} et leur relation avec les structures électroniques sont également mis en place.

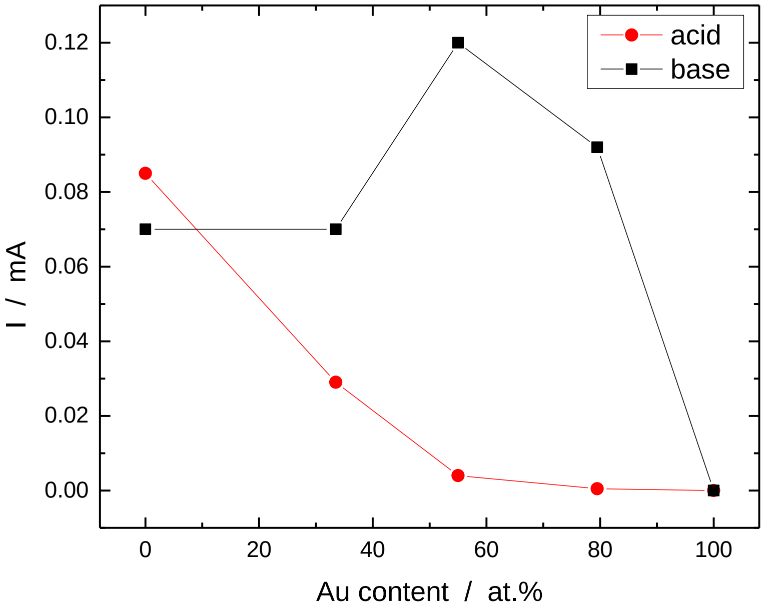

Figure 5: Courants obtenus après 900 s d'électrolyse en présence de 0,5 M CH_3OH en fonction de la teneur en Au dans les alliages PtAu en millieu acide et alcalin.

Cette thèse décrit également les résultats de l'oxydation électrocatalytique de la dopamine (DA) et de l'acide ascorbique (AA) sur les nanoparticules Au_xPt_{100-x}. L'activité des nanoparticules AuPt pour l'oxydation électrochimique de la dopamine et de l'acide ascorbique sont fortement dépendantes de la composition des nanoparticules. Il est important de remarquer que l'activité à l'oxydation DA diminue avec l'augmentation de la teneur en Pt dans les alliages (figure 6A). Cette diminution de l'activité a été attribuée à une diminution du nombre de sites d'adsorption de DA sur la surface des nanoparticules. De plus, les nanoparticules d'Au et les nanoparticules Au-Pt riches en Au ont montré une excellente activité électrocatalytique pour l'oxydation de l'AA, avec l'alliage $Au_{70}Pt_{30}$ avec l'activité la plus élevée (Figure 6B). Cela suggère un effet synergique entre le Pt et l'Au lorsque présent sous forme d'alliage.

L'augmentation importante du courant de pic d'oxydation de l'acide ascorbique est attribué à la fois au décalage négatif du potentiel du pic d'oxydation et à l'effet électronique favorable de l' d'alliage Au Pt. En d'autres termes, l'activité catalytique de l’ alliage $Au_{70}Pt_{30}$ est grandement améliorée grâce à un effet synergique.

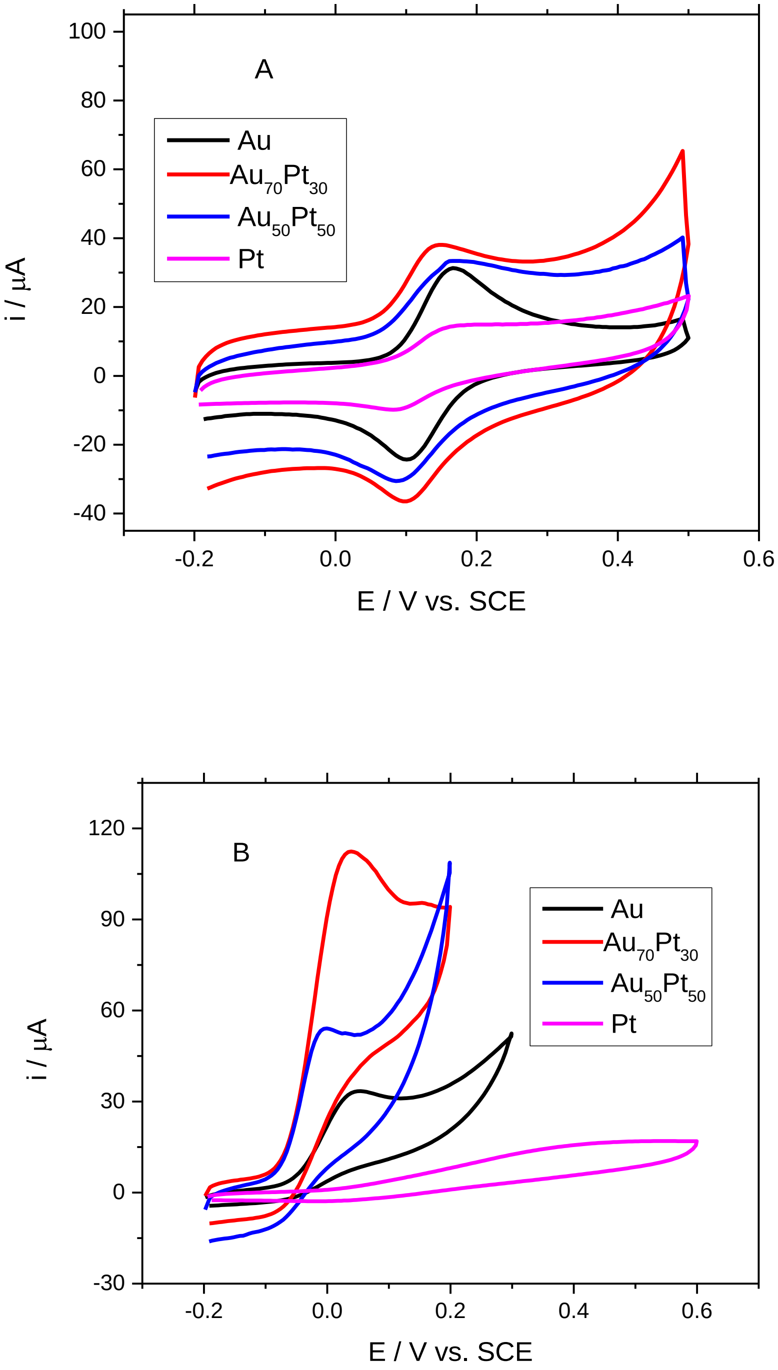

Figure.6: CVs de (a) 20 µM DA et (b) 2.0 mM AA des nanoparticules Au_xPt_{100-x} à un pH de 7.0 0.1 M PBS et à une vitesse de balayage de 50 mVs^{-1}.

Les études électrochimiques par voltamperométrie pulsée différentiel ont montré que l'oxydation de DA et de l’AA sur des nanoparticules de AuPt avienne avec une séparation des potentiel de 156 mV et 190 mV sur l’Au et sur l’alliage $Au_{50}Pt_{50}$, respectivement. Ceci est assez significatif pour la détermination de la DA même en présence de AA (figure 7A). Les courants en présence de DA et AA augmentent linéairement avec leurs concentrations pour toutes les électrodes sélectionnées (figure 7B).

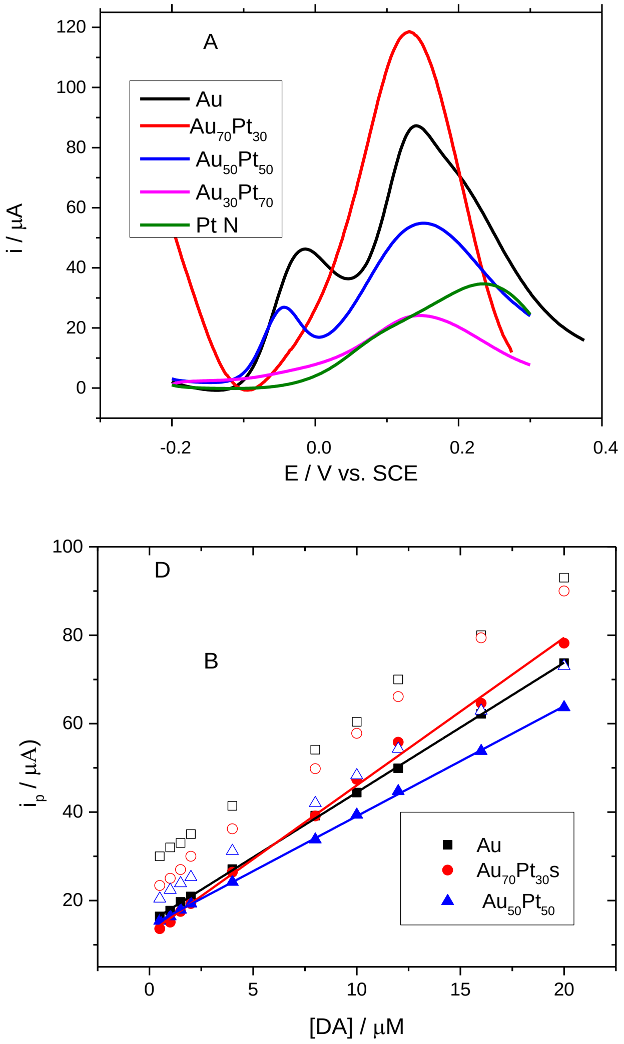

Figure 7: (a) DPV des alliage AuxPt100-x en présence de 20 uM DA + 2,0 mM AA ;PBS 0,1 M à pH 7,0 conditions DPV: vitesse de balayage, 20mVs-1; amplitude, 50mV; largeur d'impulsion, 50 ms; période d'impulsion, 200ms et (b) des courbes d'étalonnage pour DA seul (symboles ouverts) et DA, en présence d'AA (symboles pleins).

Références

1. J.S. Spendelow , A. Wieckowski , Phys . Chem. Chem. Phys . 9 (2007) 2654 - 2675 .
2.] J. Zhang , DN Oko , S. Garbarino , R. Imbeault , M. Chaker , A. C Tavares , D. Guay , D. Ma, .J. Phys . Chem. C (2012), 116 (24), 3413-13420
3. C.V. Rao , C.R. Cabrera , Y. Ishikawa , J. Phys . Chem. C 2011 , 115 , 21963-21970
4. H.A. Kozlowska , B.E. Conway , A. Hamelin , L. Stoicoviciu , J. Electroanal . Chem. 228 (1987) 42916
5. D. V. Heyd, D.A. Harrington, J. Electroanal. .Chem.. 335, (1992) 19
6. D. V. Heyd, D. A. Harrington, J. Power sources, 197 (2012) 72-79 .
7. M. Markovic, J. Phys. Chem. B (2005), 109, 14433.
8. K. A. Friedrich, F. Henglein, U. Stimming, W. Unkauf, Electrochimica Acta 45 (2000) 3283
9. K. A. Friedrich , F. Henglein, W. Unkauf , colloïdes Surf . A 134 (1998) 193
10. A.V. Ruban, H. L. Skriver, J. K. Norskov, Phys . Rev B (1999), 59, 15990 - 16000
11. Y. Shao -Horn, W. C. Sheng, S. Chen, P. J. Ferreira, E. F. Holby, D. Morgan, Top 10 Catal. (2007) 1244-9000
12. M. D. Obradovic, S. L. Gojkovic, J. Electronaal. Chem. 664 (2012) 152-155
13. X. Yu , PG Pickup, J. Power Sources 182 (2008) 124 .